Enhancing hydrogen production on Earth-abundant electrocatalysts: A computational investigation

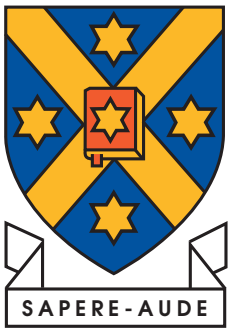

Charlie Ruffman

Department of Chemistry

University of Otago

A thesis submitted for the degree of Doctor of Philosophy

at the University of Otago, New Zealand

September 8, 2021

"All models are wrong, but some are useful."

– George Box

Acknowledgements

My deepest thanks go first to Anna Garden, my supervisor. Anna has supported me at every turn on the journey through this PhD – whether that is bringing her determination and insight to sit down and solve a tough problem, or simply being happy to talk through things that have been stressing me. Both in supervision and teaching, Anna brings a resounding understanding that the person she's talking to is more than just their work, and she spends the time to help in the ways that are most valuable. In continuing forward in science and research, I can say without a doubt that Anna is an inspiration to me. I hope that one day I can find the same patience, kindness, and alacrity that you bring to research, and I look forward to the possibility of working together in the future.

To my partner, Marissa, I cannot express just how thankful I am for the wonderful support you have so kindly given throughout the years we have been together. You have been beyond understanding, I adore your company, and I greatly appreciate all the experiences we have had during our time at Otago. I hope to be there for you in any way I can as you come towards the end of your PhD.

My heartfelt thanks go out to all the other members of the Garden group, both past and present. I never expected to be lucky enough to work with such a great group of people, and it makes me very happy to count you all friends. I would like to make special mention of Calum Gordon, Ciaran Ward, Tom Gilmour, Frank Mackenzie and Chris Mills, who have all worked alongside me on hydrogen evolution. I would also like to specifically thank my close friend Caitlin Casey-Stevens – going through the PhD process alongside you has been a (great) time, and I wish you the very best for the future.

I would also like to thank my co-supervisor Sally Brooker, who's sage career advice and scientific wisdom have been much appreciated.

To those who have so kindly given up your time and the ink in your red pens to proofread this thesis – Marissa Le Lec, Ciaran Ward, John Whiting, Chris Mills, and Nicholas Smith – thank you for catching what I missed.

Throughout my time in the Chemistry Department here at Otago, there have been many people who have inspired and helped me along the way. To Carla Meledandri, thank you for your willingness to help me out whenever I've asked. I greatly appreciate the chats we have had, be that when teaching together or simply when I bump into you. To James Crowley, one could not ask for a more supportive postgraduate coordinator, and I always value your help, advice, and banter.

To my Mum and Dad, I am so deeply thankful that you sparked my curiosity in science, and laid the groundwork that led me to where I am now. Thank you also for all the love and help you have given me during this whole journey. Mum, you have always been able to bring a smile to my face, and you know exactly how to cheer me up. Dad, you have been a rock of support for me, and I so greatly value the times we've spent together working on projects or having coffee.

The MacDiarmid Institute have also been incredibly supportive to all the students under their umbrella, both in terms of providing opportunities for professional growth, and offering support during hard times. During the Coronavirus lockdown in 2020, the Institute rallied together to provide extensions for PhD students, and I can safely say that this time allowed me to finish the research in this thesis to a much higher standard.

Lastly, to anyone reading this – be you a future student in the group or simply an interested party – I wish you the best in your endeavours, and I hope the work contained here may be of help.

Abstract

In the move towards a carbon-zero energy economy, molecular H_2 offers great promise as a clean energy storage and transport mechanism. The production of H_2 in a carbon-neutral and environmentally sustainable manner is therefore a critically important step towards mitigating anthropogenic climate change. Electrocatalytic splitting of water is an ideal route to clean H_2 production on an industrial scale, but this requires an effective and affordable catalyst. In this thesis, density functional theory calculations are used to explore two different nanostructured catalysts in this role. The optimisation of molybdenum disulfide (MoS_2), which is an Earth-abundant and low-cost material, is explored in depth. Several structural modifications which significantly improve its activity are reported. Following this, a preliminary investigation into nanostructured tantalum nitrides (TaN and Ta_3N_5) as related binary catalysts is also performed.

First, the mechanism for hydrogen evolution on MoS_2 is studied using a detailed model of the electrochemical cell that accounts for both solvent and potential. The effects of two common support materials (graphene and Au(111)) below MoS_2 are also considered. It is found that hydrogen evolution proceeds by a Volmer-Heyrovský type process, where H first adsorbs to an S atom on the edge of MoS_2, diffuses to an Mo atom, then reacts with another proton from solution to form H_2. This dominant mechanism stays the same with MoS_2 on either a graphene or Au(111) support. The different supports primarily influence the reaction rate through changing the adsorption energy of H, which determines the reaction thermodynamics. The overall activation barrier is calculated to be about 1.30 eV (at 0 V *vs* the standard hydrogen electrode) for both supported cases. However, the support is also found to strongly influence how the barrier responds to changes in potential,

with the barrier on MoS_2/Au(111) dropping much more rapidly as the potential becomes more negative.

Unfortunately, neither the Au(111) nor graphene support notably improve the hydrogen evolution activity of MoS_2. Thus, in a following study, we screen across a wide range of different support materials for the catalyst, all based on doped graphene derivatives. Here, the free energy of H adsorption ($\Delta G_{H_{ads}}$) is examined, as this was found to capture the majority of change in the reaction rate in response to different supports in the previous chapter. A high degree of tunability of $\Delta G_{H_{ads}}$ is observed on both the MoS_2 basal plane and the edge sites. Critically, it is found that an N-doped graphene support yields ideal thermoneutral (0 eV) H adsorption on the Mo-edge, suggesting this would make a very active catalyst for hydrogen production. For the basal plane, no support is able to bring $\Delta G_{H_{ads}}$ close to 0 eV with the lowest value being about 1.4 eV. However, the changes observed in $\Delta G_{H_{ads}}$ are rationalised using density of states analyses, which show that $\Delta G_{H_{ads}}$ decreases towards 0 eV with the addition of supports that shift the energy of the filled S atom states towards the Fermi level. A different pattern is observed for the MoS_2 edge, where $\Delta G_{H_{ads}}$ is found to increase towards 0 eV when supports that donate more electron density to MoS_2 are added. The discovery of these trends assists in understanding the key factors contributing to catalyst activity, and aids in the design of novel catalysts.

To explore further improvements to the activity of the MoS_2 basal plane, which makes up a large portion of the material but was not strongly activated by the addition of supports, we also examine both armchair and zigzag nanotube forms of MoS_2. Here, the strain induced by coiling significantly lowers $\Delta G_{H_{ads}}$, such that smaller (more highly strained) nanotubes adsorb H more strongly. With the induction of S-vacancy defects in the nanotubes, which are known to commonly occur during synthesis, a thermoneutral $\Delta G_{H_{ads}}$ value is found for nanotubes around 20 Å in diameter. The trends in $\Delta G_{H_{ads}}$ with nanotube diameter are once again rationalised using density of states arguments, showing that $\Delta G_{H_{ads}}$ decreases alongside the energy gap between filled S atom p-states and unfilled Mo d-states.

Lastly, an exploratory study into the nanoparticulate structures of TaN and their hydrogen evolution activity is performed. Possible nanoparticle structures are determined

using a recently developed machine-learning-assisted global optimisation algorithm. Two compositions, TaN and Ta_3N_5, and two sizes, 16 and 24 atoms, are studied. For the 1:1 composition, regular Ta core structures are observed with adsorbed N atoms around the nanoparticle surface. In contrast, at the 3:5 composition notably more open structures are found, where N integrates into the centre of the cluster. The nanoparticle structures adsorb H much more strongly than the (100) and (111) surfaces of TaN, and H favours different adsorption sites, suggesting that their hydrogen evolution properties are very different from the bulk. However, future work will need to perform a more detailed study at higher H coverages and considering competing reactions.

The work in this thesis contributes to our understanding of the factors governing nanoscale catalyst activity for the hydrogen evolution reaction. Several synthetically accessible modifications to the MoS_2 catalyst that could greatly improve its activity are suggested, representing a step towards affordable and sustainable hydrogen production on an industrial scale.

Publications

The following publications are integrated components of this thesis:

1. **Ruffman, C.**, Gordon C. K., Skúlason E., and Garden, A. L. "Mechanisms and potential-dependent energy barriers for hydrogen evolution on supported MoS_2 catalysts," *Journal of Physical Chemistry C*, **2020**, *124*, 17015–17026.

2. **Ruffman, C.**, Gordon, C. K., Mackenzie, F. D., Gilmour, J. T. A., and Garden, A. L. "Enhancing the hydrogen evolution activity of MoS_2 basal planes and edges using tunable carbon-based supports," *Nanoscale*, **2021**, *13*, 3106–3118.

3. **Ruffman, C.**, Gilmour, J. T. A, and Garden A. L., "Size-dependent trends in the hydrogen evolution activity and electronic structure of MoS_2 nanotubes," *Nanoscale Advances*, **2021**, *accepted*.

The following publications from the duration of this PhD are not included in the thesis:

1. Casey-Stevens, C. A., Lambie, S. G., **Ruffman, C.**, Skúlason E., and Garden, A. L. "Geometric and electronic effects contributing to N_2 dissociation barriers on a range of active sites on Ru nanoparticles," *Journal of Physical Chemistry C*, **2019**, *123*, 30458-30466.

2. Gilmour, J. T. A., Casey-Stevens, C. A., **Ruffman, C.**, and Garden, A. L. "The selective reduction of NO to N_2 on Pt(111) and Pd(111) surfaces," *Journal of Physical Chemistry C*, **2021**, *submitted*.

Contents

List of Figures

List of Tables

List of Abbreviations

$\Delta G_{\mathrm{H_{ads}}}$	Hydrogen adsorption free energy
$\Delta E_{\mathrm{H_{ads}}}$	Electronic hydrogen adsorption energy
U	Applied potential
E_a	Activation energy (or barrier)
AIMD	*Ab initio* molecular dynamics
B3LYP	Becke-3-parameter-Lee-Yang-Parr
BDG	Boron doped graphene
BEEF-vdW	Bayesian error estimation functional with van der Waals correlation
BO	Born–Oppenheimer
CC	Coupled Cluster
CI	Configuration Interaction
CPU	Central processing unit
DFT	Density functional theory
DOS	Density of states
FCC	Face centred cubic
FS	Final state
GGA	Generalised gradient approximation
GO	Graphene oxide
GOFEE	Global optimisation with first principles energy expression
GPR	Gaussian process regression
GTO	Gaussian type orbital
$\mathrm{H_{ads}}$	Adsorbed hydrogen
HBN	Hexagonal boron nitride
HER	Hydrogen evolution reaction
HF	Hartree-Fock
IS	Initial state
KS	Kohn–Sham
LDA	Local density approximation
MEP	Minimum energy path
mGGA	Meta generalised gradient approximation
ML	Monolayer
NDG	Nitrogen doped graphene
NEB	Nudged elastic band
OER	Oxygen evolution reaction
PAW	Projector-augmented wave
PBE	Perdew-Burke-Ernzerhof
PES	Potential energy surface
SDG	Sulfur doped graphene
SHE	Standard hydrogen electrode
STM	Scanning tunnelling microscopy
TMN	Transition metal nitride
TS	Transition state
VASP	Vienna *Ab initio* Simulation Package
vdW	van der Waals

Enhancing hydrogen production on Earth-abundant electrocatalysts: A computational investigation

Chapter 1

Introduction

1.1 The motivation for hydrogen

Over one hundred years ago Svante Arrhenius, Professor of physical chemistry, presented an article to the Royal Swedish Academy of Science entitled: *"On the influence of carbonic acid in the air upon the temperature of the ground"*.[1] This treatise, although originally intended to explain past ice ages, is often regarded as the first prediction of climate change caused by the release of greenhouse gasses such as carbon dioxide (CO_2). Arrhenius' model suggested, in his own words, that:

> *"...if the quantity of carbonic acid increases in geometric progression, the augmentation of the temperature will increase nearly in arithmetic progression."*

Since its publication in 1895, the paper would later become recognised as a core foundation of modern climate science. Though its message – that the release of CO_2 into the atmosphere results in climate warming – did not receive large amounts of scientific attention until much closer to the modern day.[a]

It is now known that a drastic reduction in the emission of CO_2 from the combustion of fossil fuels and carbonaceous materials must be achieved by 2050 at the latest in order to limit climate warming to 2 °C.[2,3] As a result, there is both a widespread and pressing drive to move away from fossil fuels and towards carbon-neutral energy carriers.

[a] Indeed, one could argue that public attention to this problem lags even further behind.

Molecular hydrogen (H_2) is one such alternative energy carrier that has received a great deal of attention,[4–10] primarily because its combustion to release stored energy produces only water as a product (Equation 1.1).

$$2\,H_2 + O_2 \longrightarrow 2\,H_2O \tag{1.1}$$

In this way, H_2 fuels are both carbon-zero and avoid many other harmful by-products such as SO_x and NO_x species that are associated with combustion of fossil fuels.[11] It also has certain advantages over traditional fuels in terms of energy efficiency, including low ignition temperatures[12] and excellent gravimetric energy density,[13] making it a leading contender for rocket or aircraft fuel.

Gaseous H_2 is not only an alternative fuel but also a critical industrial reactant used across many reactions. One of its largest current uses is in the Haber-Bosch process to generate ammonia for nitrogenous fertiliser, which accounts for 2-3 % of global energy demands[14] and produces 3300 t of ammonia each day.[15] H_2 also plays a key role as a reductant in the electronics industry, allowing the epitaxial growth of silicon for circuit manufacturing,[16] and in metallurgy, where it is used in the steel refining process.[17] Overall, it is abundantly clear that an efficient and environmentally sustainable way of obtaining H_2 is required.

Unfortunately, the use of H_2 as both a fuel and a reactant is not without its challenges. Firstly, the storage and transport of H_2 is somewhat limited by its low volumetric density.[18] Additionally, while its flammability is a big advantage in terms of fuel ignition efficiency, this poses some safety concerns for storage. Currently, the most common technique to store H_2 is as a compressed gas.[19] However, many existing and emerging technologies are more efficient and safe.[20–22] For example, H_2 can be stored as a metal-hydride with the lighter metals (e.g. Li, Na, Mg),[22] in a metal-organic framework,[23] or in carbon nanostructures such as nanotubes.[20,24] While the storage of H_2 doubtlessly deserves attention, it is not the topic of this thesis.

The second major challenge associated with H_2 is its production. Although natural reservoirs of H_2 exist on Earth – often buried, similar to hydrocarbon-based natural

gasses[25] – it is infeasible to harness these on an industrial scale, primarily due to the fact that H_2 is the lightest possible molecule and has a very low density by volume. As such, it readily escapes drilling and extraction. Therefore, H_2 must instead be produced synthetically. This challenge of producing H_2 efficiently and cleanly is the primary focus of this thesis.

Presently, the vast majority of H_2 (about 95 %) is produced *via* steam reformation of methane (Equation 1.2),[26–28] followed by the water-gas shift reaction (Equation 1.3):

$$2\,CH_4 + \frac{1}{2}\,O_2 + H_2O \longrightarrow 5H_2 + 2CO \tag{1.2}$$

$$CO + H_2O \longrightarrow CO_2 + H_2 \tag{1.3}$$

The infrastructure for this process is well established and it can produce H_2 on a relatively large scale. However, it is fundamentally flawed for long-term sustainability. Primarily, the use of methane in steam reforming draws on dwindling fossil fuel reserves, and still results in the release of CO or CO_2. Additional environmental harm is caused by the fact that steam reforming reactors require high temperatures and pressures to function, which have a large energy cost.[29] In this way, H_2 from steam reforming is often referred to as "brown" hydrogen, in that it does not address the environmental concerns that motivate using H_2 as a fuel.[30] Other industrial processes to form brown H_2, such as coal gasification, also suffer from the same general flaws.[26]

In contrast, it is possible to produce "green" H_2 without reliance on fossil fuels or emission of CO_2 *via* the electrolysis of liquid water.[8,31] This process is often referred to as the water splitting reaction (Equation 1.4).

$$2\,H_2O \xrightarrow{\text{catalyst}} 2\,H_2 + O_2 \tag{1.4}$$

The electrical energy required to drive the reaction can be readily provided by renewable electric energy sources such as solar, wind, or hydro power.[8,9] H_2 that is produced in this manner and then used as a fuel in places of need gives a carbon-zero energy cycle, as is displayed in Figure 1.1.

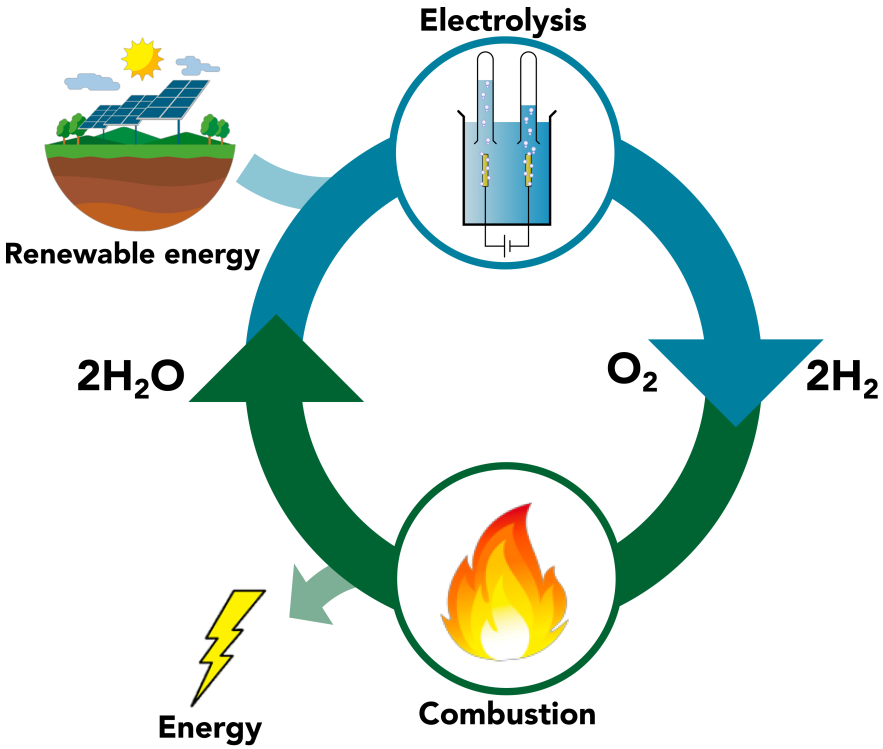

Figure 1.1: A schematic depiction of the hydrogen cycle, where electrocatalytic water splitting is powered by renewable energy sources to produce H_2 and O_2. The H_2 can be burned at a time and place where energy is needed, for instance in motive transport or to meet surges in electricity demand, producing only water vapour as the product.

1.2 Producing green hydrogen from water

As with all electrolysis processes, the water splitting reaction is composed of two half-reactions. At the anodic side of the electrochemical cell, H_2O is oxidised to produce protons and electrons in the oxygen evolution reaction (OER, Equation 1.5). The protons and electrons generated are recombined at the cathodic side of the cell in the hydrogen evolution reaction (HER, Equation 1.6).[32,b]

$$2\,H_2O \longrightarrow O_2 + 4\,H^+ + 4\,e^- \tag{1.5}$$

[b]The reactions addressed in this thesis all take place in acidic media, which is where the majority of work on water splitting has been done. In alkaline media, OH^- plays a role[33] which is not completely understood, and the reaction proceeds much slower.[34] Therefore, while interesting as a future goal, alkaline water splitting is not as pertinent to current industrial applications and is therefore omitted from further discussion.

$$4\,H^+ + 4\,e^- \longrightarrow 2\,H_2 \tag{1.6}$$

The process requires both a catalyst (or catalysts) and an applied voltage (or potential difference) in order to proceed at industrially relevant rates.[32,35,36] The electrons and voltage required to drive water splitting can be supplied to the catalyst from an external electrical source, such as a battery or a current generated directly by renewable energy sources. This overall process is referred to as electrocatalysis.[c]

There is a great deal of ongoing work regarding overall (or bifunctional) water-splitting catalysts that are able to drive both the OER and the HER at the same time.[37–40] Promising materials include CoP films,[41] metal oxide nanoparticles of IrO_2[42] or $NiFeO_x$,[43] and hybrid materials such as Fe-Ni phosphides supported on Ni foam.[44] However, one unique advantage of an electrochemical processes is that the reduction and oxidation reactions can be spatially separated, occurring on different sides of the cell (as is seen in Figure 1.2). Therefore, rather than using one catalyst for the whole water splitting reaction, an alternative approach is to design specialised catalysts for the HER and OER which can be separately applied at the cathode and anode, respectively. In this way, the problem of catalyst design and optimisation is simplified and refined down to just one half-reaction at a time. In this work, the HER will be studied in depth. It is a deceptively simple reaction where its catalysis requires much attention and research to be viable on an industrial scale.

It is widely established that Pt-based solid metal catalysts are the most active for driving the HER,[36,45,46] and they also have the added benefit of long-term stability, being composed of a noble metal.[47] Experimental studies have reported high rates of hydrogen evolution on the common low-index surface facets of Pt crystals: (100), (110), and (111).[48–50] Many works also implicate the surface defects, such as atomic steps or edges, as the most active sites.[51,52]

Unfortunately, the scarcity and expense of Pt make the pure metal economically undesirable as an industrial catalyst. Pt prices at the time of writing are around $40

[c] Alternatively, the energy can come directly from light capture by a dye or photo-absorber, which is called photocatalysis.[37,38] The light absorption causes an energetic promotion of an electron which is then transferred to the catalyst to do work. Electrocatalysts can often be applied to photocatalytic scenarios by simply attaching them to light absorbing substrates with the right properties.[37]

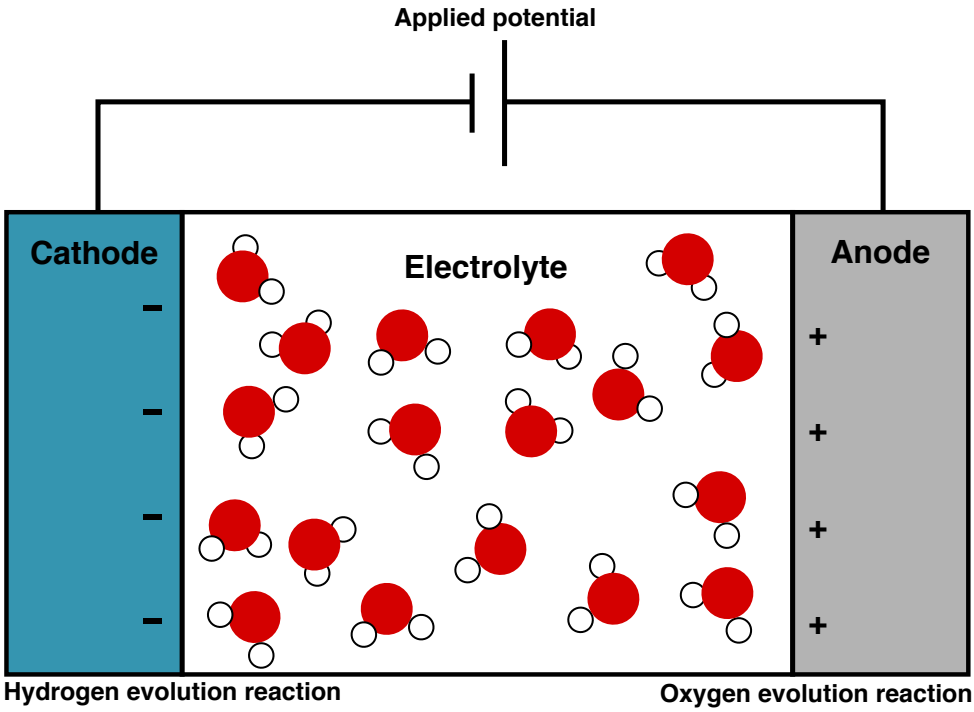

Figure 1.2: A schematic of an electrochemical water splitting cell. A current and voltage are supplied to drive oxygen evolution at the anodic side, and hydrogen evolution at the cathodic side. Note that these two reactions are spatially separate, and can be catalysed independently.

USD per gram, placing it as one of the most expensive precious metals, and these prices have been increasing over the last 20 years (by a factor of about 1.5).[53] Some research has sought to overcome the problem of cost by reducing the amount of Pt used in the catalyst. One idea is to incorporate Pt nanoparticles into a cathode made of a cheap conducting material such as polyaniline.[54] As nanoparticles have a high surface-area-to-volume ratio, this reduces the amount of Pt used per unit of exposed surface. Similarly, by alloying Pt with the more abundant Bi, Greeley *et al.* achieved a rate of H_2 production that was even slightly higher than that of a pure Pt electrode.[36] Although both of these options reduce the amount of Pt required, and are discussed as promising in recent reviews,[55] their reliance on the rare metal continues to make them commercially unfavourable. Indeed, Zuttel *et al.*[9] argue that economically successful hydrogen production relies on the existence of an effective and cheap catalyst for the process that is constructed out of Earth-abundant materials.[56]

The search for non-precious catalysts for the HER has revealed several promising materials, including Ni-Mo alloys,[57,58] doped nanoporous-graphene,[59] certain transition metal nitrides,[60] and also transition metal sulfides.[61–63] Molybdenum disulfide (MoS_2) is one interesting material that has demonstrated highly promising catalytic activity towards H_2 evolution,[5,64] and it will make up the primary focus of this thesis.

1.3 MoS_2 as a hydrogen evolution catalyst

The MoS_2 catalyst was initially inspired by the presence of Mo in hydrogenase enzymes,[5] which catalyse the reversible production of H_2 in biological systems using metal-sulfur assemblies.[65] In its naturally occurring 2H form,[d] MoS_2 is composed of stacked sheets, similar to graphite, with each sheet composed of a layer of Mo atoms sandwiched by two layers of S atoms.[66] The sheets of MoS_2 are held together *via* weak van der Waals interactions, and thus can be cleaved to give single-layer 2-dimensional (2D) structures (Figure 1.3) akin to graphene.[62] Like their carbon-based analogues, the 2D MoS_2 sheets have been shown to form fullerene-like nanostructures[67] and nanotubes,[68] yet they can also give rise to smaller nanoparticulate structures.[69–71] Scanning tunnelling microscopy techniques revealed that the nanoparticles exist as triangular or hexagonal crystallites, usually ranging in size from $Mo_{10}S_{24}$ to $Mo_{78}S_{204}$ (reaching about 30 Å wide, Figure 1.4).[69,70]

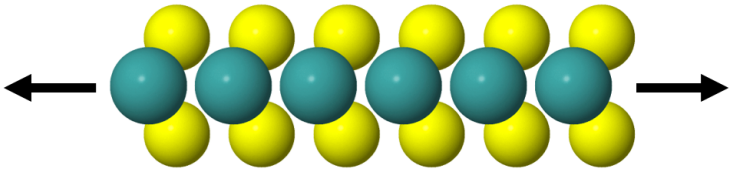

Figure 1.3: A side-on view of single layer MoS_2 showing the S and Mo layers. Arrows indicate the direction of periodic repeat. Key: Mo – teal, S – yellow.

Many of the structural forms of MoS_2 discussed above show promising activity for the HER, demonstrated both in experimental work[61,64,72] and in density functional theory

[d] Here, 2H refers to the specific phase of MoS_2 where the coordination geometry around each Mo atom is octahedral. There also exists a synthetically produced 1T form, where this geometry is tetrahedral instead.

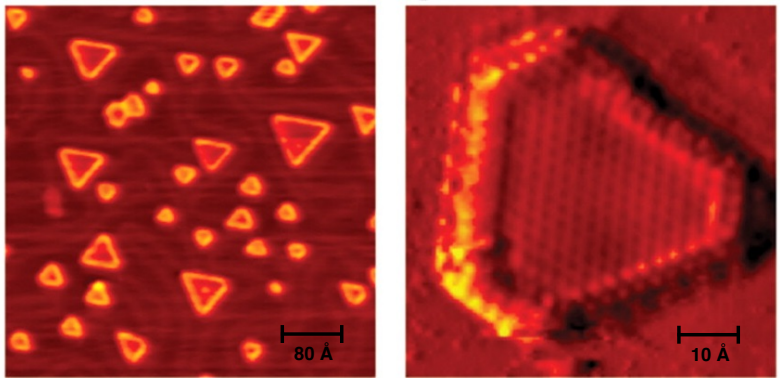

Figure 1.4: Scanning tunnelling microscopy images of triangular and hexagonal MoS_2 nanoparticles. Figure adapted from Jaramillo *et al.*[64]

(DFT) calculations.[5] In comparison with traditional pure metal HER catalysts, the most active structures of MoS_2 have a higher rate of H_2 production per square centimetre than non-precious metals (e.g. Cu, Ni, Co).[73] However, the rate still falls short of Pt by around two orders of magnitude.[64,73,74,e] Furthermore, Pt is found to reach an industrially applicable rate of H production at only –0.02 V,[73] compared to –0.17 V for MoS_2,[75] translating to a lower energy cost for performing the reaction. While MoS_2 catalysts currently perform worse than Pt, the latter has had over 50 years of research to be optimised for hydrogen evolution, whereas MoS_2 has only relatively recently received close attention. It therefore has a great deal of potential for improvement.[36,74] Of particular interest in this work are the single-layer and nanoparticulate forms of MoS_2. Due to their atomic-scale size and low dimensionality the properties of these structures could be readily tuned and improved, for example, through the addition of supporting materials.

In its single-layer form MoS_2 has a large flat basal plane (Figure 1.5) which makes up the majority of the catalyst area. Both experimental[64] and theoretical evidence[5,76] has indicated this basal plane is mostly inactive to hydrogen evolution. However, nanoscale MoS_2 catalysts also have exposed edges, which are found to dominate the reactivity,[64,77] despite making up a relatively small proportion of the material. The surface cuts that expose these edges are also shown in Figure 1.5, where it can be seen that there are

[e]This may seem like quite a large difference at first glance. However, given that the activation barrier of a reaction exponentially affects its rate, this difference could be readily mitigated by even small reductions to the barrier of 0.1 eV.

actually two different types of edge possible: an Mo-terminated edge and an S-terminated edge. Based on the experimental work of Jaramillo *et al.*[64] it is believed that the Mo-edge in particular is the most active site for hydrogen evolution.

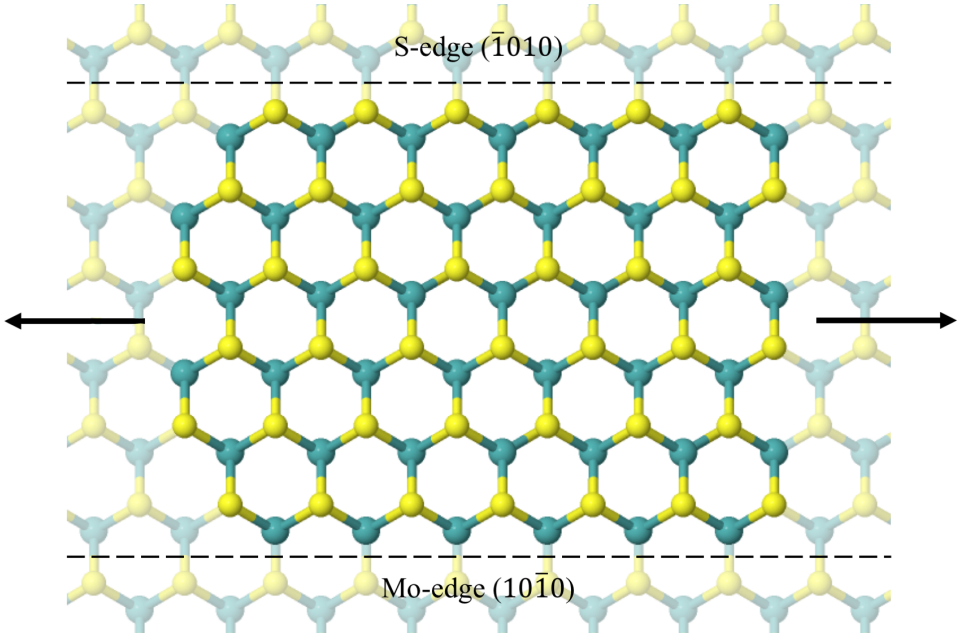

Figure 1.5: A top view of single-layer MoS_2, showing the flat basal plane and the cuts (dashed lines) which expose the edges. Two different edge structures are possible, the Mo- and S-edge. These will be discussed in more detail in Chapter 3. Arrows on the diagram indicate the direction of periodic repeat.

Routes to improving HER catalysis on MoS_2 could focus on either fine-tuning and optimising the already active edges, or designing a significant perturbation to the material in order to improve the currently poor activity on the basal plane. This thesis will cover both of these methods towards optimisation, as they each show promise.

1.4 Transition metal nitrides for hydrogen evolution

While the vast majority of this thesis will focus on MoS_2 catalysts, transition metal nitride (TMN) materials are another class of electrocatalyst that has emerged as promising for the HER,[78] and have received limited recent attention in this role.[60,79,80] Some notable TMNs that have been synthesised and studied for HER activity include: TiN (nanoparticles and nanowires),[81,82] MoN,[83,84] and Ta_3N_5.[85] As was the case for MoS_2, the activity of TMNs for the HER currently tends to fall around two orders of magnitude short of being

competitive with Pt-based catalysts.[79,85,86] However, these materials can show markedly varying activity with different structural analogues.[81] Therefore, TMN materials also make interesting candidates for further optimisation and study.

In the past, computational work on the TMNs has focused only on extended surface structures.[60] While these extended surfaces have appreciable activity, one possible route towards improving this activity is to utilise nanoparticulate structures instead. Recall that, for both Pt and MoS_2, nanoparticulate forms often show increased activity relative to the extended material.[54,64] Nanoparticle (or cluster) TMN structures have been of past interest for their localised surface plasmonic resonance properties,[87] and can be synthesised at small sizes (e.g. <10 nm for TiN).[88] Experimentally, forming either extended 2-dimensional sheets or nanoparticles has been shown to improve the HER activity of certain TMNs (e.g. MoN and Ta_3N_5).[78,79] However, the structures of these nanoparticles, and thus what active sites are responsible for the high HER activity, are not currently known. Therefore, the aim of the final section of this thesis is to understand what types of nanostructures one particularly active TMN material, TaN, may take, identify the possible active sites for hydrogen evolution, and test their activity. This provides a complementary study to the more detailed work on MoS_2 by examining other Earth-abundant binary materials in the same catalytic role.

1.5 Outline of this thesis

The aim of this thesis is to use computational electronic structure methods to explore Earth-abundant hydrogen evolution catalysts, with specific attention foremost on MoS_2 materials, and to a lesser extent TaN. Focus is directed towards both the mechanisms for hydrogen evolution and catalyst activity. In the first three results chapters, MoS_2 is explored in depth, with a specific focus on approaches that could be used to enhance catalytic activity. In the final results chapter, an exploratory study is conducted on novel transition metal nitride clusters to identify their active sites for hydrogen evolution. Overall, insight is gained into how H_2 is formed on these highly interesting binary materials, several methods to optimise catalytic activity show demonstrable success, and the precise structural and electronic properties underlying this activity are identified.

In Chapter 2 the general methodology that is applied to calculate the energy and geometry of structures is discussed in detail, including a background to solving electronic structures using density functional theory. Standard methodology for modelling the free energy of adsorption to solid surfaces is presented, alongside methods for calculating reaction mechanisms and activation energies (also referred to as barriers). The details of specific models and techniques which are only relevant to a single chapter are left to the chapter that they pertain to.

In Chapter 3, the mechanism of the hydrogen evolution reaction on MoS_2 edges is determined for the first time with a realistic model for solvent and electrochemical potential. This mechanism is compared with MoS_2 on two different support materials which are commonly used in experiments: Au(111) and graphene. The results allow a deep understanding of the active sites involved in the HER, the effect of the electrode potential on the mechanism, and the influence that support materials have on the reaction barriers. Furthermore, the results show the critical importance of the thermodynamics of elementary reaction steps (i.e H adsorption and desorption).

Because of the large effect of the H adsorption thermodynamics and the fact they were altered with support materials, in Chapter 4 the H adsorption free energy ($\Delta G_{\mathrm{H_{ads}}}$) is used as a simple descriptor for the hydrogen evolution activity in order to screen across a wide array of graphene-based support materials for MoS_2. Here, the basal plane and edges of MoS_2 are studied with the aim of finding supports that improve the activity of each of these different catalytic sites. Very significant changes in $\Delta G_{\mathrm{H_{ads}}}$ are observed with different supports and some materials are even found to induce near-ideal thermodynamic performance on the MoS_2 edges. However, $\Delta G_{\mathrm{H_{ads}}}$ on the basal plane of MoS_2 remains too high to be favourable. The electronic structures and charge distributions of all materials are analysed in depth, and subsequent explanations for how the supports are altering $\Delta G_{\mathrm{H_{ads}}}$ are proposed.

In Chapter 5, H adsorption to MoS_2 nanotube structures is studied. Experimentally, these nanotubes have been shown to have increased hydrogen evolution activity relative to the flat basal plane, possibly due to the effects of curvature and strain. Therefore, using the nanotube form of MoS_2 presents a different route to optimising the basal plane

portion of the catalyst, which was not sufficiently perturbed by support-tuning in the previous chapter. The work reported here represents the first theoretical study of hydrogen evolution catalysis on MoS_2 nanotubes. We find interesting relationships between nanotube diameter and the catalytic activity, with smaller (more strained) nanotubes adsorbing H more strongly. We rationalise these trends with detailed analyses of the electronic structure of the materials.

Chapter 6 represents the final substantive chapter, which focuses on TaN catalysts for hydrogen evolution. These binary materials share some similarities with MoS_2, but work on the structure of nanomaterials and their catalytic activity is at an earlier stage. In this chapter we use a recently developed global optimisation algorithm based on machine learning techniques to generate a set of possible structures for small TaN and Ta_3N_5 nanoparticles. We then study the adsorption of H to these systems in order to determine their active sites and probe their hydrogen evolution activity.

Finally, in Chapter 7, the main findings of this thesis are reviewed and concluded. Specific attention is directed towards the links between different research chapters, and the generalisability of our findings to other materials or reactions.

Chapter 2

Theoretical methods

2.1 Electronic structures and energies

The starting point for any theoretical study on catalysis is selecting a way in which the electronic structures, and therefore energies, of systems of interest can be solved. It is a central postulate of quantum mechanics that each system of electrons is described by a wavefunction, ψ, which contains all possible information about the system.[89,90] By operating on ψ, the value of a desired property (e.g. momentum, electronic positions, or total energy) can be extracted. The operator for determining the total energy of a system, E, is referred to as the Hamiltonian, $\hat{H}$, and it functions in an eigenvalue equation referred to as the Schrödinger equation:[a]

$$\hat{H}\psi = E\psi \tag{2.1}$$

The exact form of the Hamiltonian differs depending on nature of the system at hand. For chemical systems containing nuclei and electrons, the Hamiltonian operator is composed of five separate terms (Equation 2.2) referring to the kinetic energy of the nuclei ($\hat{T}_N$) and the electrons ($\hat{T}_e$), as well as the potential energy of Coulombic repulsive interactions between positively charged nuclei ($\hat{V}_{NN}$) and Coulombic attraction between nuclei and electrons ($\hat{V}_{Ne}$). The fifth term in Equation 2.2 ($\hat{V}_{ee}$) is the most interesting,

[a] This is the time independent and non-relativistic Schrödinger equation, which is relevant to the systems studied here. For those who have interest in time dependence or relativistic effects, the reader is referred to Ref 90 for a detailed and well-written discussion.

and it represents the potential energy of electron-electron repulsion.

$$\hat{H} = \hat{T}_N + \hat{T}_e + \hat{V}_{NN} + \hat{V}_{Ne} + \hat{V}_{ee} \tag{2.2}$$

The form and solution to both of the kinetic energy terms is relatively trivial, as they can be obtained by quantising the classical solution to kinetic energy.[90] The result is as shown in Equations 2.3 and 2.4.[b]

$$\hat{T}_N = -\frac{1}{2M}\sum_v \nabla_v^2 \tag{2.3}$$

$$\hat{T}_e = -\frac{1}{2}\sum_i \nabla_i^2 \tag{2.4}$$

where M is the nuclear mass, and ∇^2 is the square of the Laplace operator which can be written in full as: $\frac{\partial^2}{\partial x^2} + \frac{\partial^2}{\partial y^2} + \frac{\partial^2}{\partial z^2}$. The v and i indices represent each nucleus and electron in the system, respectively.

The Coulombic nuclear repulsion and nuclei-electron attraction are both classical terms and thus are readily expressed as shown in Equations 2.5 and 2.6.

$$\hat{V}_{NN} = \sum_v \sum_{u \neq v} \frac{Z_v Z_u}{|R_v - R_u|} \tag{2.5}$$

$$\hat{V}_{Ne} = \sum_i \sum_v \frac{Z_v}{|r_i - R_v|} \tag{2.6}$$

where Z represents the nuclear charge, $|R_v - R_u|$ is the distance between two nuclei (u and v) at coordinates R, and $|r_i - R_v|$ is the distance between an electron at r and a nucleus.

The final electron-electron repulsion term ($\hat{V}_{ee}$) can be written as the Coulombic repulsion summed over two-electron pairs:

$$\hat{V}_{ee} = \sum_i \sum_{j \neq i} \frac{1}{|r_i - r_j|} \tag{2.7}$$

[b]Here, and throughout this theory section, atomic units are used in order to simplify mathematical expressions.

Although it looks no more complicated than the other terms in the full Hamiltonian, this repulsion term poses great difficulty to solve, and it will be revisited in depth in Section 2.1.2.

2.1.1 Born–Oppenheimer approximation

An initial simplification to the Hamiltonian in Equation 2.2 can be made by applying the Born–Oppenheimer (BO) approximation.[91] This states that the motion of nuclei and electrons are on different time scales, due to the large difference in their relative masses. In other words, the more massive nuclei are effectively stationary on the timescale of electronic motion. In this way, the electronic structure can be solved for a given arrangement of static nuclei. Mathematically, invoking the BO approximation means the nuclear kinetic energy term from the Hamiltonian in Equation 2.2 is zero, and the nuclear repulsion term is constant. Thus, the electronic Hamiltonian can be expressed as:

$$\hat{H}_{\text{elec}} = -\frac{1}{2}\sum_{i}\nabla_i^2 - \sum_{i}\sum_{v}\frac{Z_v}{|r_i - R_v|} + \sum_{i}\sum_{j\neq i}\frac{1}{|r_i - r_j|} \tag{2.8}$$

These terms represent those which involve electrons in the full Hamiltonian (Equation 2.2) given above. Interestingly, the second term in Equation 2.8, describing the attraction between electrons and nuclei, can now be treated as the potential energy from electrons moving within a external field generated by the static nuclei. The constant nuclear-nuclear repulsion term is excluded here, as it is typically added on as a constant after the pure electronic energy has been evaluated.

2.1.2 Difficulties in correctly describing electrons

Revisiting the electron-electron repulsion energy in the Hamiltonian (the final term in Equation 2.8), it can be seen that quantifying the potential energy of this interaction requires knowledge of the instantaneous repulsion between every pair of electrons in the system. In general, this is referred to as electron correlation, and it can be conceptually treated as electrons responding to the movement of other electrons in the system. For

many-electron systems (i.e. more than one electron) there is no analytical solution to electron correlation when using a full many-electron wavefunction, ψ, as the resolution to the many-body problem is unknown. This represents the first major problem when it comes to solving the Schrödinger equation, and it requires certain approximations to be made. These approximations to capture electron correlation are typically referred to as the quantum mechanical method (or the level of theory).

The second major problem that arises when trying to represent electrons stems from the fact they are quantum particles and therefore have some finite probability to exist in any region of space. Naturally, it is impossible to computationally account for all regions of space with high accuracy. Therefore, the electronic wavefunctions – or, probability densities, which describe where the electrons are located – must be constructed out of a set of finite basis functions. These are chosen specifically to capture the relevant regions of space where the electrons are likely to be. The set of functions is called the basis set.

The approximations made to capture electron correlation (the method) and those made to represent electrons (the basis) are completely separable. One could have a superb method that near-perfectly captured electron-electron interactions, but if their wavefunctions are not well represented in space then the solution will likely be inaccurate. The same is of course true in reverse – that well represented electrons with poorly captured interactions will yield a poor solution. This is presented schematically in Figure 2.1.

Ultimately, it would be ideal to have both a complete basis and a method that perfectly accounted for correlation, but this is unattainable for the reasons described above. In reality, it is pragmatic to choose a method that accounts for as many of the important electron-electron interactions as possible, and a basis set that can describe the key electronic environments. Section 2.2 describes a number of wavefunction-based methods that can be used to solve the Schrödinger equation. These methods lay the groundwork for density functional theory, which is applied in the present thesis and is covered in detail in Section 2.3. Together, these two sections address the approximations made to capture electron correlation (horizontal axis on Figure 2.1). Following this, Section 2.4 covers different basis sets for describing electrons (vertical axis on Figure 2.1).

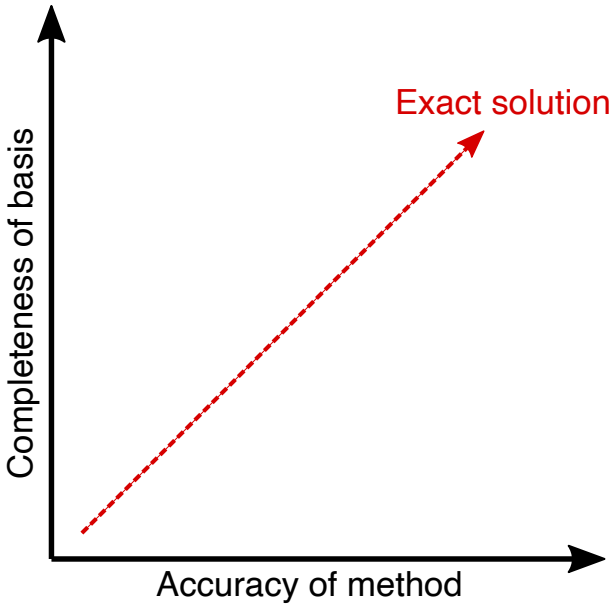

Figure 2.1: A schematic of how the chosen quantum mechanical method, which describes the electron-electron interaction, and basis set, which determines how electrons are spatially described, relate to the accuracy of the solution to the Schrödinger equation.

2.2 Wavefunction-based methods

2.2.1 Hartree–Fock theory

One of the early methods to account for many-body electron interaction was proposed by Douglas Hartree, which later made up the core of Hartree–Fock (HF) theory.[92] The HF treatment ignores instantaneous electron correlation and instead represents each individual electron in an isolated fashion, but accounts for a mean repulsive field produced by the average of all other electrons. At first glance this model may seem very inaccurate, as key information about electron-electron interaction is not included. However, HF theory correctly captures a large portion of the total energy, and it is considered as the starting point for many higher-level methods.

The origin of HF theory comes from Hartree's proposal that one can represent a many-electron wavefunction by combining the products of multiple one-electron wavefunctions in a so called Hartree-product, ψ_{HP}, as shown below:

$$\psi(r_1, r_2, r_3 ... r_n) = \phi(r_1)\phi(r_2)\phi(r_3)...\phi(r_n) \tag{2.9}$$

where n represents the total number of electrons in the system.

Because electrons are fermions, the wavefunction chosen to represent them must be antisymmetric with respect to the exchange of spin and spatial coordinates. In other words, if electrons exchange quantum numbers, the sign of the wavefunction must invert:

$$\psi(x_1, x_2, x_3...x_n) = -\psi(x_1, x_3, x_2...x_n) \tag{2.10}$$

This gives rise to the requirement that two electrons cannot have the same quantum numbers (spin and spatial), commonly known as the Pauli exclusion principle. The Hartree-product does not inherently satisfy this requirement. However, this is addressed by writing ψ_{HP} as a Slater determinant of the possible one-electron wavefunctions:

$$\psi_{\text{HP}} = \frac{1}{\sqrt{n!}} \begin{vmatrix} \phi_1(r_1) & \phi_2(r_1) & \dots & \phi_n(r_1) \\ \phi_1(r_2) & \phi_2(r_2) & \dots & \phi_n(r_2) \\ \vdots & \vdots & \ddots & \vdots \\ \phi_1(r_n) & \phi_2(r_n) & \dots & \phi_n(r_n) \end{vmatrix} \tag{2.11}$$

where the $\frac{1}{\sqrt{n!}}$ term serves only for normalisation. In this way, the antisymmetry of the wavefunction is enforced, as ψ_{HP} is zero if the exclusion principle is violated.

With ψ_{HP} as an expression for the wavefunction of the system, it can now be operated upon with $\hat{H}_{\text{elec}}$ to extract the HF energy. The electronic Hamiltonian here is conveniently separated into one-electron (h_i) and two-electron (g_{ij}) terms:

$$\begin{aligned} \hat{H} &= \sum_i \hat{h}_i + \sum_i \sum_{j \neq i} \hat{g}_{ij} \\ \hat{h}_i &= -\frac{1}{2} \sum_i \nabla_i^2 - \sum_i \sum_v \frac{Z_v}{|r_i - R_v|} \\ \hat{g}_{ij} &= \frac{1}{|r_i - r_j|} \end{aligned} \tag{2.12}$$

where the one-electron term is simply the kinetic and electron-nuclear potential energy operators, and the two-electron term describes the electron-electron interaction. From this point, it is possible to obtain the HF energy of a system by taking the expectation

value:

$$E_{\mathrm{HF}} = \langle \psi^*_{\mathrm{HP}} | \hat{h}_i | \psi_{\mathrm{HP}} \rangle + \langle \psi^*_{\mathrm{HP}} | \hat{g}_{ij} | \psi_{\mathrm{HP}} \rangle \tag{2.13}$$

which evaluates to:

$$E_{\mathrm{HF}} = \int \psi^*_{\mathrm{HP}} (-\frac{1}{2} \sum_i \nabla_i^2 - \sum_i \sum_v \frac{Z_v}{|r_i - R_v|}) \psi_{\mathrm{HP}} \; dr + \sum_i \sum_j (J_{ij} - K_{ij}) \tag{2.14}$$

The first (one-electron) part of Equation 2.14 is readily soluble and yields the sum of one-electron orbital energies. In the second (two-electron) part, J_{ij} and K_{ij} refer to the Coulomb repulsion and electron exchange integrals, respectively. The Coulomb integral is effectively summing the average repulsion electron i experiences from all other electrons, j, in their one-electron orbitals.[c] On the other hand, the exchange energy is a quantum effect that arises from the fact that fermions are indistinguishable particles and undergo exchange. The full forms of both of these integrals are given below:

$$J_{ij} = \iint \phi^*_i(r_i) \phi_i(r_i) \frac{1}{|r_i - r_j|} \phi^*_j(r_j) \phi_j(r_j) \tag{2.15}$$

$$K_{ij} = \iint \phi^*_i(r_i) \phi_j(r_i) \frac{1}{|r_i - r_j|} \phi_i(r_j) \phi^*_j(r_j) \tag{2.16}$$

It is here that the benefit of using separable one-electron orbitals to represent the wavefunction finally becomes clear. Without this approach, solving J_{ij} by considering all electrons would be thwarted by the many-body problem. Using one-electron orbitals instead allows each pair of electrons to be treated separately.

Using Equation 2.14, the HF energy for any given set of one-electron orbitals can be evaluated, but these orbitals do not necessarily represent the optimal HF wavefunction. To achieve this, the energy must be minimised with respect to changes in the one-electron orbitals (which are subject to orthonormality constraints). However, because the form of each one-electron orbital also depends on all the others (*via* the mean field interaction), the energy must be solved self-consistently. The process by which this is done is outside

[c] It is from this that the mean field nature of HF theory arises.

the scope of this thesis. However, the HF method provides the starting point for many more advanced methods, which will be discussed in the following sections.

2.2.2 Configuration Interaction and Coupled Cluster

As mentioned before, HF theory does not account for so-called dynamic electron correlation, as the wavefunction is composed of one-electron terms that only experience the mean-field repulsion of the others. Therefore, methods which recover some of this electron correlation can improve upon the accuracy of calculated energies. One way this can be achieved is by mixing in a selection of excited state determinants to the HF wavefunction, rather than simply using a single ground state (Slater) determinant. The inclusion of excited determinants allows greater flexibility in describing the interactions between electrons. This is the basis for both the Configuration Interaction (CI) and Coupled Cluster methods.[93]

In CI, a linear combination of the HF determinant and certain selected exited state determinants is used to compose the wavefunction:

$$|\psi_{CI}\rangle = \alpha\,|\psi_{HF}\rangle + \sum_i c_i\,|\psi_i\rangle \tag{2.17}$$

where the CI wavefunction can be optimised by varying the weighting coefficients α and c_i variationally. Within this methodology, the one-electron orbitals, ψ_i, are obtained directly from a HF treatment, and are held constant while the coefficients, c_i, are optimised.

In principle, CI can account for all possible excitations of all electrons simultaneously, which is referred to as full CI. This is known to fully capture electron correlation,[90] returning an exact solution within the time-independent Schrödinger equation for the given basis set used.[d] Unfortunately, the size of the full CI wavefunction depends factorially on the number of possible one-electron orbitals in the HF treatment, making this method completely intractable for all but the smallest systems.[94,95] To the best of the author's knowledge at the time of writing, the current largest full CI calculation

[d] Note here that the basis set determines what excited determinants are available in CI. So a full CI treatment is still limited by the completeness of the basis.

is likely that for a single N_2 molecule described by a 4s3p1d atomic natural orbital basis set.[96] Therefore, in practice, CI is not used to account for *all* possible electronic excitations. Instead, only a certain number of electrons can be simultaneously excited (i.e. not in the ground state configuration) in any one determinant that is mixed in to make ψ_{CI}. Allowing single excitations (CIS) actually offers no improvement over the HF level, as singly excited determinants do not interact with the HF ground state according to Brillouin's theorem.[90] However, CI with single and double excitations (CISD) does offer substantial improvement over pure HF, and can be applied to fairly small systems.[97] The typical highest level for standard CI calculations includes singles, doubles, and certain important triples (CISD(T)). This method actually captures the vast majority of the full CI energy, as most triple and higher excitations have little impact on the energy.[90]

An alternative method to CI is Coupled Cluster (CC), which differs primarily in that the excited state determinants are included with the ground state HF wavefunction in product form, instead of by linear combination. The CC wavefunction is constructed as:

$$|\psi_{CC}\rangle = e^{T_i} |\psi_{\mathrm{HF}}\rangle \tag{2.18}$$

where ψ_{HF} is the ground state determinant and T_i is the cluster operator which generates excited state determinants with i excitations. Here, e^T is expressed as a Taylor series:

$$e^{T_i} = 1 + T_i + \frac{T_i^2}{2!} + \frac{T_i^3}{3!} + ... \tag{2.19}$$

If T_i is taken through to the total number of electrons in the system, we have the exact same treatment as full CI, as this represents all electrons being free to be excited. Therefore, for computational feasibility, T is often truncated to include single and double excitations (CCSD), or some triple excitations (CCSD(T)).

As the result of some mathematical finesse, CC offers a key advantage over CI in that it is size extensive,[90] meaning that the energy of a given system scales correctly with the number of electrons. The truncated form of CI on the other hand is not size-extensive, meaning it cannot be used to compare the energies of systems of different sizes. It is

for this reason that CCSD(T) has become the gold standard of computational accuracy when solving the electronic Schödinger equation. However, even with restricted allowed excitations, CC and CI are both far too computationally expensive to be applied to large chemical systems such as those studied in this thesis.

2.2.3 Limitations of wavefunction-based methods

While it is certainly natural to attempt to solve the electronic Schödinger equation using the wavefunction of a system, it does come with certain limitations that are primarily manifested through the scaling of computational expense with system size. The size of a system refers to the number of basis functions used to represent that system (N_{basis}). Larger systems with more electrons, and thus more basis functions, will typically take longer to solve. However, the central processing unit (CPU) time taken to solve a given system does not scale with size the same way for every method.

Taking a pure HF treatment of a system, the calculation time scales at N_{basis}^4,[90] which is due to the computational expense in evaluating the four-index integrals across all electron pairs. This scaling creates a so-called "exponential wall" where it is very difficult to compute systems that have greater than a certain number of basis functions. Another consideration is that, in forming the one-electron orbitals to construct a Slater determinant, there must be enough computational storage space (usually in the form of random access memory) to hold all the possible electron-wavefunction pairs. This represents the storage of $3N_{\text{basis}}$ variables. Moving to the more advanced and more accurate CC and CI methods, the extra computational time involved in representing the excited state determinants and optimising the weighting coefficients brings the scaling up to between N_{basis}^{6-7}, depending on how many simultaneous excitations are allowed. Many of these limitations also exist for other wavefunction methods that have not been directly discussed here, such as Møller-Plesset perturbation theory.[98] As a result, for calculations involving large systems with hundreds of electrons (such as those in this thesis), wavefunction-based methods are often not applicable.

2.3 Density functional theory

Density functional theory (DFT) is an alternative to wavefunction-based methods for approximating the electronic Schrödinger equation, and it is the method chosen for application in all studies within this thesis. It is based around the idea that the electron density, $\rho(r)$, is a unique and complete descriptor of the energy of a system.[99] The density is a simple function of three Cartesian coordinates (and, optionally, one spin coordinate) that describes the probabilistic spatial distribution of the electrons in a system, and is written as:

$$\rho(r) = \sum_i |\psi_i(r)|^2 \tag{2.20}$$

DFT typically scales better than wavefunction methods, formally at N_{basis}^3, which is at least an order of magnitude better than HF.[90,100,e] The primary reason for this is that the Coulomb interaction integrals can be evaluated over the electron density, which is a three-dimensional function, as opposed to the four-index integrals in HF.[101] Critically, DFT also retains some description of electron correlation (though not exact), meaning it is often chosen to study systems that are too large for CC or CI methods.

In order to apply DFT, we first must understand how the electron density can be used to describe an electronic system. In 1964 Hohenberg and Kohn first proved that the ground state energy of a many electron system can be determined, in principle exactly, from its density.[89,90,99] The first Hohenberg-Kohn theorem[102] states that the energy may be written as a unique functional[f] of the electron density ($E[\rho(r)]$). In this way, it is shown that the electron density completely determines all the ground-state properties of a system. A detailed proof can be found in Walter Kohn's 1999 Nobel address,[99] where the prize was awarded for his pioneering work on DFT. However, actually solving for the energy of a system first requires a way to formulate and express this density, $\rho(r)$, the framework for which is given by the second Hohenberg-Kohn theorem. This states that the electron density can be determined variationally, such that the true electron density

[e] Strictly speaking, practical implementations of DFT often scale somewhere between N_{basis}^{2-4},[99] but there is always some variability in scaling between different implementations of any method.

[f] A functional is a higher-order function which takes a function as input and returns a scalar value. Here, the energy functional takes the electron density function as input and returns the total electronic energy.

is that which gives rise to the lowest energy.[102,103] As a result, one is able to repeatedly generate candidate densities and if they yield lower energies they are closer to the true density.

The two Hohenberg-Kohn theorems taken together give rise to what is now called "orbital-free" DFT which states that the energy, E, can be determined by an expression highly analogous to the electronic Hamiltonian (given at the start of this chapter in Equation 2.8):[89,90,103]

$$E = min_{\rho}\left[T_{\mathrm{TF}}[\rho(r)] + \int V_{\mathrm{nuclei}}(r)\rho(r)d^3r + J[\rho(r)] + K[\rho(r)]\right] \tag{2.21}$$

where $T_{\mathrm{TF}}[\rho(r)]$ is the kinetic energy term, the nuclei-electron attraction term is treated as being some potential generated by the nucleus, $V_{\mathrm{nuclei}}(r)$, attracting the electron density, $J[\rho(r)]$ is the Coulomb repulsion of the density with itself, and $K[\rho(r)]$ is the exchange energy. While we saw in the previous section on HF theory that the kinetic energy of a Slater determinant of one-electron orbitals is exact and readily soluble, the kinetic energy of an interacting electron density is poorly defined. Early approaches use Thomas-Fermi theory, treating the density as a uniform electron gas in order to solve for the kinetic energy, but this leads to large errors, especially for molecular calculations.[90] Indeed, there are still no appropriate functional forms to calculate the kinetic energy from the electron density with acceptable error, and as a result orbital-free DFT is rarely applied in practice.

One year after the original Hohenberg-Kohn theorems and orbital-free DFT, Kohn and Sham developed an elegant approach to circumvent the problem of the kinetic energy functional.[104,g] Kohn-Sham (KS) formalism assumes a fictitious system of non-interacting electrons that give rise to the same density as the real system of interacting electrons once an external potential, V_{ext}, is applied. Within this non-interacting system, it is possible to construct a series of one-electron functions referred to as Kohn-Sham orbitals (ϕ_{KS}), which have a known kinetic energy, calculated in an analogous fashion to HF theory – as a sum of the one-electron energies. When taken together these KS orbitals give a

[g] In a talk at the Asia-Pacific Association of Theoretical and Computational Chemists Conference in 2019, a leader in the field of method development – Professor Martin Head-Gordon – aptly described the Kohn-Sham approach as "a beautiful sidestep."

Kohn-Sham density:

$$\rho(r)_{\mathrm{KS}} = \sum_i |\phi_i(r)|^2 \tag{2.22}$$

And, they yield the true density by application of the external potential, V_{ext}:

$$\rho(r) = \sum_i |\phi_i(r)|^2 + V_{\mathrm{ext}} \tag{2.23}$$

These may seem like a trivial reformulations of the earlier-presented Equation 2.20, but we will see they are critically important to practically solving for the energy.

The overall result of this is that we can now write an expression for the energy functional, $E[\rho(r)]$, that accounts for kinetic energy (first term), nuclear-electron potential energy (second term), and electron-electron Coulomb repulsion energy (third term) in a manner highly analogous to HF theory:

$$E[\rho(r)] = \sum_i \left(\phi_i^*(\int -\frac{1}{2}\nabla_i^2 \; d^3r)\phi_i - \phi_i^*(\int V_{\mathrm{nuclei}}(r)\rho(r) \; d^3r)\phi_i \right. \\ \left. + \phi_i^*(\iint \frac{1}{2}\frac{\rho(r_i)\rho(r')}{|r_i - r'|})\phi_i \right) + E_{\mathrm{XC}}[\rho(r)] \tag{2.24}$$

The first kinetic energy term is calculated identically to HF theory, and the second nuclei-electron potential term is the same as was seen for orbital-free DFT. The third Coulomb repulsion term is slightly reformatted from HF theory, as it now represents the repulsion of the electron density at point r_i with the density at point r'.[h] The final term, $E_{\mathrm{XC}}[\rho(r)]$, will be discussed momentarily.

At this point, it should be noted that this equation relies both on the true density, $\rho(r)$, and also the functions of the KS orbitals, ϕ. Recall from Equation 2.22, that the KS orbitals give a density, ρ_{KS}, but $\rho(r)$ in Equation 2.24 is the *true* density of the interacting system. As a result, this equation has to be solved iteratively until the KS density gives a energy which is consistent with the KS orbitals. Practically, this translates to repeatedly

[h] You may note that there is no reason points r_i and r' cannot be the same, meaning the density at a given point also repels itself. Of course, an electron repelling itself is non-physical, and this gives rise to the so-called self-interaction error within DFT. This effect can be an issue in certain chemical systems.

solving Equation 2.24 using iteratively updated guesses for the KS orbitals (and thus also the density, through Equation 2.23), until the energy reaches a minimum.

Returning to the final $E_{\mathrm{XC}}[\rho(r)]$ term in Equation 2.24; this is perhaps the most interesting term as it contains expressions for the electron exchange energy, the correlation energy not already captured by the Coulomb repulsion, and also the remainder of the kinetic energy not captured by the one-electron non-interacting system. Indeed, this term is actually *defined* as the energy of all the missing components from Equation 2.24:

$$E_{\mathrm{XC}}[\rho(r)] = (T[\rho(r)] - T_{\mathrm{S}}[\rho(r)]) + (E_{ee}[\rho(r)] - J[\rho(r)]) \tag{2.25}$$

where, in the first term, $T[\rho(r)]$ is the exact kinetic energy of the interacting system and $T_{\mathrm{S}}[\rho(r)]$ is the non-interacting KS orbital kinetic energy. In the second term $E_{ee}[\rho(r)]$ is the exact electron-electron interaction and $J[\rho(r)]$ is the Coulomb repulsion that has already been accounted for. Up until this point DFT has been formally exact, and thus Hohenberg and Kohn have shown that an exact form for $E_{\mathrm{XC}}[\rho(r)]$ must exist.[99] However, the form is unknown, and approximate exchange-correlation functionals must therefore be applied in practice to solve for energy. This nature of these approximate functionals for the exchange-correlation energy will be the focus of the next section.

2.3.1 Exchange-correlation functionals

A vast number of different formulations for exchange-correlation functionals exist, which some authors have gone as far as to describe as a "zoo" of functionals.[105] Here, we broadly classify these functionals are into four different groups: local density approximations, generalised gradient approximations, meta generalised gradient approximations, and hybrid functionals. Each of these groups will be discussed separately in the following sections, and they are presented in the order of increasing complexity and rigour. In most cases, expressions for the exchange energy, ϵ_x, and the correlation energy, ϵ_c, are fitted either to known physical properties of the electron density or to experimental observables.

Local density approximation

The simplest way to derive an energy expression from the density is given by a local density approximation (LDA). This method takes $E_{XC}[\rho(r)]$ at any given point, r, to depend only on the value of the density at that specific point.[90]

$$E_{\mathrm{XC}}^{\mathrm{LDA}}[\rho(r)] = \int \rho(r)\epsilon_{xc}[\rho(r)]\ dr \tag{2.26}$$

Here, ϵ_{xc} simply represents the sum of the exchange and correlation contributions. This approximation is highly attractive in its simplicity, as one need only consider the density to be single-valued at each point and not represent the overall behaviour or changes in the density. Furthermore, the only formulations of LDA that are practically implemented are those which consider the density to be the *same* at each point. This avoids a discontinuous density, and again returns to the Thomas-Fermi approximation of a uniform electron gas.[90]

One very popular LDA formulation comes from Perdew and Zunger,[106] where the authors reintroduce the uniform electron gas approximation to define the exchange energy as:

$$\epsilon_x = -\frac{3}{4}\left(\frac{3}{\pi}\right)^{\frac{1}{3}} \int \rho(r)^{\frac{4}{3}}\ dr \tag{2.27}$$

The correlation energy on the other hand does not have a simple expression. It is instead numerically fitted based on Monte Carlo simulations as a linear combination of logarithmic functions.

LDA functionals are undeniably computationally inexpensive, and are often said to produce reasonably accurate structural geometries.[107,108] Indeed, for extended metallic systems, LDA tends to slightly underestimate lattice constants with an error compared to experiment of up to 5.1%.[109] However, predictions of more complex quantities such as bulk moduli or heats of formation have a much larger mean relative error of about 15%.[109,110] For molecular systems, the inaccuracies of LDA are exacerbated significantly, which is reasonable considering electrons in molecules are clearly dissimilar to a uniform electron gas, which is not always the case for those in extended metallic systems. LDA

significantly over-binds many molecular interactions, producing strong bond energies and short bond lengths.[111]

It is clear that the assumption of a spatially uniform electron density is non-physical.[90] As a result LDA poorly describes covalent bonding, which by definition encompasses a fluctuation in electron density.[107] Therefore, LDA functionals are not ideal for studying the catalytic processes that are the topic of this thesis. Instead, more complex and accurate approximations to the exchange-correlation functional must be used.[112]

Generalised gradient approximation

Generalised gradient approximation (GGA) functionals add to the LDA approach by considering not just the electron density at a point, but also the gradient of that density, $\nabla\rho(r)$. This additional factor is usually added directly to the LDA exchange-correlation energy:

$$E_{\mathrm{XC}}^{\mathrm{GGA}}[\rho(r)] = \epsilon_{xc}^{\mathrm{LDA}}[\rho(r)] + \delta\epsilon_{xc}\left[\frac{|\nabla\rho(r)|}{\rho^{\frac{4}{3}}(r)}\right] \tag{2.28}$$

Functionals within the GGA class do not treat the density as uniform, resulting in a more physically realistic electronic system.

GGA functionals have become incredibly popular, likely because they add relatively little computational expense over the LDA level and yet they describe bonding far better. Most GGAs have a similar error to LDA on the lattice constants of solids – this time overestimating by between 2.5 and 4.5%.[109,110] However, when it comes to ionisation, atomisation, and binding energies, GGAs typically perform far better.[90,112–115] GGAs also offer an advantage in molecular systems, reducing the over-binding of LDA by almost a factor of five.[111] For solid surface adsorption energies – which are particularly relevant to this work – the mean absolute error of most common GGAs is about three times smaller than the LDA equivalent.[116] Therefore, GGAs are the natural choice for catalysis studies in large systems, where bonding must be captured accurately but a higher level method is too expensive. The calculations performed in this thesis are all at the GGA level, representing an acceptable balance between computational tractability and accuracy.

Meta generalised gradient approximation

It is possible to improve on the GGA level of theory by including more information about the overall form of the electron density. In meta GGA (or mGGA) functionals, the second derivative of the density, $\nabla^2\rho(r)$, is added to the formulation of the exchange-correlation energy, providing information on the curvature. In a general sense, this is expressed as:

$$E_{\mathrm{XC}}^{\mathrm{mGGA}}[\rho(r)] = \rho(r)\epsilon_{xc}[\rho(r), \nabla\rho(r), \nabla^2\rho(r)] \tag{2.29}$$

While it is true that mGGA functionals usually offer some improvement in accuracy over the pure GGA level, particularly in molecular systems,[111] this comes at a large computational cost due to the fact the second derivative matrix of the density (or Laplacian) must be calculated at each iteration when solving for self-consistency. Therefore, these methods are not easily applied to the fairly large solid systems studied in this work.

Hybrid functionals

The final class of exchange-correlation functional discussed here are hybrid functionals. These functionals work by mixing some portion of the Hartree-Fock exchange energy into a pure DFT calculation in order to more correctly describe the antisymmetry of the wavefunction.[i] As we saw in Section 2.2, the exchange energy within HF theory, K_{ij}, is formally exact and thus it seems very reasonable to apply it here in the exchange part of ϵ_{xc}. Mathematically, this is expressed as:

$$E_{\mathrm{XC}}^{\mathrm{hybrid}}[\rho(r)] = \rho(r)(1-\xi)\epsilon_x\epsilon_c[\rho(r), \nabla\rho(r)] + \xi E_x^{\mathrm{HF}} \tag{2.30}$$

where ξ determines the proportion of the HF exchanged that is mixed in. Across the many different options for hybrid functionals, ξ can have any value up to including 100% of the

[i] Note that this hybrid methodology can be applied to mGGA, GGA, or even LDA functionals. However, it makes little sense to use an expensive hybrid correction with an LDA functional that has other larger flaws.

HF exchange. However, for many systems, mixing in between 10 and 40% HF exchange tends to yield the best results.[117,j]

Hybrid functionals generally produce more accurate results in the calculation of atomisation and bond energies than their pure DFT counterparts,[90] and thus have become widely used (especially for molecular systems). Indeed one particular hybrid functional has gained extreme popularity: B3LYP,[118] even though its accuracy is significantly lower than many alternatives.[105] Unfortunately, the inclusion of Hartree-Fock exchange in calculations of extended periodic systems such as those studied in this thesis is difficult. This is because Hartree-Fock is a mean-field model which averages the effect of all electrons in the system.[90,109] As it is impossible to average the effect of an infinitely repeated number of electrons, in order to apply hybrid functionals to periodic systems other computationally expensive corrections must be employed.[119] As a result, hybrid functionals are not practical for use in the present work.

2.3.2 Accounting for van der Waals interactions

In many chemical systems, long-range van der Waals (or dispersive) forces can play a large role in determining the electronic energy.[120] These forces are primarily made up of electrostatic interactions between spatially separated regions of electron density. However, it is known that within a GGA description of the electron density, these long-range dispersive interactions are poorly described.[121,122] For the systems studied in this thesis, many of which comprise of catalyst and support structures separated by over 3 Å, the dispersion forces are critical.

The lack of description of van der Waals (vdW) interactions within classic GGA functionals can be circumvented by the application of a correction factor on the energy that accounts for these long-range effects.[120] One set of popular current formulations for this correction factor are DFT plus dispersion (DFT-D) methods – pioneered by Stefan Grimme[123] – where atomic dispersion forces are added on in the form of pairwise (E_2)

[j] Keeping the proportion of HF exchange at less than 100% is more accurate due to a fortuitous cancellation with other errors inherent in DFT.

and three-way (E_3) corrections:

$$E_{\mathrm{DFT-D}} = E_{\mathrm{DFT}} + [E_2 + E_3] \tag{2.31}$$

The correction factors are empirically fitted from damped interatomic potentials. This methodology is able to produce binding energies for vdW clusters within 10 - 30 % of benchmark standards.[122]

A common critique of DFT-D methods is that the fitting of dispersion forces is not specific to a given chemical system, and thus their accuracy may have an upper limit.[k] As a result, an alternative has been to design vdW-DF approaches (where DF stands for density functional), with long-range dispersion directly accounted for in the correlation energy functional.[124] The exchange-correlation functional predominately used in the present thesis, BEEF-vdW,[116] takes this approach. Here, the exchange-correlation energy is fitted to both high quality *ab initio* and experimental datasets which specifically include systems dominated by non-local vdW interactions. BEEF-vdW tends to perform on-par with other vdW-corrected functionals, or even slightly better in the case calculating adsorption energies or surface reactions.[125,126]

2.4 Basis sets

Up to this point, the method to capture electron-electron interactions has been addressed in detail, but the actual representation of these electrons has not been covered. The basis set of a calculation is a series of finite-valued functions that can be combined (e.g *via* linear combination) to spatially describe the electrons. In the case of wavefunction-based methods such as HF, the one-electron wavefunctions are constructed out of the available basis functions. For DFT, which is applied in this work, the Kohn-Sham orbitals are composed of a linear combination of basis functions, and this gives rise to the electron density. There are two broadly different approaches to forming basis sets, which are discussed in the following two sections.

[k] At the time of writing there is some disagreement in the field as to whether this is a large issue, and development of DFT-D methods is ongoing.

2.4.1 Atom-centred basis sets

For molecular systems, it is very natural to describe electrons using functions that resemble atomic orbitals, similar to early valence bond or molecular orbital theory. These so-called atom-centred basis functions describe a region around each atom with reference to the nucleus. A linear combination of known atom-centred basis functions, $\chi_\mu(r)$, can be taken to build the one-electron orbitals, $\phi_p(r)$:[90]

$$\phi_p(r) = \sum_\mu c_{\mu p}\chi_\mu(r) \tag{2.32}$$

where $c_{\mu p}$ represents the coefficient weighting the contribution of each different basis function to the overall wavefunction, and the index μ runs over all basis functions.

Most common basis functions, $\chi_\mu(r)$, take the form of hydrogenic s, p, d and f orbitals. Diffuse basis functions with increased amplitudes further from the nucleus also exist, and can be added to capture long-range interactions.[95] Mathematically, these basis functions are smoothed exponentials with one of two different forms: Slater type orbitals (STOs) given by Equation 2.33,

$$\chi_\mu(r) = NY_{l,m}(\theta,\eta)\ r^{n-1}e^{-\xi r} \tag{2.33}$$

or Gaussian type orbitals (GTOs) given by Equation 2.34.

$$\chi_\mu(r) = NY_{l,m}(\theta,\eta)\ r^{2n-2-l}e^{-\xi r^2} \tag{2.34}$$

In both of the above equations, N is a normalising constant, $Y_{l,m}(\theta,\eta)$ are spherical harmonic functions determining the angular component of the wavefunction, and the two equations differ primarily by their radial component, depending on $-r$ and $-r^2$, respectively. Here, ξ also determines the decay of the function. In practice, GTOs are preferentially used because their analytical integrals can be easily computed.[90]

2.4.2 Periodic systems and plane wave basis sets

For extended solids, such as bulk metals or similar, the system can be represented very differently to molecular cases. An extended system essentially repeats with a periodic crystal lattice, meaning that there is a primitive unit cell with periodic boundary conditions.[127] When expanded in all directions, this cell captures the character of the entire material. Electrons in this extended system can theoretically range between periodic repeats, especially if the system is metallic in nature with delocalised electrons.[95] As a result, rather than using atom-centred basis functions, where the amplitude falls off rapidly from the nucleus, it is common to use basis functions that have appreciable amplitudes at infinite ranges – such as plane waves:

$$\chi_k(r) = e^{i\mathbf{k}\cdot\mathbf{r}} \tag{2.35}$$

Plane waves are a complex number function expended in three dimensions, where $\mathbf{r}$ is the position vector and $\mathbf{k}$ is the wave vector. Waves with a high $\mathbf{k}$ value oscillate rapidly, indicating a higher energy wave than those with small $\mathbf{k}$.

Through Bloch's theorem, plane waves can be used to express the wavefunctions of electrons in an infinite crystal lattice by taking the product of a plane wave with a function of the periodicity of the crystal lattice (Equation 2.36).[128]

$$\chi_{n\mathbf{k}}(\mathbf{r}) = e^{i\mathbf{k}\cdot\mathbf{r}} u_{n\mathbf{k}}(\mathbf{r}) \tag{2.36}$$

Where $e^{i\mathbf{k}\cdot\mathbf{r}}$ is the plane wave term and $u_{n\mathbf{k}}(\mathbf{r})$ refers to the periodic cell. One can also express the whole periodic cell as an infinitely extended wave, by expanding it in terms of a number of plane waves, giving Equation 2.37, where the values of $\mathbf{G}$ are the reciprocal lattice vectors of the crystal.[129]

$$\phi_n(\mathbf{r}) = \sum_{\mathbf{G}} C_{(n,\mathbf{k}+\mathbf{G})} e^{i(\mathbf{k}+\mathbf{G})\cdot\mathbf{r}} \tag{2.37}$$

Modelling an extended system with this method would require integrals to be computed over an infinite range of values of the wave vector, **k**. Because this is impossible, the Brillouin zone – which is the primitive unit cell defined in reciprocal space – must instead be sampled at a finite number of k-points. The finer this k-point mesh, the more accurate the integration.

In general, plane waves are easier to compute than atom-centred basis functions, yet a large number of them are required to appropriately describe variations in the electron density or wavefunction. Including higher energy plane waves (larger **k**) adds flexibility to the description, yet also increases computational cost. Thus a kinetic energy cut-off is specified to determine the maximum energy of included plane waves. Complex systems with localised electron density or adsorbates such as hydrogen require higher energy plane waves to describe them.

Plane wave basis sets are used exclusively in this thesis, as we are primarily interested in extended solid surfaces. To model a surface, which is periodically extended in either one or two dimensions but by definition must not be extended in at least one dimension, a vacuum space is added to the simulated unit cell and only one k-point is sampled in this dimension. While the model is technically still extended infinitely in the dimension with the vacuum gap, if the separation between periodic repeats is sufficiently large and only the Brillouin zone (one k-point) is sampled, this removes any direct interaction between repeats. In this way, periodic DFT can still be used to capture 2-dimensional, 1-dimensional, and even 0-dimensional (i.e. nanoparticle or molecular) structures.

2.4.3 Description of core electrons for heavy elements

A central aspect of modelling any system with heavier elements (typically metals) is describing the core electrons. Because large metal atoms have a high nuclear charge, the Coulomb potential near the nucleus exists as a very deep well. This results in a highly oscillatory wavefunction near the core region (below the cut-off radius, r_c, in Figure 2.2), which would require many basis functions to fully describe. To make modelling this region computationally feasible, the true Coulomb potential near the nucleus (V_{nuclei})

is often replaced by a pseudopotential (V_{pseudo}) with a different form, improving the manageability of the core wavefunction (ψ_{pseudo} in Figure 2.2). Outside the cut-off radius (r_c) the Coulomb potential, and thus the wavefunction, retain their true form.

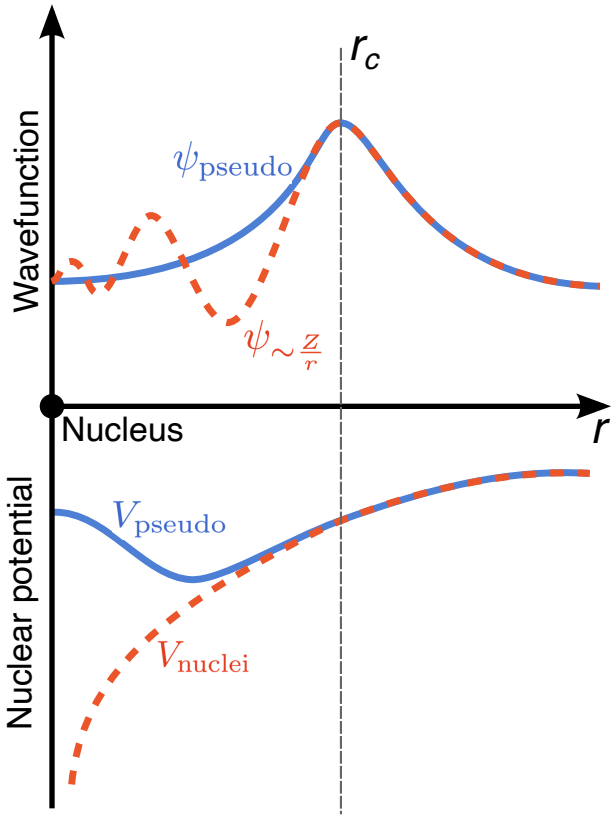

Figure 2.2: A comparison of the wavefunction of the core electrons, ψ, when the true Coulomb potential is used (orange) and when the potential is replaced by a pseudopotential (blue). r_c is the cut-off radius above which the pseudopotential and the true potential are identical.

In this thesis, the core electrons are technically not described by a pseudopotential, but instead using the projector augmented wave (PAW) method,[130] which accomplishes the same result. The key difference is that a PAW potential is still an all-electron method that preserves information about the core electrons and gives the full electron density, where pseudopotentials do not. It achieves this by freezing the core electrons,[131] making the wavefunction soluble in this region, though inflexible. Because this affects only the low energy core electrons, which are typically not involved in bonding, it vastly reduces the difficulty of calculations while still retaining high accuracy for properties of interest.

2.5 Surface adsorption and reaction mechanisms

Given the focus on catalysis, large portions of this thesis involve calculations of surface adsorption energies (usually of H) and subsequent reaction mechanism or barrier calculations. The following sections briefly outline the general methodology used for these calculations, but chapter-specific details are presented in the section they concern.

2.5.1 H adsorption free energies

Understanding the adsorption and desorbtion of H from a catalyst surface is critical to studying the HER. The electronic H adsorption energies ($\Delta E_{\mathrm{H_{ads}}}$) are calculated using the standard DFT techniques outlined in the previous sections, and are computed directly as:

$$\Delta E_{\mathrm{H_{ads}}} = E_{\mathrm{catalyst+H}} - (E_{\mathrm{catalyst}} + \frac{1}{2}E_{\mathrm{H_2}}) \tag{2.38}$$

where $E_{\mathrm{catalyst+H}}$ is the energy of the catalyst structure (usually MoS_2) with H adsorbed, E_{catalyst} is the energy of only the clean catalyst, and $\frac{1}{2}E_{\mathrm{H_2}}$ is half the energy of H_2 in a box with 20 Å vacuum space in all directions. Electronic adsorption energies are converted to Gibbs free energies by accounting for the change in zero-point vibrational energy, Δ(ZPVE), and entropy, ΔS, before and after H adsorption, as shown in Equation 2.39:

$$\Delta G_{\mathrm{H_{ads}}} = \Delta E_{\mathrm{H_{ads}}} + \Delta(\mathrm{ZPVE}) - T\Delta S \tag{2.39}$$

where T is the temperature (chosen as 298 K for all studies here). For surface adsorbed species, Δ(ZPVE) and ΔS are obtained through normal mode analysis. Only the vibrational entropy was considered as an extended system cannot undergo net translation or rotation. The differences are taken relative to gas phase hydrogen. Because the calculation of entropy for single molecules can be unreliable, the experimental value for the standard molar entropy of H_2 was sourced from Ref. 132 and the zero-point vibrational energy from Ref. 133.

2.5.2 Reaction barriers and mechanisms

The transition state (TS) of a reaction path refers to the point at which the energy is at a maximum along the reaction coordinate, but a minimum in all other dimensions of the potential energy surface (PES; point B in Figure 2.3). A TS can be thought of as the highest point on the minimum energy pathway (MEP) that converts reactants into products. The energy of the TS determines the activation energy of a reaction, and thus is critical to determining mechanisms and reaction rates. Often, MEPs are represented along one dimension (the reaction coordinate), such as that shown in the right of Figure 2.3. In reality the PES is many-dimensional, and finding the TS of a MEP requires minimising the energy in all but one of these dimensions. The activation energy (or barrier) of a reaction is defined here as the energy of the TS minus that of the initial state (IS).

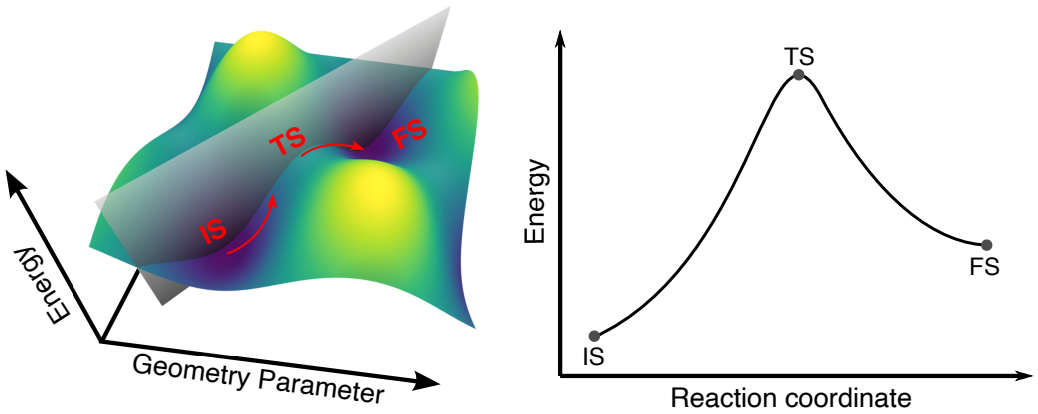

Figure 2.3: A depiction of a two-dimensional potential energy surface (left) and the corresponding reaction pathway along the reaction coordinate (right) in one dimension. The minimum energy path is represented by the grey plane.

There are many techniques which can be used to locate transition states. These techniques usually require knowledge of at least the IS of the reaction, but often also need either a direction to follow or a representation of the final state (FS).

Nudged elastic band

The nudged elastic band (NEB) method[134] is one of many advanced techniques to locate a TS, and it does this by calculating the entire MEP (from which the TS can be identified). In the NEB method, the initial and final states of the reaction are first connected by

a series of "images" representing structural geometries along the path (see Figure 2.4). These images are linked by mathematical elastic bands, where they experience a spring force, F_i^s, on their nuclei pulling in the direction of the neighbouring images. This spring force is always parallel to the direction of the MEP. The images in the NEB are then optimised in concordance with each other, but minimising only the forces perpendicular to the MEP and maintaining the spring force. Mathematically, this entails minimising the following expression:

$$F_i = F_i^s(r_{i-1}, r_i, r_{i+1})_{\parallel} - \nabla E(r_i)_{\perp} \tag{2.40}$$

where F_i is the total force on image i, and $\nabla E(r_i)_{\perp}$ is the gradient of the PES perpendicular to the MEP for coordinates r of the image. It is highly important that the gradient of the PES is projected only perpendicular to the MEP so that the images strung along it do not slide towards the initial and final states.

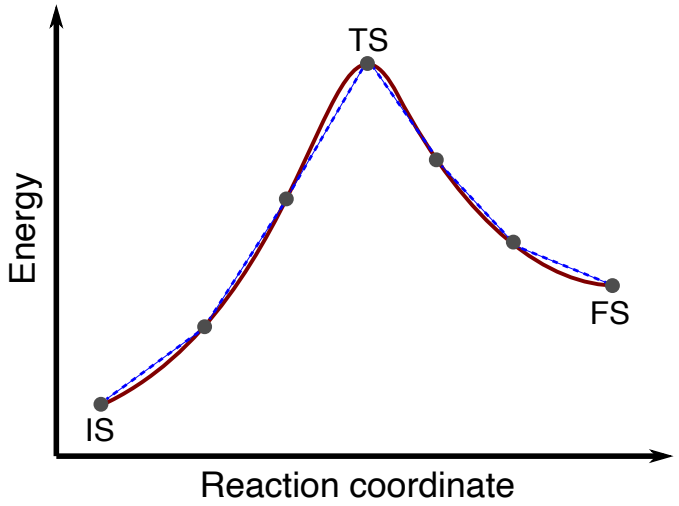

Figure 2.4: A schematic representation of a nudged elastic band path, showing the images (grey circles) along the true reaction path (red curve) linked by mathematical elastic bands (blue dashed lines). The initial state (IS), transition state (TS), and final state (FS) for this reaction are also noted on the path.

As an extension to the regular NEB method, climbing image NEB[135] can be used to find the exact TS and prevent any corner cutting by "pushing" the highest energy image up to the apex of the reaction pathway. Climbing image is usually turned on when the

rest of the MEP is well converged. Mathematically, when climbing image is turned on, the spring forces on the highest energy image are removed, and the gradient of the PES parallel to the path is reversed such that the force acting on this image can be written as:

$$F_{i,max} = \nabla E(r_{i,max}) - 2\nabla E(r_{i,max})_{\parallel} \tag{2.41}$$

This methodology results in a more accurate estimate of the TS without having to rely on an extrapolation between images.

2.6 Analysis of electronic structure

2.6.1 Projected density of states

When considering the electronic states in extended periodic systems such as those modelled here, instead of the discrete orbitals at fixed energies that are expected for molecular systems, one finds a more continues distribution of possible energy levels that electrons can occupy. This follows from considering that the overlap of electronic wavefunctions results in a splitting of energy levels. As more and more electrons (or wavefunctions) overlap, representing the extension to an infinitely repeated system, the splitting between states becomes finer until the states are effectively continuous. The density of these states (DOS) represents the number of possible states within an energy interval (dE) that electrons can occupy for a given amount of k-space.[127] The DOS is a useful tool for electronic structure analysis that is applied throughout several chapters in this thesis. From an already solved electronic structure, where the energies of states are known, DOS can be calculated by simply summing up the possible states within a discrete energy bound:

$$DOS(E) \propto \frac{\sum n_{\text{states}}}{dE} \tag{2.42}$$

where n_{states} is the number of states within the energy interval, dE.

It is also highly useful to be able to link states with specific atoms, and assign their angular momenta (projected DOS). Within the Vienna *Ab initio* Simulation Package, this

is accomplished by projecting the Kohn-Sham states (ϕ_{KS}) onto the spherical harmonics (Y_{lm}^{α}) around each atom (α) within its Wigner–Seitz radius (R_{w}).[l] The angular momentum weight ($w_{i,l}$) for each projected Kohn-Sham state is given as:[136]

$$w_{i,l}(R_{\mathrm{w},\alpha}) = \sum_{m} \int_{0}^{R_{\mathrm{w},\alpha}} r^2 |f_{i,l,m}(r)|^2 \, dr \tag{2.43}$$

Here $f_{i,l,m}(r)$ is given by:

$$f_{i,l,m}(r) = \int Y_{lm}^{\alpha}(r) \phi_{KS,i}(r) \, dr \tag{2.44}$$

where i is the index of the Kohn-Sham state, and l and m are the angular momentum and magnetic quantum numbers, respectively. Because the energies of the Kohn-Sham states are discrete, the values of $w_{i,l}(R_{\mathrm{w},\alpha})$ are broadened using a Gaussian distribution ($\sigma = 0.01$ eV) in order to allow visualisation.[137]

2.6.2 Bader charge analyses

Another highly useful tool that is commonly applied in this thesis is charge partitioning *via* a Bader charge scheme.[138] The aim of this analysis is to assign electronic charge to specific nuclei, thus allowing assessment of the charge on each atom. This aids understanding how electrons are distributed in systems, and can give information on how the charge character of different atoms changes in the event of bonding.

The Bader analysis works by locating planes of zero-flux on the charge density surface, where the charge volume encompassed within them is treated as a single Bader region and assigned to a given atom.[139] The process is shown schematically in Figure 2.5. First, a grid-based three-dimensional representation of the charge density is assembled. Then, starting at one point (i_1, j_1, k_1 in Figure 2.5A), the steepest ascent path along grid points in the charge density is followed (red line) until a maximum (m_1) is found. The maximum corresponds to an atomic nucleus, where charge density would be highest. All the points

[l] The Wigner–Seitz radius is a spherical representation for the atomic volumes based on the volume per free electron in a solid.[127]

along the ascent trajectory are then assigned to one Bader region and the search is started again from a new grid point (i_2, j_2, k_2). If this second climbing path (purple line) – or indeed any future one – encounters a point along a previously assigned Bader region, all points within the new path are also assigned to that same Bader region. The search is repeated until all grid points have been covered, and the surface is partitioned into regions separated by planes of zero-flux. The result is a set of separate Bader regions (blue and green in Figure 2.5B) that can be treated as atomic regions of charge.

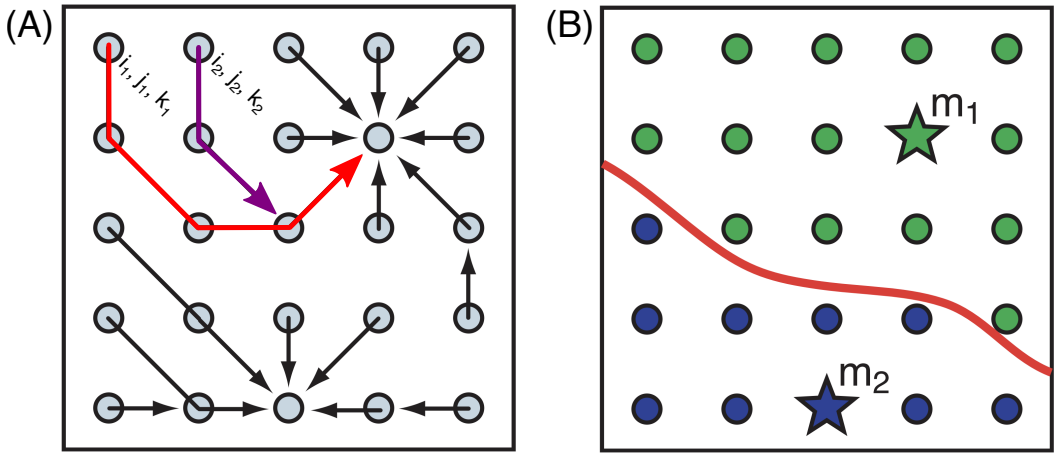

Figure 2.5: A graphical representation showing the process of a Bader charge analysis on a representative grid of charge density. (A) Shows the process of iteratively climbing paths of steepest ascent on the charge density grid, starting with point i_1, j_1, k_1 and following the red line, then moving to point i_2, j_2, k_2 and following the purple line. (B) Shows the divided charge surface, the green half of which is assigned as belonging to maximum m_1, and the blue half to m_2. These maxima can be thought of as the nuclei of atoms. The image is adapted from Tang *et al.*[140]

2.7 Summary of general computational details

All the electronic structure calculations in this thesis are performed using plane wave DFT, as implemented in the Vienna *Ab initio* Simulation Package (VASP).[141,142] A Bayesian error estimation exchange-correlation functional (BEEF-vdW)[116] is used, which is a GGA formulation of DFT. This functional also includes the simulation of van der Waals forces, which are necessary to correctly describe the interaction between MoS_2 and support materials. The BEEF-vdW functional has been designed to capture surface catalysis

processes,[116] and also includes an inbuilt estimation of the possible spread of energies that may be obtained if one were to use different functionals to calculate the same system. We do not currently use the error estimation capability in this work, as it adds a small computational cost. However, it can readily be applied to our current results should it ever be needed in the future.

The valence electrons in all systems were described using a plane wave basis set with a 500 eV kinetic energy cut-off, and core electrons were accounted for using the projector augmented wave method. The electron density was solved with iterative diagonalisation of the Kohn-Sham Hamiltonian, where electronic states were smeared using a Fermi-Dirac distribution of width $k_BT = 0.1$ eV. All reported energies were extrapolated to $k_BT = 0$. When calculating density of states, the smearing width was reduced to 0.01 eV. In all systems electronic convergence was defined as an energy difference of less than 10^{-5} eV between successive electronic solutions. In geometry optimisations, all structures were optimised until the forces on all centres were less than 0.03 eV/Å.

Chapter 3

Mechanisms for hydrogen evolution on supported MoS_2

In this chapter the mechanisms for the hydrogen evolution reaction (HER) are studied in depth on the Mo-edge of MoS_2. Two catalyst support materials which are commonly used in experiments are introduced underneath MoS_2: Au(111) and graphene. These supports are known to modify the properties of single-layer MoS_2, so here it is examined whether they alter the rate and mechanism of HER catalysis.

First, a detailed investigation into possible models for the electrochemical environment at the cathode is performed, considering both solvent and potential.[a] These two features are required to simulate the Heyrovský step in the overall HER mechanism. We show that a proton shuttling model for the Heyrovský step does not accurately capture the processes involved on MoS_2, and instead a full water model must be used. The application of this large-scale model poses significant computational expense, and thus we demonstrate a number of ways in which it can be made tractable without significantly reducing accuracy.

In terms of catalytic investigations, the thermodynamics of adsorbing H to different sites on the Mo-edge are calculated first. From this, we determine what coverage of hydrogen would likely exist on the surface at catalytically relevant potentials. We also

[a] In this chapter, the term potential is used exclusively to refer to the electrode potential. This is the electrochemical driving force (i.e. the applied voltage) during reduction at the cathode. Reduction potentials are, by convention, presented as negative numbers.

identify sites on the surface where H_2 combination may be likely to occur. Going forwards, we calculate reaction barriers for two possible mechanisms of H_2 combination: Volmer-Tafel and Volmer-Heyrovský, where the detailed solvent and potential model discussed above is applied to the latter. Finally, the effect of the support (Au(111) or graphene) on the barriers for the HER is quantified. We find qualitative agreement with experimental literature, and demonstrate the critical importance of choosing an appropriate catalyst support material.

This chapter is substantially based on the published article: Ruffman, C., Gordon C. K., Skúlason E., and Garden, A. L. "Mechanisms and potential-dependent energy barriers for hydrogen evolution on supported MoS_2 catalysts," *Journal of Physical Chemistry C*, **2020**, *124*, 17015–17026.[143] Calum Gordon ran a portion of the H adsorption and Tafel combination calculations for graphene-supported MoS_2. Professor Egill Skúlason (University of Iceland) contributed discussions and advice around implementing the full water model for potential and solvent.

3.1 Introduction

Knowledge of reaction mechanisms is highly sought after for a number of processes, ranging from industrial reactions such as ammonia formation for fertilizers,[144–146] to biological reactions such as methionine oxidation and the role it plays in Alzheimer's disease.[147] For the HER, understanding where on a catalyst (i.e. the active site) and how the reaction takes places offers several significant benefits.[46,148,149] Firstly, with knowledge of the active site, existing catalysts can be improved by increasing the site density, which has previously been very successful for different forms of Pt HER catalysts.[150] Secondly, with understanding of the reaction mechanism, the rate-limiting step, and specifically *how* a catalyst increases the rate, certain features can be engineered into the active site to improve performance. For example, the HER rate on Pd catalysts is known to be limited by strong Pd-H bonds, making it hard for desorbtion to occur.[151] Using this information, Wang *et al.*[152] engineered Pd nanocrystals with surface-intercalated H that accelerated the H_2 desorption step and greatly improved the overall reaction rate.

Mechanistic and active site knowledge can also allow new catalysts to be developed, for instance by screening across a range of candidate materials. As touched on in the general Introduction, Greeley *et al.*[36] were able to develop a new Pt-based catalyst for the HER using knowledge of where and how H reacts on metal surfaces. The authors screened across over 700 Pt alloy materials and isolated a promising Pt-Bi catalyst, which later showed excellent HER activity in experimental tests. In summary, mechanistic knowledge allows the rational design and improvement of catalyst materials, where targeted steps can be taken to optimise performance for a given reaction.

Using electronic structure simulations to study reaction mechanisms computationally gives many key insights which can be difficult to obtain directly from experimental data. It can be challenging to characterise surface active sites and intermediates experimentally,[153,154] and the main way of comparing different electrochemical mechanisms is *via* measuring differences in the Tafel slope.[64,b] This is not always reliable due to non-linear behaviours which may be caused by the rate or mechanism changing with applied potential.[155] Furthermore, using linear sweep voltammetry or cyclic voltammetry to calculate a Tafel slope is also subject to many assumptions, and depends strongly on factors such as scan rate, making it an unreliable tool in the eyes of some researchers.[156] In contrast, mechanistic and rate information can be directly extracted from simulations and then compared to experimental results.

It is known that the HER involves the combination of two identical reactants (H^+) in the presence of a catalyst. The first step must be to adsorb H^+ to the catalyst, including a formal reduction of the proton. This step is referred to as the Volmer reaction:

$$H^+(aq) + e^- \longrightarrow H_{ads} \tag{3.1}$$

From here, the HER could proceed either *via* Tafel combination of two surface H_{ads} (Equation 3.2),[157] or *via* Heyrovský combination of a surface H_{ads} and a H^+ from solution

[b] This slope refers to the gradient of a plot of electrochemical reaction rate (e.g. current density) against the applied potential. The Tafel slope is often taken at an overpotential of 0.1 V.

(Equation 3.3).[158]

$$H_{ads} + H_{ads} \longrightarrow H_2 \tag{3.2}$$

$$H_{ads} + H^+(aq) + e^- \longrightarrow H_2 \tag{3.3}$$

Because the HER is a two-step process, regardless of whether it proceeds through a Volmer-Tafel or a Volmer-Heyrovský mechanism, both paths go through the same surface H_{ads} intermediate state. Thus, the H adsorption free energy ($\Delta G_{H_{ads}}$) can fully capture the thermodynamic cost of the overall reaction – but it does not contain any information about the favoured mechanism. Following the Sabatier principle,[159] the thermodynamically optimal catalyst is one where H adsorbs with $\Delta G_{H_{ads}} \simeq 0$ eV. This idea is highly relevant to Chapter 4, and will be discussed in detail there.

Several past studies have used $\Delta G_{H_{ads}}$ to quantify HER activity changes on different materials.[55,74,76,160] For instance, one pertinent example is that $\Delta G_{H_{ads}}$ on MoS_2 can be altered between -0.25 and 0.20 eV by the addition of graphene or Au(111) support materials beneath the catalyst,[76] indicating that the overall reaction rate may also be affected. However, while using $\Delta G_{H_{ads}}$ as an approximation of activity is computationally simple, and it demonstrates the possibility of optimising MoS_2 as a catalyst through the use of support materials, it does not provide any insight into the reaction kinetics or the mechanisms taking place. The kinetic barriers are required in order to quantitatively predict reaction rates, and detailed mechanistic information can be critical to rationally improving the design of any catalyst.

The HER mechanism has been extensively studied on Pt surfaces both experimentally and computationally across a series of works. In studies on single-crystal Pt, Marković *et al.*[50,161,162] report not only different reactivity on different surface facets, but different mechanistic preferences. Pt(110) was found to be most active, followed closely by Pt(100), with Pt(111) being notably less active than either of the former. The authors suggest the HER proceeds *via* a Volmer-Tafel mechanism on Pt(110), but on Pt(100) a Volmer-Heyrovský process dominates. No conclusion was able to be reached about the mechanism on the Pt(111) surface, which is known to be the most stable pristine surface facet.[163,164]

On polycrystalline Pt, there is some evidence that the Volmer-Heyrovský reaction is prevalent.[149] Computationally, there is support from DFT calculations for the Volmer-Tafel preference on Pt(110),[165] and Skúlason *et al.* use advanced DFT models that include electrolyte and potential to predict that a Volmer-Heyrovský mechanism is favoured on Pt(111).[45,46] Overall, these works studying the HER on Pt demonstrate both the importance of understanding the full mechanism, and also how the mechanism can greatly depend on features of the catalyst structure (such as different surface facets).

Moving to MoS_2, an investigation into the HER kinetics on the active edges has been reported by Huang *et al.*, where DFT is used to simulate the Volmer-Tafel and Volmer-Heyrovský reactions.[166] An unsupported cluster model of MoS_2 was employed, and the authors focused on the 50% sulfided Mo-edge. As mentioned in the general Introduction, the Mo-edge is believed to be most active for hydrogen evolution, and the 50% sulfur coverage represents the experimentally observed structure for an industrial-style MoS_2 catalyst.[167] The potential and pH were both accounted for in Huang's work by linearly scaling the energies of e^- and H^+ in the system based on empirical values for their chemical potential under the definition of the standard hydrogen electrode (SHE). The stable forms of MoS_2 under given potential and pH conditions could then be predicted. From these stable forms, the authors calculated reaction barriers using standard methodology, without further consideration of the potential. It was reported that, at -0.15 V *vs* SHE, the Volmer-Heyrovský mechanism (0.78 eV barrier) dominated over the Volmer-Tafel mechanism (0.98 eV barrier). For both mechanisms, the H_2-formation step was limiting, as opposed to the Volmer step to adsorb H onto the surface. The results from this unsupported MoS_2 model agreed closely with the experimental rate determined by Jaramillo *et al.*[64] However, the experimental rate was reported for MoS_2 supported on Au(111), and to the best of our knowledge, there has been no work to date examining how the kinetics of the HER change with different MoS_2 supports. Because changes to $\Delta G_{H_{ads}}$ on MoS_2 are possible with different support materials,[77] it seems likely that the supports may also have a significant effect on the reaction kinetics. Other work has also demonstrated the large effect supporting materials can have when it comes to the electronic and structural properties of MoS_2.[168]

Additionally, Huang *et al.*'s model of the electrochemical potential captures only the potential dependence of the energies of stable intermediates, but it is not able to capture the explicit effects of potential on the transition states. Because the Volmer and Heyrovský steps both involve formal electron transfers, their barriers, mechanisms, and the energies of involved states will all be highly sensitive to the potential. It has previously been shown that a full model for solvent and electrochemical potential is key to correctly modelling the transition states for the Heyrovský reaction on Pt surfaces.[46]

In this chapter, we investigate the mechanisms and kinetics of the Volmer-Tafel and Volmer-Heyrovský reactions for the HER on supported MoS_2 catalysts using detailed models of the electrochemical cell that capture both solvent and potential.[46] In order to examine the tuning of reaction kinetics with different catalyst supports,[77] two support materials which are commonly used in experiments were chosen for study: Au(111)[64,69] and graphene.[61,72] Overall, we examine the reaction kinetics of MoS_2 on both these supporting materials across a range of potentials from 0.0 to -0.9 V. Our results show good agreement with the trends in available experimental data, and provide insight into the rate limiting reaction steps as a function of applied potential.

3.2 Methodology and model testing

3.2.1 Structure models

All systems were modelled as repeating periodic slabs with at least 12 Å of vacuum separation in the z-direction. MoS_2 edges were represented using a semi-finite stripe model,[169] where an extended sheet of MoS_2 was cut to expose the Mo $(10\bar{1}0)$ and S $(\bar{1}010)$ edges. Images of the supported models are shown from the top and side views in Figure 3.1. At least 6 Å of separation was kept between repeating stripes in the non-periodic direction. The exposed Mo and S edges at the S coverages studied in this work can also been seen in Figure 3.1. A stripe model that was four Mo atoms in the periodic direction was chosen in order to ensure the model was computationally tractable while still allowing for a variety of different hydrogen coverages to be reached. The model was also four Mo

atoms long in the non-periodic direction. The lattice constant for MoS_2 was found to be 3.18 Å, in close agreement with the experimental value of 3.16 Å.[170] The support material beneath the MoS_2 stripe was periodic in both lateral directions (x and y). The Au support (a = 4.21 Å) was represented as three layers of Au(111) with the MoS_2 stripe found to optimise approximately 2.5 Å above the (111) surface of the Au. The bottom layer of Au was fixed to simulate the bulk. The graphene support was represented by a single layer of graphene (a = 2.45 Å). The MoS_2 stripe was found to be stable approximately 3.5 Å above the graphene. Both Au(111) and graphene supports were strained by less than 8% of their respective lattice constants in order to avoid mismatch with MoS_2. Past work has indicated that the H adsorption energy on the MoS_2 basal plane can be slightly modified by inducing strain.[171] Thus, to match the lattices we only strain the support here. It is unlikely that this minimal strain on the support will affect the catalytic activity of MoS_2.

3.2.2 Modelling the Volmer reaction

The Volmer reaction involves the reduction of a proton at the catalyst surface to form H_{ads}. The energetics of this reaction can be described as a function of the electrode potential using the computational hydrogen electrode (CHE),[172] in which the free energy of an $H^+ + e^-$ pair is taken to be equal to that of $\frac{1}{2}H_2$ under standard conditions at $U = 0$ V *vs* the standard hydrogen electrode (SHE). The effect of potential (U) on the H adsorption energy is therefore included *via* the relation:

$$\Delta G_{H_{ads}}(U) = \Delta G_{H_{ads}} - eU \tag{3.4}$$

where $\Delta G_{H_{ads}}$ is the H adsorption free energy and e is the elementary charge. This relation shows that the Volmer reaction is spontaneous at potentials more negative than $eU = -\Delta G_{H_{ads}}$, whereas at more positive potentials there will be a thermodynamic cost to the Volmer reaction. This is a widely used methodology in the field of computational electrochemistry, and has previously been applied to study the HER on various metal surfaces,[45] and also to look at the CO_2[173] and NO_3[174] reduction reactions.

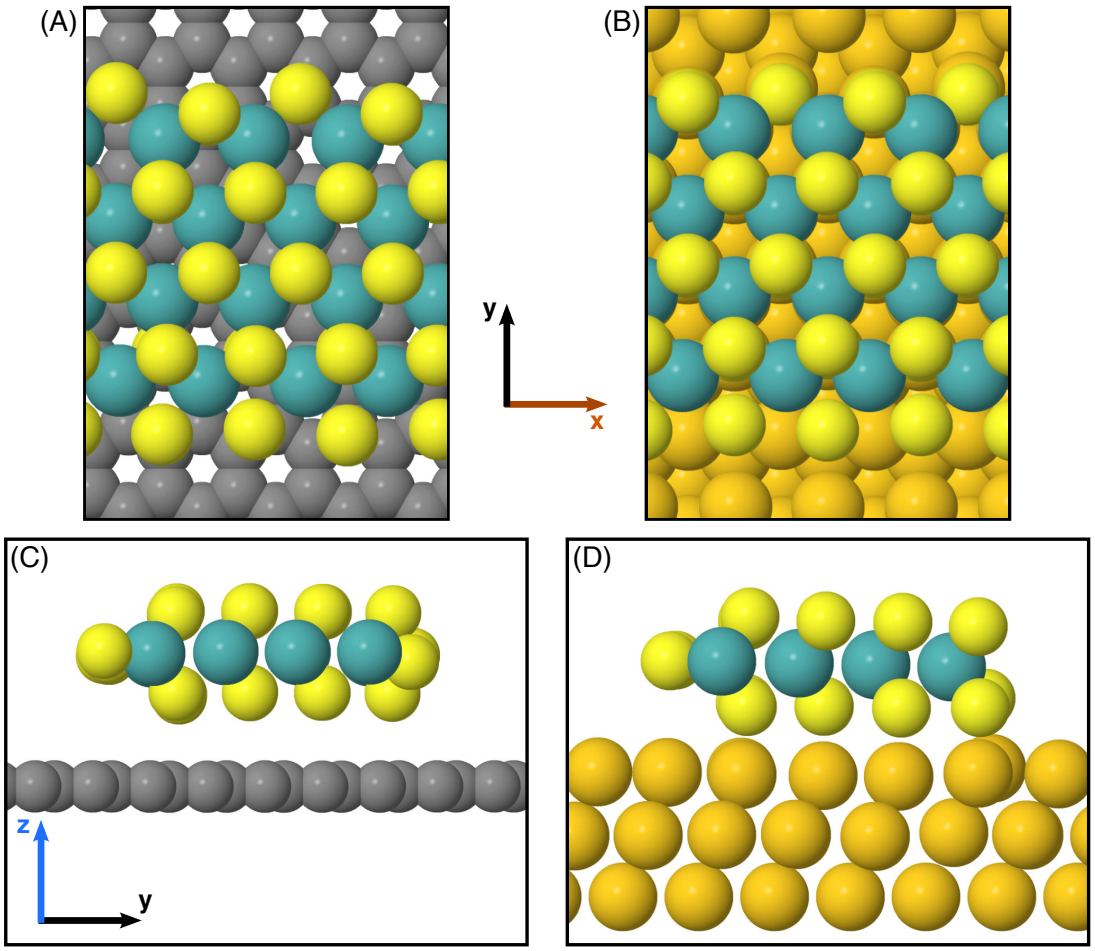

Figure 3.1: Top view of optimised semi-finite stripe models of MoS_2 supported on (A) graphene and (B) Au(111). Side views are also included in (C) and (D).

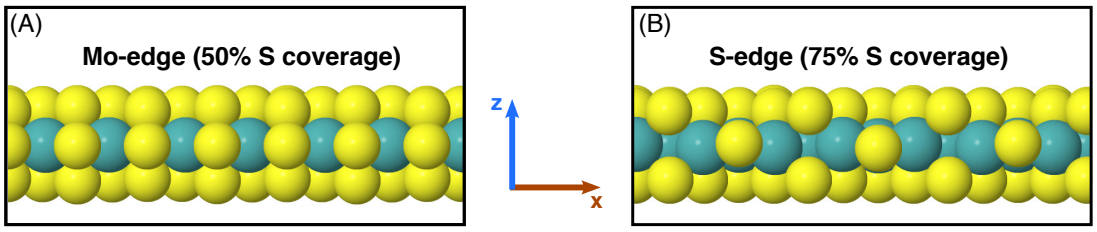

Figure 3.2: End-on views of (A) the catalytically interesting 50% sulfided Mo-edge of MoS_2, and (B) the 75% sulfided S-edge. Even though catalysis is not studied on the S-edge, it is impossible to form a semi-finite stripe model of MoS_2 without having both types of edge, thus it is simulated at an industrially realistic S coverage.[167]

Huang *et al.*'s previous work on MoS_2[166] has indicated the Volmer reaction has a lower barrier than the following steps to combine H_{ads} on the surface. A similar situation is also observed in experimental and theoretical work on Pt, where the Volmer reaction is typically found to have a low barrier and to be a very fast process.[46,161] Thus, in the present work only the thermodynamics and not the kinetic barriers for the Volmer reaction are considered. Practically, this means all H adsorption steps in reaction free energy diagrams are treated as barrierless, though any thermodynamic energy differences between states are still accounted for.

3.2.3 Modelling the Tafel reaction

The Tafel reaction for H combination does not involve a formal electron transfer and therefore the energetics do not directly depend on the electrode potential. However, the reaction is indirectly affected by potential, as it determines the H coverage on the catalyst surface, which in turn influences the Tafel barriers.[45] The surface H coverage at a given potential can be calculated using a slight reformulation of the CHE to that given previously:

$$\Delta G_{\mathrm{H_{ads,diff}}} = -eU \tag{3.5}$$

where $\Delta G_{\mathrm{H_{ads,diff}}}$ is the differential hydrogen adsorption free energy which describes the energy required to adsorb one additional H atom to the catalyst surface at the H coverage it presently has. This relation states that, for a given U, H atoms will adsorb to the surface spontaneously up until the free energy becomes endergonic. Once we know the potential at which different H coverages spontaneously exist, the Tafel kinetic barriers can be calculated using standard climbing image nudged elastic band methodology (CI-NEB, described in Chapter 2).[134,135] A separate CI-NEB calculation is performed at each of the different H coverages simulated, with each one corresponding to a different applied potential.

Accounting for changes in the H coverage has been shown to capture the majority of the effect of applied potential for the Tafel reaction on Pt catalysts.[46] Furthermore, it has been noted in past work on Pt(111) that the inclusion of solvent in the form of

an explicitly simulated water layer above the electrode makes minimal difference to the Tafel barriers.[45] In the present work a water layer was excluded when modelling the Tafel reaction in order to maintain computational tractability. This methodology has also been used for other catalyst materials such as transition metal nitrides[60] and an alternate phase of MoS_2 (1T).[175]

3.2.4 Modelling the Heyrovský reaction

The Heyrovský reaction for H combination (Equation 3.3) includes a formal electron transfer and involves a solvated proton. It therefore requires a more advanced model of the electrochemical cell than that for the Tafel reaction. Ideally, the model would have three key features: (1) the solvated proton (H^+(aq)) would be accurately represented, (2) the energy of states involving H^+ and e^- would correctly scale with potential, and (3) during the course of a Heyrovský combination the potential difference and electric fields should remain constant, as they would in a real electrochemical cell. These three conditions of the model are summarised schematically in Figure 3.3, which shows a hypothetical set-up for the Heyrovský reaction at the cathode. In the present thesis two separate models were explored in an attempt to capture some or all of these features. Note that each of these models will be discussed in depth in the following sections, including results on their applicability and tractability. The full Results and Discussion section that follows (Section 3.3) focuses only on the catalysis results produced by the preferred of the two Heyrovský models.

Proton shuttling model

Initially, it was attempted to model the Heyrovský mechanism using the proton shuttling method developed and applied by Janik *et al.* across several works.[176–178] For an inner sphere proton-coupled electron transfer,[c] Janik's group propose that an analogous *non-electrochemical* reaction can be simulated and the reaction barriers can be calculated using standard DFT methods such as CI-NEB.[176] Then, the potential dependent reac-

[c]Meaning the oxidant and reductant are closely associated and the electron transfer does not go through other species.

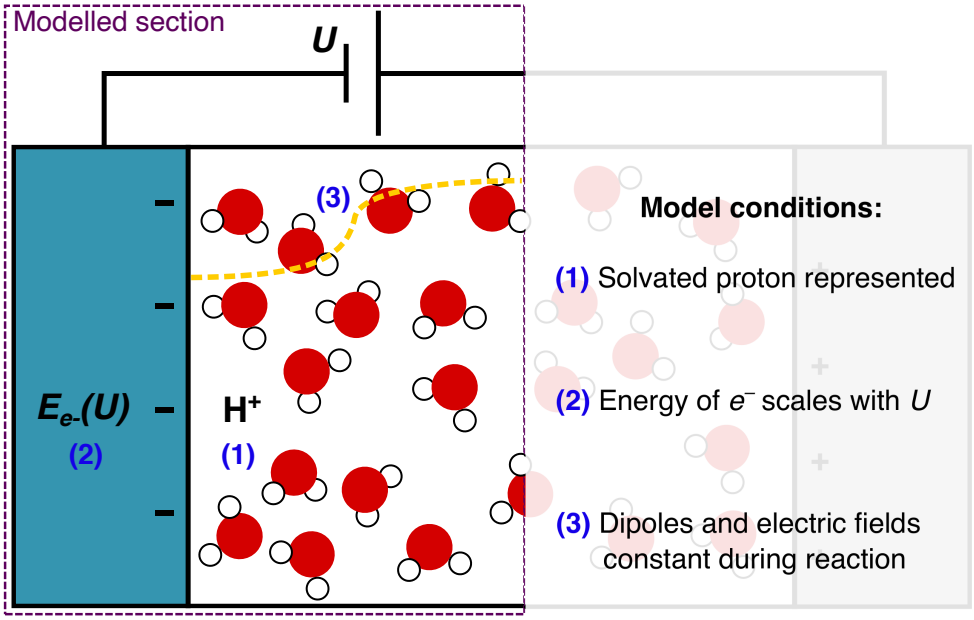

Figure 3.3: A schematic showing the three desirable conditions for a model of the Heyrovský reaction at the cathode. The dashed yellow line indicates the electric field arising from the negatively charged cathode. This image is adapted from Figure 1.2 in the general Introduction.

tion barriers can be extrapolated from this result. The advantage of this methodology is its computational tractability, and the lack of requirement to explicitly account for computationally difficult features such as electron transfer.

A simple non-electrochemical activation barrier for the Heyrovský reaction can be described using a proton-shuttling mechanism,[177] where a small cluster of one or two water molecules is simulated above MoS_2, which has both a "reactant" H and a "dummy" H adsorbed. The reactant H_{ads} is the one which will undergo Heyrovský combination, whereas the dummy H serves only to replace one of the H atoms in the water molecules when they donate H in the Heyrovský combination. The process is depicted schematically with one water molecule in Figure 3.4. Overall, it constitutes shuttling of the dummy H from the surface to the water cluster at the same time as a the reactant H combines with one of the H atoms from the water cluster. This mimics the real process of H^+ coming from the bulk electrolyte. The position of this dummy H_{ads} within the simulation cell is irrelevant, provided that it can freely move to facilitate the lowest energy transition state.

In this work it was found in testing of different dummy H positions on MoS_2 that this did not significantly change any calculated reaction barriers or transition states.

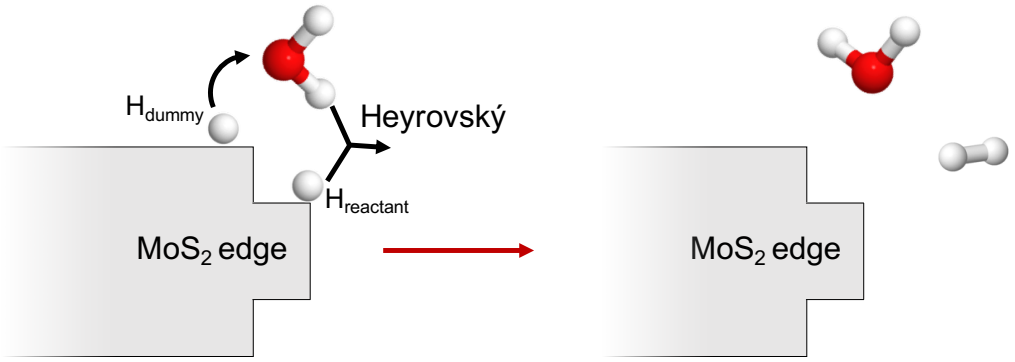

Figure 3.4: A schematic representation of the non-electrochemical proton shuttling reaction used to represent a Heyrovský combination on the MoS_2 edge.

The activation energy for this non-electrochemical process, $E_a^0(U^0)$, is assigned to be at the equilibrium potential, where the energy of the adsorbed dummy H atom is equal to the energy of the proton-electron pair in solution, $H^+ + e^-$. This is the point at which there the dummy H spontaineously leaves the surface to replace H in the water cluster, and is calculated as the potential at which the dummy H can adsorb and desorb with no energy cost. The idea is akin to that of the computational hydrogen electrode,[172] initially discussed in Section 3.2.2. The Heyrovský barrier can then be extrapolated to any potential, $E_a(U)$, using Equation 3.6:

$$E_a(U) = E_a^0(U^0) + \beta(U - U^0) \tag{3.6}$$

where β denotes the reaction symmetry factor that describes how far the transition state sits along the reaction coordinate from initial to final state. For most hydrogenation reactions, β can simply assumed to be 0.5, as deviations from this value are generally small (less than 0.1).[172,177,179] This assumption is also made in the present work. In reality the value of β would shift depending on the electrochemical potential, U. Akhade *et al.*[179] detail a method by which Marcus theory can be applied to calculate a potential-

dependent β value, yet this was deemed unnecessary as the potential still has minimal effects on β near 0 V.

Assessing the applicability of the proton shuttling method

The proton shuttling method has previously been applied to various C-H bond formation steps in CO_2 reduction,[177,178] but has not been applied to hydrogen evolution on MoS_2. Thus, a series of tests first had to be performed to assess whether it was an appropriate model for the HER. We first examined unsupported MoS_2, in order to have a guide for the supported systems. Reaction barriers for Heyrovský combination were calculated with the reacting H_{ads} on either an S or an Mo atom on the Mo-edge. For the H_{ads} on S case (H_S), proton shuttling was tested with either one or two explicit water molecules above the Mo-edge, in order to see whether this had an effect on the overall calculated barriers. The barriers for unsupported MoS_2 are presented in Table 3.1, extrapolated to 0 V using Equation 3.6 (i.e. $E_a(0\,\mathrm{V})$), and the energies are given without entropic corrections and relative to the preceding H adsorbed state. The parameters required to extrapolate the barrier *via* Equation 3.6 ($E_a^0(U^0)$ and U^0) are also given in Table 3.1.

Table 3.1: Barriers for Heyrovský combination of H atoms on unsupported MoS_2 calculated at 0 V *vs* SHE ($E_a(0\,\mathrm{V})$) *via* the proton shuttling method. The parameters taken directly from the DFT calculation ($E_a^0(U^0)$ and U^0) that are used in Equation 3.6 to extrapolate the potential dependent barrier are also given.

System	$E_a^0(U^0)$ / eV	U^0 / V	$E_a(0\,\mathrm{V})$ / eV
H_S (one water)	1.53	-0.65	1.86
H_S (two water)	1.46	-0.57	1.75
H_{Mo} (one water)	0.30	-0.74	0.67

Examining Heyrovský combination with the reacting H on S, when comparing between the case with one water molecule *versus* two above MoS_2, it is clear that the addition of a second water molecule for proton shuttling appears to reduce the barrier by about 0.1 eV at 0 V of potential. This difference between one and two water molecules is roughly consistent with the 0.2 eV reduction in barrier that Janik *et al.* report with two water molecules instead of one when looking at C-H bond formation.[177,178] The authors argue

this degree of barrier change is fairly minor, and within the range of error that might be expected from DFT. Though, we note here this could still be rather significant in cases where barrier is already small. It appears that the proton shuttling method may very slightly overestimate the barriers relative to a more realistic solvent model, where a number of water molecules would be available around the reacting site.

From the barriers at 0 V given in Table 3.1, it is also clear that the Heyrovský combination barrier is prohibitively high (1.75 eV) when the surface-adsorbed H is situated on an S atom, whereas when the reacting H is on an Mo atom (H_{Mo}) this barrier is much smaller at 0.67 eV. In their study of the HER mechanisms on unsupported MoS_2, Huang *et al.*[166] also report a very high (1.77 eV) Heyrovský combination barrier with H_{ads} on S, which is very close to the barrier reported presently. The authors suggest the reaction is more likely to go through the H_{Mo} structure, where they report a 0.28 eV barrier. Here, the barrier calculated from the H_{Mo} state with the proton shuttling method is also more favourable than from H_S. However, it is about twice as high as that reported by Huang *et al.* This is a significant difference, especially considering the close agreement that was observed for the barriers from the H_S state. It is often expected that different models for electrochemical reactions may produce slightly different barriers (e.g. 0.1 to 0.2 eV different),[45] yet the proton shuttling method has previously shown excellent agreement with both experimental work and alternative computational models for the C-H bond formation steps in CO_2 reduction.[178] Therefore, it was clear that a discrepancy was arising for the HER on MoS_2 case that is not present in past work using proton shuttling.

The issue with applying proton shuttling to the HER became clear when looking at calculations of the net surface dipole moment. Over the course of a proton shuttle, we found that the dipole moment perpendicular to the MoS_2 surface (μ) would change significantly. This went from $\mu = -0.69$ eÅ in the initial state with H_{Mo} on unsupported MoS_2, to only $\mu = -0.04$ eÅ in the final state with H_2 formed. In testing of Heyrovský combination on graphene- and Au(111)-supported MoS_2, similar changes in dipole were also observed.[d] This magnitude of dipole change (0.65 eÅ) has notable consequences, as

[d]For Au-supported MoS_2 the net dipole moment went from 0.00 eÅ in the initial state to 0.34 eÅ in the final state of the proton shuttle, and for graphene supported MoS_2 this change was from 0.64 eÅ to 2.00 eÅ.

the electric fields generated by the surface dipoles can stabilise or destabilise electrochemical intermediates and transition states. The transition states are particularly strongly affected because charge is being exchanged at the surface in a formal reduction.[172] Janik *et al.*[178] have previously justified that the net dipole moment does not change significantly when applying the proton shuttling model to C-H bond formation steps in CO_2 reduction (differences of less than 0.1 eÅ between initial and transition states). Thus, the large shifts in the dipole moment appear to be a problem unique to the HER. We propose here that when a multi-atom species that has polar bonds is adsorbed to a catalyst (e.g. CO_2 in Janik *et al.*'s case),[e,178] it can compensate for the change in dipole as a reduction reaction occurs by reorienting its geometry slightly. For Heyrovský combination and H-H bond formation, this is not possible as the surface adsorbed species is H. Adsorbed H is not polar nor can it notably rearrange to balance a dipole shift. Thus, while the proton shuttling method applies well to cases such as CO_2 reduction, it appears flawed when applied to the Heyrovský reaction. Indeed, this methodological flaw likely accounts for the difference in the barrier calculated here from the H_{Mo} state compared to that calculated previously by Huang *et al.*[166]

It is known that methods exist to correct for changing electric fields or potentials during the course of a proton transfer reaction,[180,181] some of which will be discussed in the following section. Accounting for these changes could, in theory, correct for a changing dipole moment. However, these methods typically deal with explicitly charged species, and it is unclear how they would be applied to the case of proton shuttling where there is movement of both a dummy and reacting H. Therefore, the issue of changing dipoles ultimately meant that the present work had to shift away from the proton shuttling method and towards a more expensive and advanced technique to model the Heyrovský reaction.

In review, the proton shuttling method deals adequately with requirement (1) from the conditions outlined at the start of this section (see also Figure 3.3), by representing a "solvated" H^+ with minimal inclusion of explicit water molecules.[177,178] Here only small

[e] Of course, molecular CO_2 is linear and thus does not have a net dipole. However, CO_2 forms a bent geometry when adsorbed on a surface and therefore has a dipole.

differences in the barrier are noted if the number of water molecules are changed. It also accounts for requirement (2), that the energies of H^+ and e^- correctly change with potential, by cleverly calculating the barriers in a non-electrochemical manner and scaling the energies implicitly from this point. The biggest assumption made by this approach is that the non-electrochemical transition state for the reaction will be analogous in structure to the true electrochemical reaction, but Janik *et al.*[177] show that this assumption is valid for elementary proton transfer reaction steps like that involved in the Heyrovský reaction. However, for the Heyrovský combination of H on MoS_2, it was discovered that the proton shuttling method does not correctly account for requirement (3), that the potential and electric fields remain constant during the course of the reaction, as the dipole moment of the surface changed markedly as species reacted. As a result, it could not be used to accurately represent this reaction in its current form.

Full water model

Going forwards with Heyrovský mechanism calculations, a different model for the solvent and potential was employed. Originally proposed and applied to Pt catalysts by Skúlason *et al.*,[45,46] this model centres around the explicit simulation of a water layer above the catalyst. The large number of explicit water molecules addresses condition (1), of accurately representing a solvated proton. Unlike previous cases where this method has been applied for flat surface catalysts, the present work deals with supported MoS_2 stripes, and thus the water molecules must extend over the edges of the MoS_2 model and down to the catalyst support. The structure of water above any electrode surface is non-trivial, even for planar metal electrodes.[182] Here, the water structure above MoS_2 stripe models was determined through *ab initio* molecular dynamics (AIMD) simulations, following methodology established for planar metal electrodes,[183] and more recently applied to simulate water around carbon nanotubes.[184]

AIMD simulations were used to equilibrate the structure of 45 water molecules above graphene-supported MoS_2 and 40 water molecules above the Au(111)-supported catalyst. The numbers of molecules were calculated based on the density of liquid water at room temperature, and were selected so that water would occupy the space up to approximately

6 Å above the MoS_2 stripe. Each AIMD run (summarised in Figure 3.5) was initialised with a random water structure, and then was propagated at 450 K for 8 ps of simulation time before being cooled down to 298 K over 4 ps. Once at 298 K the structure was allowed to stabilise at this temperature for a following 2 ps of time.

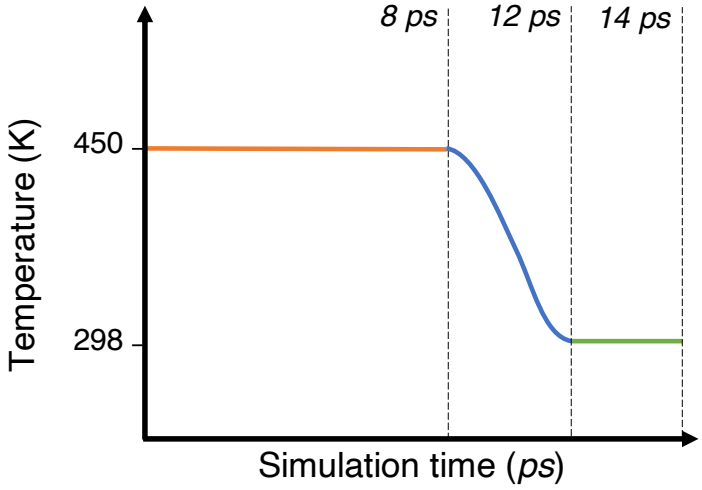

Figure 3.5: A schematic of the simulated annealing process in an AIMD run, showing the propagation of random input water structure at 450 K (orange line), the cooling phase (blue line), and the equilibration time at 298 K (green line).

The classical equations of motion were solved using a Verlet algorithm and a time step of 1 fs, simulating a canonical ensemble where the temperature was allowed to change in sets of 20 fs blocks *via* coupling to a Nosé-Hoover thermostat.[185] Only one constrained layer of Au(111) was included under MoS_2 for AIMD simulations in order to make them computationally tractable, and the plane wave cut-off was reduced from the usual 500 eV to 350 eV.

Snapshots of the equilibrium water structures for graphene- and Au-supported MoS_2 are shown in Figure 3.6, and additional snapshots are available in Appendix A. As is observed above pure transition metals,[183] the water molecules here tended to reside at least 3 Å above the MoS_2 basal pane and edges. There is no clear evidence of the hexagonal or linear ordering which has been previously observed above flat metal surfaces such as Pt, Ag and Pb.[183,186] Instead the water structure above the edge models of MoS_2 appears to be highly disordered.

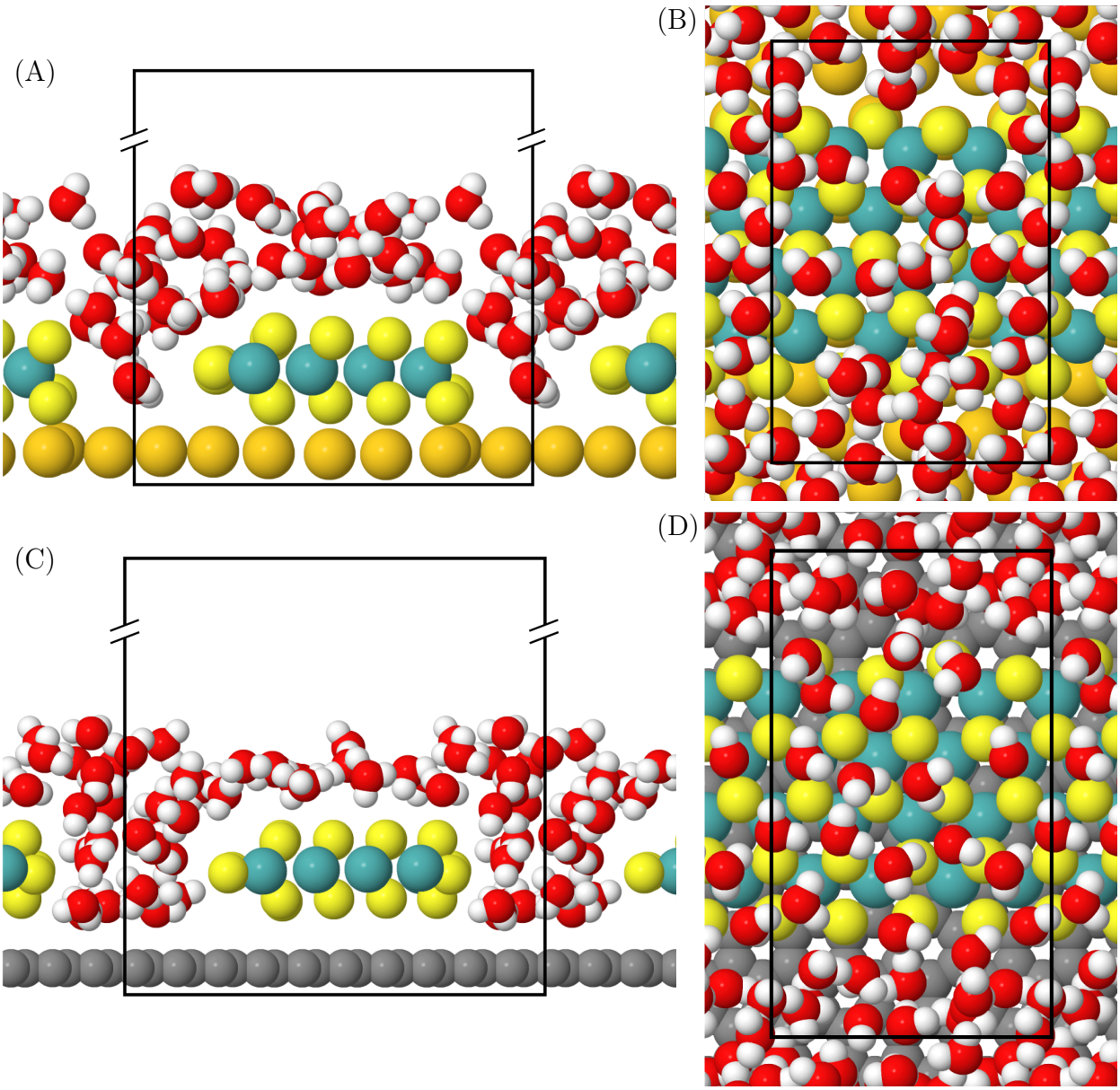

Figure 3.6: Snapshots of AIMD simulations of a water layer on Au(111)-supported MoS_2 at 13 ps since initialisation from (A) the x-direction and (B) the z-direction. Snapshots for graphene-supported MoS_2 at 13 ps since initialisation from (C) the x-direction and (D) the z-direction.

Some of the water molecules in the present simulation appear to be somewhat confined between the periodic repeats of the MoS_2 stripe model. In working with this very large computational system, extending the size of the model to avoid the clustering of water was not feasible. However, it is believed this effect will not significantly alter the Heyrovský reaction barriers calculated with this system, as Skúlason *et al.*[46] have previously indicated that barriers and energy differences are relatively insensitive to the precise water structure provided it is kept the same in all calculations.

Using a single snapshot of the water structures selected from the AIMD calculations at 298 K, the charge separation in the initial state of the Heyrovský reaction ($H^+(aq) + e^-$) was modelled using a related method also developed by Skúlason *et al.*[45] In this method, one (or more) additional H atoms are added to the water above a catalyst surface. For pure metal catalysts, under DFT relaxation, electron density from the additional H atom is found to partially transfer to the metal surface, leaving a nucleus with the character of a solvated proton in the water layer. In the present work for MoS_2, the formation of H^+ in the water layer upon electronic relaxation was also observed. This is displayed in Figure 3.7, showing charge density difference plots which represent the charge difference between the system with an additional H in the water layer (ρ_{MoS_2/H_2O+H}) *versus* the charge sum of the MoS_2/H_2O and H systems separately.[45,46] For both the graphene- and Au-supported models, a region of negative charge is located primarily on the Mo and S atoms directly underneath the H added to the water layer. A region of positive charge is also observed around the additional H in the water layer, giving it the character of a solvated proton.

Calculations of the Bader charge in the Au(111)-supported MoS_2 system (Table 3.2) reveal that the negative charge lost by H appears to be directly associated with MoS_2, rather than the support material, as the Bader charge in the support changes by less than 0.05 e^- when H is added. If multiple H atoms are added to the water layer, each additional H is associated with a charge transfer of 0.68 e to the MoS_2 (Figure 3.8). This suggests that approximately 68% of the electron in each added H becomes associated with the surface, which compares very closely with the 70% reported by Skúlason *et al.* for a H above a Pt(111) surface.[45] Adding more than three H atoms to the water layer

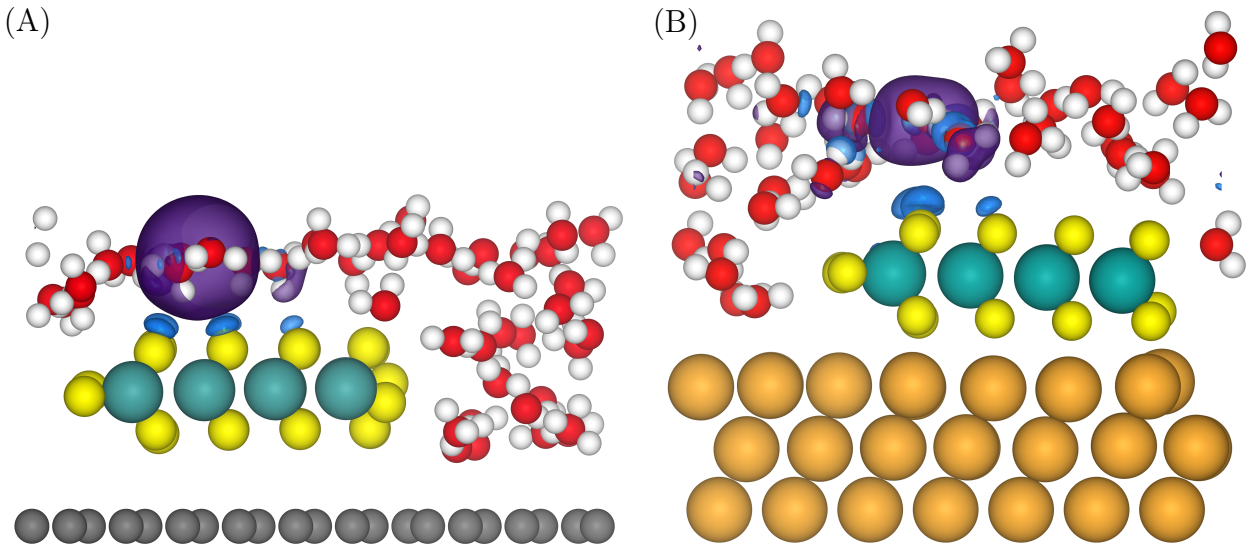

Figure 3.7: Charge density difference isosurface plots showing the rearrangement of charge on addition of a single H atom to the water layer. The difference is represented as the total density of the MoS_2 system with a single additional H in the water layer above (ρ_{MoS_2/H_2O+H}) subtracted by the density of the MoS_2/H_2O system and an isolated H atom, at the same geometry as the overall system ($\rho_{MoS_2/H_2O} + \rho_H$). Here, (A) shows graphene-supported MoS_2, and (B) shows Au-supported MoS_2. Blue indicates regions which are more negative (mainly on the MoS_2 surface) and purple indicates regions which are more positive, such as the added H in the water layer (isosurface level = 0.001 e^-Å^{-3}).

resulted in an unstable structure that formed H_2 when relaxed with DFT. Considering the large amount of positive charge in the water layer with four H^+, which creates a thermodynamic driving force towards forming H_2, it follows that this may be located by the local optimisation.

Table 3.2: The net Bader charge (e^-) in different parts of the MoS_2 and support system for Au-supported MoS_2. The values are shown both before and after an additional H has been added to the water layer.

Net Bader charge in:	No additional H	One additional H
MoS_2	-1.12	-1.95
Au support	1.25	1.20
MoS_2 + Au	0.12	-0.75

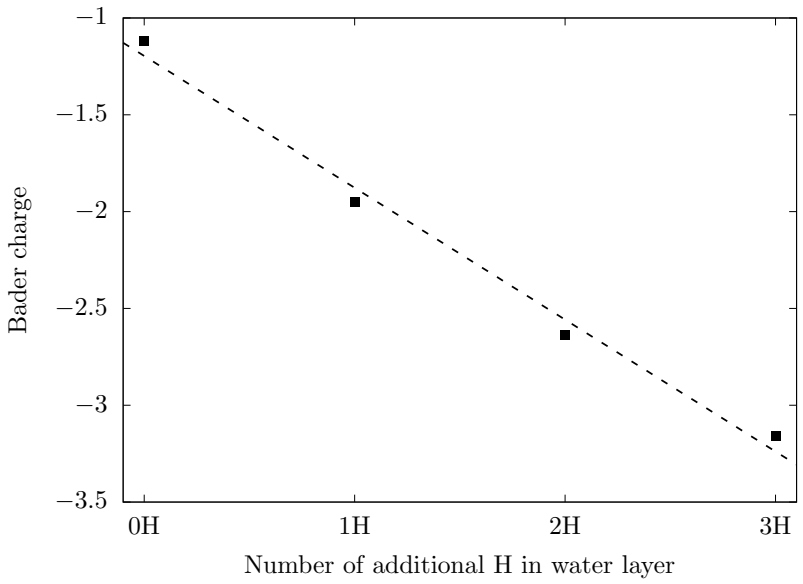

Figure 3.8: The calculated Bader charge (in units of e^-) on the MoS_2 for the Au(111)-supported catalyst as a function of the number of additional H in a water layer above the surface. The equation is: Bader charge $= 0.681 \cdot n(\mathrm{H}) - 1.20$

For simulating the Heyrovský mechanism, only one H was added to the water layer. The position of the additional H atom in the water layer was chosen such that minimal rearrangement of solvating water molecules was required in order for Heyrovský combination to occur. This meant the H^+(aq) was situated nearly directly above H_{ads}. It is possible that choosing different positions for this proton or different snapshots of the

water layer may influence the barriers, yet here it was found that the absolute energies of several possible proton and water configurations differed by less that 0.2 eV. By adding the proton in a similar position for both the graphene- and Au-supported catalyst it is attempted to keep this effect the same for both materials.

The charge separation between the positive solvated proton in the water layer and the negative MoS_2 surface below introduces an internal potential difference to the system (U), which can be estimated relative to the SHE based on the work function of the system (ϕ) and the work function of the SHE *versus* vacuum (ϕ_{SHE}) *via* Equation 3.7.[45]

$$U = \phi - \phi_{\mathrm{SHE}} \tag{3.7}$$

The system work function represents the amount of energy it takes to move an electron from the solid MoS_2 surface into the vacuum, which has a natural relation to the energy of the electron. By definition, the potential of the system determines the energy each free electron has. Therefore, the work function can be calculated by:

$$\phi = U_{\mathrm{vac}} - E_F \tag{3.8}$$

where U_{vac} is the vacuum electrostatic potential in the simulation cell which determines the energy of the dissociated (free) e^-, and E_F is the Fermi energy which represents the highest energy electrons in the system. The work functions of the asymmetric systems here are calculated using dipole corrections as detailed in past work from Skúlason *et al.*[45] To determine the vacuum potential, the plane-averaged electrostatic potential was computed as a function of distance normal to the MoS_2 surface (i.e in the z-direction). An example of this is plotted in Figure 3.9 for an Au-supported MoS_2 system. At a sufficient distance from the MoS_2 and into the vacuum above the model, the potential converges. Here, the vacuum potential is taken to be the average of ten data points after this potential has converged (red square in Figure 3.9). The work function of the SHE in Equation 3.7, ϕ_{SHE}, has been determined experimentally to lie in the range of 4.28 to

4.86 V,[187,188] but the majority of estimates place it around 4.4 V. Here, a value of 4.44 V is adopted, based on the work of Fawcett *et al.*[184,189]

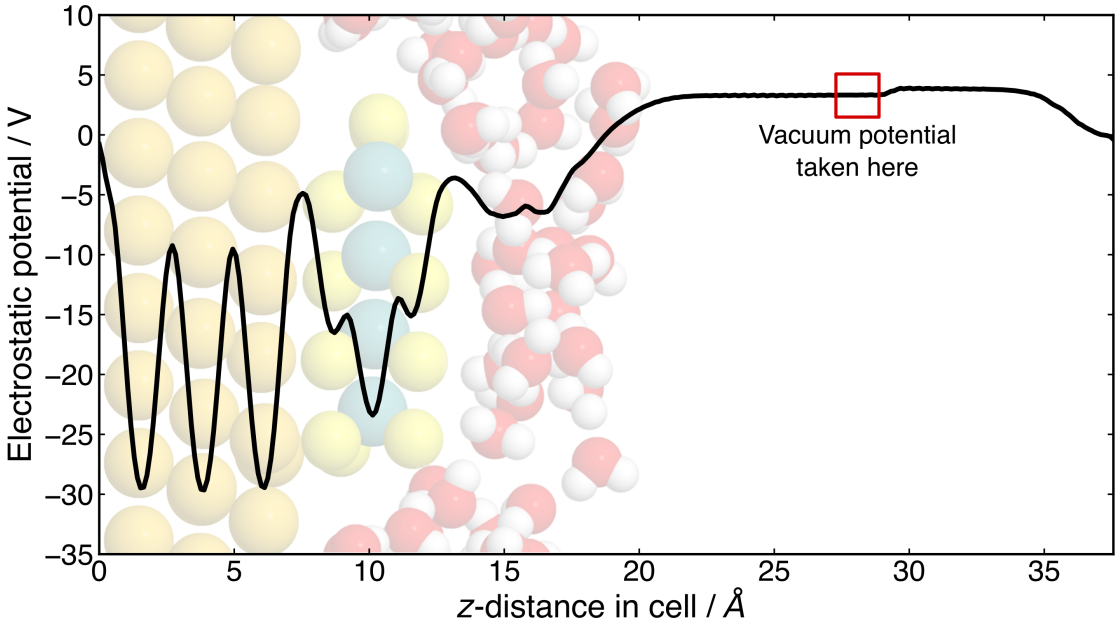

Figure 3.9: An example of the plane-averaged electrostatic potential in an Au-supported MoS_2 system. Peaks can be seen coinciding with nuclei as regions of high attractive potential, then in the vacuum in the cell the potential converges. The electrostatic vacuum potential, U_{vac}, is taken from the average of ten data points in the region where the potential is converged (red square). There is a slight discontinuity at the mid-point between periodic repeats just after where the vacuum potential is taken, which is a result of the asymmetric dipole corrections.

With the charge separated initial state of the Heyrovský reaction appropriately represented, standard techniques (i.e. climbing-image NEB calculations) were used to locate the transition state for H^+(aq) reacting with a surface H_{ads}. In order to conserve computational resources when simulating such a large model, the Heyrovský barriers on graphene- and Au-supported MoS_2 were calculated with only one additional H^+(aq) in the water layer (representing a single potential).

When the H^+(aq) combines with the surface-adsorbed H, the potential difference that it generated in the cell is naturally lost, meaning that the potential shifts during the course of the reaction. Therefore, the full water model on its own would not meet condition (3) raised at the start of this section. Indeed, this can be an issue for any formal electron transfer reaction within a finite size simulation cell. Therefore, a charge extrapolation

scheme[180] was used to circumvent this issue of shifts in potential during the reaction. In this method, the barrier directly from DFT, $E_a(DFT)$, can be adjusted to the fixed potential of the initial state based on the difference in the net charge between the transition state and the initial state ($q_{TS} - q_{IS}$) as well as the potential shift between the two states ($U_{TS} - U_{IS}$):

$$E_a(U_{IS}) = E_a(DFT) - \frac{(q_{TS} - q_{IS})(U_{TS} - U_{IS})}{2} \tag{3.9}$$

Note that $q_{TS} - q_{IS}$, henceforth Δq, was estimated by a Bader charge analysis of the MoS_2 surface and any adsorbates.[138,139] Including the support (either graphene or Au) in this Bader charge analysis did not change the value of Δq, therefore it has been excluded for simplicity. The H_{ads} directly involved in the Heyrovský reaction was included in the Bader charge calculation of q_{IS}, but was taken to be mostly desorbed from the surface in the transition state and thus excluded from q_{TS}. Once the barrier at a constant initial state potential has been obtained ($E_a(U_{IS})$ from Equation 3.9), it can be extrapolated to any potential, U,[181] using Equation 3.10.

$$E_a(U) = E_a(U_{IS}) - \Delta q(U - U_{IS}) \tag{3.10}$$

In this way, barriers for the Heyrovský mechanism can be calculated at any potential of interest with a realistic model for solvent, charged species, and potential.[f]

Converging mechanistic calculations using the full water model

While the full water layer model of the Heyrovský reaction above MoS_2 is a comprehensive representation of the solvent, it is also incredibly computationally expensive to run calculations on. This expense presents itself in two ways: first, there are many electrons in the simulation (>1500), meaning that each electronic relaxation takes up significant computational resources (in terms of both memory and processor time). Secondly, there

[f] You may notice that Equation 3.10 is highly analogous to Equation 3.6 reported in the proton shuttling section just prior. The reason for this is that both equations are essentially performing the same extrapolation, which relies on the energy of a proton-electron pair being equivalent to the energy of a single H at 0 V vs. SHE. The difference in the present equation is that the reaction symmetry factor, β, is replaced by the charge difference term, Δq. However, both of these terms aim to accomplish the same goal in describing how far the reaction has progressed at the point where the DFT barrier is obtained.

are many free-moving nuclei in the model (around 250), and thus many degrees of freedom. Due to the complexity of the potential energy surface, geometry relaxations often have to explore a number of similar structures that differ by only small rearrangements of atoms and are close in energy, resulting in very long and difficult to converge calculations. This effect is further exacerbated for the NEB calculations used to determine reaction mechanisms, which are already computationally intensive and do not scale well with more complex systems. Indeed, initial attempts to perform minimum energy path calculations were running for several months without any signs of converging. As a result, we had to explore a number of different tools in order to correctly converge calculations within an acceptable time-frame. These solutions were all explored on the Au-supported MoS_2 system, as it has the most electrons and thus should be the most challenging.

In an initial attempt to reduce the number of electrons in Au-supported MoS_2, the bottom two layers of Au atoms from the three-layer support were removed. These atoms were situated at the base of the support, and therefore were unlikely to have a large effect on the processes taking place on the MoS_2 catalyst. This approach initially seemed to be improving calculation speed; however, when comparing to the three-layer system, it was observed that the geometry of the MoS_2 changed somewhat in the one-layer support case. In Figure 3.10A it can be seen that with H adsorbed to a S atom the whole MoS_2 model tilts, with the Mo-edge raising up off the support. The distance between the S which H is adsorbed to and the Au beneath is 4.65 Å, whereas in the same case with three layers of Au (Figure 3.10B), this distance is only 4.27 Å. The difference of nearly 0.5 Å strongly suggests that one layer of Au does not fully represent the Au solid and thus we could not proceed with the smaller support.

In a different approach, it was attempted to completely constrain the relaxation of any water molecules that were distant from the reacting site on the MoS_2 catalyst, and therefore unlikely to move significantly during the course of the reaction. Practically, this involved fixing any water molecule where all three of its nuclei (O and both H atoms) moved by less than 0.1 Å over a linear interpolation of the reaction path from initial to final state. Critically, this was only done for molecules that were more than 5 Å from the reacting protons at all times. These nuclei were held static in all three dimensions for

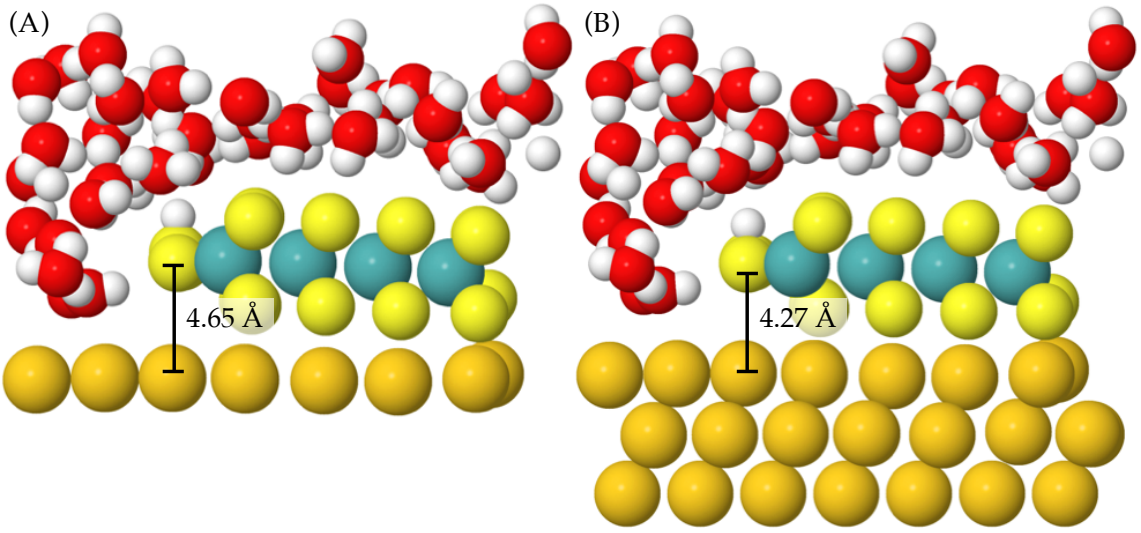

Figure 3.10: The geometry of the H adsorbed on S state with either (A) one or (B) three layers of Au as a support beneath. There is a slight preference for MoS_2 to tilt more when there is only one layer of Au.

all images in the NEB calculation. Note that the position of these water molecules could still change between images, but they were not be relaxed within a given image. While this did not overcome the problem of having many electrons in the system, it did notably reduce the degrees of freedom and flexibility in the water layer.

A test was performed on the first 150 structural steps taken by an NEB calculation with these constrained and unconstrained water systems. The energy and forces on the highest energy image in the NEB (i.e. the closest to the transition state) are plotted in Figure 3.11. Comparing the energy convergence first, we see fairly similar behaviour, with perhaps slightly more stable energies in the constrained case. However, looking at the force convergence, it can be seen that the net forces on nuclei are notably more well-behaved for the constrained case, deviating by less than 0.5 eV $Å^{-1}$ after they have initially settled. When the water molecules are unconstrained, the forces are seen to spike up (rising to over 2 eV $Å^{-1}$) even within the fairly short test range of 150 steps. This suggests constraining these water molecules could aid the force convergence in a full-length NEB.[g] As a result, the model with constrained water molecules was used for all NEB calculations going forwards.

[g] Additionally, from a purely qualitative standpoint, constraining the water molecules did appear to reduce the number of structural steps required to reach high levels of convergence in the NEB calculations.

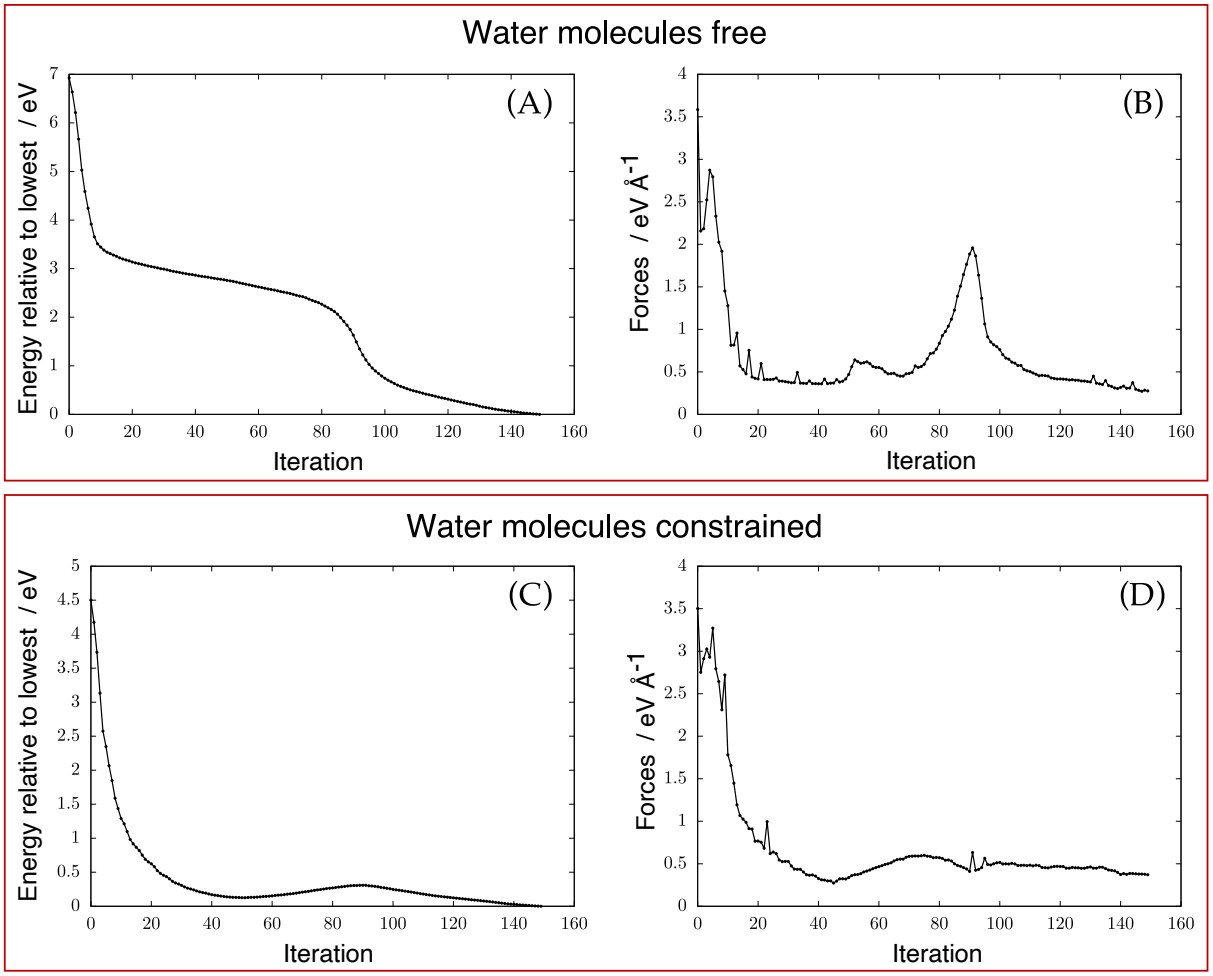

Figure 3.11: (A) and (B) show energy and force convergence plots, respectively, for the highest energy image of a Heyrovský reaction NEB with the full water layer left free to move (unconstrained). In (C) and (D) the same is shown for the case where water molecules that are both distant from the reaction site and do not move significantly during the course of the reaction are constrained in all directions. Note that in all cases the forces do continue to decrease past 150 iterations.

While constraining water molecules was observed to help convergence, the timescale of these calculations was still undesirably large.[h] Therefore, additional approaches to speed up the NEB were examined. One tested approach was to start NEB calculations with a very loose force convergence criterion then tighten this incrementally. The idea here would be to allow the NEB to be run in manageable segments, with the hope that each run would iteratively improve on the last guess. Indeed, this methodology is somewhat similar to standard approaches for converging NEB calculations (see Refs 45 and 144 for examples), but differs in that the increments to the force convergence tested here were much smaller (changing by 0.01 eV $Å^{-1}$ per calculation instead of the usual 0.20 or 0.10 eV $Å^{-1}$).

Unfortunately, it was found that with such a small step-down in the force convergence criterion, the calculation tended to become "stuck" generating geometries that corresponded a relatively stable reaction path, but not the overall minimum energy path. As a result, the NEB would often converge to a point (e.g. forces of 0.1 eV $Å^{-1}$), but then be unable to converge further as the guess it started with was too far down a non-optimal reaction path. This phenomenon where the NEB gets stuck, can be observed in Figure 3.12. Here, the energy and forces on the highest energy image on the reaction path are tracked over a long time period (over 1000 NEB steps, representing at least a month of calculation wall-time). It is clear that the NEB reaches a point where the energy on the tracked image has lowered and is somewhat stable (i.e. above 650 iterations), but the forces on that image continue to oscillate and remain high. There is no overall trend of a decrease in forces, which one would expect to see given the calculation is being run with a force based optimiser that serves to minimise the forces acting on each image.[i] This behaviour is something that we have observed is less likely to happen if NEB calculations are allowed to run more freely for longer durations.

[h] After several months of wall-time, the Heyrovský NEB on the Au-supported system still showed little sign of approaching convergence.

[i] There is a small caveat to this in that the optimiser is only minimising the forces perpendicular to the reaction path, not those parallel (see Section 2.5.2 on NEB calculations in Chapter 2). However, one would still expect to see an overall decrease in the net force as the perpendicular forces were minimised, which is not observed here.

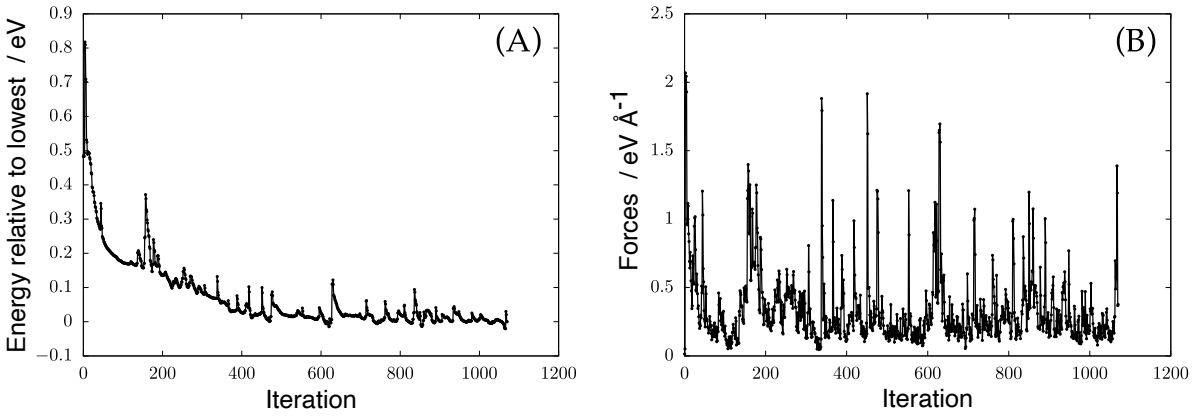

Figure 3.12: (A) Energy and (B) forces of the highest energy image along the Heyrovský nudged elastic band path for Au-supported MoS_2 with a full water layer model above. Note that here the force is given as the maximum net force experienced by any nucleus.

We are still somewhat unsure as to the exact reason that the calculation becomes stuck when using small steps down in the force convergence. One possibility is that these small steps result in a very stochastic optimisation where, if the path falls below a certain force threshold simply by chance, it is immediately stopped and check-pointed there, regardless of whether it was moving towards the true minimum energy path or not. It was decided that stepping the force convergence down slowly should not be pursued further as, despite multiple restarts, sampling enough different geometries to get a converged minimum energy path solution did not appear to be possible.

Finally, in conjunction with the water molecule fixing process outlined earlier, the methodology that allowed NEB paths to be successfully converged to 0.03 eV $Å^{-1}$ was discovered. In the previous testing, it was noticed that converging the reaction paths to have forces below 0.10 eV $Å^{-1}$ tended to be the most difficult step, and this step also coincided with the point where the climbing image functionality was switched on in the calculation. As was outlined in Section 2.5.2 of Chapter 2, climbing image works by taking the highest image in a relaxed NEB path which has already been loosely converged (e.g. to 0.10 eV $Å^{-1}$ as mentioned above), and reversing the force component parallel to the path along the potential energy surface. Ordinarily, this would serve to push a relatively good guess at the transition state up to the actual transition state and prevent corner-cutting, where the apex of a path may be missed. Unfortunately, because the potential energy

surface of the water molecules above MoS_2 had so many degrees of freedom, we suspect that the loosely converged NEB path may not lie exactly along the true minimum energy path. Thus, when climbing image was switched on in these calculations it may push the highest image up in energy along other degrees of freedom and not just that of the true reaction path. It is highly possible that this was responsible for many of the convergence difficulties observed in Figure 3.12. As a result, we tested tightly converging the NEB path to 0.03 eV $Å^{-1}$ without climbing image switched on, which ran not only smoothly but relatively quickly. Of course, climbing image must still be applied in order to locate the transition state. To accomplish this, a linear extrapolation was used to insert an extra NEB image manually between the two highest energy neighbouring images on the highly converged path, and the two adjacent images were fixed to make a small, single image, path (Figure 3.13). From here, the climbing image NEB could be run so that it would act on this inserted image. There was no advantage to calculating all the images along the whole of the NEB path, as these are already converged to 0.03 eV $Å^{-1}$, thus we optimised only the single inserted image, treating its neighbours as the initial and final states. Indeed, with this well-converged representation of the reaction path, convergence was achieved fairly rapidly, and a transition state was located. The overall NEB process, which allowed convergence of these Heyrovský reaction mechanisms, is summarised graphically in Figure 3.13.

Calculation of current densities

Once the relevant transition states had been located for both the Volmer-Tafel and Volmer-Heyrovský mechanisms, the calculated activation energy barriers were then converted to electrochemical current densities, i, in order to allow comparison to experimental findings. This was achieved using Equation 3.11.

$$i = keN/A \tag{3.11}$$

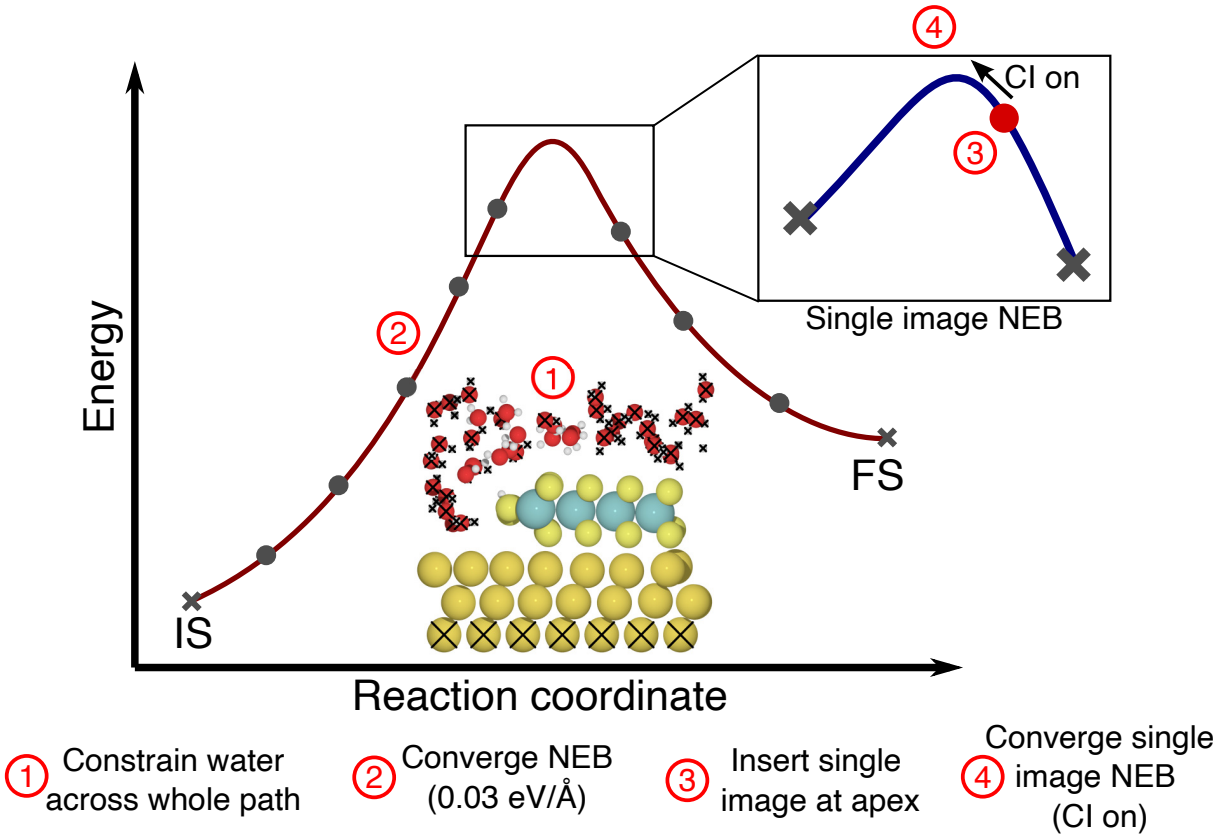

Figure 3.13: A graphical summary of the single image NEB process that was able to converge Heyrovský reaction paths with a full water later model. The steps to this process are listed 1 to 4 along the bottom of the image. X symbols on the path indicate initial and final states (IS and FS) for both the full-path (red line), and single image (blue line) NEB calculations. For the structure shown in step 1, crosses on atoms indicate they are constrained.

where e is the elementary charge and N/A is the number of active sites per unit of surface area. The rate constant, k, is given by Equation 3.12:

$$k = \nu e^{(-E_a/k_B T)} \tag{3.12}$$

where ν is the attempt frequency (which is assumed to be 10^{13} site^{-1} s^{-1}, following common estimates for the HER),[190] E_a is the activation barrier (i.e. $E_{\mathrm{TS}} - E_{\mathrm{IS}}$), k_B is the Boltzmann constant, and T is the temperature. The value of N/A is chosen to be the same as Pt(111): $N/A = 1.51 \times 10^{15}$ site cm^{-2}, in order to normalise the current density to represent the intrinsic activity of MoS_2 in a way that does not depend on the size of the MoS_2 systems. This procedure has previously been used for experimental data on MoS_2,[64] so employing it here allows fair comparisons to be made to experimental work. If this approach is not taken, then the value of N/A varies depending on the size of MoS_2 nanoparticle catalysts as they have different amounts of active Mo-edge per area,[64] making comparisons difficult.

3.3 Results and discussion

3.3.1 The structure of the Mo-edge

Previous theoretical work has shown that the under-coordinated Mo atoms on the 50% S covered Mo-edge of MoS_2 tend to reconstruct and form groups of three (henceforth triads).[71,166] While this configuration is more stable than alternatives, it can only exist for MoS_2 structures where the edges are a multiple of three Mo atoms in length. In the present work, preliminary studies observed triadic grouping of Mo in a 6-Mo wide model, yet it was desirable to use a smaller model for computational tractability. When a 4-Mo wide model was used the Mo atoms instead were found to form pairs where the Mo atoms in a pair were slightly closer to each other (2.91 Å) than their neighbours (3.46 Å). The triadic configuration was found to be 0.1 eV more stable per Mo atom than the pairs. A more complete discussion of the edge structures and their stability is given in Appendix A.2. The main consequence of this size-dependent Mo grouping is that, regardless of

whether triads or pairs are present, there are always two types of non-equivalent S atom of the Mo-edge: those positioned between Mo atoms that are closer together as a pair or triad (henceforth the "close S" position) and those that are between two Mo atoms that are spaced out (henceforth the "spaced S" position).

3.3.2 The Volmer-Tafel reaction

H Adsorption Profile

The first steps in the Volmer-Tafel mechanism are two Volmer reactions, in which two H atoms adsorb to the catalyst surface (to make H_{ads}), after which Tafel combination can occur. Therefore, we initially consider the energetics of adsorption of H to the Mo-edge of unsupported MoS_2 as well as on Au(111)- and graphene-supported MoS_2. In Figure 3.14A, the relation of the differential H adsorption free energy ($\Delta G_{H_{ads,diff}}$, defined in methodology Section 3.2.3 of this chapter) and the H coverage is shown for MoS_2. The H coverage is expressed in terms of monolayers (ML), which represent the number of H atoms adsorbed per Mo atom on the edge (four in this case). Therefore, 1 ML denotes four adsorbed H. The order with which different adsorption sites are populated is also shown in the Figure 3.14A inset. It is found that the order of adsorption is the same regardless of supporting material. H initially favours adsorbing to a spaced S atom. The second H adsorption, bringing the surface to 0.5 ML coverage, also occurs on a spaced S atom which means it is not directly adjacent to the site where the first H adsorbed. We find that the spaced S adsorption sites are consistently and significantly favoured over the close S by up to 0.6 eV. However, above 0.5 ML coverage all the spaced S sites are saturated. To reach 0.75 ML H coverage, we find adsorption to either an Mo atom or one of the remaining S sites are within 0.05 eV in energy, and thus either of these configurations are likely accessible. Regardless of which site is populated here, the other becomes directly populated at 1 ML coverage. Past this point adsorption alternates between Mo and S until 2 ML.

The overall shape of the adsorption profile is similar for unsupported and both supported MoS_2 systems. Therefore, the H adsorption free energy profile for unsupported

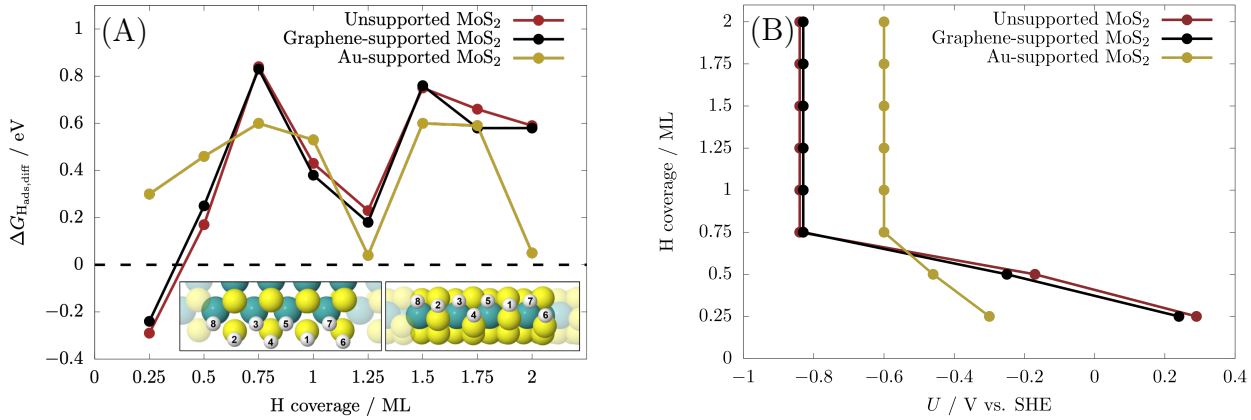

Figure 3.14: (A) Differential H adsorption free energy as a function of the H coverage on MoS_2. One ML of coverage corresponds to having four H_{ads} on the Mo-edge, which is four Mo atoms wide. *Inset:* Order in which adsorption sites preferentially become populated, which is the same for both supported and unsupported MoS_2 systems. (B) The relation of H coverage to applied potential calculated using Equation 3.5.

MoS_2 is discussed first, and the effects of different supports are considered after. It can be seen that $\Delta G_{H_{ads,diff}}$ initially becomes more positive with increasing H coverage, reaching a maximum of $\Delta G_{H_{ads,diff}} = 0.84$ eV at 0.75 ML. The pattern of adsorption at these low H coverages is consistent with that reported previously.[77] Above 0.75 ML a decrease in $\Delta G_{H_{ads,diff}}$ is observed, such that no additional energy is required to reach any of the higher coverages. Although $\Delta G_{H_{ads,diff}}$ begins to increase again at coverages above 1.25 ML, the free energy still remains lower than that at 0.75 ML, meaning these coverages can still spontaneously be populated once 0.75 ML has been reached.

The oscillatory adsorption profile is interesting as it is different to that observed on the close-packed pure metals (e.g. Pt, Pd, Ru, Cu),[46] which show reliable increases in $\Delta G_{H_{ads,diff}}$ with increasing coverage. However, it has recently been documented that several transition metal nitrides (TaN, HfN and YN)[60] show a similar oscillatory H adsorption profile to MoS_2. This behaviour can be rationalised by the idea that adsorption of H to one of the elements in a binary material may weaken the polarised bond between metal and non-metal, leaving the other element increasingly free to bind H. Hence adsorption to this adjacent site becomes more favourable. However, once the newly created favourable adsorption site is saturated, the adsorption energy increases again.

In examining the effects of graphene and Au(111) supports on the H adsorption profile, it is clear there is very little difference between graphene-supported MoS_2 and the unsupported catalyst. This is likely due to the existence of only very weak catalyst-support interactions between graphene and MoS_2, with the adhesion energy of MoS_2 on graphene being only -0.15 eV per Mo atom. In contrast, an Au support has a much larger effect on the H adsorption profile, which is likely a product of the much larger adhesion energy of -0.52 eV per Mo. Au-supported MoS_2 has a a similarly shaped H adsorption profile to that of graphene or unsupported MoS_2, but with notable differences in the magnitude of $\Delta G_{\mathrm{H_{ads,diff}}}$. The Au support appears to raise the energy required to adsorb H at low coverages, but lower it somewhat at higher coverages such that the adsorption profile is more flat than for graphene-supported MoS_2.

Relation of potential and H coverage

The differential H adsorption free energy in Figure 3.14A was used to calculate the surface H coverages that would be expected at different applied potentials (Figure 3.14B), following Equation 3.5 from Section 3.2.3. Because the differential hydrogen adsorption free energy reaches a maximum at 0.75 ML for both graphene- and Au-supported MoS_2, it can be assumed that any coverage greater than this is accessible without applying additional potential. Thus the vertical lines in Figure 3.14B are observed. The high degree of similarity between unsupported and graphene-supported MoS_2 can again be observed. Indeed, when we go on to examine the Tafel barriers on graphene-supported and unsupported MoS_2, we again find very little difference between the two (see Appendix A.3). Therefore, for brevity, unsupported MoS_2 is omitted from all following results and discussion, and all the data pertaining to it can be found in the Appendix.

For graphene-supported MoS_2, the lower H coverages are readily reached at potentials close to zero, yet it takes an applied potential of -0.84 V in order to reach the higher H coverages above 0.75 ML. For Au-supported MoS_2, more negative potentials are required to begin populating the surface, but relatively little extra applied potential is required to reach the higher H coverages.

Volmer-Tafel reaction profile

From Figure 3.14B the thermodynamic cost of the Volmer reaction as a function of potential can be determined. Furthermore, it informs the expected hydrogen coverage at a given potential. This is important because, although the Tafel barriers themselves are independent of potential, they are influenced by the H coverage.[46] Reaction free energy diagrams (FEDs) showing the overall Volmer-Tafel mechanism are presented for graphene- (Figure 3.15A) and Au-supported MoS_2 (Figure 3.15B). The first two steps in the FED represent Volmer adsorptions of H to the catalyst. It can be seen that, at potentials more positive than -0.24 V on graphene-supported MoS_2 and -0.46 V on Au-supported MoS_2, the Volmer reactions to get at least two H onto the surface (0.5 ML) are endergonic and thus contribute to the overall Volmer-Tafel barrier. Below these potentials, the Volmer reactions are spontaneous.The FEDs are shown at 0 V, and at the potential where the Volmer reactions spontaneously occur.

The next step in the Volmer-Tafel mechanism involves diffusion of the surface H_{ads} to adjacent sites such that they can combine to form H_2. After testing various Tafel pathways, it was determined that combination with the H_{ads} at an Mo-S site was significantly favoured over all other options (see Appendix A.4). Indeed when attempting to locate S-S or Mo-Mo combination pathways, it was consistently found that one H_{ads} would preferentially diffuse and then undergo combination from an Mo-S site, which is in agreement with the findings of Huang *et al.*[166] on unsupported MoS_2. Thus the diffusion from the preferred H adsorption sites at the spaced S positions (H_SH_S in Figure 3.15) to the H_SH_{Mo} reacting site gives the third step in the Volmer-Tafel mechanism. This diffusion process is shown by the black line in Figure 3.16 with two H adsorbed.

The energy barrier for one of the surface H_{ads} to diffuse to an Mo site (from an S site) was calculated as 1.11 eV on graphene-supported MoS_2, and 0.72 eV on Au-supported MoS_2. These barriers are notably high, especially when considering that the highest H diffusion barrier between any two sites has been calculated as 0.05 eV on Pt(111),[191] and is found not to exceed 0.3 eV on other close-packed transition metals.[192] Even on other edge structures, such Pt steps, the maximum diffusion barriers remain below 0.5 eV.[52] The

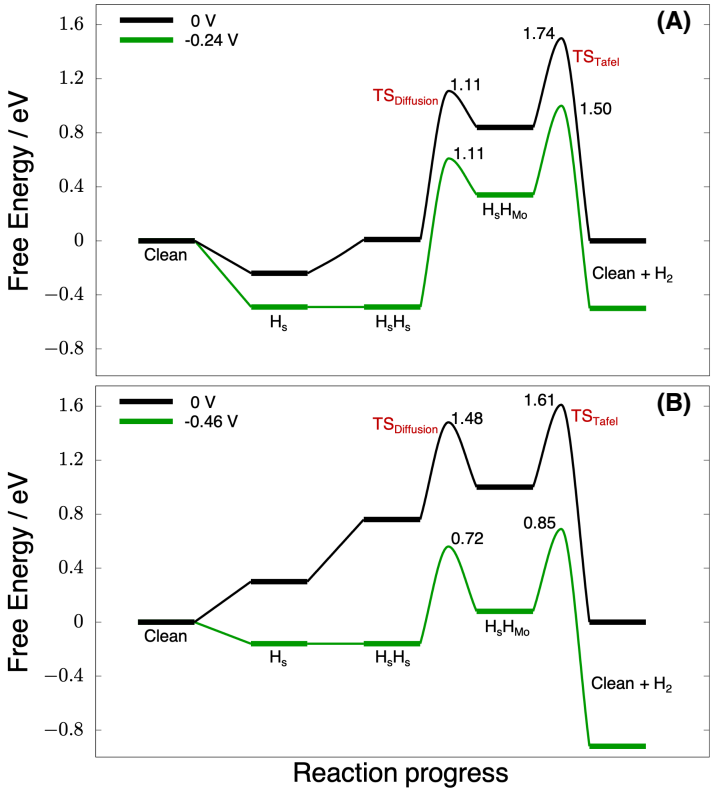

Figure 3.15: Reaction free energy diagrams for the Volmer-Tafel reaction on (A) graphene-supported MoS_2 and (B) Au-supported MoS_2 with the electronic energy barriers between intermediates on the free energy landscape. The numeric values display the barrier relative to the lowest energy preceding intermediate. The profiles are presented at 0 V and at the potential where the Volmer reactions to get two H onto the surface are spontaneous. Energies of intermediates are scaled using the computational hydrogen electrode (see Section 3.2.2).

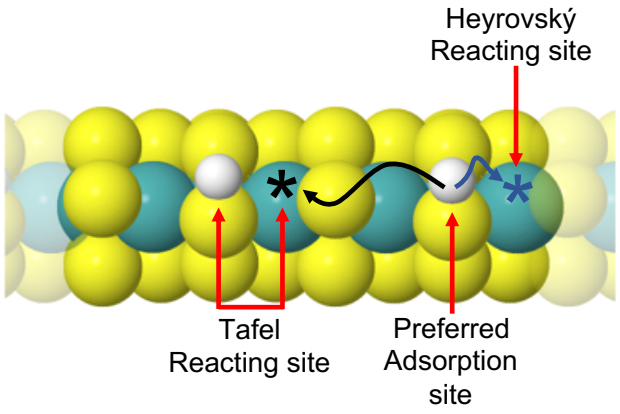

Figure 3.16: Diffusion of H on the Mo-edge of MoS_2 to allow Tafel combination at an Mo atom (black line). The diffusion required to get to a Heyrovský reacting site is also shown (blue line), which will be relevant to a later section.

high diffusion barriers reported here are primarily a result of the large thermodynamic energy differences between adsorption sites on MoS_2, which can be observed in Figure 3.15. For instance, H diffusing from an S atom to an Mo on graphene-supported MoS_2 has a thermodynamic energy difference of 0.83 eV, leaving an additional barrier to diffusion of only 0.27 eV which is more comparable to that of the transition metals.[192] In contrast, the thermodynamic energy difference between S and Mo on Au-supported MoS_2 is only 0.24 eV, which explains the lower overall barrier to diffusion. However, the additional barrier is somewhat higher (0.48 eV) than on graphene. Based on Figure 3.14, diffusion of H is not required prior to Tafel combination at or below potentials of -0.84 V on graphene-supported MoS_2 and -0.60 V on Au-supported MoS_2, because both the S and Mo sites are spontaneously populated.

It is worth noting that, because catalysis occurs under dynamic non-equilibrium conditions, it may be possible to get desorption and re-adsorption of H to attain the H_SH_{Mo} state without having to undergo diffusion of H on the edge. Ideally, a full kinetic model considering the relative rates of both H diffusion and this desorption-adsorption process would be employed here. However, this was not feasible in the time-frame of this work. Because the majority of the H diffusion barriers reported here can be accounted for by thermodynamic energy differences, it seems possible that including consideration of desorption and re-adsorption processes may not change the overall picture. Yet, it would be an interesting topic for future study.

The final step in the Volmer-Tafel mechanism is Tafel combination to form H_2. Interestingly, while the Volmer and diffusion steps showed notable differences between MoS_2 on graphene and Au supports, the Tafel barriers are similar: 0.66 and 0.61 eV at 0 V, respectively (see Figure 3.15). These Tafel barriers compare favourably to those on the traditional HER catalyst, Pt(111), where the Tafel barrier is approximately 0.80 eV at 0 V.[45] However, on Pt(111) there is no need for H diffusion on the surface before reaction, whereas diffusion from S to Mo accounts for a large portion of the cost to the overall Volmer-Tafel mechanism on MoS_2.

The overall Volmer-Tafel energy barriers, calculated relative to the lowest energy preceding state,[j] are plotted as a function of applied potential in Figure 3.17. For graphene-supported MoS_2, the Volmer-Tafel barrier at potentials close to 0 V are prohibitively high (1.74 eV) – a feature which is largely attributable to the thermodynamic cost of populating the H_SH_{Mo} reacting site *via* H diffusion. Au-supported MoS_2 also has a high Volmer-Tafel barrier at 0 V (1.61 eV). In this case the H diffusion barriers are much lower, but the Volmer reactions to adsorb H to the surface in the first place have a large thermodynamic cost (see Figure 3.15), which drives the Volmer-Tafel barrier up. For

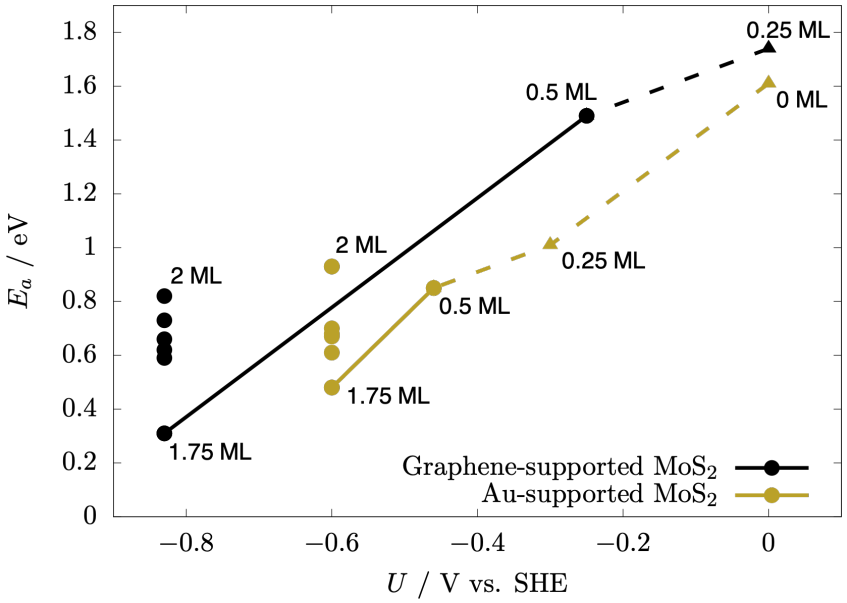

Figure 3.17: Volmer-Tafel energy barriers on supported MoS_2 as a function of applied potential. The solid lines and circles indicate barriers at potentials where the Volmer reaction is spontaneous, leaving only the Tafel barrier to consider. The dashed lines and triangles indicate points where the thermodynamic cost to the Volmer reaction is contributing to the overall Volmer-Tafel barrier. In both cases, the lines are included to connect the lowest barriers at different potentials and serve only to guide the eye. For the 0.5 ML coverage and all coverages lower than this, the diffusion barriers are also included in the overall Volmer-Tafel barrier.

both support materials, the Volmer-Tafel barrier tends to decrease quite rapidly as the potential becomes more negative. At moderate potentials ranging from -0.35 to -0.60 V, Au-supported MoS_2 has a lower barrier compared to graphene-supported by between 0.15

[j] This state is used as a reference because it represents the lowest energy configuration of the catalyst (i.e. with a certain H coverage) under specific conditions (e.g. a given potential).

to 0.40 eV. This is a result of Volmer reactions becoming spontaneous at more negative potentials.

At -0.60 V on Au-supported MoS_2 and -0.84 V on graphene-supported, the Mo-edge has access to H coverages all the way up to fully covered at 2 ML with no additional energetic cost (Figure 3.14B). Once these potentials are reached, a variety of possible H coverages may exist. It is believed that the Tafel barriers at any of these H coverages would be accessible once the threshold potential has been reached. While the barriers at each of these coverages were tested (see the vertical points on Figure 3.17), only the lowest barrier is of interest to the overall mechanism. For both supported catalysts, one barrier is notably lower than the others, and this corresponds to the surface being covered at 1.75 ML. Examining the structure of the Mo-edge present it appears this particularly low barrier is due to two features which are unique at 1.75 ML coverage: (1) a reacting H_{ads} is adsorbed directly on-top of S, instead of at an angle which is the case at all other coverages; and (2) the S atom with a reacting H on it is elevated above the Mo atoms in the edge (see Appendix A.5).

It is clear that the choice of catalyst support primarily affects the Volmer-Tafel mechanism though changing the thermodynamics of both the Volmer reaction and H diffusion. The Tafel combination barriers themselves remain fairly similar between graphene- and Au-supported MoS_2. This feature is also reflected in Figure 3.17, which suggests that both supported catalysts could ultimately access similarly low Volmer-Tafel barriers, yet the potential at which they can achieve these low barriers differs (-0.84 V on graphene-supported MoS_2 and -0.60 V on Au-supported). It is the thermodynamics of the Volmer reaction that controls these potentials.

3.3.3 The Volmer-Heyrovský reaction

The Volmer-Heyrovský mechanism proceeds first with one Volmer reaction, which behaves as was discussed in the Volmer-Tafel Section 3.2.3. H adsorbs to an S atom which is spontaneous for graphene-supported MoS_2 but endergonic for Au-supported MoS_2 (at 0 V, see Figure 3.14). Then, as for the Tafel combination step, Heyrovský combination

with H_{ads} on Mo is preferred. Indeed, having H_{ads} on Mo was the only site from which a Heyrovský combination path could be successfully converged. In trying to converge a Heyrovský reaction path with H_{ads} on an S atom, the minimum energy reaction path that was located suggested that it would be more favourable for H_{ads} to diffuse to an adjacent Mo and then react from this site. Previous work has successfully converged a Heyrovský barrier with H_{ads} on S,[166] but reports the overall Volmer-Heyrovský barrier was almost twice as high compared to H_{ads} diffusing then undergoing combination on Mo. Thus, we consider the second step in the Volmer-Heyrovský reaction to be diffusion of the H_{ads} from S to an Mo atom (see Figure 3.16), and the final step to be the actual Heyrovský combination from the Mo site.

Free energy diagrams showing the overall Volmer-Heyrovský process are presented in Figures 3.18A (graphene-supported MoS_2) and 3.18B (Au-supported MoS_2). As was seen for the Volmer-Tafel mechanism, at 0 V, adsorption of H to S is favourable on graphene-supported MoS_2, but there is a large diffusion barrier of 1.29 eV in order to reach the H_{Mo} state. The subsequent Heyrovský step, however, is barrierless at 0 V. Indeed, on linearly scaling this Heyrovský barrier to a constant potential using the charge extrapolation method discussed earlier,[180,181] this barrier goes from near-zero to slightly negative (see Appendix A.7). The negative barrier is purely a result of this linear scaling, when in reality other factors such as pH and the diffusion of a proton from the bulk solution to the surface would cause this barrier to be small but non-zero. Rossmeisl *et al.*[193] estimate the entropic effects of proton transfer from the bulk solvent to a surface could contribute a barrier of 0.1 - 0.2 eV. However, whether the Heyrovský barrier is treated as zero or close to zero makes little difference in this case, as surface diffusion of H is found to be the limiting step regardless.

For Au-supported MoS_2, the Volmer step is endergonic and there exists a diffusion barrier of 0.94 eV to access the H_{Mo} state. In contrast to graphene-supported MoS_2, with an Au support Heyrovský combination is not barrierless (0.26 eV) and thus the overall Volmer-Heyrovský reaction has a barrier of 1.31 eV. The net result is that the overall Volmer-Heyrovský barriers are close to 1.3 eV on both supported catalysts but different factors contribute to each. For graphene-supported MoS_2, the overall barrier height is

determined by a non-electrochemical step (diffusion of H_{ads}). In contrast, on Au-supported MoS_2, the Volmer reaction, thermodynamics of diffusion, and the Heyrovský combination barrier all contribute to the overall barrier height.

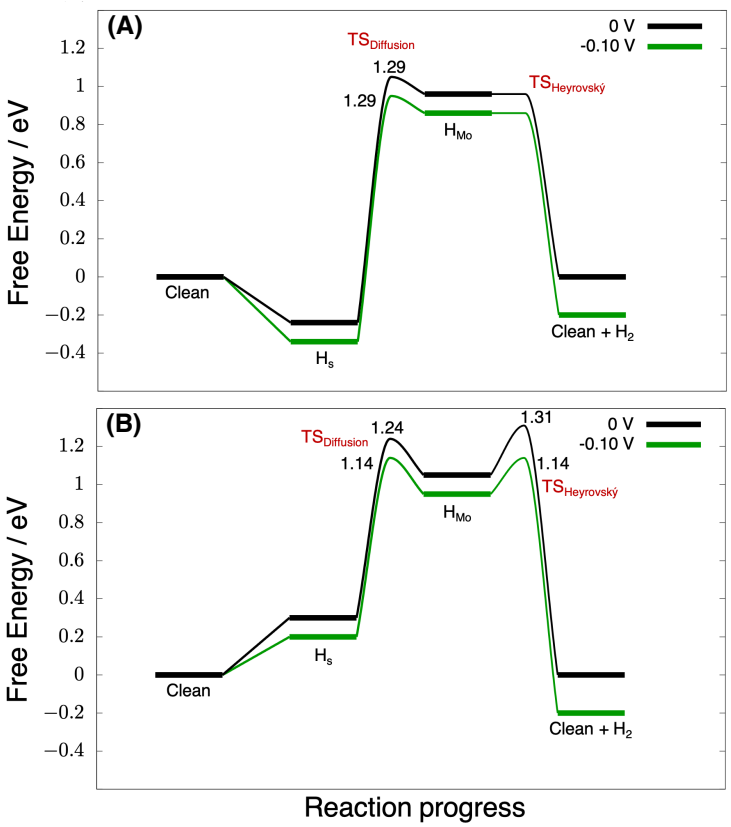

Figure 3.18: Reaction free energy diagrams for the Volmer-Heyrovský mechanism on (A) graphene-supported MoS_2 and (B) Au-supported MoS_2 with the electronic energy barriers between intermediates on the free energy landscape. The numeric values displayed represent the energy barrier relative to the lowest energy preceding intermediate. The pathways are presented at 0 V and at -0.1 V, where the barrier to diffusion becomes the limiting process on Au-supported MoS_2. The energies of the intermediates presented here are calculated using the computational hydrogen electrode (see Section 3.2.2), and the diffusion barriers are added directly to the energy of the preceding intermediate as they are not potential dependent.

The potential dependence of the Volmer-Heyrovský barriers, calculated relative to the lowest energy preceding state, is presented in Figure 3.19. As potential becomes more negative, the barrier on Au-supported MoS_2 is seen to decrease, whereas that on graphene-supported MoS_2 initially remains constant. Because Volmer-Heyrovský combination on graphene-supported MoS_2 is limited by a non-electrochemical diffusion step, no response

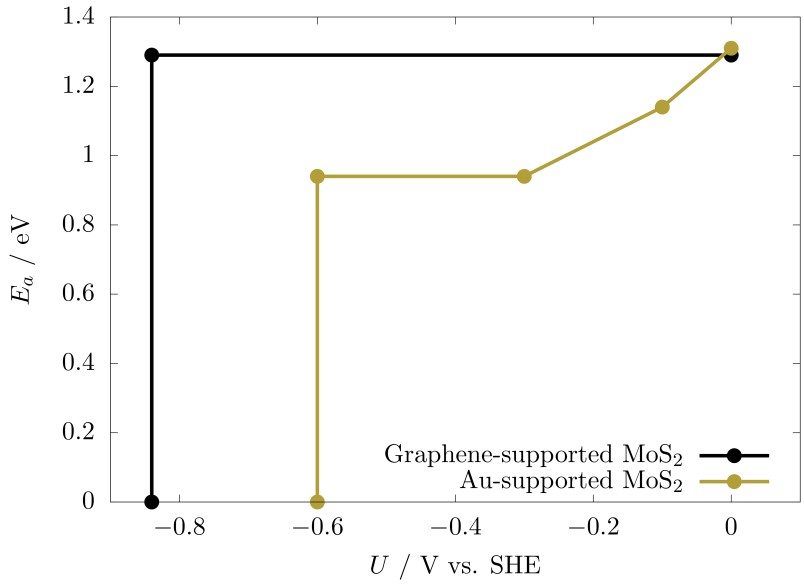

Figure 3.19: Volmer-Heyrovský barriers as a function of potential, calculated using the charge extrapolation scheme on graphene- and Au-supported MoS_2. For both supports, the sections in which the barrier does not change with potential are regions in which the potential independent diffusion barrier is limiting the overall barrier height. It is seen that, the Volmer-Heyrovský reaction becomes barrierless at negative potentials, which coincide with the point where the Mo atom site on the Mo-edge is spontaneously populated with H_{ads}, removing the need for diffusion.

to potential is observed. In contrast, the barrier on Au-supported MoS_2 has contributions from diffusion but also from the Volmer and Heyrovský steps, which are electrochemical in nature, therefore the overall barrier responds to potential changes. At -0.10 V the Heyrovský barrier with MoS_2 on Au has decreased enough that the diffusion barrier is higher (see Figure 3.18B). However, the overall barrier still decreases as potential becomes more negative because the energy cost of the electrochemical Volmer reaction becomes smaller. Once this H_S state is in equilibrium with the clean surface (-0.30 V), electrochemical steps no longer contribute to the overall barrier height and thus it remains constant from -0.30 to -0.60 V.

At more extreme potentials where the Mo reacting site is spontaneously populated (-0.60 V for Au-supported, and -0.84 V for graphene-supported MoS_2), diffusion is not required for the Volmer-Heyrovský mechanism to take place. At this point, it is found that the Heyrovský reaction has no barrier above the H_{ads} on Mo state for both catalysts

(reaction energy diagrams are available in the Appendix A.7). Thus, it is predicted that the overall Volmer-Heyrovský reaction would be effectively barrierless at this point for both materials. This is seen in Figure 3.19 where the barrier falls to 0 eV.

3.3.4 Comparison of the Volmer-Tafel and Volmer-Heyrovský mechanisms

The barriers for the Volmer-Tafel and Volmer-Heyrovský mechanisms are compared at potentials where data exists for both reactions in Figure 3.20.[k] For graphene-supported MoS_2 (Figure 3.20A), the Volmer-Heyrovský reaction has a lower barrier than the Volmer-Tafel reaction by between 0.2 and 0.5 eV at all potentials. For Au-supported MoS_2 (Figure 3.20B) the Volmer-Heyrovský reaction is also favoured over the Volmer-Tafel at 0 V. However, in the mid ranging potentials the Volmer-Tafel and Volmer-Heyrovský barriers are very similar, and it is likely both mechanisms would contribute to the overall reaction. At more negative potentials the Volmer-Heyrovský reaction is again dominant, being a barrierless process. For both graphene- and Au-supported MoS_2, the Volmer-Heyrovský reaction is favoured at electrochemically relevant potentials close to 0 V.

Using Equations 3.11 and 3.12 given in Section 3.2.4, an electrochemical current density at 0 V *vs* SHE was calculated for graphene-supported MoS_2 at 3.69×10^{-13} A cm^{-2} (barrier: 1.29 eV) and for Au-supported MoS_2 at 1.69×10^{-13} A cm^{-2} (barrier: 1.31 eV) . These values suggest the activity of both supported catalysts would be very similar at 0 V. In experimental work on single-layer MoS_2, Jaramillo *et al.*[64] report an exchange current density for Au-supported MoS_2 of 7.9×10^{-6} A cm^{-2}, and the same researchers report a current density of 1.2×10^{-6} A cm^{-2} for MoS_2 supported on carbon paper in a second study.[72] Carbon paper likely has a somewhat different structure to the graphene sheet here, but given that MoS_2 is only weakly perturbed by a graphene support, we believe this study to be a suitable comparison. The experimental findings in these two studies suggest a similar reaction rate on both materials with a slight advantage to Au-supported

[k] Note that the lines joining points are omitted from this figure so as to discourage comparisons between mechanisms in extrapolated regions. Given the different methodology used to describe each reaction, comparing the regions between calculated data-points would stretch our assumptions.

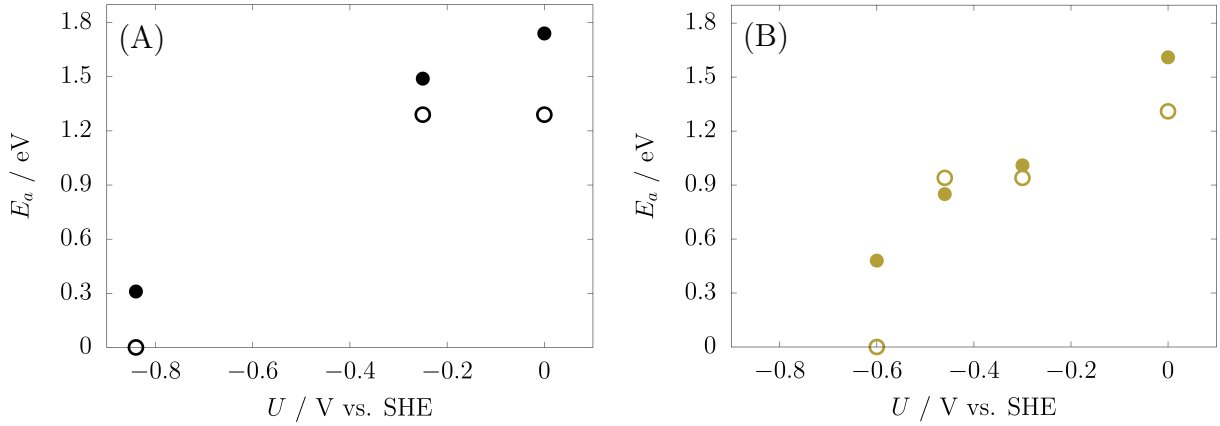

Figure 3.20: Energy barriers for the Volmer-Tafel and Volmer-Heyrovský reactions compared as a function of potential for (A) graphene-supported MoS_2 and (B) Au-supported MoS_2. Filled points indicate the Volmer-Tafel mechanism, and hollow points the Volmer-Heyrovský mechanism.

MoS_2. The calculations reported here also predict very similar activity between catalysts at 0 V. However, the absolute magnitude of the calculated current density is substantially underestimated compared to experiment. Calculations of current density are inherently highly sensitive to any inaccuracy that may be present in the activation barrier – the differences between calculation and experiment observed here represent a difference of only 0.3 eV in the barrier. This range of could be accounted for in DFT calculations when considering different choices of exchange-correlation functional or solvent and potential model. Furthermore, the difference between experiment and calculation is the same for both support materials, suggesting a systematic shift in the calculated barriers that would not interfere with any trends in the data. However, exploring the effects of the solvent/potential model and computational model size on the calculated barriers are a current focus of ongoing work within our research group.

The present calculations suggest the reaction rate on Au-supported MoS_2 would increase more rapidly than that for graphene-supported MoS_2 when sweeping to negative potentials, as the barrier with MoS_2 on graphene is limited by a non-electrochemical diffusion step, while the limiting electrochemical reaction steps on Au-supported MoS_2 are directly affected by applied potential. In experiment, the significantly lower Tafel slope reported for Au-supported MoS_2 (55 to 60 mV per decade)[64] compared to graphene

supported MoS_2 (120 mV per decade)[72] is qualitatively in line with this prediction. However, the experimental data is obtained over a much narrower potential range than that considered here, making more concrete or precise comparisons difficult.

The calculation of explicit reaction barriers reported in this work is highly computationally intensive. For this reason it is interesting to compare the present findings to the conclusions that can be made from common simplified models. The most simple description of HER activity is the H adsorption free energy ($\Delta G_{H_{ads}}$), which in this case correctly captures many of the features of the reaction. On graphene-supported MoS_2 ($\Delta G_{H_{ads}} = -0.24$ eV), it correctly suggests that the Volmer step is facile and that subsequent combination of H is difficult. On Au-supported MoS_2 ($\Delta G_{H_{ads}} = 0.30$ eV), this metric suggests the inverse is true – the Volmer step should be difficult, but the combination and desorption of H will occur readily. This is substantiated in the present work as once H_{ads} is on Au-supported MoS_2 the energetic cost to reach the H_{Mo} reacting site and combine to H_2 is considerably smaller than that for graphene-supported MoS_2. Furthermore, because both values of $\Delta G_{H_{ads}}$ are around 0.3 eV from the ideal value of 0 eV, this descriptor predicts similar HER activity at 0 V, which is consistent with both experimental results and our more detailed barrier calculations.

However, simply looking at the thermodynamics with $\Delta G_{H_{ads}}$ provides no insight into the mechanism of desorption, and does not capture the importance of the Mo site in the reaction. Based on the present data, some additional information can be obtained by considering the energies of all intermediates in the reaction path (i.e. including H_S and H_{Mo}) through a thermochemical model description. Indeed, the thermochemical model predicts the energy difference between the H_S and H_{Mo} states is key contributor to the overall barriers on both supports. However, the inclusion of kinetic barriers reveals the two supports have notably different Heyrovský and diffusion barriers. It is only from the calculation of these explicit barriers the different response to applied potential on graphene- and Au-supported MoS_2 can be rationalised.

The overall conclusion is that measuring $\Delta G_{H_{ads}}$ can correctly capture the activity of a supported MoS_2 systems at potentials near 0 V, but a full mechanistic description is required to understand the activity at different potentials. This suggests $\Delta G_{H_{ads}}$ is still

a valid tool to use for screening studies when comparing across a number of different materials. However, after promising candidates have been identified the mechanisms could be studied in detail to determine the role of processes such as H diffusion and the importance of the Mo reacting site.

With the detailed picture of the HER on supported MoS_2 obtained in this work, a sufficient understanding of the factors governing reactivity has been reached to allow suggestions for the rational design of improved catalysts. For graphene-supported MoS_2, a promising way to improve the reaction rate may be to attempt to reduce the thermodynamic energy difference between the H_S and H_{Mo} states (e.g. *via* tuning $\Delta G_{H_{ads}}$), which could possibly be achieved by doping the Mo-edge,[194] by creating defects,[195] or by modifying the support material with functional groups.[160] The present findings also suggest this route to optimisation may benefit Au-supported MoS_2, yet there would still exist a Heyrovský combination barrier on top of the H_{Mo} state which attention must also be devoted to.

3.4 Future work

One of the most significant limitations that was encountered during this study was the computational expense of working with a large MoS_2/support structure and water layer when modelling the Heyrovský reaction. Indeed, this was so time-consuming and difficult to converge that it became clear future mechanistic studies would require a more tractable model. Of course, this future model should also preserve the accurate representation of solvent and potential gained by using a full water model. Along these lines, there is now an ongoing project in our research group which aims to use a piece of very recently developed software, VASPsol,[196,197] to accurately capture the electrochemical environment while using fewer resources. VASPsol is an extension package to regular VASP, which provides an implicit solvent model for the plane wave DFT code. The implicit solvent can be used to represent most of the water in the electrochemical cell. In conjunction, one need only simulate around five explicit water molecules in order to represent Volmer or Heyrovský steps, where the water serves only to correctly capture the donation of H^+.

However, the key benefit of VASPsol is that it can be used to simulate a system at a targeted applied potential. The package can automatically adjust the potential difference in a simulation cell by adding or removing electrons from the DFT simulation, and then balancing any resulting net charge on the cell by adding background charge to the implicit solvent. VASPsol has recently been applied to electrochemical mechanisms on Pt systems to much success,[198] and we seek to apply it to our larger and less tractable MoS_2 systems here.

Another natural extension of the present work is to study a wider array of support materials, which may have more promising effects than the two supports tested in this chapter. Given the large gap between the properties conferred by graphene and Au(111), a finer degree of tuning would be desirable. Indeed, screening across readily modifiable supports will be the focus of Chapter 4, where we will observe how flexible the support-tuning of MoS_2 can be.

3.5 Conclusions

The energy barriers for the hydrogen evolution reaction on graphene- and Au(111)-supported MoS_2 have been calculated across a range of experimentally relevant potentials. This was done using density functional theory and detailed atomistic models of the electrochemical solid-liquid interface that allow for explicit consideration of applied potential. Initially, the proton-shuttling method was explored for simulating hydrogen evolution processes on MoS_2. This method was found to be unsuitable for surface adsorbates such as H_{ads}, which are unable to compensate for a change in dipole during the course of an electron transfer reaction. Instead, it was found that a full water model provides a more accurate description of the system. A number of methods and tools were tested for converging mechanistic calculations on the complex potential energy surface that a full water model entails. The most successful of these was tightly converging a nudged elastic band reaction path before switching on the climbing image functionality on a reduced section of the path.

Using this full water model, it was found that the Volmer-Heyrovský mechanism likely dominates over the Volmer-Tafel mechanism on supported MoS_2 at potentials near 0 V *vs* SHE. For graphene-supported MoS_2 the Volmer-Heyrovský reaction remains favourable across all tested potentials. However, for Au-supported MoS_2, our results suggest competition between the Volmer-Heyrovský and Volmer-Tafel mechanisms would take place at mid-ranging potentials (around -0.3 to -0.5 V), before the Volmer-Heyrovský reaction again becomes dominant at negative potentials (below -0.6 V).

Considering the more favourable Volmer-Heyrovský reaction, graphene-supported and Au-supported MoS_2 were found to have similar barriers at 0 V, both being approximately 1.3 eV. However, the supports influenced the energetics of individual steps in the overall Volmer-Heyrovský reaction path in differing ways. The Heyrovský step on graphene-supported MoS_2 was found to be barrierless, yet there was a large non-electrochemical barrier for H diffusion to reach the reacting site. In contrast, a lower barrier for diffusion to the reacting site was observed for Au-supported MoS_2, but the electrochemical Volmer and Heyrovský barriers both contributed, and thus can be influenced by applied potential. The differing effects induced by these two supports demonstrates the possibility of flexibility in support-tuning for catalysis on MoS_2, and allows explanation of why the reaction rate may respond differently to changes on potential. Indeed, this work shows the importance of considering full electrochemical reaction barriers when trying to predict rates as a function of electrochemical potential. However, for fixed potentials close to 0 V (i.e. typical industrial conditions), the adsorption energy of H to MoS_2 – which represents the reaction thermodynamics alone – is found to capture most of the effect of employing different supports.

Chapter 4

Improving H adsorption on MoS_2 using carbon-based supports

Where Chapter 3 of this thesis primarily concerned itself with understanding the effects of just two different support materials (Au(111) and graphene) on the hydrogen evolution reaction (HER) activity of MoS_2, this next chapter directly continues on by examining how a variety of support materials may be used to obtain fine-grained changes in activity. In the previous chapter we clearly observed the large influence of Au and graphene supports on the MoS_2 catalyst, but neither material was able to shift the properties of the catalyst to the right point, and therefore they did not result in an improvement in activity relative to unsupported MoS_2.[166,199] Thus, in this chapter, a range of readily modifiable supports are screened across to determine whether HER activity can be enhanced using fine-tuning of the catalyst properties.

Highly expensive mechanistic calculations for each and every material are naturally not possible in a screening study of this nature. Yet, in Chapter 3 it was shown that the catalyst support primarily affects the HER activity by altering the thermodynamic cost to adsorb H to MoS_2 (i.e. the Volmer step). At industrially relevant electrochemical potentials near 0 V, the H_2 combination barriers *via* either Tafel or Heyrovský processes were effectively unchanged by supports. Thus in this chapter we chose to study how the

free energy of hydrogen adsorption ($\Delta G_{H_{ads}}$) changes across materials, with the goal of obtaining facile H adsorption and desorption with no energetic cost.

The $\Delta G_{H_{ads}}$ is studied on both the basal plane and edges of MoS_2 supported by a series of two-dimensional, mostly carbon-based, support materials, including graphene oxides, heteroatom (S, B, and N) doped graphene, and some insulators (hexagonal boron nitride and graphitic carbon nitride). For the basal plane of MoS_2, a wide range of values for $\Delta G_{H_{ads}}$ are observed (between 1.4 and 2.2 eV) depending on the support material used. We use density of states analyses to explore how the supports induce electronic changes in the MoS_2 catalyst, and how this directly relates to $\Delta G_{H_{ads}}$.

On the Mo-edge of MoS_2, different supports induce smaller variations in $\Delta G_{H_{ads}}$, with values ranging between -0.27 and 0.09 eV. However, a graphene support doped with graphitic N atoms produces a $\Delta G_{H_{ads}}$ value of exactly 0 eV, which is thermodynamically ideal for hydrogen evolution. Once again the electronic structure of these materials is explored, this time using charge density analyses and Bader charge calculations, in order to understand the effect of the support material. $\Delta G_{H_{ads}}$ is found to relate closely and linearly to the amount of charge transfer between MoS_2 and support when they adhere together. The support-induced tuning of $\Delta G_{H_{ads}}$ on MoS_2 observed here provides a useful tool for improving current MoS_2 catalysts, and the discovery of variables which mediate changes in $\Delta G_{H_{ads}}$ contributes to the rational design of new hydrogen evolution catalysts.

This chapter is based on the published article: Ruffman, C., Gordon, C. K., Mackenzie, F. D., Gilmour, J. T. A., and Garden, A. L. "Enhancing the hydrogen evolution activity of MoS_2 basal planes and edges using tunable carbon-based supports," *Nanoscale*, **2021**, *13*, 3106–3118.[199] In this work, Calum Gordon was responsible for calculating some of the early models for graphene oxide support materials. He also helped to determine a method by which to minimise catalyst/support lattice mismatch. Frank Mackenzie also calculated some early models for MoS_2 on graphene oxide. Dr James Gilmour helped with the presentation of the density of states plots for the various systems studied here, and also provided many helpful discussions and advice around interpreting these plots, specifically, those concerning the support material below MoS_2.

4.1 Introduction

As was first touched on in Chapter 3, a large amount of information about the HER activity of a catalyst can be obtained by calculating the free energy of H adsorption, $\Delta G_{H_{ads}}$, which captures the overall thermodynamics of the HER.[5,76,77] Recall that, regardless of the precise mechanism, hydrogen evolution first requires H atoms to adsorb to the catalyst surface, then for H_2 to desorb once reacted. Thus, in accordance with the Sabatier principle,[159] the active site on a catalyst should not bind H too weakly for the reactants to adsorb (i.e. $\Delta G_{H_{ads}} >> 0$), yet also not too strongly for the products to desorb after a reaction has taken place (i.e. $\Delta G_{H_{ads}} << 0$). An ideal catalyst has a $\Delta G_{H_{ads}}$ of 0 eV, and promising catalysts sit close to this value. For the MoS_2 edges under standard industrial conditions, Tsai *et al.*[77] used DFT to calculate $\Delta G_{H_{ads}} = -0.36$ eV, whereas Li *et al.*[171] report the basal plane as $\Delta G_{H_{ads}} = 2.2$ eV. Taken together, these values support the idea that the edges of MoS_2 are currently the most promising active site. In comparison, calculations for Pt(111) reveal $\Delta G_{H_{ads}}$ is -0.03 eV under typical electrochemical conditions,[74] where the very small deviation from thermoneutral ($\Delta G_{H_{ads}} = 0$) assists in explaining why Pt is such an ideal HER catalyst.

As a result, there has been a large drive to bring $\Delta G_{H_{ads}}$ of both the MoS_2 basal plane and the edge sites closer to zero *via* approaches such as introducing S vacancies and defects,[171,195] straining the catalyst,[171] doping it,[200] or by supporting it on top of other materials.[77,160] Examining how $\Delta G_{H_{ads}}$ changes with these modifications instead of performing full-scale mechanistic calculations is a more computationally tractable approach, especially when comparing across a range of candidates to obtain trends. Critically, in Chapter 3 it was shown that the majority of the effect different catalyst supports had on the activity of MoS_2 was captured through changing the value of $\Delta G_{H_{ads}}$. This suggests $\Delta G_{H_{ads}}$ is an ideal metric to use for screening studies on supported MoS_2.[143]

Using catalyst supports to alter the activity of MoS_2 by improving the $\Delta G_{H_{ads}}$ is the focus of the present chapter, as these supports offer synthetically accessible options to fine tune the H adsorption energy, and could be used in conjunction with any other methods that may generate more substantial changes. Unlike Chapter 3, which focused only on the

MoS_2 edge, here the study is expanded to include the basal plane. While the basal plane is known to be less intrinsically active, it still makes up the majority of as-synthesized MoS_2 materials.[64] Therefore, improving the HER activity on this section of the catalyst could have significantly larger effects on the overall reaction rate once active site density is taken into account.

Past work on MoS_2 has shown that $\Delta G_{H_{ads}}$ is significantly affected by modification of the catalyst-support adhesion energy[77] and/or improvement of charge transfer kinetics between catalyst and support. Voiry *et al.*[201] showed the activity of MoS_2 supported on SiO_2 increases due to improved electrical coupling and thus more rapid charge transfer. Chen *et al.*[202] used DFT to show that, by varying a transition metal support beneath MoS_2 (Ru, Pd and Ir), the binding energy of H to the basal plane can be reduced by as much as 0.4 eV. The authors suggest that the greater the charge transferred from the substrate to MoS_2 the stronger it is able to bind H. Tang *et al.*[160] showed using DFT that graphene oxide supports for MoS_2 increase the energy of the valence band electrons relative to the Fermi level, thus increasing conductivity and therefore catalytic activity. These works on the basal plane of MoS_2 show that support materials can have a large impact on $\Delta G_{H_{ads}}$, but there are a range of explanations for how this impact comes about.

The value of $\Delta G_{H_{ads}}$ on the MoS_2-edge can also be altered by support materials, though the literature on this front is more sparse. As was seen in Chapter 3 of this thesis, exchanging a graphene support underneath MoS_2 for an Au(111) support shifted $\Delta G_{H_{ads}}$ on the edge from 0.30 eV to -0.25 eV.[143] Tsai *et al.*[77] have also studied $\Delta G_{H_{ads}}$ on both the Mo- and S-edges of MoS_2 with graphene, Au(111), and stacked MoS_2 supports. The authors show that $\Delta G_{H_{ads}}$ can vary between -0.37 and 0.39 eV depending on the support, and a relationship between $\Delta G_{H_{ads}}$ and the adhesion energy of MoS_2 to the support is reported. Here, stronger MoS_2/support adhesion (e.g. in the case of Au) resulted in H binding to MoS_2 more weakly. The results from Chapter 3 and from Tsai *et al.* suggest that there may be an optimal support material (between graphene and Au) that would tune the activity of the MoS_2 edges to have $\Delta G_{H_{ads}} = 0$. However, the difference between the properties of Au and graphene supports is large, and therefore the ability to precisely tune the edges of unsupported MoS_2, which are already quite close to $\Delta G_{H_{ads}} = 0$, is

limited. Instead, a material which can be readily modified to confer the precisely desired properties to MoS_2 edges would be ideal.

In the present work, $\Delta G_{H_{ads}}$ on MoS_2 is studied with a selection of carbon-based supports including graphene oxide, N-doped graphene, B-doped graphene, and S-doped graphene, all of which are readily synthetically accessible from pristine graphene.[203] Multiple accessible doping coverages exist for each, allowing exploration of fine-tuning. Other 2D support materials that are not graphene derivatives, including graphitic carbon nitride and hexagonal boron nitride are also studied. Critically, many of these materials are also commonly used experimental supports for other catalysts.[204]

In modifying or tuning MoS_2 catalysts, it is also informative to look for descriptors and electronic explanations which can capture how and why $\Delta G_{H_{ads}}$ shifts. This can offer great insight into why certain modifications are favourable, and provide options to improve existing materials. For the MoS_2 basal plane, trends in $\Delta G_{H_{ads}}$ have in the past been related to the energy of the p-orbital states in MoS_2,[195] the amount of charge on the S atom binding site,[205] and, for supported MoS_2 systems, the energy of the MoS_2/support valence band.[160] In one very recent work looking at H adsorption on the basal plane of MoS_2, Liu *et al.*[206] proposed a novel descriptor to capturing changes in the H adsorption energy based on the difference in energy between the occupied S p-orbital states and the unoccupied Mo d-orbital states in doped MoS_2 systems. In this chapter, we also wish to relate any observed changes in $\Delta G_{H_{ads}}$ to underlying electronic factors in the catalyst, so that the behaviour can be rationalised.

Overall, H adsorption is studied on both the basal plane and edges of MoS_2 with a range of graphene-derived supports. Readily modifiable supports with different dopant coverages are chosen in order to allow fine-tuning of the MoS_2 system. Trends in $\Delta G_{H_{ads}}$ are rationalised by comparison to the properties of the catalyst/support system, including adhesion energy, electronic structure, and degree of charge transfer.

4.2 Methodology

4.2.1 Structure models

The basal plane of MoS_2 (lattice constant 3.18 Å) was modelled as a single-layer periodic slab with at least 12 Å of vacuum separation in the z-direction. The unit cell was 5×5 Mo atoms in size. The structure of the MoS_2 basal plane supported by pristine graphene is shown in Figures 4.1A and B.

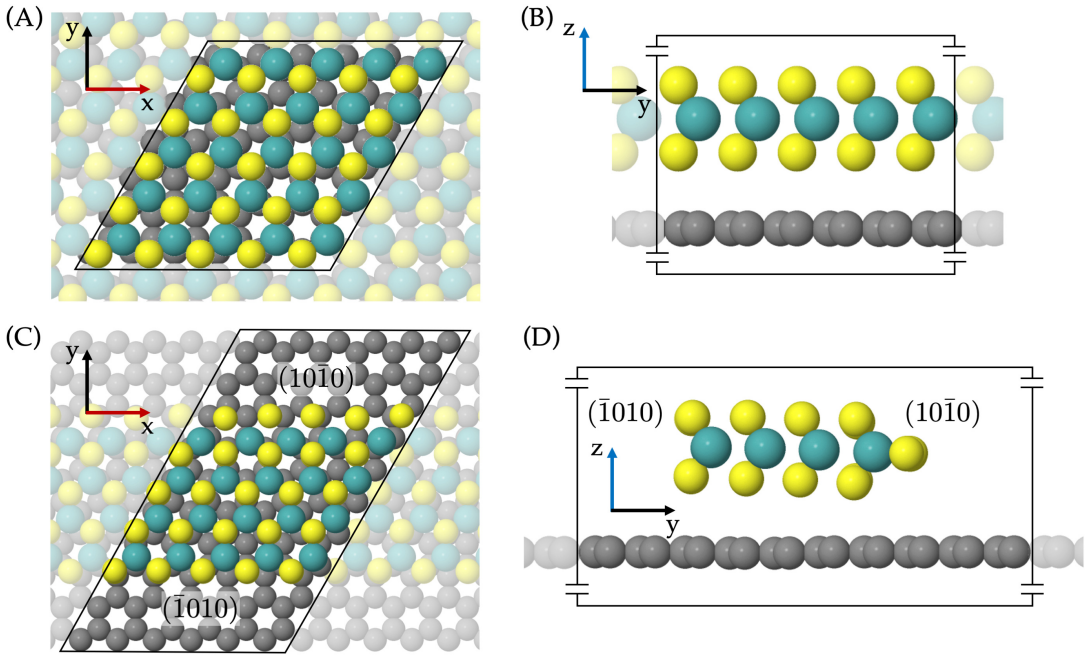

Figure 4.1: The MoS_2 basal plane model shown with a pristine graphene support from the (A) top and (B) side view. (C) Top and (D) side views of a supported MoS_2 stripe model that exposes the Mo-edge (10$\bar{1}$0) and the S-edge ($\bar{1}$010). Ball and stick models showing the connectivity of these structures are available in Appendix B.1.

As was done for Chapter 3, the edge of MoS_2 was represented using a semi-finite stripe model (shown supported by graphene in Figures 4.1C and D),[169] in which a single sheet of MoS_2 was cut along the (10$\bar{1}$0) and ($\bar{1}$010) vectors in order to expose the Mo- and S-edges, respectively. These MoS_2 stripes had at least 10 Å of space between their repeats in the y-direction, and 12 Å in the z-direction. The model was 5 Mo atoms wide in the periodic x-direction, and 4 Mo atoms in the non-periodic y-direction. The support was continuous below the MoS_2 stripe. Based on previous findings,[64,207] the Mo-edge of MoS_2

was assumed to be the catalytically active site (as opposed to the S-edge). The Mo-edge was simulated with 50% S coverage, and the S-edge with 100% S-coverage, in order to match structures found under industrial conditions.[167] Note that this is a higher S-edge coverage than was simulated in Chapter 3. This is because a 75% coverage cannot be reached on a model that is 5 Mo-atoms in the periodic direction. However, Hansen *et al.*'s results[167] do indicate the S-edge may be either 75 or 100% covered.

The size of both the basal plane and edge models was chosen as a reasonable compromise with respect to computational cost and minimising the strain due to lattice mismatch with underlying carbon-based supports. In this work, the carbon-based supports were strained slightly in order to ensure the model size was commensurate with MoS_2. These strains were typically around 7%, and never exceeded 9%. All calculated strains and cell lengths are given in Appendix B.2. We believe straining the support by these relatively small amounts is unlikely to have a large impact on the properties of the MoS_2 above, whereas if similar strains are applied to the MoS_2 model itself, previous work has found this has a small effect on the adsorption energy of H.[171]

The following carbon-based support materials were explored in the present work: graphene, graphene oxide with epoxide groups (GO-epoxide), graphene oxide with hydroxide groups (GO-hydroxide), N-doped graphene with graphitic doping (NDG-graphitic), N-doped graphene with pyridinic doping (NDG-pyridinic), N-doped graphene with pyrrolic doping (NDG-pyrrolic), substitutional B-doped graphene (BDG), substitutional S-doped graphene (SDG), hexagonal boron nitride (h-BN), and graphitic carbon nitride (*gt*-C_3N_4). These materials are all shown in Figure 4.2. Images showing the structures for all dopant coverages can be found in Appendix B.3. The graphene base was chosen in part because of the recent success of MoS_2/graphene materials,[208] and the ease with which it can be modified.

The graphene oxide (GO) materials are characterised as a pristine graphene sheet which is decorated by either epoxide groups (O bonded to two C) or hydroxide groups (OH bonded to one C) above and below the plane of the graphene.[209,210] Because there are a wide array of possible arrangements of these decorating groups, especially when different coverages are considered, some restrictions were placed on the graphene oxides

simulated here. First, although mixed hydroxide and epoxide functionalisation is likely in experiment, here the epoxide and hydroxide covered graphenes were initially considered separately. This approximation may be less experimentally realistic, but it allows separation of the effects that each type of functionalisation may have, which is consistent with past methodology.[160] Second, only graphene oxides with one-sided coverage were considered. When forming MoS_2/support structures, the MoS_2 was always placed above the functionalised side of the graphene oxide. The reason for only considering one-sided graphene oxides was that early testing with highly covered graphene oxide models (between 25 and 100 atomic %)[a] indicated an oxide layer facing away from the MoS_2 had very little effect on the H adsorption energy. The data to support this conclusion are available in Appendix B.4. It should be noted that these tests were conducted with a fairly unrealistic GO model both in terms of high coverages and completely evenly spaced and distributed functional groups. While this is not ideal for studying realistic GO supports, it still suggests a minimal effect from a second layer of functional groups on the side facing away from MoS_2.

Simple testing of where a second O preferred to bind once one O was already on the graphene suggested that situating these adjacent to each other was most favourable. For GO-epoxide, coverages of 5, 10, 15 and 25 atomic % were tested, and for GO-hydroxide 5 and 10% were studied. The coverages in the hydroxide systems were more limited as those higher than 10% resulted in large structural distortions at the unit cell size used here.

Three different types of N-doped graphene (NDG) were examined: (1) NDG-graphitic, where a carbon in the graphene lattice is directly substituted for a N, (2) NDG-pyridinic, where three carbons adjacent to a central carbon are directly substituted for N and then the central carbon is removed leaving a vacancy, and (3) NDG-pyrrolic, which is similar to pyridinic doped but one of the pyridinic rings has a carbon removed to form a pyrrolic ring.[203] For NDG-graphitic, the locations of the N in graphene sheet were chosen randomly, following what is known about the material experimentally.[203] Both

[a] Atomic percent refers to the percentage of dopant atoms per total number of carbon atoms. All coverages given in this chapter refer to an atomic percent coverage.

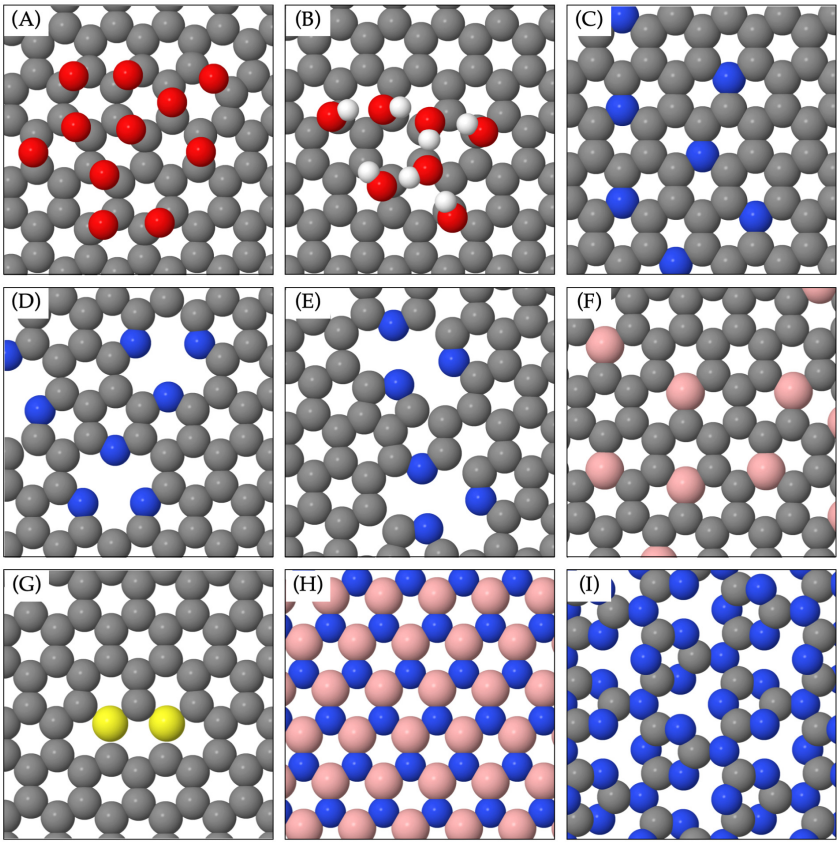

Figure 4.2: Structures of the carbon-based support materials studied in the present work (in addition to pristine graphene, which is not shown). Most supports are graphene derivatives with different functional groups. (A) GO-epoxide, (B) GO-hydroxide, (C) NDG-graphitic, (D) NDG-pyridinic, (E) NDG-pyrrolic, (F) BDG, (G) SDG, (H) h-BN, (I) *gt*-C_3N_4. Ball and stick models showing the connectivity of these structures are available in Appendix B.1.

the NDG-pyridinic and pyrrolic structures usually occur with N atoms in a tri-subsituted configuration around a carbon vacancy.[211] Here, for NDG-pyrrolic, two out of the three N are actually pyridinic, which is analogous to models used previously.[212] We found that creating a tri-substituted vacancy with all pyrrolic N was unstable, and resulted in the buckling of the support. N doping coverages of 4, 8, 12 and 16 atomic % were explored for NDG-graphitic and NDG-pyridinic, whereas just the 4 and 8% were tested for NDG-pyrrolic. These coverages span the range that past work has suggested is synthetically accessible.[203] N and S doped graphene materials have previously been combined with MoS_2 in order to activate Pd nanoparticles for the HER,[213] making them interesting candidates here.

Substitutional BDG, where a C atom in the graphene lattice is directly swapped for a B atom, was examined at 1.4, 4, 8 and 12% coverages. These coverages are lower than the materials discussed above as experimental evidence indicates the range of accessible doping coverages is slightly lower for BDG.[203] The locations where B was substituted into the sheet were randomly selected as no strong thermodynamic preference was found for localising B atoms next to or distant from each other. Substitutional SDG was generated using the same treatment, but at the lower 1.4 and 2.4% coverages, which represent the synthetically accessible range.[214]

There are two support materials included in this study that are not doped graphene derivatives, but were included for their structural similarity to graphene and because they are both used experimentally as catalyst supports.[204] The first, h-BN, forms an extended flat hexagonal sheet, similar to graphene where the elements alternate in adjacent positions between B and N. The second, graphitic carbon nitride, has a more interesting structure that is buckled in the plane of the sheet. Melissen *et al.*[215] suggest several computational models for graphitic carbon nitride, and here we chose the *gt*-C_3N_4 type primarily due to it requiring minimal strain to match the lattice of MoS_2 and also its interesting corrugated structure. Both h-BN and *gt*-C_3N_4 have large band gaps and behave as insulators, making them an interesting point of comparison to the other materials which are all conducting.

One possible concern in constructing MoS_2/support structures is whether the position of the dopants or functional groups on the carbon-based support below MoS_2 would influence the H adsorption energy. For the basal plane of MoS_2, this idea was tested by adsorbing H in different locations on top of the MoS_2, where the adsorption sites should be identical aside from the possible effects of localised dopants underneath. To take the graphene oxides as one example, where the effect of localised dopants should be at its largest with clustered oxide groups below MoS_2, we found the H binding energy changed by less than 0.04 eV across three different test adsorption sites. In the edge models of MoS_2, it is also possible that the position of the exposed Mo-edge relative to the dopants on the support underneath could also have a larger effect than was the case for the basal plane. To minimise this, again for the graphene oxides which should see the largest effect from localised dopants, several different positions of the MoS_2 stripe model on top of

the support were tested. In each case, the hydrogen adsorption energy was taken at the lowest energy geometry. For the other support materials where the dopants were randomly distributed and not clustered, the position of the stripe should have a smaller effect. Regardless, in all cases, the H adsorption energy on the MoS_2 stripe in several different positions was found to vary by less than 0.04 eV.

4.2.2 Computational details

All calculations in this chapter were performed using the same general specifications outlined at the end of Chapter 2. For the basal plane models of MoS_2, the unit cell was sampled with a $4 \times 4 \times 1$ Monkhorst-Pack k-point scheme. For the supported edge models a $4 \times 2 \times 1$ scheme was used, and for the unsupported edge model a $4 \times 1 \times 1$ scheme was used. The electronic and free adsorption energies of H were calculated as described in Chapter 2, Section 2.5.1. Only the first H adsorption is studied, as the results from Chapter 3 indicated this is the critical intermediate to the favourable Volmer-Heyrovský reaction, and higher H coverages are not generally observed on MoS_2 at industrially relevant potentials near 0 V.

The adhesion energies between MoS_2 and support were calculated as shown in Equation 4.1.

$$E_{\text{adhesion}} = E_{\text{MoS}_2/\text{support}} - (E_{\text{MoS}_2} + E_{\text{support}}) \tag{4.1}$$

Where E_{MoS_2} is the energy of the isolated MoS_2 structure, and E_{support} is that of the isolated support. Here, the adhesion energies are reported per Mo atom in the MoS_2 in order to avoid model size dependence.

4.3 Results and discussion

Because of the very different binding character on the MoS_2 basal plane versus that on the MoS_2 edge, as well differences in the magnitude of $\Delta G_{\text{H}_{\text{ads}}}$, the results from these two systems are discussed separately here then compared later. The first two sections focus on

reporting trends in $\Delta G_{H_{ads}}$ with different supports, then possible explanations for these trends in terms of the underlying electronic structure are discussed later.

4.3.1 MoS_2 basal plane

It is found that H adsorbs to the basal plane of MoS_2 in one of two different configurations: either directly on top of an S atom (henceforth "on-top") or slightly tilted at an angle of approximately 40° from the upright (henceforth "tilted"). Both binding configurations are depicted in Figure 4.3. These configurations are around 0.5 eV more favourable than

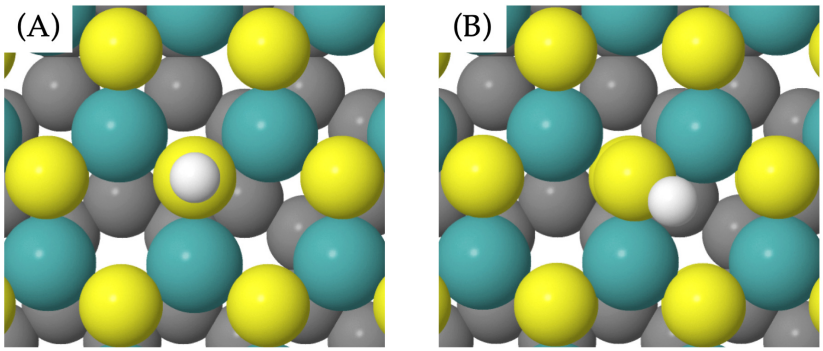

Figure 4.3: The structures for H adsorption to the basal plane of MoS_2 supported by pristine graphene in (A) an on-top configuration, and (B) a tilted configuration.

possible alternatives, including H binding to an Mo atom or at a bridged position between an S and Mo. In Table 4.1 $\Delta G_{H_{ads}}$ is presented for both binding configurations on the range of MoS_2/support combinations tested here. While the on-top structure could be stably located on all materials, the tilted configuration was only found with certain supports. For unsupported MoS_2, tilted binding of H was found to be more favourable than on-top binding by about 0.2 eV, a result which is consistent with very recent work that first reported the tilted configuration.[206] However, $\Delta G_{H_{ads}}$ for tilted H is relatively invariant to the choice of support, whereas the on-top binding energies appear to be significantly influenced. As a result, the on-top binding geometry becomes favourable when moving to supports which reduce $\Delta G_{H_{ads}}$. Given that the on-top configuration is more interesting from a support-tuning perspective, and ultimately provides the lowest $\Delta G_{H_{ads}}$ values with the right supports, this will make up the main focus of the following discussion.

The $\Delta G_{\mathrm{H_{ads},on\text{-}top}}$ value on unsupported MoS_2 of 2.22 eV is seen to agree closely with the 2.2 eV reported previously.[171] Adding a pristine graphene support below MoS_2 has very little effect on this value, lowering it to 2.14 eV, yet $\Delta G_{\mathrm{H_{ads},on\text{-}top}}$ varies notably with other carbon-based supports. At a maximum, $\Delta G_{\mathrm{H_{ads},on\text{-}top}}$ is 2.23 eV with MoS_2 on either *gt*-C_3N_4 or NDG-graphitic (16% coverage) supports. $\Delta G_{\mathrm{H_{ads,on\text{-}top}}}$ is reduced at least slightly with addition of the majority of supports tested here, and falls to a minimum of 1.44 eV with a B-doped graphene support (12% coverage).

B-doped graphene is perhaps the most interesting class of support material tested here, as it causes the largest reduction in $\Delta G_{\mathrm{H_{ads},on\text{-}top}}$ on the MoS_2 basal plane. At low dopant coverages (1.4 and 4%), the B-doped support lowers $\Delta G_{\mathrm{H_{ads},on\text{-}top}}$ by between 0.4 and 0.5 eV relative to pristine graphene. Yet, at slightly higher coverages (8 and 12%) $\Delta G_{\mathrm{H_{ads},on\text{-}top}}$ drops to between 1.4 and 1.5 eV, approximately 0.7 eV lower than with the pristine graphene support. Because the decrease in $\Delta G_{\mathrm{H_{ads},on\text{-}top}}$ observed here appears to strengthen at the higher B coverages, this suggests it would be a valid synthetic goal to be able to produce these higher coverages with reliability. While the majority of B-doped graphene materials have been synthesised at relatively low coverages ($\leq$ 3% coverage),[203,216] certain synthetic techniques have allowed coverages as high as around 14% to be reached.[217]

Another support that modifies $\Delta G_{\mathrm{H_{ads},on\text{-}top}}$ significantly is graphene oxide with epoxide functionality. For instance $\Delta G_{\mathrm{H_{ads,on\text{-}top}}}$ on MoS_2 supported by 25% epoxided graphene is 1.63 eV, about 0.5 eV lower than that for pristine graphene. At lower epoxide coverages ranging from 5 to 15% $\Delta G_{\mathrm{H_{ads},on\text{-}top}}$ varies between 2.01 and 1.89 eV, suggesting that the support is not having a large effect in this range. This is an interesting case, as Tang *et al.*[160] have previously demonstrated a trend of stronger H binding (decreasing $\Delta G_{\mathrm{H_{ads}}}$) as oxide group coverage on the support increases in the range of 6 to 14 atomic %. While the same overall trend is seen in the present epoxide data, it is not evident until higher coverages (such as 25%) are reached. However, Tang *et al.* studied randomly distributed oxide groups instead of the clustered oxide groups examined in the present work, which could potentially account for differences in sensitivity to epoxide coverage. Unlike for the epoxides, graphene oxide with hydroxide groups (5 or 10% coverage) as a

Table 4.1: H adsorption free energy ($\Delta G_{H_{ads}}$) for the basal plane of MoS_2 supported on a series of carbon-based supports at different dopant coverages. Adsorption energies are given for both the on-top H binding geometry and the tilted geometry (in cases where it could be located). The MoS_2/support adhesion energy per Mo atom, and the valence band maximum (VBM) of the p-orbital states of the S atom adsorption site are also presented.

Support	Coverage / %	$\Delta G_{H_{ads}}$ on-top / eV	$\Delta G_{H_{ads}}$ tilted / eV	$E_{adhesion}$ per Mo / eV	VBM of p-states / eV
Unsupported	—	2.22	2.04	—	-0.41
Pristine graphene	—	2.14	2.03	-0.11	-0.98
GO-Epoxide	5	1.89	1.89	-0.10	-0.65
	10	2.01	2.01	-0.10	-0.57
	15	1.93	1.93	-0.09	-0.38
	25	1.63	—	-0.10	-0.18
GO-hydroxide	5	2.18	1.96	-0.07	-1.22
	10	2.09	1.96	-0.06	-1.10
NDG-graphitic	4	2.21	1.95	-0.03	-1.52
	8	2.19	1.88	-0.05	-1.37
	12	2.20	1.94	-0.16	-1.43
	16	2.23	1.81	0.02	-1.43
NDG-pyridinic	4	1.94	—	-0.12	-0.75
	8	1.83	—	-0.11	-0.64
	12	1.82	—	-0.11	-0.57
	16	1.80	—	-0.11	-0.60
NDG-pyrrolic	4	1.82	—	-0.12	-0.55
	8	1.72	—	-0.12	-0.50
BDG	1.4	1.83	—	-0.12	-0.55
	4	1.70	—	-0.12	-0.49
	8	1.50	—	-0.12	-0.27
	12	1.44	—	-0.12	-0.27
SDG	1.4	2.16	1.98	-0.12	-1.19
	2.8	2.18	1.95	-0.12	-1.19
h-BN	—	2.22	2.01	-0.12	-0.42
gt-C_3N_4	—	2.23	2.02	-0.10	-0.41

support for MoS_2 does not change $\Delta G_{H_{ads},\text{on-top}}$ relative to graphene. Higher coverages of clustered hydroxide groups were not accessible within the present simulation cell size as they resulted in non-physical buckling of the graphene sheet, so it is unclear whether $\Delta G_{H_{ads},\text{on-top}}$ would be modified at higher hydroxide coverages as was the case for epoxides.

Two of the supports tested here, h-BN and *gt*-C_3N_4, do not have any effect on $\Delta G_{H_{ads},\text{on-top}}$ compared to unsupported MoS_2, despite having a similarly strong adhesion to the MoS_2 sheet as many of the other supports. One notable distinction for these two materials, compared to the other supports studied, is that they are insulators with a large band gap. This idea can be used to rationalise why they do not affect $\Delta G_{H_{ads},\text{on-top}}$, and will be revisited later in the discussion.

With respect to the general trends in $\Delta G_{H_{ads},\text{on-top}}$ across different carbon-based support materials it is clear that, where different dopant coverages are available on the support, increasing the dopant coverage either has no effect on the $\Delta G_{H_{ads}}$ value or serves to decrease it. Here we find no examples of increasing dopant coverage in the support causing a systematic increase in $\Delta G_{H_{ads},\text{on-top}}$ for MoS_2.

4.3.2 MoS_2 edge

Unlike the basal plane of MoS_2, where H can adsorb to any of the equivalent S sites on top of the sheet, the 50% sulfided Mo-edge has a selection of non-equivalent H adsorption sites on S and Mo atoms. The results from Chapter 3 showed that the H adsorption profile on the Mo-edge is complex, and when dealing with higher H coverages above 0.75 ML, H atoms often adsorb to both Mo and S atoms.[143] As our primary interest here is in the tuning effects of catalyst supports, only the first H adsorption is studied. Consistent with past works,[143,166] it is found that H preferentially adsorbs to an S atom on the edge. Only one binding geometry of H was located, and the $\Delta G_{H_{ads}}$ value for this adsorption process (-0.30 eV on unsupported MoS_2) demonstrates that H binds much more readily to the edge than the basal plane, which is also consistent with prior reports.[76]

In Table 4.2, $\Delta G_{H_{ads}}$ is presented for the supported MoS_2 edge models tested here. In contrast to the basal plane, for the MoS_2 edge the carbon-based supports appear to have

much smaller magnitude effects on $\Delta G_{H_{ads}}$. The range of $\Delta G_{H_{ads}}$ values spans only about 0.4 eV, from a minimum on unsupported MoS_2 ($\Delta G_{H_{ads}} = -0.30$ eV) up to a maximum on the NDG-graphitic support ($\Delta G_{H_{ads}} = 0.09$ eV). This 0.39 eV range compares to the 1.02 eV range on the basal plane. Furthermore, on the MoS_2 edge, very little difference in $\Delta G_{H_{ads}}$ is induced moving between dopant coverages on the support (usually $\leq$0.1 eV), and the majority of variability comes from comparing different classes of carbon-based support.

Despite the smaller range of $\Delta G_{H_{ads}}$ values, because the unsupported MoS_2 edge already has a $\Delta G_{H_{ads}}$ value that is reasonably close to the thermodynamically ideal 0 eV, the variability induced by supports is enough to encompass this 0 eV point. Notably, the NDG-graphitic support produces $\Delta G_{H_{ads}}$ values of –0.01 eV and exactly 0.00 eV at 4 and 16% N coverage, respectively. Additionally, the 8 and 12% dopant coverages here also produce $\Delta G_{H_{ads}}$ values that are close to 0 eV, suggesting the promising nature of this material is not particularly sensitive to the support dopant coverage. Pt(111), which is often considered as a gold standard comparison for HER catalysts, has a $\Delta G_{H_{ads}}$ value of –0.03 eV,[74] which suggests that MoS_2 with a NDG-graphitic support could be competitive with Pt in terms of HER thermodynamics. The tuning effect this NDG-graphitic support has on H binding to the MoS_2 edge contrasts its behaviour as a support to basal plane models of MoS_2, where it induced effectively no change in $\Delta G_{H_{ads}}$. This suggests that the MoS_2 edge binds H differently to the basal plane, and that supports may offer tuning through different mechanisms.

Pyridinic and pyrrolic N-doped graphene supports do not induce the same favourable $\Delta G_{H_{ads}}$ that the graphitic N-doped support does. Indeed, these two material types do not significantly modify $\Delta G_{H_{ads}}$ compared to a pure graphene support. Thus, one possible hurdle to obtaining the promising graphitic N-doped support is in the synthesis, as it must be possible to preferentially induce graphitic doping of N over either pyridinic or pyrrolic. However, graphitic N doping is generally considered to be the most stable form,[212,218] and modern synthetic techniques are available to enrich the concentration of graphitic N in the doping process.[219] Therefore, it is believed this material is not only promising but obtainable, especially if work is devoted to further improving the synthesis of graphitic

Table 4.2: H adsorption free energy ($\Delta G_{H_{ads}}$) on the 50% sulfided Mo-edge of MoS_2 supported on a series of carbon-based supports at different dopant coverages. The MoS_2/support adhesion energy and the charge transferred from the support to the MoS_2 stripe (determined *via* Bader charge analyses) are both shown per Mo atom.

Support	Coverage / %	$\Delta G_{H_{ads}}$ / eV	$E_{adhesion}$ per Mo / eV	MoS_2 charge excess per Mo / $\times 10^{-2}\, e^-$
Unsupported	—	-0.30	—	—
Pristine graphene	0	-0.20	-0.12	-3.20
GO-epoxide	5	-0.23	-0.15	-2.25
	10	-0.27	-0.13	-0.93
	15	-0.24	-0.12	-0.06
	25	-0.26	-0.12	0.64
GO-hydroxide	5	-0.17	-0.11	-2.95
	10	-0.14	-0.09	-3.74
NDG-graphitic	4	-0.01	-0.17	-6.96
	8	0.06	-0.19	-7.80
	12	0.09	-0.19	-8.25
	16	0.00	-0.06	-8.35
NDG-pyridinic N-doped	8	-0.22	-0.12	-3.20
	16	-0.21	-0.11	-2.10
NDG-pyrrolic	8	-0.23	-0.12	-1.85
BDG	1.4	-0.20	-0.13	-2.82
	4	-0.22	-0.2	-2.30
	8	-0.24	-0.24	-1.57
	12	-0.22	-0.22	-1.50
SDG	1.4	-0.09	-0.13	-5.10
	2.8	-0.13	-0.12	-5.35
h-BN	—	-0.27	-0.11	-0.90
gt-C_3N_4	—	-0.26	-0.10	-0.26

N-enriched graphene. The idea of multiple types of N-doping simultaneously existing on a support will be covered later in Section 4.3.4.

In comparing the overall activity of the MoS_2 edge to that of the basal plane, the present data affirms the idea that it is the edge sites on MoS_2 that are primarily responsible for HER catalysis,[64] due to the much more favourable $\Delta G_{H_{ads}}$ values. Support tuning on the MoS_2 edge can produce a thermodynamically optimal catalyst, whereas the H adsorption on the basal plane had a cost of 1.44 eV even with the most promising support tested here. This suggests that improving the synthesis of edge-rich MoS_2 (which could be supported by NDG-graphitic materials) would be of much benefit. While carbon-based supports do show some promising effects on the MoS_2 basal plane, the present data suggests a more substantial modification to MoS_2 is required to activate the basal plane. This idea will be revisited in Section 4.3.4, and is the topic of Chapter 5.

4.3.3 Factors influencing the H adsorption energy

Having observed changes in $\Delta G_{H_{ads}}$ for MoS_2 with different carbon-based supports, it is interesting to investigate what factors may be responsible for the tuning, in order to inform the design of future catalysts. Past work has suggested the tuning of $\Delta G_{H_{ads}}$ on the MoS_2 edge relates to the strength of adhesion between MoS_2 and support.[77] Tsai *et al.* report a linear relation between MoS_2/support adhesion energy and $\Delta G_{H_{ads}}$ when studying Au, graphene, and stacked MoS_2 supports. These results indicated that stronger adhesion energies led to weaker H adsorption to MoS_2. However, for the carbon-based materials studied here, very little variance in the adhesion energy is observed for either the edges or the basal plane. Furthermore, what little variance is present does not appear to relate to $\Delta G_{H_{ads}}$ (see Tables 4.1 and 4.2). Therefore, it is suggested that a relationship between adhesion energy and $\Delta G_{H_{ads}}$ is only observed when considering supports that induce large variations in the adhesion energy, such as the 0.4 eV per Mo difference between graphene and Au supports.[77] When comparing supports derived primarily from the same structure and elements, such as the carbon-based materials here, adhesion energy does not vary largely and thus has no effect on $\Delta G_{H_{ads}}$.

Given the adhesion energy cannot explain the variance observed in $\Delta G_{H_{ads}}$ across carbon-based supports, alternate explanations are sought in terms of the electronic factors governing H binding. Due to differences in the magnitude of the $\Delta G_{H_{ads}}$ on the MoS_2 basal plane and edges, they are discussed separately.

Understanding trends in H adsorption on the basal plane

As previously discussed, two adsorption geometries exist for H on the MoS_2 basal plane: on-top and tilted. The tilted geometry is favoured on unsupported MoS_2, but $\Delta G_{H_{ads,tilted}}$ is invariant to the choice of catalyst support and remains high, whereas many of the supports studied here serve to reduce $\Delta G_{H_{ads},on\text{-}top}$ significantly, such that this geometry becomes favoured. When examining density of states (DOS; see Chapter 2, Section 2.6.1) plots for both types of binding on a MoS_2/graphene system (Figure 4.4, for other materials see Appendix B.5), it is evident that the two geometries have different binding character. As originally noted by Liu *et al.*,[206] it is found here that tilted binding of H forms low energy H s-states that occur at the same energy as S p-states, suggesting formation of a covalent S-H bond, as these two sharp features are overlapping. Additionally, a strong Mo d-state (d_{xy}) arises at the Fermi level, meaning it is partially occupied. This has previously been explained by the idea that the S atom (with a full valence shell) transfers one electron to a neighbouring Mo so that it can form a covalent bond with H.[206] In the DOS, the Mo d-state that arises is entirely associated with the Mo atom opposite where H is positioned in the tilted configuration. This suggests the electron transfer is highly directional.

The on-top configuration of H binding also shows strong low energy H s-states, again overlapping with S p-states, indicating a covalent bond. However, in the on-top case there is no appearance of a distinct and half-filled Mo d-state at the Fermi level for the MoS_2/graphene. There is still arguably some very slight filling of Mo d-states directly at the Fermi level; yet, while the S atom in on-top binding must still be redistributing some electron density in order to form a covalent bond, this does not appear to be going to a single Mo.

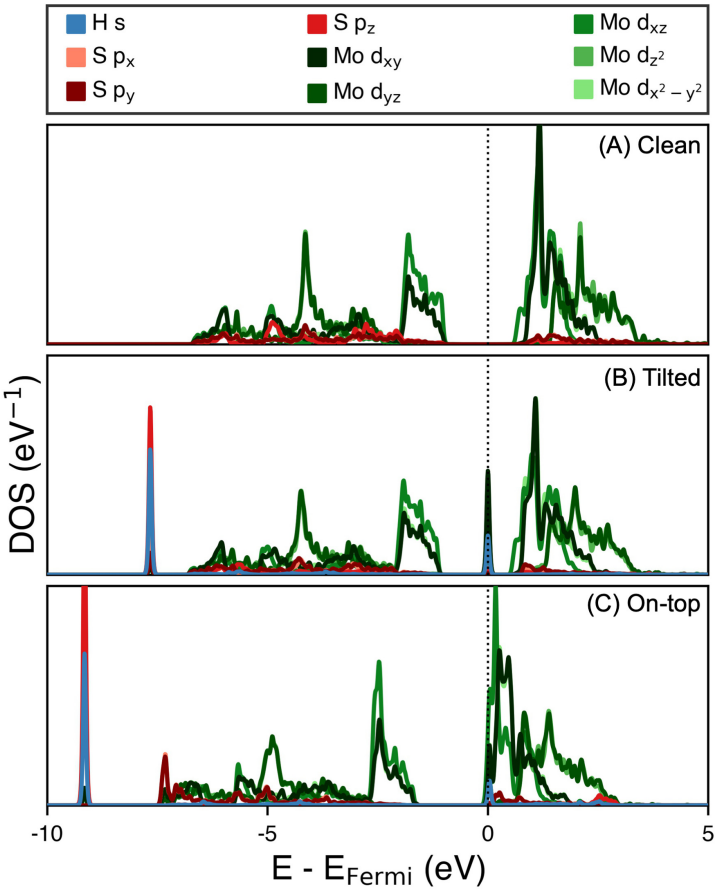

Figure 4.4: Angular momentum resolved density of states plots showing the p-states of the S atom adsorption site, the d-states of the three neighbouring Mo atoms, and the s-states of adsorbed H (where applicable). (A) Pristine MoS_2/graphene material without H adsorbed, (B) H adsorbed in the tilted configuration, and (C) H adsorbed in the on-top configuration. Note for the tilted case not all three neighbouring Mo atoms are equivalent.

Plotting $\Delta G_{\mathrm{H_{ads}}}$ against the maximum energy of the occupied S p-states in the DOS of pristine MoS_2/support surfaces (i.e. the valence band maximum, recorded in Table 4.1) reveals an interesting relation. For on-top adsorption of H (Figure 4.5A), the closer the valence band maximum of the S p-states is to the Fermi level, the more favourable the value of $\Delta G_{\mathrm{H_{ads},on\text{-}top}}$. This relation does not hold true for the tilted binding configuration of H (Figure 4.5B), for which $\Delta G_{\mathrm{H_{ads}}}$ is invariant to changes in the energy of the p-states. Using the valence band maximum to predict $\Delta G_{\mathrm{H_{ads}}}$ is not a novel idea – it has been used to understand differences in H binding before,[77,160] and also bears some similarity to the famous d-band model for describing adsorbate binding on metallic systems.[220] Furthermore, Ouyang *et al.*[195] have previously used shifts in the centre of the S p-states in

order to explain H adsorption trends to defects in MoS_2 basal planes. However, the trend reported in the present work extend these past findings to show that different catalyst supports are enough to induce substantial changes to the position of the S p-states in MoS_2 which directly reflect on the H adsorption energy.

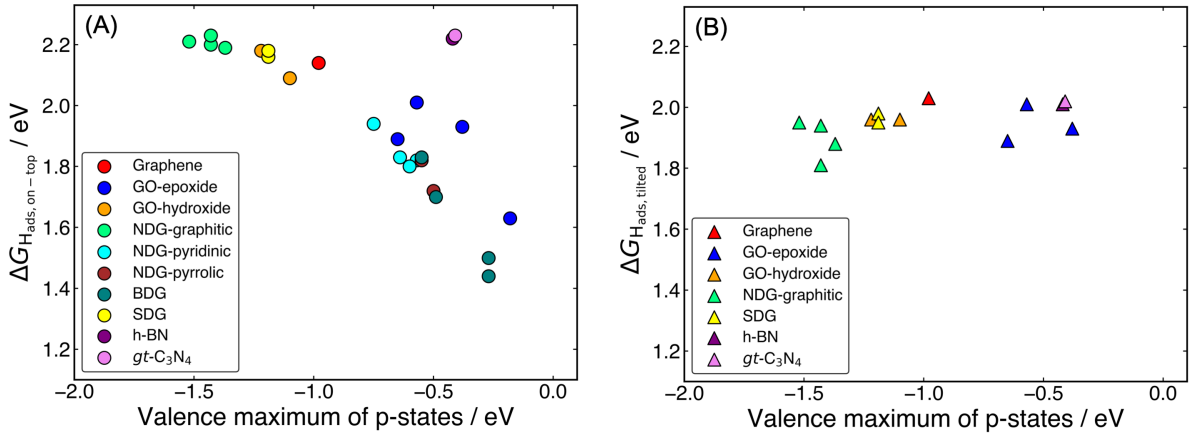

Figure 4.5: Valence band maximum of the p-states of the S atom adsorption site in supported MoS_2 plotted against $\Delta G_{H_{ads}}$ for (A) the on-top H binding configuration and (B) the tilted H binding configuration. A clear decrease in $\Delta G_{H_{ads}}$ is observed as the p-state maximum approaches zero when H is binding in the on-top configuration, but there is no relation observed for tilted H binding.

Furthermore, we show here that the different behaviour of the on-top and tilted binding configurations in response to the p-state maximum can be rationalised by electronic arguments, with consideration of the DOS of the support material. Given that the support influences the adsorption energy for on-top H binding, it is not unreasonable to expect to see a response in the electronic structure of the support when H is adsorbed in the on-top configuration that is not present in tilted binding. In Figure 4.6A, the angular momentum resolved DOS of the pristine graphene support is shown without H adsorbed, and with H adsorbed to the MoS_2 above. The DOS for the other support materials can be found in Appendix B.6. Both the on-top and tilted configurations of H adsorption are presented.

When H binds on-top, there is a clear up-shift of the Fermi level, meaning that more states are occupied. The states are p_z in character, suggesting there are more electrons present in the region between MoS_2 and the support material when H is adsorbed on-top.

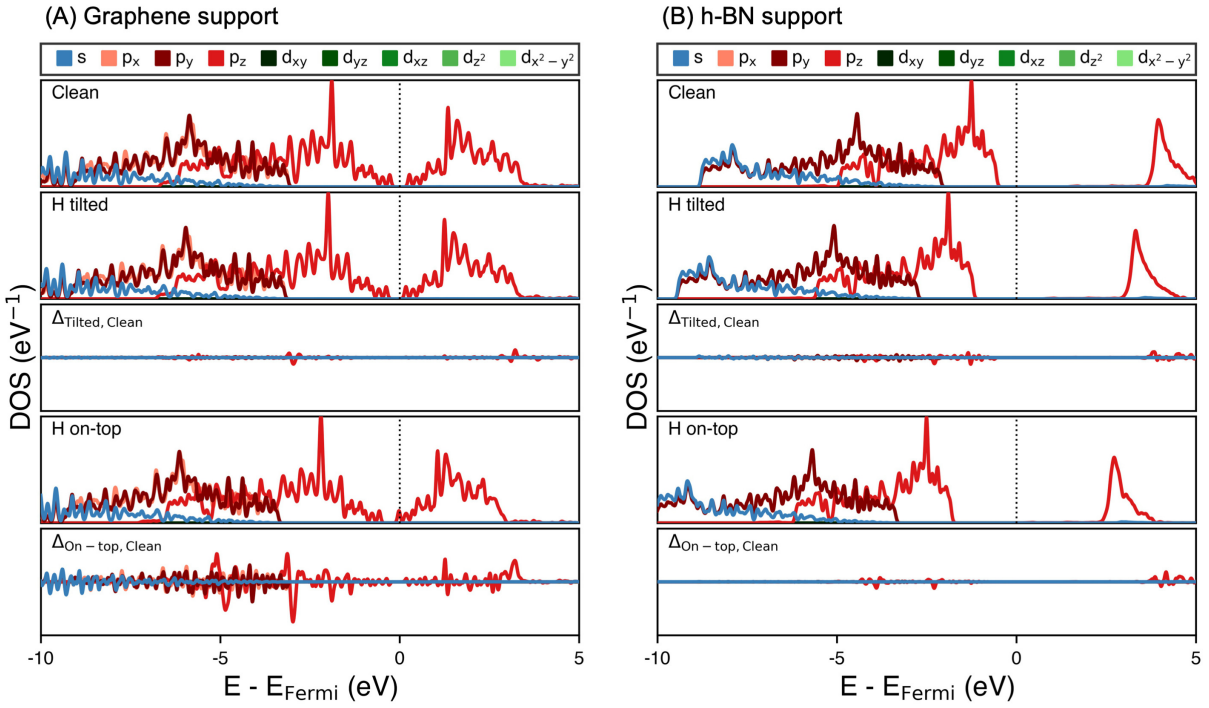

Figure 4.6: Angular momentum resolved DOS for (A) a graphene support beneath MoS_2 and (B) an insulating h-BN support. The DOS are shown for when MoS_2 has no H adsorbed (clean) and when H is adsorbed to MoS_2 in either an on-top or tilted configuration. The difference plots, $\Delta_{\mathrm{On-top,Clean}}$ and $\Delta_{\mathrm{Tilted,Clean}}$, represent the change in the support DOS when H is adsorbed in each of the above configurations. These differences are calculated by first aligning the highest intensity peak then performing the subtraction.

This is not observed when H binds in the tilted configuration. Furthermore, looking at the magnitude of change in the support DOS when H is adsorbed on-top relative to clean MoS_2 ($\Delta_{\mathrm{On-top,Clean}}$), there is clear evidence of significant perturbation to the electronic structure. This is not seen when making the same comparison with tilted H binding ($\Delta_{\mathrm{Tilted,Clean}}$). Overall these factors all point to the idea that when H binds to MoS_2 in an on-top fashion, some of the electron density from the S atom it binds to is transferred to the support material below. This finding also rationalises the observed correlation between the S p-orbital energy and $\Delta G_{\mathrm{H_{ads}}}$, as the closer in energy these p-state electrons are to the Fermi level the less energy is required to move them into the conduction band and thus the support below MoS_2. Because most of the supports tested here have states at the Fermi level, they can readily accept this extra electron density.

The insulating supports, h-BN and *gt*-C_3N_4, do not exhibit tuning of $\Delta G_{H_{ads,\ on\text{-}top}}$ with the position of the p-state maximum, and thus they do not fit the trend exhibited by the other materials in Figure 4.5A. In Figure 4.6B, which shows the DOS of an h-BN support below MoS_2, it is clear that there is very little perturbation observed in the insulating support DOS when H binds to MoS_2 in either the tilted or on-top configuration (see $\Delta_{On-top,Clean}$ and $\Delta_{Tilted,Clean}$). Furthermore, the Fermi level is always present in the band gap and neither fills nor empties states on H adsorption. This suggests that only conducting supports can accommodate the electron density displaced by on-top H binding, and thus only conducting supports will tune $\Delta G_{H_{ads,\ on\text{-}top}}$. It is suggested that insulating supports are unable to directly accommodate the electron transfer from the S p-states on MoS_2 as they do not have states at the Fermi level. To extend this idea slightly, this may also explain why certain non-zero band gap materials such as graphene and the GO-epoxides (see Appendix B.6 for support DOS) deviate slightly from the trend in 4.5A. Here, a slight additional energetic cost may have to be paid to shift the p-electrons not just to the Fermi level but also slightly higher to the unoccupied states in the support. However, until more extensive testing can be done, this remains inconclusive, as the deviations in $\Delta G_{H_{ads}}$ are relatively small and could be considered within range of error.

In contrast to on-top binding of H, tilted binding does not significantly displace electrons into the support (as was noted in Figure 4.6A), and instead requires promotion of an electron from the S p-states to the unfilled Mo d-states. Here, it is found that as the energy of the p-states increases relative to the Fermi level, so to does the energy of the unfilled Mo d-states. Thus, the supports studied here do not modify the gap between S p-states and Mo d-states, and as a result do not change the H adsorption energy for the tilted configuration.[206]

While no support material tested here brings the $\Delta G_{H_{ads},on\text{-}top}$ value on the basal plane of MoS_2 close to a thermodynamically ideal value of 0 eV, the existence of the reliable relation between the valence band maximum and $\Delta G_{H_{ads,\ on\text{-}top}}$ is still highly promising. If a support that drives the energy of the S p-states higher than those examined here could be found, this may have a more significant effect on $\Delta G_{H_{ads}}$. Alternatively, the introduction of carbon-based supports under MoS_2 could be used in conjunction with

other techniques such as metal or heteroatom doping in the MoS_2,[221,222] or creation of S vacancies,[171,223] both of which have a much larger effect on the $\Delta G_{H_{ads}}$ value but allow less fine control. Importantly, the quantifiable relation and underlying mechanism for support tuning reported here allow for the rational design and planning of new materials that can take advantage of the fine-tuning that carbon supports can offer.

Understanding trends in H adsorption on the Mo-edge

As was previously discussed, H adsorption on the edge of MoS_2 is significantly stronger than that on the basal plane, and is affected more moderately by the choice of catalyst support. The variation in $\Delta G_{H_{ads}}$ with support could not be easily explained through changes to the position of the S p-state maximum, as was the case for the basal plane. Because the edge atoms in the Mo-edge are conducting,[64] the p-state DOS for these systems always encompassed the Fermi level regardless of support. As a result, there was no change in the maximum energy of the filled p-states, so this could not explain changes in $\Delta G_{H_{ads}}$. Instead, it appears that different factors are influencing the binding of H to the MoS_2 edge compared to the basal plane.

The redistribution of charge in MoS_2 upon H adsorption is investigated for both the MoS_2 basal plane and edge. Charge density difference plots comparing the clean and H adsorbed surfaces are shown in Figure 4.7, where it is observed that S-H bond formation on the basal plane (on-top geometry) is associated with only very slight movement in charge in the adsorbed H and the S atom it is adsorbed to. These effects do not appear to extend beyond these two centres. This was also the case for the tilted binding geometry (Appendix B.7). In contrast, for the MoS_2 edge, significant charge movement is observed. The adsorbed H takes on positive charge character and negative charge appears to distribute into the catalyst. Interestingly, adsorbing H produces a dipolar shift in charge at the S adsorption site, with negative charge accumulating below the atom and positive where the H is adsorbed on top. This effect propagates along the S atoms on the Mo-edge, inducing some degree of dipole in most of the S atoms on the edge. The movement of charge also extends slightly past the edge into "bulk-like" MoS_2. It is possible the large degree of charge movement in response to H adsorption on the edge can

be attributed to it having higher conductivity than the basal plane.[64] Overall, it is clear that this movement of charge plays a large role in H binding to the MoS_2 edge where it may not for the basal plane.

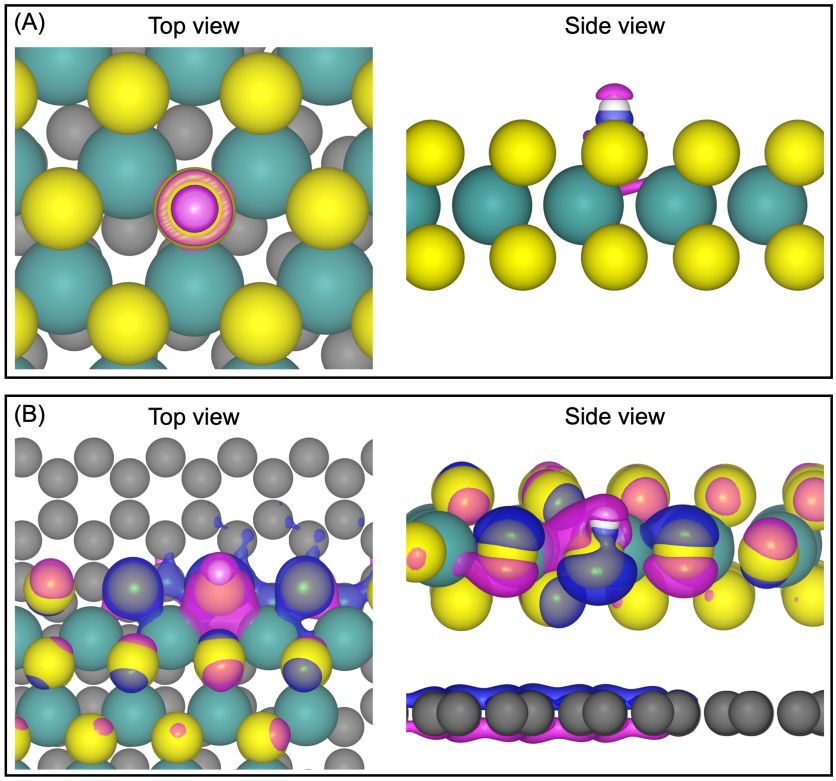

Figure 4.7: Charge density difference plots showing the movement of charge in graphene supported MoS_2 after H is adsorbed ($\rho_{MoS_2/graphene+H} - (\rho_{MoS_2/graphene} + \rho_H)$) to either an S on the basal plane in the on-top configuration (A), or an S on the Mo-edge (B). Blue indicates negative charge accumulation and pink indicates negative charge depletion. Isosurface level = 0.006 e^-/A^3.

Given the importance of charge movement in the MoS_2 edge upon H adsorption, it is pertinent to first understand how the charge character of MoS_2 is influenced by the support material before H is adsorbed. A Bader charge analysis was performed to determine the extent to which different supports were responsible for donating or withdrawing charge from the MoS_2. The MoS_2/support structures were compared to both the component materials in isolation (i.e. MoS_2 and the support material taken separately), and the amount of charge transferred from the support to the MoS_2 was calculated and is recorded in Table 4.2. This quantity is normalized to the number of Mo atoms in the model, as

proportionally more charge transfer can occur as the model size increases. A fairly large range in the degree of charge transfer is observed across different carbon-based supports. For instance a GO-epoxide support (15% coverage) transfers effectively no charge to the MoS_2 layer, yet the NDG-graphitic supports can transfer about 0.1 of an electron per Mo atom to the catalyst, which is fairly significant on net. None of the carbon supports tested here were found to draw an appreciable amount of electron density away from the MoS_2 catalyst.

Most interestingly, different charge transfer behaviour for different support materials can also be used to explain the observed variations in $\Delta G_{\mathrm{H_{ads}}}$. Indeed, Figure 4.8 shows a distinct linear relation between the amount of charge transfer between MoS_2 and support and the $\Delta G_{\mathrm{H_{ads}}}$ value. This relation shows that, compared to pristine graphene, supports that donate negative charge to MoS_2 tend to weaken the subsequent binding of H and those that withdraw negative charge can strengthen it. Pristine graphene sits near the middle of the supports tested here, donating 0.03 electrons per Mo atom. The existence of this relation could be readily used to screen across candidate support materials for MoS_2, or perhaps even other transition metal dichalcogenides[b] that have the same structure, relying on only an optimisation and electronic structure calculation of the clean system. Furthermore, it could be used to suggest modifications to supports in terms of the charge donating or withdrawing character for MoS_2/support systems that have a $\Delta G_{\mathrm{H_{ads}}}$ value that is already close to 0 eV.

The relation between support-catalyst charge transfer and $\Delta G_{\mathrm{H_{ads}}}$ can be rationalised qualitatively by inspection of charge density difference plots showing MoS_2/support structures before and after H adsorption. In Figure 4.9, the charge movement in response to H adsorption is shown for two supports which are at the extreme ends of the aforementioned relation: NDG-graphitic (8% coverage) and GO-epoxide (15% coverage). Pristine graphene, which sits nearer the middle of Figure 4.8 is also included. In all materials, the pattern of charge movement is similar to that which was observed previously in Figure 4.7. However the amount of charge movement is substantially more pronounced

[b] This is the general name for MX_2 structures that form the same octahedral arrangement of atoms that is observed for MoS_2.

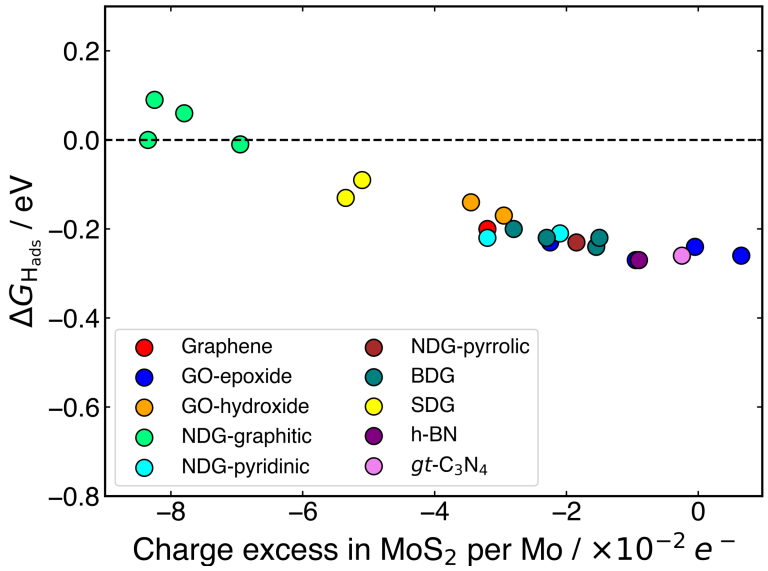

Figure 4.8: Relation of the charge transferred to MoS_2 from different support materials (determined by Bader analysis) and the $\Delta G_{H_{ads}}$ on the edge of MoS_2. A distinct linear relation is observed, where supports that transfer more negative charge weaken the binding of H on the catalyst.

for the GO-epoxide support, which does not donate as much charge to the MoS_2, and it is somewhat reduced for the NDG support which donates the most negative charge to MoS_2. We propose that, because the GO-epoxide support does not donate negative charge to the MoS_2, the catalyst is better able to accommodate the fairly long-range charge displacement that is associated with H adsorbing on the MoS_2 edge, and this strengthens the H binding. In contrast, for the NDG-graphitic support which donates the highest amount of negative charge to MoS_2 out of any of the support materials tested here, the H adsorption energy is less favourable as negative charge cannot be as easily distributed into the MoS_2.

4.3.4 Extending H adsorption studies to more realistic systems

In the previous sections the tuning of $\Delta G_{H_{ads}}$ is reported at only the S adsorption site and studying a single MoS_2 model. While this is the first step in determining catalyst behaviour and tuning properties, it does not take into account the possibility of H

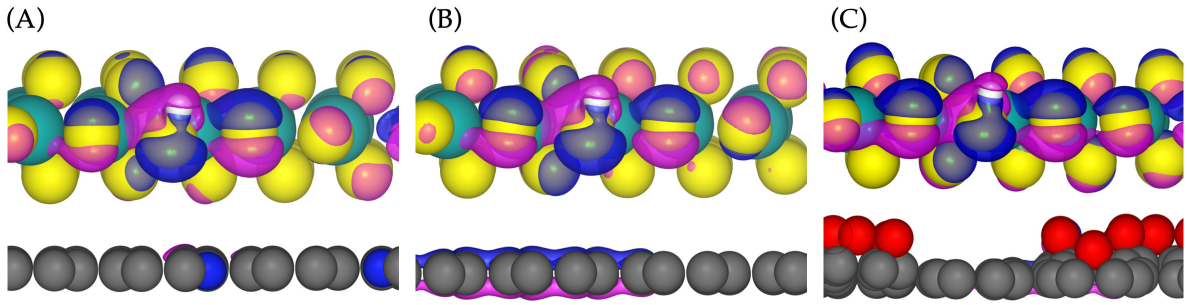

Figure 4.9: Charge density difference plots showing the movement of charge in MoS_2 after H is adsorbed to edge models that are supported by: (A) NDG-graphitic 8% coverage, (B) pristine graphene, (C) GO-epoxide 15% coverage. Blue indicates negative charge accumulation and pink indicates negative charge depletion. Isosurface level = 0.006 e^- / Å^3.

adsorbing to an Mo atom instead, or the case of defects being present on as-synthesised MoS_2.[224] These cases are also very important to consider, especially in light of the results discussed in Chapter 3, which suggested more than just the S site would be involved in both the Tafel and Heyrovský combination of H on MoS_2. Thus, we extend the current analysis here to look at Mo adsorption sites and S vacancy defect sites on both the basal plane and edges. Unfortunately, a full scale study of these sites was not feasible in the current project, but it is a topic of ongoing work in the group. Instead, two supports are chosen for each of the above cases: (1) the pristine graphene support and (2) the support which induces the largest effect on $\Delta G_{H_{ads}}$ (BDG 12% for the basal plane and NDG-graphitic 16% for the edge). These results are presented in Table 4.3. From these data it is clear that the support tuning effects are similar regardless of whether H is adsorbed to a S or Mo atom. For the models without any defects, a BDG 12% support lowers $\Delta G_{H_{ads}}$ on the basal plane by around 0.7 to 0.8 eV relative to pristine graphene for both the Mo and S adsorption sites. On the edge models, the NDG-graphitic 16% support raises $\Delta G_{H_{ads}}$ by around 0.2 eV for both adsorption sites.

If S vacancy defects are introduced to the model, $\Delta G_{H_{ads}}$ drops notably on the basal plane, and this is most significant when H is adsorbed to an Mo atom. Again, in terms of the support tuning, the BDG 12% support lowers $\Delta G_{H_{ads}}$ in both cases. However, the magnitude of this tuning is somewhat reduced compared to pristine MoS_2 models. Overall the data suggests that the tuning effects of supports are not unique to one type of MoS_2

Table 4.3: $\Delta G_{H_{ads}}$ (eV) values for the S and Mo adsorption sites on a selection of supported MoS_2 systems. $\Delta G_{H_{ads}}$ values for basal plane models with an S vacancy defect are also included, where H is adsorbed to S or Mo atoms directly adjacent to the vacancy.

	Pristine basal plane		Basal plane S-vacancy		Edge	
System	S site	Mo site	S site	Mo site	S site	Mo site
Pristine graphene	2.14	2.70	1.64	0.16	-0.20	0.92
BDG 12%	1.44	1.84	1.34	-0.03	—	—
NDG-graphitic 16%	—	—	—	—	0.00	1.17

structure or adsorption site, and could be used in conjunction with defect engineering, which produces very favourable $\Delta G_{H_{ads}}$ values on the basal plane specifically. Indeed, the MoS_2 basal plane with an S vacancy and a BDG support could be a promising candidate to take forward into further testing with a $\Delta G_{H_{ads}}$ on Mo of only -0.03 eV.

Finally, it is worth noting that, under realistic experimental conditions, the NDG-graphitic support for MoS_2, found here to produce promising $\Delta G_{H_{ads}}$ values (close to zero) on the Mo-edge, would be unlikely to exist with purely graphitic N doping. While experimental evidence suggests graphitic N are the most stable and would dominate,[203] some pyridinic and pyrrolic N may also be present. Thus, to simulate a realistic NDG supported MoS_2 edge system, the 16% NDG-graphitic support model was modified to include two pyridinic N centres and one pyrrolic N centre. $\Delta G_{H_{ads}}$ on the MoS_2 edge above this realistic mixed NDG support was found to be 0.02 eV, suggesting that the promising H adsorption behaviour for the NDG-graphitic support is robust to relatively small but synthetically relevant changes to N doping.

4.4 Future work

The promising trends and tuning observed in this chapter raise a number of interesting directions for future work. Perhaps the most obvious extension is to perform mechanistic modelling and activation barrier calculations on the promising MoS_2-edge model with a graphitic NDG support that yielded thermoneutral H adsorption. While the H adsorption energy on S was found to determine a great deal about the reactivity of a catalyst

in Chapter 3, recall that transferring H_{ads} onto the neighbouring Mo atom was still a critical step in both Tafel and Heyrovský combination. Mapping out the full reaction mechanisms, where diffusion to this Mo is considered, would allow us greater confidence in our prediction of high activity. Furthermore, with an appropriate model for applied potential, the activity could be simulated across a range of electrochemically relevant potentials.

In a different avenue of exploration, the high degree of impact that exchanging the support materials below MoS_2 has on its electronic structure prompted us to examine other methods that can induce similar electronic effects. A current project in our research group is focussing on using twistronics to modify the electronic structure, and thus $\Delta G_{H_{ads}}$ on the MoS_2 basal plane. The idea behind twistronics is that, by modifying the relative twist angle between two sheets of a 2D catalyst (or a catalyst and a support), one can perturb the electronic structure in both materials. This has previously been demonstrated with two stacked MoS_2 sheets and a MoS_2/graphene system,[225] where the band gap of MoS_2 could be tuned by altering the relative twist between the lattices. Given the relevance of the S p-state energy shown in the present chapter, we wish to extend the twistronics phenomenon to see if it can be used to tune $\Delta G_{H_{ads}}$ without even having to exchange a support.

Lastly, because the supports tested here were unable to drive $\Delta G_{H_{ads}}$ on the basal plane of MoS_2 particularly close to thermoneutral, it would be interesting to study other ways in which this could be achieved. This is particularly important, given that the basal plane makes up a large portion of the surface area of MoS_2. The question of how to improve H adsorption to the MoS_2 basal plane is the focus of Chapter 5, and will be addressed in detail therein.

4.5 Conclusions

This chapter represents the first systematic study of how carbon-based supports are able to tune the H adsorption energy on both MoS_2 basal planes and edges. For the basal plane, two configurations of H binding on S are located: a directly on-top geometry and a

tilted geometry. The H adsorption energies for tilted binding are generally high (around 2.0 eV) and are unaffected by the support. In contrast, the energy for on-top H binding can be modified in the range of 2.2 to 1.4 eV with different supports. For the MoS_2 edge, the carbon supports have a more modest effect on the H adsorption energy, but are able to alter it in the range of 0.09 to -0.27 eV. Critically, we found that a graphitic N doped graphene support produced a H adsorption energy on the MoS_2 edge of exactly 0 eV – the ideal thermoneutral value – making this synthetically accessible support a promising candidate for experimental testing. This thermoneutral adsorption energy did not shift significantly when a number of graphitic N were replaced with other types of N doping, suggesting that realistic as-synthesized N doped graphene supports could be used. Additionally, a S doped graphene support under MoS_2 was also found to produce activity close to that of N doped graphene, highlighting the benefits of screening a wide variety of supports.

The observed variations in the H adsorption energy for both the basal plane and the edges of MoS_2 with different carbon supports were also rationalised here. For the basal plane, a relation between the energy of the valence p-orbitals in MoS_2 and the on-top H adsorption energy was observed. This was attributed to the fact that higher energy p-states required less energy to transfer electrons into the conduction band of the support, a process which we find takes place in response to on-top (but not tilted) H binding. For the MoS_2 edges, the H adsorption energy was found to closely and linearly relate to the amount of negative charge each support transferred to the MoS_2 when the two materials adhered together. The greater the negative charge transferred to the MoS_2, the weaker the subsequent H binding, as the catalyst was less able to accommodate the movement of charge that takes place when H adsorbs to the edge.

Overall, the existence of trends in the H adsorption energy on both the basal plane and the edges of MoS_2 with different carbon supports allow a much deeper understanding of the role of the catalyst support. These trends can be used to screen across new candidate catalyst supports, and even direct the rational improvement of currently existing support materials.

Chapter 5

Hydrogen evolution on MoS_2 nanotubes

In the previous chapter it was shown that the MoS_2 edges can be successfully tuned to have thermoneutral H adsorption using catalyst supports. However, the range of H adsorption free energies ($\Delta G_{H_{ads}}$) induced on the MoS_2 basal plane did not come particularly close to 0 eV. Because the basal plane portion of the catalyst makes up the majority of its area, it would still be desirable to activate this section for hydrogen evolution as well. Therefore, in the present chapter we use a different structural analogue of MoS_2 – a nanotube form – in order to examine if the strain induced by curvature is able to improve the hydrogen evolution thermodynamics across the basal plane.

Here, we model armchair and zigzag MoS_2 nanotubes ranging from 12 to 22 Å in diameter. The hydrogen evolution reaction (HER) on MoS_2 nanotubes has never before been studied computationally, so we first examine what H adsorption sites are favoured and report $\Delta G_{H_{ads}}$ values as a function of nanotube diameter. We find that $\Delta G_{H_{ads}}$ can be related to the amount of strain due to curvature in the nanotube, with smaller, more highly strained, nanotubes adsorbing H more strongly. Additionally, we relate the size-dependent electronic structure changes in the nanotubes directly to the effect they have on $\Delta G_{H_{ads}}$ using density of states analyses. Lastly, because defect sites are common in the nanotube structures of MoS_2, we study how the presence of an S-vacancy defect on the nanotube surface affects $\Delta G_{H_{ads}}$.

The work reported in this chapter is also the topic of a recently accepted paper: Ruffman, C., Gilmour, J. T. A, Garden A. L., "Size-dependent trends in the hydrogen evolution activity and electronic structure of MoS_2 nanotubes," *Nanoscale Advances*, **2021**, *accepted*. In this paper, Dr James Gilmour assisted with the density of states analyses, including helping to find trends between electronic structure features and $\Delta G_{H_{ads}}$.

5.1 Introduction

As has previously been discussed, a large contributor to the poor HER activity on the MoS_2 basal plane is that the reaction thermodynamics are highly unfavourable, with the surface binding H very weakly.[5] $\Delta G_{H_{ads}}$ on the pristine basal plane of MoS_2 is found to be around 2.20 eV,[199] which indicates a very unfavourable adsorption. In Chapter 4 it was shown that $\Delta G_{H_{ads}}$ on the basal plane could be brought somewhat closer to the desired thermoneutral value of 0 eV by the addition of conducting carbon-based supports.[199] However, even the most promising supports still produced $\Delta G_{H_{ads}}$ values that were above 1.4 eV, indicating H would still be unlikely to adsorb favourably. It is also possible to improve $\Delta G_{H_{ads}}$ on the basal plane by doping with heteroatoms,[221,222] creation of S-vacancy defects,[223] or laterally straining the MoS_2 sheet.[226]

In terms of experimental work, Shi *et al.*[221] have shown that the HER activity of the basal plane can be improved by uniformly doping pristine MoS_2 with Zn atoms, which replace certain Mo. This more than triples the turnover frequency to hydrogen from 3.83 s^{-1} to 15.4 s^{-1}. A small degree of improvement is also seen when doping with Cu atoms, but Ni, Fe and Co were found to offer no promotion of the catalyst. Computationally, Gao *et al.*[226] have shown that doping MoS_2 with Rh, Pd or Ag can bring $\Delta G_{H_{ads}}$ on the basal plane within 0.2 to 0.4 eV from thermoneutral. The authors were able to further improvement by applying precise lateral strains to the MoS_2 sheet. It was also shown in Chapter 4 that a B-doped graphene support in conjunction with the creation of an S-vacancy defect yielded an H adsorption energy close to thermoneutral. Thus, there are several promising techniques for activating the basal plane, specifically when two or more techniques can be used in conjunction with each other.[226] However, these process can also

be highly synthetically complex, require precision, and could affect the long-term stability of the catalyst. Furthermore, the literature is sparse on examples of *systematic* tuning of $\Delta G_{H_{ads}}$ where an easily controllable parameter can be modified to produce the desired activity.

An alternative way to activate the basal plane would be to use a structural form of MoS_2 that has an innately lower $\Delta G_{H_{ads}}$ and therefore higher intrinsic activity. Perhaps the most well known of these is 1T-MoS_2, where an artificially induced phase-transition causes a shift to metallic behaviour on the basal plane.[62,227] However, recently, several experimental studies have reported high HER activity from nanotube structures formed out of single-layer MoS_2,[228–230] where the catalyst is coiled up, analogous to how carbon nanotubes are formed by rolling graphene. The nanotube form of MoS_2 is relatively easy to synthesise, either with a single wall, multiple walls, or with a different core material.[231,232]

The enhanced catalytic activity of the nanotubes compared to flat structures suggests that the strain placed on the basal plane by rolling it into a tube may somehow activate it to adsorbing H. This is reasonable to expect, as Shi *et al.*[233] have previously shown that mechanical bending of flat forms of MoS_2 can strengthen the H adsorption energy. Furthermore, the electronic structure in MoS_2 nanotubes is known to change compared to flat structures, showing smaller band gaps[234,235] and enhanced charge carrier mobility,[236] both of which are features that are associated with catalytic activity.[199] Specifically, in light of the relation between the energy of the S p-states and $\Delta G_{H_{ads}}$ reported in Chapter 4, modifications to the band gap in MoS_2 nanotubes are very likely to have an effect on the catalytic activity. Very recently, Cardoso *et al.*[237] were able to show that electronic structure changes in nanotubes of alternative dichalcogenides, WS_2 and WSe_2, were responsible for improved H adsorption energies, and thus better HER performance. As a result, it is of great interest to understand how the electronic structure in MoS_2 nanotubes differs from that of the flat basal plane, and whether this can be related to HER performance.

In addition to simply being different from the flat basal plane, it has long been established that the surface and electronic properties of MoS_2 nanotubes are also highly size dependent. Seifert *et al.*[238] show that the strain energy of MoS_2 nanotubes between

8 and 26 Å in diameter increases notably as the tubes get smaller. At the same time, the smaller nanotubes begin to behave more like conducting materials instead of semiconductors. More recently, Ansari *et al.*[239] reported a near-linear decrease in the band gap of MoS_2 nanotubes as the diameter reduced. If this relation is extrapolated, the band gap would approach 0 eV (i.e. conducting) at around 10 Å in diameter. In studying charge carrier mobility, Xiao *et al.*[236] report notable differences between the electron and hole mobility for two different ways of coiling MoS_2 nanotubes: armchair and zigzag. The authors also find that the carrier mobility changes notably with the size of the nanotube. Given that altered electronic conductivity and a reduction of the band gap are critical to HER catalysis,[199] in the present work we also study how the H adsorption free energy shifts between different sized nanotubes, for both armchair and zigzag structures. Any observed effects on $\Delta G_{\mathrm{H_{ads}}}$ can then be linked to changes in the underlying electronic structure.

Lastly, in this work we also look at S-vacancy defect sites both on the flat basal plane and on MoS_2 nanotubes. Multiple high-resolution transmission electron microscopy studies have suggested that S-vacancy defects are common in the basal plane of MoS_2,[240] with site densities of up to 10^{13} per cm^2.[241] Density functional theory (DFT) studies also confirm the likelihood of S-vacancies in the basal plane,[171,195,223] finding that they have an effect on both the electronic properties of the basal plane and significantly lower the H adsorption energy.[171,222] Previous reports on defects in MoS_2 nanotubes report S-vacancies form readily,[242] and modify the mechanical[243] and electronic or magnetic properties,[242] but the H adsorption energy has yet to be explored.

In this chapter, calculations of $\Delta G_{\mathrm{H_{ads}}}$ on MoS_2 nanotubes are used to explore the activation of the basal plane by reducing the thermodynamic cost of adsorbing or desorbing H. Armchair and zigzag nanotubes of diameters varying from 12 to 22 Å are studied, and both pristine and S-vacancy defect sites are considered. We find a reliable tendency for H adsorption to become more favourable as nanotube diameter decreases, regardless of adsorption site. Density of states calculations are used to rationalise this trend in terms of the energetic position of the S p-states and Mo d-states involved in bonding H.

5.2 Methodology

5.2.1 Structure models

The flat basal plane of MoS_2 was simulated using a single-layer slab, periodic in two dimensions, with an explicit unit cell measuring 5×5 Mo atoms (a = 3.18 Å). At least 12 Å of vacuum separation was ensured between repeats in the non-periodic direction, perpendicular to the basal plane.

To form MoS_2 nanotubes, an extended sheet of flat single-layer MoS_2 was coiled about a chiral vector, $\overrightarrow{Ch}$, as seen in Figure 5.1A. In this case, the shaded region makes up the atoms in the nanotube, and the two dark grey ends will meet when coiled. $\overrightarrow{Ch}$ runs along the circumference of the coiled nanotube. The length and direction of $\overrightarrow{Ch}$ comes from the sum of two vectors, $\overrightarrow{n}$ and $\overrightarrow{m}$ which are at 60° to each other. Coiled nanotubes are described by the length of their $\overrightarrow{n}$ and $\overrightarrow{m}$ vectors in terms of the number of primitive cell repeats, ($\overrightarrow{n}$, $\overrightarrow{m}$). The example in Figure 5.1A is a (3, 3) tube, which is smaller than is realistic and is included for illustration purposes only. Armchair nanotubes are defined by $\overrightarrow{n}$ and $\overrightarrow{m}$ having the same length, whereas for zigzag nanotubes the $\overrightarrow{m}$ vector is always zero and $\overrightarrow{n}$ can have any value. Examples of realistic coiled armchair and zigzag nanotubes are also given in Figure 5.1B to E.

In a computational representation of the nanotubes, there is one periodic direction along the length of the tube and there are two non-periodic directions. The explicitly simulated repeating cell in the periodic direction was 4 units long, as shown in Figure 5.1C and E. At least 12 Å of vacuum spacing was ensured in the non-periodic directions either side of the nanotube.

In this work, the following armchair nanotubes were explored: (8, 8), (9, 9), (10, 10), (11, 11), (12, 12), (13, 13), and (14, 14). The zigzag nanotubes studied were: (14, 0), (15, 0), (17, 0), (19, 0), (20, 0), (22, 0) and (24, 0). These sizes were chosen such that both armchair and zigzag nanotubes had a similar range of internal diameters. The largest of these nanotubes has 112 Mo atoms and 224 S atoms, which represents close to the upper limit of what could be feasibly computed within the time-frame of this work.

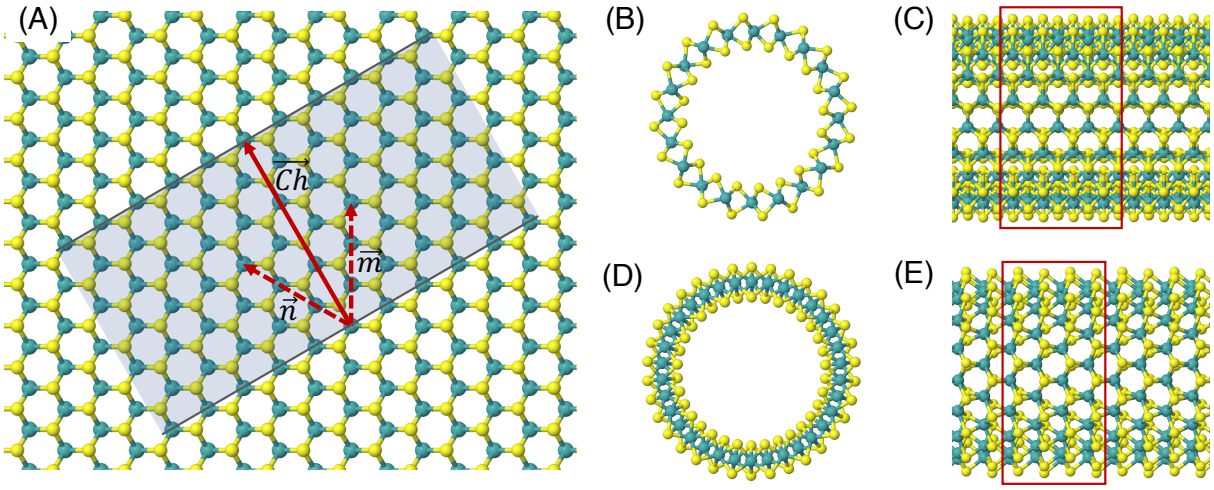

Figure 5.1: (A) A schematic showing how MoS_2 nanotubes are related to the flat basal plane. The shaded area indicates the nanotube that could be rolled along chiral vector, $\overrightarrow{Ch}$, so that the two darker edges meet. The sum of the $\vec{n}$ and $\vec{m}$ vectors define the length and direction of $\overrightarrow{Ch}$, here giving a (3, 3) armchair nanotube. The (B) end-on and (C) side views of a (10, 10) armchair nanotube. The (D) end-on and (E) side views of a (17, 0) zigzag nanotube. Note that these two examples both have approximately the same internal diameter. The red boxes give and indication of the unit cell in the periodic direction, but the heights of these boxes are not to scale.

5.2.2 Computational details

The DFT calculations reported in this chapter were all conducted using the same general methodology that is reported in Chapter 2. For flat basal plane models, reciprocal space was sampled using $4 \times 4 \times 1$ Monkhorst-Pack k-point scheme. For nanotubes, where only one dimension is periodic, a $4 \times 1 \times 1$ scheme was used instead.

The strain on nanotube models due to their curvature, ΔE_{strain}, was calculated per Mo atom relative to a flat surface of the same size, following established methodology:[244]

$$\Delta E_{\text{strain}} = \frac{E_{\text{tube}} - E_{\text{flat}}}{n_{\text{Mo}}} \tag{5.1}$$

where E_{tube} is the electronic energy of the pristine nanotube, E_{tube} is the energy of an equivalent flat MoS_2 surface, and n_{Mo} is the number of Mo atoms in the model.

In terms of converting electronic H adsorption energies to free energies, the value of the $[\Delta(\text{ZPE}) - T\Delta S]$ contribution in Equation 2.39 (see Chapter 2) was tested across

multiple different adsorption sites. On the flat basal plane, this term was found to be consistently around 0.23 eV regardless of the site H adsorbed to. On the MoS_2 nanotubes, the value was slightly higher at 0.25 eV, and it did not depend on nanotube size. For adsorbing H to S-vacancy sites, $[\Delta(\text{ZPE}) - T\Delta S]$ was lower at 0.21 eV on both the basal plane and nanotubes.

5.3 Results and discussion

5.3.1 Pristine MoS_2 nanotubes

The optimised values for the lattice constant (in the periodic direction along the axis of the nanotube) and the diameter of the different armchair and zigzag nanotubes tested here are presented in Table 5.1. For all the armchair nanotubes, the lattice constant is very slightly longer than that for the extended basal plane of MoS_2. In contrast, for the zigzag nanotubes, the lattice constant is shorter. These patterns are consistent with past results.[235] When moving to larger sizes, the lattice constant for both types of nanotube appears to trend in the direction of the bulk value.

In terms of the nanotube internal diameters, a reasonable range is able to be simulated for both armchair and zigzag nanotubes, spanning in total from 11.91 Å to 21.88 Å. While most of the sizes reported here are smaller than those that are typically observed in experiment,[232] the largest of the MoS_2 nanotubes crosses over with the size of some of the smaller cases observed experimentally.[67] The diameter range we report is similar to that of other DFT works.[236,238]

The strain energy due to curvature (calculated *via* Equation 5.1) is also presented in Table 5.1. There is a consistent trend for strain to increase as the nanotube diameter, d, gets smaller (Figure 5.2). The strain appears to follow a a non-linear $\frac{1}{d^2}$ relation with nanotube diameter, which was originally reported by Seifert *et al.*[238] Some of the smallest nanotubes studied here can be considered highly strained, with an energy difference of 0.73 eV per Mo atom compared to the flat surface.

Table 5.1: Optimised geometric parameters of the pristine nanotubes studied in the present work. The lattice constant is measured in the periodic direction along the axis of the nanotube, and the diameter is measured internally from two S atoms on the inside of the tube. Also shown is the strain energy per Mo atom for the nanotube relative to a flat surface of the same size, ΔE_{strain}, and the free energy of H adsorption, $\Delta G_{\text{H}_{\text{ads}}}$, at both an S and Mo site on the outside of the nanotubes.

System ($\overrightarrow{n}$, $\overrightarrow{m}$)	Lattice constant / Å	Diameter / Å	ΔE_{strain} per Mo / eV	$\Delta G_{\text{H}_{\text{ads}}}$ S / eV	$\Delta G_{\text{H}_{\text{ads}}}$ Mo / eV
Basal plane	3.18	—	—	2.24	2.79
Armchair					
(8, 8)	3.21	11.91	0.73	1.39	1.55
(9, 9)	3.21	13.56	0.59	1.51	1.70
(10, 10)	3.21	15.16	0.49	1.60	1.83
(11, 11)	3.20	16.75	0.41	1.67	1.91
(12, 12)	3.20	18.60	0.34	1.74	2.01
(13, 13)	3.20	20.36	0.30	1.79	2.11
(14, 14)	3.20	22.08	0.26	1.82	2.13
Zigzag					
(14, 0)	3.14	12.26	0.69	1.44	1.52
(15, 0)	3.14	13.16	0.61	1.52	1.67
(17, 0)	3.16	15.00	0.49	1.60	1.80
(19, 0)	3.16	16.96	0.40	1.70	1.88
(20, 0)	3.17	17.91	0.36	1.72	1.90
(22, 0)	3.17	19.97	0.30	1.79	2.06
(24, 0)	3.17	21.88	0.26	1.82	2.06

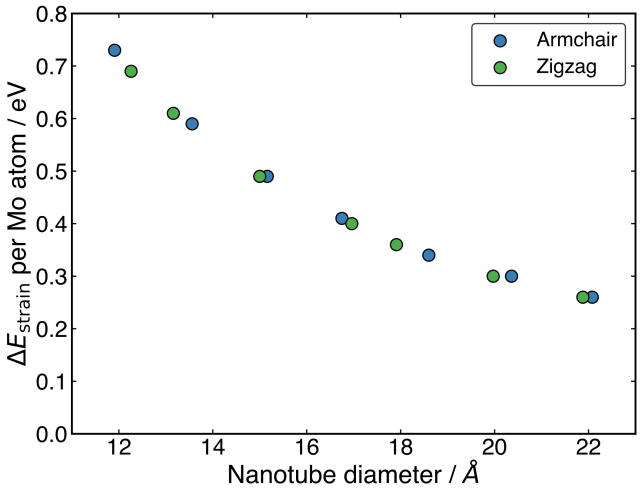

Figure 5.2: The strain energy per Mo atom of armchair and zigzag MoS_2 nanotubes of different diameters.

On the MoS_2 basal plane, three stable H adsorption sites are located: directly on-top of an S atom (Figure 5.3A, $\Delta G_{H_{ads}} = 2.24$ eV), in a tilted configuration on an S atom at approximately 40° from the upright (Figure 5.3B, $\Delta G_{H_{ads}} = 2.04$ eV), and directly on an Mo atom ($\Delta G_{H_{ads}} = 2.79$ eV). Note that these configurations are identical to those discussed in Chapter 4, although the Mo site was not considered in depth there. Each of these three H adsorption sites were tested on the MoS_2 nanotubes. However, the tilted H configuration could not be located on nanotubes of any size tested here, despite it being preferable on the flat MoS_2 basal plane - a feature which is consistent with past work.[206] Locating the titled geometry was also difficult in the work in Chapter 4 on flat MoS_2 also, where certain supports beneath the catalyst prevented it being found.[199] It is suggested that this tilted configuration is highly sensitive to perturbations of the MoS_2, and thus we proceed only with the stably located S on-top and Mo sites for the nanotubes.

Unlike the flat basal plane which has symmetric faces, the sites inside and outside of the MoS_2 nanotubes are non-equivalent. To compare inside and outside H adsorption, three sizes for each of armchair and zigzag nanotubes were chosen as a representation of different diameters: (8, 8), (11, 11) and (14, 14) for armchair, and (14, 0), (19, 0) and (24, 0) for zigzag. The raw electronic adsorption energies for the inside and outside sites on these structures are presented in Table 5.2. The overall trends indicated a strong and

reliable preference for H adsorption on the outside of the nanotube as opposed to the inside, by on average 0.30 eV for S sites and 0.85 eV on Mo sites. The geometries of these favourable outside binding sites are pictured for an armchair nanotube in Figure 5.3 at the S site (C and D) and the Mo site (E and F).

Table 5.2: Electronic H adsorption energies, $\Delta E_{\mathrm{H_{ads}}}$, compared between the inside and outside of MoS_2 armchair and zigzag nanotubes of three different sizes.

System	$\Delta E_{\mathrm{H_{ads}}}$ S		$\Delta E_{\mathrm{H_{ads}}}$ Mo	
$(\overrightarrow{n}, \overrightarrow{m})$	Outside	Inside	Outside	Inside
Armchair				
(8, 8)	1.13	1.48	1.31	2.40
(11, 11)	1.41	1.71	1.67	2.50
(14, 14)	1.56	1.81	1.89	2.53
Zigzag				
(14, 0)	1.18	1.51	1.28	2.33
(19, 0)	1.44	1.73	1.64	2.51
(24, 0)	1.56	1.81	1.82	2.59

One possible reason for the preference to adsorb on the nanotube outside is a small but consistent charge disparity between the S atoms on the outside of the tube and those on the inside. Bader charge analyses of these centres in (8, 8) armchair MoS_2 indicated the average net charge on the outside S atoms was $-0.68e^-$, and for the inside S atoms was $-0.57e^-$. This is in contrast to the flat basal plane, where the average Bader charge on the S atoms lies somewhere between these two values, at 0.61 e^-. A similar pattern was observed for larger nanotubes and also the zigzag nanotubes. Plots showing the charge localisation trend across multiple sizes are available in Appendix C.1. Considering the fairly large number of atoms this charge differential is distributed over, it indicates a reliable preference for electron density to be on the outside of the nanotube. It is possible this can be rationalised through classical charge repulsion arguments which would indicate that e^- with more room to move on the outside of the circumference of the nanotube are more energetically favourable.

The $\Delta G_{\mathrm{H_{ads}}}$ values for the favourable S and Mo sites on the outside of all nanotubes studied here are presented in Table 5.1, and these values are plotted against the nanotube

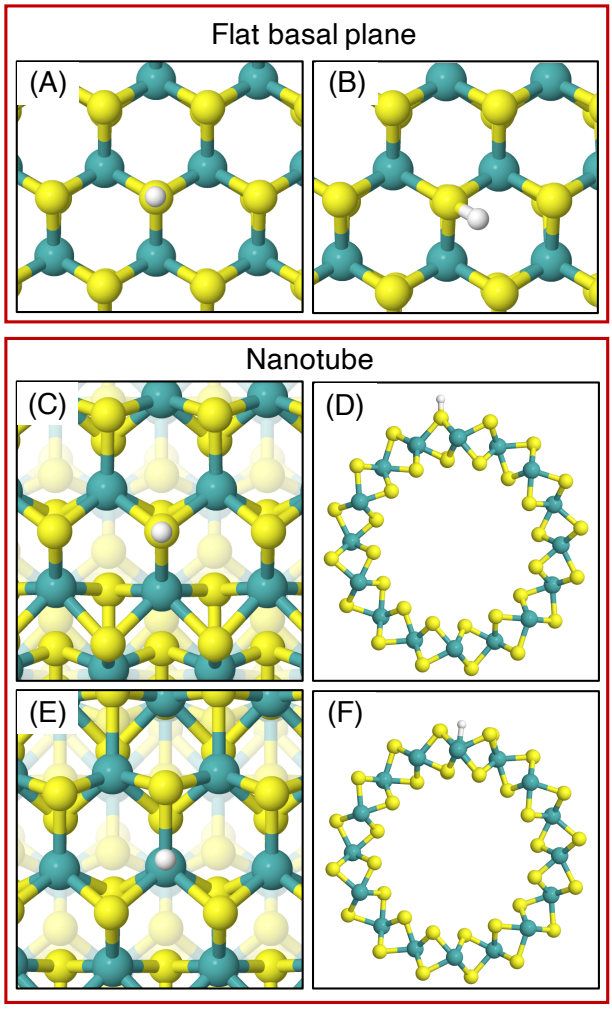

Figure 5.3: Favourable adsorption site geometries on the basal plane and on the outside of an armchair nanotube. (A) shows the on-top S site and (B) shows the tilted S site, both on the basal plane. (C) and (D) show top and side views of H adsorption to an outside S on the armchair nanotube, and (E) and (F) show the same for Mo adsorption. These geometries are also representative for H adsorption on the zigzag nanotubes.

diameter in Figure 5.4A. There is a clear preference for the S site over the Mo at the largest nanotube sizes – by 0.31 eV on the armchair nanotubes and 0.24 eV on the zigzag nanotubes. However, this difference in energy drops to only 0.16 eV and 0.08 eV (on armchair and zigzag, respectively) at the smallest sizes. This is clearly clearly observed in Figure 5.4A, in the region around 12 Å in diameter. For all nanotubes, this difference is significantly smaller than the 0.55 eV gap between Mo and S sites on the flat basal plane, suggesting that these two sites are far more competitive on nanotubes, especially those with small diameters. This may have mechanistic ramifications, as H diffusion to an Mo atom was implicated as an important step in the HER on MoS_2 edge structures in Chapter 3,[143,166] though this has not currently been explored on the basal plane of MoS_2.[245]

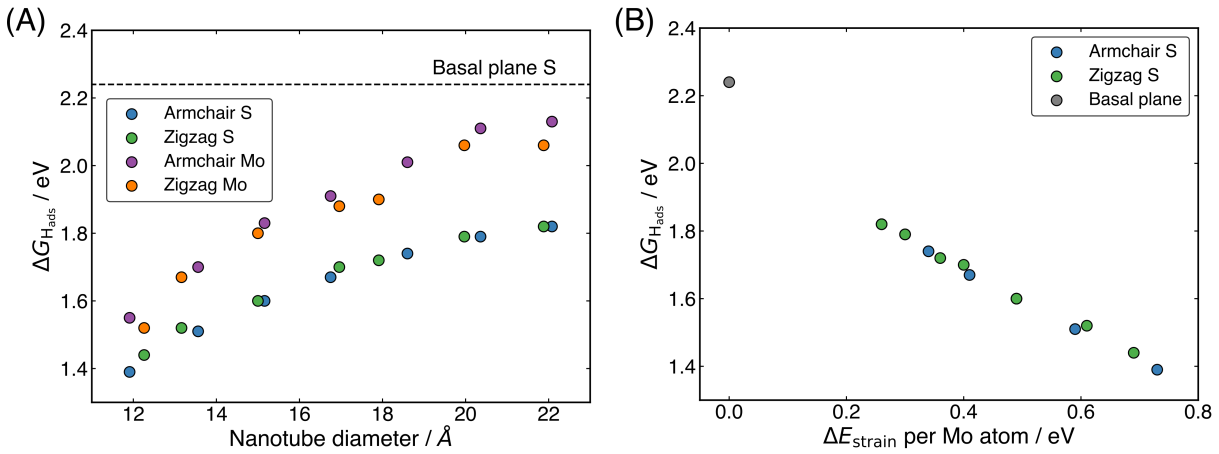

Figure 5.4: (A) The hydrogen adsorption free energy, $\Delta G_{H_{ads}}$, as a function of diameter for both armchair and zigzag nanotubes. (B) The linear relation between strain energy, ΔE_{strain}, and $\Delta G_{H_{ads}}$. Note that it may appear there are fewer armchair nanotube data points than zigzag, but this is because several values fall in exactly the same place on the plot. For both plots, $\Delta G_{H_{ads}}$ on the flat basal plane S site is also shown for comparison.

Examining how $\Delta G_{H_{ads}}$ changes with the diameter of different nanotubes, there is a clear trend for H adsorption to become more favourable as the nanotubes get smaller (Figure 5.4A). Interestingly, no notable difference in $\Delta G_{H_{ads}}$ between armchair and zigzag nanotube structures is observed, other than that induced by their slightly different diameters. This suggests that the local electronic and geometric structure around the H adsorption site is the same for both classes of nanotube. The most favourable adsorption

energy found here is 1.39 eV, reported at an S atom site on the (8, 8) armchair nanotube with a diameter of slightly less than 12 Å. This is significantly lower than the 2.24 eV adsorption energy on the flat basal plane of MoS_2, suggesting the nanotubes would have enhanced HER activity. However, $\Delta G_{H_{ads}}$ is still significantly higher than thermodynamically ideal, and it is similar to the best (B-doped graphene) supported system from Chapter 4.

The enhanced catalytic activity in nanotubes can be partly explained by smaller nanotubes having higher strain energies. In Figure 5.4B, it can be seen that the $\Delta G_{H_{ads}}$ relates very closely to ΔE_{strain}. This linear relation may be highly useful for predicting $\Delta G_{H_{ads}}$ values on different sized nanotubes, or even curved MoS_2 surfaces. However, while it makes sense intuitively that higher strained materials may bind H stronger, it remains unclear what electronic and bonding factors underpin this behaviour. This point will be revisited and addressed in Section 5.3.3.

One interesting question is to what extent the relation between $\Delta G_{H_{ads}}$ and nanotube diameter or strain can be extrapolated. For instance, it is possible that $\Delta G_{H_{ads}}$ values closer to 0 eV could be reached going to nanotubes smaller than 12 Å in diameter, corresponding to higher strain energies. When this idea was tested here, it was found these nanotubes were highly unstable, and tended to distort and break apart when H was adsorbed to the system. The breaking apart of the nanotubes is not overly surprising, given these particularly small systems are under relatively high strain (0.73 eV per Mo atom). This suggests that 12 Å diameters may pose a lower limit on the size of single-walled MoS_2 nanotubes, for surface catalysis applications at least. Looking at the larger sizes of nanotubes, it is possible that the relation could be extrapolated to a nanotube of infinite diameter, which should in theory match the $\Delta G_{H_{ads}}$ of the basal plane. However, without additional testing of H adsorption on nanotubes larger than the maximum size reported here, making this extrapolation is difficult as it is unclear whether the relation between diameter and $\Delta G_{H_{ads}}$ is linear in nature or curvilinear (in which case it may asymptote). Unfortunately, larger sizes were outside the scope of the DFT calculations able to be performed here. Though, it is possible future work could be done using a

limited selection of larger nanotubes or models that had fewer repeats in the periodic direction of the tube.

5.3.2 S-vacancy defects in MoS_2 nanotubes

Given that even the smallest MoS_2 nanotubes obtainable here still produced $\Delta G_{H_{ads}}$ values that were much higher than the desired thermoneutral 0 eV, this alone was unlikely to be able to explain the experimentally observed enhanced catalytic activity of the nanotubes relative to the basal plane.[229,246,247] Therefore, nanotubes with S-vacancy defects were also investigated. As raised in the Introduction, studies exist on defects in MoS_2 nanotubes modifying the mechanical[243] and magnetic properties,[242] thus they may also have an effect on the H adsorption energy. Here, single S-vacancies are studied where one S atom is removed from the outside of the nanotube. This was done for each of the sizes of pristine nanotube tested in the previous section. No notable structural distortion was observed on relaxation after a defect had been created.

The different H adsorption sites available at the S-vacancy were then investigated. On the flat basal plane with an S-vacancy the most favourable adsorption site was found to be at the centre of three Mo atoms directly below where the S had been removed (Figure 5.5A), which is consistent with past work.[171] This position was at least 0.5 eV more favourable than when H was situated on the S atoms surrounding the defect. If H was positioned directly on-top of one of the Mo atoms at the S-vacancy, it always relaxed such that it was centred between all three Mo. Interestingly, this was not the most favourable site on the defective MoS_2 nanotubes – where H instead preferred to adsorb at a bridged position between two of the Mo atoms underneath the S-vacancy for both armchair and zigzag nanotubes (Figure 5.5B and C). The different adsorption site preference for nanotubes is likely the result of inequivalent Mo atoms in the triangle below the S-vacancy defect. Because of the strain induced by coiling into a tube, two sides of the triangle of Mo atoms have longer bond lengths than the other. In the (8, 8) armchair nanotube the long Mo-Mo bonds are 3.47 Å and the short bond is 3.15 Å. For the (14, 0) zigzag nanotube, there is one long bond of 3.53 Å and two short bonds of 3.23 Å. H

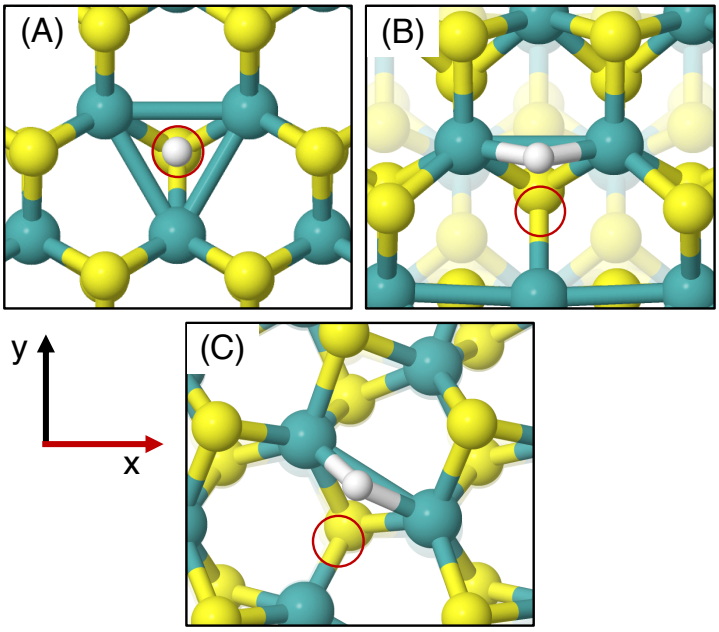

Figure 5.5: Geometries of the most favourable H adsorption sites for systems with an S-vacancy defect. (A) shows the flat basal plane, (B) the armchair nanotube, and (C) the zigzag nanotube. Note the preferred adsorption at a bridged position between Mo atoms for the nanotube cases compared to the threefold site for the flat basal plane. In all cases the red circles indicate the position of the S atom removed to create the vacancy.

adsorbing in the bridged position at any of the short Mo-Mo bonds is the preferred site. Indeed, a stable adsorption geometry in the long bond position could not be located, and instead H would always diffuse to the short Mo-Mo bond site during relaxation.

The $\Delta G_{H_{ads}}$ values for adsorption at the S-vacancy sites across all the nanotubes tested here are reported in Table 5.3. A substantial drop in $\Delta G_{H_{ads}}$ compared to the pristine surfaces (seen earlier in Table 5.1) is observed both on the flat basal plane, and across all nanotubes. First looking at the flat basal plane, the $\Delta G_{H_{ads}}$ of 0.15 eV is much closer to thermoneutral than for the pristine surface, a finding which is in close agreement with past work[223] and indicates that the S-vacancy site is far more likely to be active for hydrogen evolution. The $\Delta G_{H_{ads}}$ values were already seen to decrease relative to the flat basal plane for pristine nanotubes, and here at the S-vacancy site $\Delta G_{H_{ads}}$ was further lowered and is actually negative for many of the sizes tested here. The negative values indicate that some nanotube S-vacancies actually bind H too strongly to be thermodynamically ideal, in stark contrast to the very weak H binding on the pristine flat basal plane of MoS_2.

Table 5.3: H adsorption free energies, $\Delta G_{H_{ads}}$, at S-vacancy defect sites on MoS_2 nanotubes and the flat basal plane.

System ($\overrightarrow{n}$, $\overrightarrow{m}$)	$\Delta G_{H_{ads}}$ S-vacancy / eV
Basal plane	0.15
Armchair	
(8, 8)	-0.30
(9, 9)	-0.22
(10, 10)	-0.16
(11, 11)	-0.13
(12, 12)	-0.08
(13, 13)	-0.05
(14, 14)	-0.05
Zigzag	
(14, 0)	-0.12
(15, 0)	-0.10
(17, 0)	-0.05
(19, 0)	-0.02
(20, 0)	-0.01
(22, 0)	0.01
(24, 0)	0.03

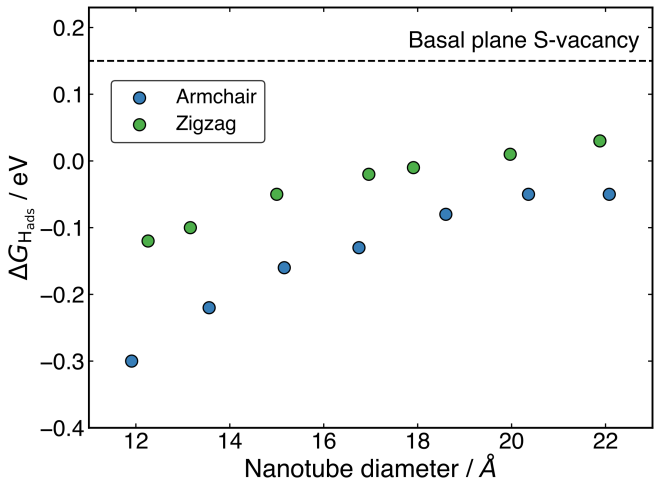

Figure 5.6: The hydrogen adsorption free energy, $\Delta G_{H_{ads}}$, at the S-vacancy defect as a function of diameter for both armchair and zigzag nanotubes. $\Delta G_{H_{ads}}$ on the flat basal plane S-vacancy site is also shown for comparison.

Examining the effect of nanotube diameter on $\Delta G_{H_{ads}}$ for the S-vacancy sites (Figure 5.6), it is clear that there is still a degree of tuning with size. However, compared to the pristine nanotubes, where $\Delta G_{H_{ads}}$ on S spanned in total 0.43 eV across diameters from approximately 12 to 22 Å, here $\Delta G_{H_{ads}}$ only varies by 0.25 eV for armchair and 0.15 eV for zigzag nanotubes across the same range. Interestingly, the range of $\Delta G_{H_{ads}}$ values that are produced with different diameters spans the thermodynamically ideal region around 0 eV. These data suggest that nanotubes around the size of 17-22 Å in diameter would have S-vacancies with near ideal $\Delta G_{H_{ads}}$ values for hydrogen evolution. Given that it is well known that specific active sites can dominate a catalyst's reactivity, even if they are not overly abundant,[52,248] these S-vacancy sites could easily explain the high HER activity observed on experimentally synthesised MoS_2 nanotubes. An interesting topic for further study would be to explore $\Delta G_{H_{ads}}$ values as the nanotubes get larger than 22 Å in diameter. The trend observed here suggests $\Delta G_{H_{ads}}$ could remain close to 0 eV at these larger diameters.

From Figure 5.6 it is also clear that H adsorbing to armchair nanotube S-vacancies is consistently more favourable than the same site on zigzag nanotubes. This contrasts to the pristine structures, where armchair and zigzag tubes produced very similar $\Delta G_{H_{ads}}$ values. This difference is likely a result of different Mo-Mo bond lengths at the bridged H adsorption site on the S-vacancy. As mentioned earlier, the Mo-Mo bonds are slightly shorter for the armchair nanotube (3.15 Å) than the zigzag (3.23 Å). This fits with the idea that it is more favourable for H to bind at short Mo-Mo bonds. As a result, while zigzag nanotubes span the ideal thermoneutral range between 17 and 22 Å in diameter, the armchair nanotubes still bind H slightly too strongly in this same diameter range. Indeed, it seems that slightly larger armchair nanotubes may be ideal, where these larger tubes are also perhaps easier to obtain experimentally.[232]

5.3.3 Explaining the trends in H adsorption

In order to better understand what factors might be underpinning the changes in $\Delta G_{H_{ads}}$ observed with different nanotube diameters, investigations into the electronic structure

were performed. In this section we consider only the most favourable H binding sites, which for the pristine nanotubes is on an S atom, and for the defective nanotubes is at a bridged position between Mo. Density of states (DOS) calculations were performed for all the clean and H adsorbed nanotubes. Furthermore, the charge movement arising from H adsorption was explored using Bader charge analyses. The results from these calculations are discussed separately for the pristine and S-vacancy systems in the following sections.

Pristine MoS_2 systems

DOS plots for the atoms around the H adsorption site on the basal plane, smallest and largest armchair nanotubes, and the smallest and largest zigzag nanotubes are all presented in Figure 5.7. DOS plots are shown for the system with and without H adsorbed, allowing us to observe the electronic structure change after H binds to the surface. The same DOS analyses were performed for all sizes of nanotubes studied here, and the plots are available in Appendix C.3.

As was observed for the supported MoS_2 systems in Chapter 4, when H adsorbs directly on-top of an S atom on the flat basal plane (Figures 5.7A and B) a sharp low-energy state with H s and S p character arises, indicating a S-H covalent bond has formed. Additionally, in the H_{ads} system, a new feature arises at the Fermi level primarily composed of partially filled Mo d-states, suggesting that the Mo d orbitals are also involved in bonding. Recall from Chapter 4 that this pattern is highly consistent with Liu *et al.*'s recent model for H binding on MoS_2 surfaces,[206] where it is argued that S in the flat MoS_2 basal plane has a full valence and must displace an electron to a neighbouring atom to form a bond with H. In the previous chapter, evidence was found for electron transfer to the support material below MoS_2, but given there is no support here the electron density must be displaced elsewhere. We suggest that some of the S atom's electron density instead becomes shared across the neighbouring Mo atoms. This is supported by Bader charge analyses of the clean and H_{ads} systems showing that the S adsorption site loses about 0.2 electron-equivalents of charge and the surrounding Mo atoms together gain around 0.1 e^-. This may be what gives rise to the partially filled Mo d-states at the Fermi level seen in the DOS plots.

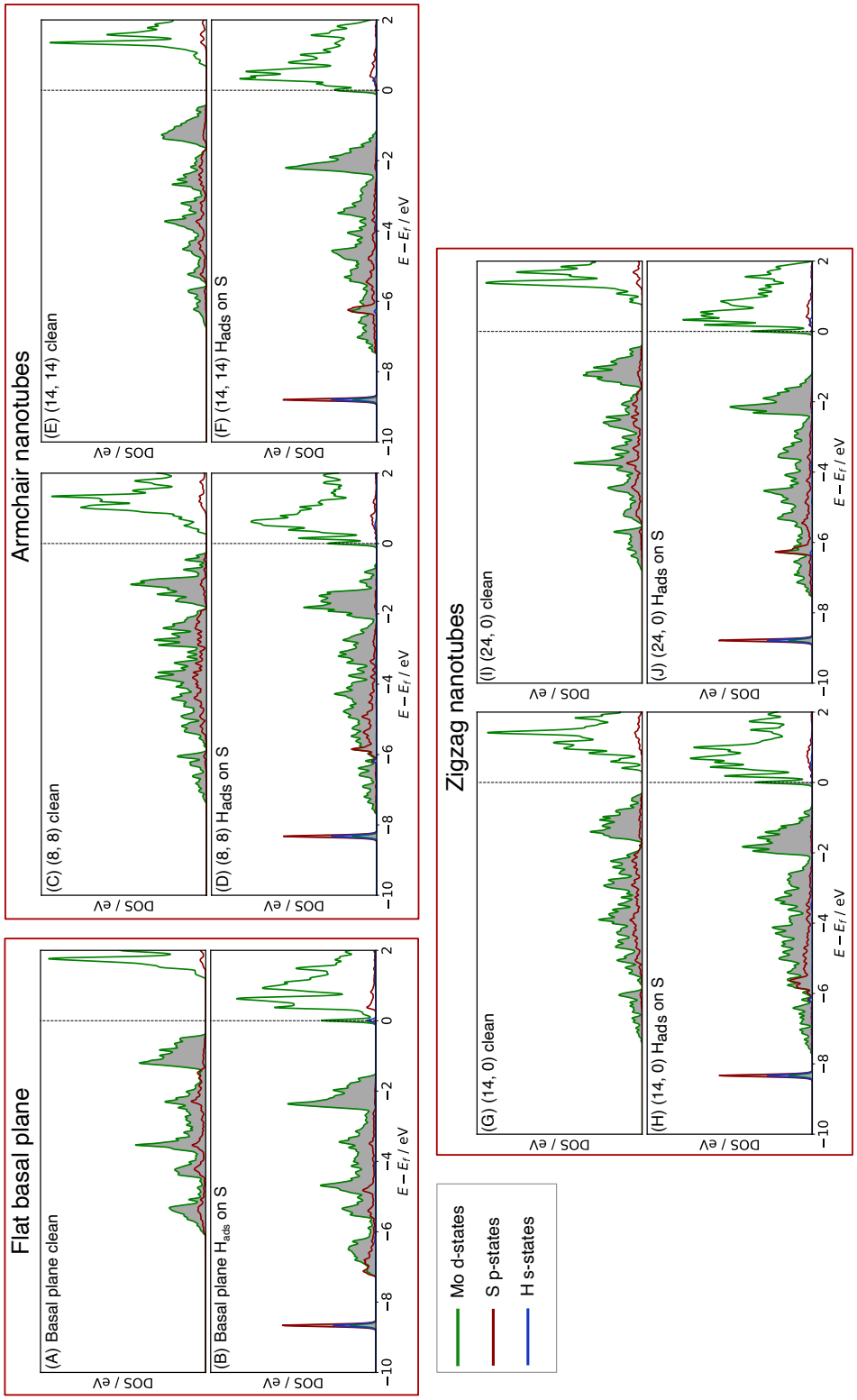

Figure 5.7: Density of states (DOS) plots for the MoS_2 basal plane either (A) clean or (B) with H_{ads} on S. Plots (C) through to (F) show the same cases for (8, 8) and (14, 14) nanotubes, which are the two size extremes of the armchair nanotubes studied here. Plots (G) through (J) show this for the (14, 0) and (24, 0) zigzag nanotubes, again on the edges of the size range explored here. In all cases, the H s-state density is taken from the single adsorbed H, the S p-state density is from the S adsorption site, and the Mo d-state density is from all three directly neighbouring Mo atoms.

When H adsorbs to the MoS_2 nanotubes (Figures 5.7C through J), a very similar pattern of S-H bond formation and electron displacement to Mo is observed. This indicates that the mode of H binding is likely the same as on the flat basal plane. However, there are notable differences in the DOS between nanotubes of different sizes. Specifically, in the clean nanotube DOS, it appears that the gap between the edge of the filled S p-states and the unfilled Mo d-states reduces in smaller nanotubes. It has previously been found that the overall band gap of MoS_2 nanotubes reduces with their diameter,[236,239] but here the S p- and Mo-d states are studied specifically, because H binding involves an electron transfer between these two states. We propose that the lowering of $\Delta G_{H_{ads}}$ values on smaller nanotubes is a direct result of the reduction of this energy gap. Indeed, a very reliable linear correlation can be drawn between $\Delta G_{H_{ads}}$ and the energy gap between filled S p- and unfilled Mo d-states (Figure 5.8). Extrapolating the linear trend suggests that, as the energy gap approaches zero, the $\Delta G_{H_{ads}}$ value will fall to ~0.8 eV, at which point the energy cost to adsorbing H may predominantly relate to the relaxation and movement of the nuclei rather than electronic rearrangement.[195] The flat basal plane of MoS_2 is also included in Figure 5.8, and lies closely on the trend described by nanotubes of different diameter. This is further evidence that the mode of H binding is the same.

Interestingly, a linear relation was not observed when $\Delta G_{H_{ads}}$ was plotted against the energy of the S p-state edge on its own (Figure 5.9), suggesting it is specifically the electron transfer from S to Mo that is responsible for the energy cost to adsorbing H. This demonstrates that, while the p-state energy may play a role in determining $\Delta G_{H_{ads}}$, it is only the energy difference between the S p- and Mo d-states (i.e. the ones directly involved in electron rearrangement on H adsorption) that yields a direct correlation to $\Delta G_{H_{ads}}$.

Recalling the trend between S p-states and $\Delta G_{H_{ads}}$ reported for supported MoS_2 materials in Chapter 4, we propose that this same behaviour is not observed here because the electron displacement on H binding goes from S to a neighbouring Mo atom, rather than to the support beneath MoS_2. In the previous chapter it was shown that the carbon-based supports had states spanning the Fermi level, and therefore they could accept an electron with no additional energetic cost. As a result, it follows that it would only be

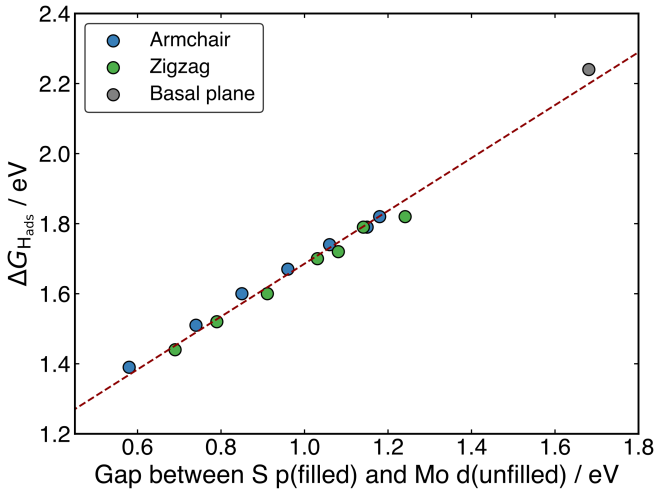

Figure 5.8: The linear relation between $\Delta G_{H_{ads}}$ at an S atom and the energy gap between the filled S p-states of the adsorption site and the unfilled Mo d-states of neighbouring atoms. The data from armchair and zigzag nanotubes of different sizes are plotted here, and the flat basal plane is also shown to fit on the same trend.

the position of the S p-states relative to the Fermi level that determined $\Delta G_{H_{ads}}$. In the present chapter, the Mo atoms that accept electron density on H adsorption do not have unfilled states at the Fermi level, and thus an additional energetic cost must be paid to move electrons based on the position of these states.

S-vacancy defect sites

In the case of H adsorbing to the S-vacancy site, the much more favourable $\Delta G_{H_{ads}}$ values than the pristine surface indicate that this binding could be governed by different factors. Indeed, in looking at the DOS plots for the defective flat basal plane (Figure 5.10A and B; see Appendix C.4 for all DOS plots), it is clear that there is no distinct covalent bond between H and the surface like there was when H bound to an S site on the pristine surface. Instead, the H s-state density appears to overlap with both S p- and Mo d-state density across a wider region. This broad region is more pronounced for the nanotube cases which are also presented in Figure 5.10. Rather than the sharp S-H bond state observed for the pristine MoS_2 materials, the broad region of H s-state overlap is more characteristic of H binding to flat transition metal surfaces.[249] Indeed, a very similar pattern is observed in

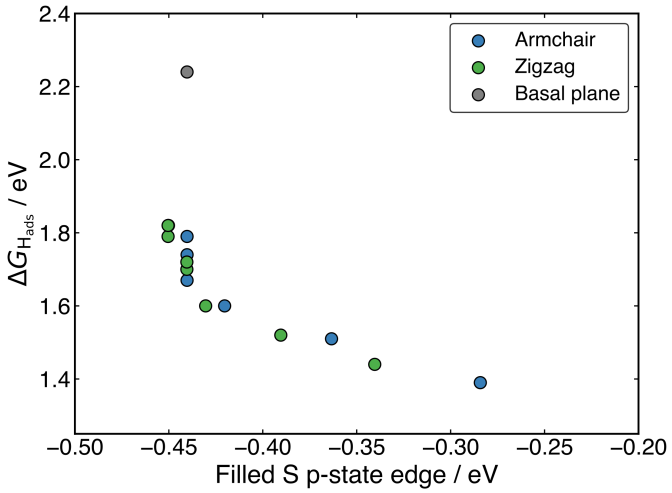

Figure 5.9: A plot showing that there is no clear linear relation between the energy of the S p-states taken alone and the H adsorption free energy across all nanotube systems studied here and the flat basal plane. This demonstrates that, while the p-state energy is important to determining $\Delta G_{H_{ads}}$, it is not enough to consider this alone and the Mo d-state energy must also be taken into account.

the DOS for H adsorbing to a Pt(111) surface at either the fcc or top site (pictured in Figure 5.11). Therefore, it is suggested that H adsorption on Mo at the S-vacancy defect may be governed by similar factors to H adsorption on transition metal surfaces.

Another interesting feature that arises in the DOS when H adsorbs to S-vacancy sites is a sharp partially occupied state with S p and Mo d character at the Fermi level. In the case of H adsorbing to transition metal surfaces (e.g. Pt(111) in Figure 5.11), this state is not visible, perhaps due to the conducting nature of the surface which has states already spanning the Fermi level. It is possible that this state is evidence of electron transfer from Mo to H as a bond forms. Indeed, Bader charge analyses of the flat and nanotube surfaces indicate that H gains negative charge density on adsorbing (0.4 e^- equivalents), and the Mo atoms it binds to also lose about 0.3 e^- equivalents together.

With H binding to Mo atoms at the S-vacancy defect on the flat basal plane,[195] it has been previously found that the adsorption can be understood using d-band theory,[220] which is typically applied to understand adsorption to pure metal surfaces. This model suggests that the binding strength of H will be proportional to the energy gap between the H s-state (set to 0 eV) and the centre of the Mo d-states. A smaller gap results in stronger

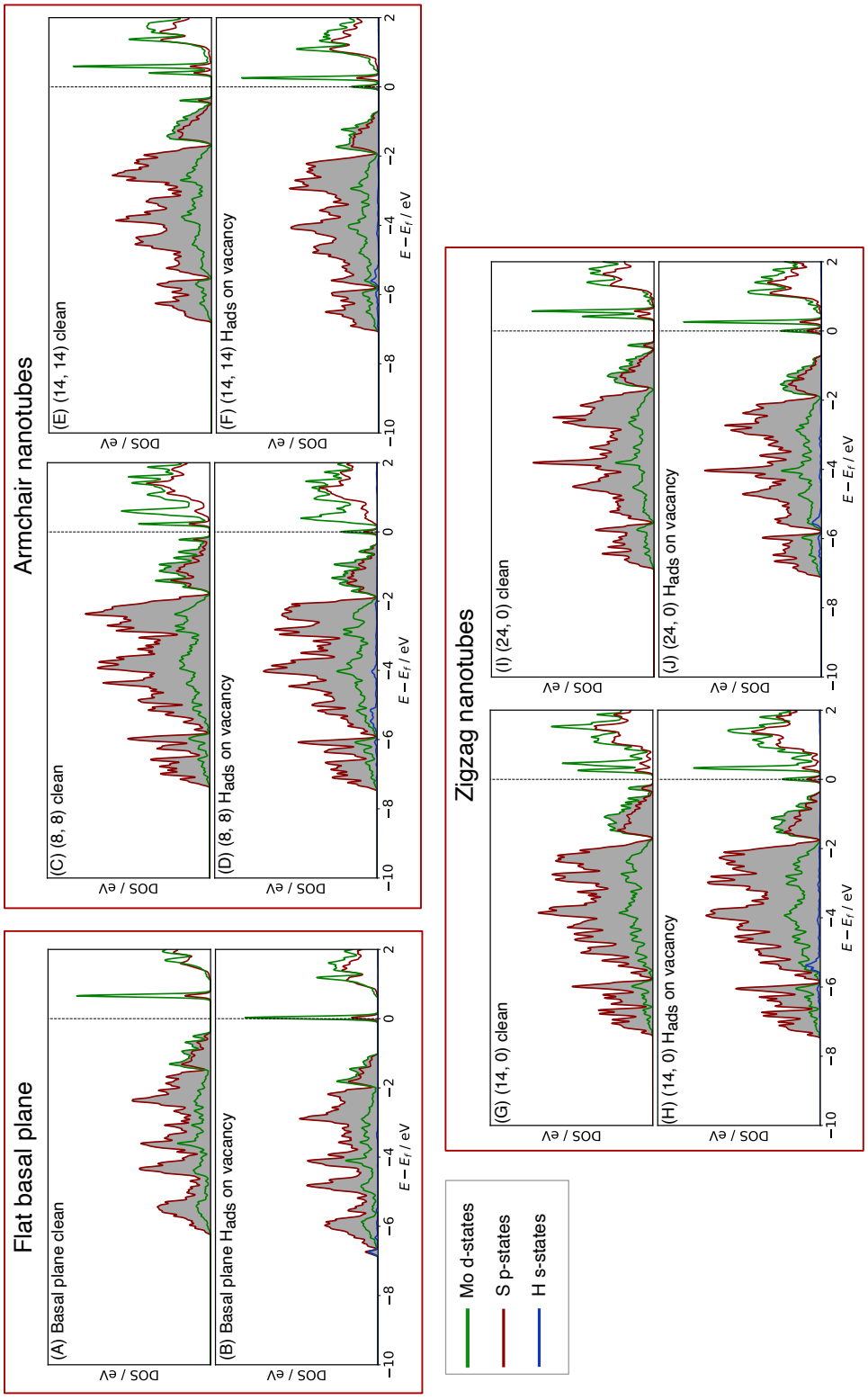

Figure 5.10: Density of states (DOS) plots for the defective S-vacancy MoS_2 basal plane either (A) clean or (B) with H_{ads} at the vacancy site. Plots (C) through to (F) show the same cases for (8, 8) and (14, 14) nanotubes, which are the two size extremes of the armchair nanotubes studied here. Plots (G) through (J) show this for the (14, 0) and (24, 0) zigzag nanotubes, again on the edges of the size range explored here. In all cases, the H s-state density is taken from the single adsorbed H, the Mo d-state density is from the Mo atoms directly where H adsorbs (three atoms for the flat surface, and two for the nanotubes), and the S p-state density is from all neighbouring S atoms.

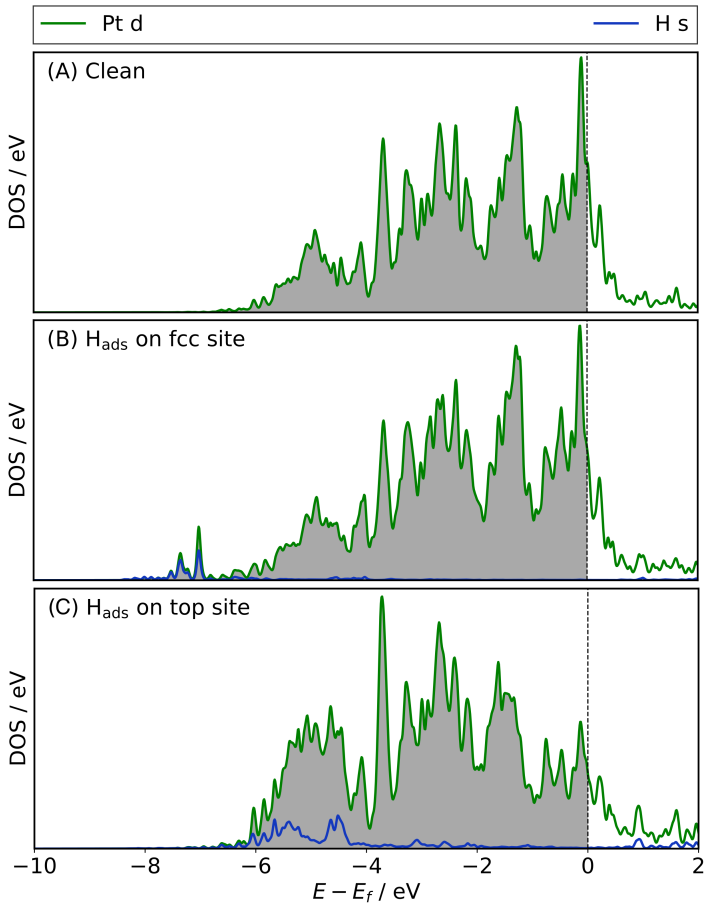

Figure 5.11: Density of states plots showing Pt(111) as (A) a clean surface, (B) with H adsorbed to the fcc site, and (C) with H adsorbed to the top site. A clear region of broad overlap between the Pt d-states and the H s-states is observed in both H adsorbed cases.

H adsorption. Application of this model to the S-vacancy is rational when considering the DOS analyses indicate H adsorption character very similar to that on flat transition metals. However, Ouyang *et al.*[195] have previously found that there is no relation between $\Delta G_{H_{ads}}$ and the *centre* of the Mo d-band in flat MoS_2, as it is only the states close to the Fermi level that are involved in adsorbing H. In the present work we affirm this for MoS_2 nanotubes. If $\Delta G_{H_{ads}}$ is plotted against the d-band centre for both armchair and zigzag nanotubes, no clear relation is seen (See Appendix C.2). Instead, when plotting only the edge of the Mo d-band against $\Delta G_{H_{ads}}$ (Figure 5.12), an interesting pattern is observed. A linear relation exists, yet this relation appears to have a different slope for the armchair and zigzag nanotubes. Returning to the d-band model,[220] the slope of the

relation here would be determined by the amount of overlap between the H atom states and the Mo states which is referred to as the coupling matrix, V, and relates to the H adsorption energy through:

$$\Delta G_{\mathrm{H_{ads}}} \propto -\frac{V^2}{|E_{\mathrm{d}}|} \tag{5.2}$$

where E_{d} is the energy of the Mo d-state edge. Here, V clearly controls the slope of any relation present.

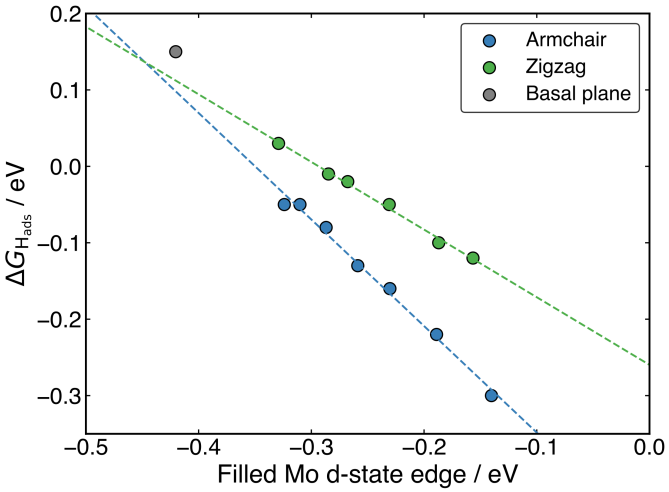

Figure 5.12: The relation between the Mo d-state edge and the H adsorption free energy at S-vacancy defect site across different MoS_2 nanotubes and the flat basal plane. Note that two linear relations of different slope describe the armchair and zigzag nanotubes respectively.

For armchair nanotubes, H binds between two Mo atoms that are closer together than on the zigzag nanotube (as outlined in a previous section). This would suggest a larger coupling matrix for H adsorbing on the armchair nanotube, which is likely what gives rise to the steeper slope for the armchair nanotubes in Figure 5.12. The flat basal plane lies somewhat offset from the line described by either form of nanotube, indicating the coupling matrix may be once again different in this case.

Overall, the existence of this trend suggests that the d-band model can accurately be applied to H adsorption at MoS_2 S-vacancy sites, provided one uses only the Mo d-states that are involved in bonding (i.e. the highest energy ones, represented by the edge of the d-band). Indeed, the relation in Figure 5.12 suggests that ideal HER thermodynamics

($\Delta G_{H_{ads}} = 0$) arise for MoS_2 materials with d-band edges between -0.4 and -0.3 eV below the Fermi level. However, this depends on the specific structure of the Mo atoms in S-vacancy defect, which determines the coupling matrix.

5.4 Future work

While it is naturally a good starting point to reduce $\Delta G_{H_{ads}}$ so that H can favourably adsorb to the basal plane of MoS_2, it would also be highly interesting to understand which sites are directly involved in the combination and desorption step of H_2 (*via* a Tafel or Heyrovský process). Recall from Chapter 3 that both the S and Mo sites played a role on the edges of MoS_2.[143] However, as it currently stands, the mechanism for hydrogen evolution on the basal plane of 2H-MoS_2 has not yet been determined.[a] On the pristine nanotubes it is unclear whether both the S and Mo sites would be involved in the combination step to form H_2. However, it was found that the energy gap for H adsorption between the S site and the Mo site reduces with nanotube diameter. Thus, nanotube size could provide a useful route to tuning not just the adsorption thermodynamics, but perhaps also the thermodynamics and kinetics of the desorption step. Furthermore, for the nanotube S-vacancy sites, a different adsorption site to that on the flat basal plane was observed – at a bridged site between Mo atoms as opposed to a three-fold site. This may have large ramifications for the mechanism of H-H combination, especially considering that it could be possible for two H to simultaneously be adsorbed at neighbouring bridged positions in the S-vacancy. We aim to explore this possibility in detail going forwards.

There are also certain structural features of MoS_2 nanotubes that the present work could be expanded to capture. For instance, the terminating ends of the nanotubes can form edges or caps,[238] which may play a significant role in HER catalysis. This would be especially pertinent to study, given that the edges of flat MoS_2 are known to dominate reactivity.[64] In large MoS_2 nanotubes it is also possible to get deformations, such

[a] Here, the author specifically notes the naturally occurring 2H form of MoS_2, which is the same that is studied through the whole of this thesis, as mechanistic studies have been preformed on synthetic 1T-MoS_2. However, the results are unlikely to generalise to 2H-MoS_2 as the two materials have different core structures.

that the circumference of the nanotube is not circular but rather square[250] or partially triangular.[251] These analogues of the classic nanotube structure could provide new active sites, and would also make interesting candidates for further study.

Lastly, considering the large effect of support materials on MoS_2 observed in Chapter 4,[199] it would be interesting to extend work on MoS_2 nanotubes to consider tubes with different core materials. These core-shell MoS_2 nanotubes have previously been observed with ZnO cores,[230] MoO_x cores,[252] and even with the MoS_2 tube constructed around a graphene nanotube.[246,253] It is possible that structures of this nature could be used to bring $\Delta G_{H_{ads}}$ lower on the pristine nanotubes, without the need to consider defect sites. Furthermore, they may offer more precise control over the MoS_2 nanotube diameter, making selective synthesis more straightforward.

5.5 Conclusions

This work represents the first computational study of hydrogen evolution on MoS_2 nanotubes. Density functional theory was used to systematically examine the H adsorption energies for pristine armchair and zigzag nanotubes, as well as nanotubes with an S-vacancy, across a range of different diameters. For the pristine nanotubes, we find a strong preference for H to adsorb on the outside (as opposed to the inside) of the nanotube, and the favourable adsorption site is directly on-top of an S atom. We also observe a relationship between the nanotube diameter and $\Delta G_{H_{ads}}$, such that smaller and more strained tubes adsorb H stronger. $\Delta G_{H_{ads}}$ decreases from 1.82 to 1.39 eV as the nanotube diameter decreases from 22 to 12 Å. From density of states calculations across the different sized nanotubes, a very reliable linear relation is found between $\Delta G_{H_{ads}}$ and the energy gap between the filled S p-states and the unfilled Mo d-states. These two states are implicated in electron transfer when H adsorbs, and thus we propose this energy gap – which is seen to close as the nanotubes get smaller – is determining the H adsorption energy.

For the S-vacancy sites on the MoS_2 nanotubes, H adsorbs with significantly more strength than on the pristine nanotubes. $\Delta G_{H_{ads}}$ values range from 0.03 to -0.30 eV

depending on the nanotube diameter. For zigzag nanotubes of around 20 Å diameter, the $\Delta G_{H_{ads}}$ values are exactly at the 0 eV mark, which is thermodynamically ideal for hydrogen evolution. Given S-vacancy defects are common in MoS_2 nanotubes,[240,241] this suggests tubes of approximately this diameter would be highly promising hydrogen evolution catalysts. From density of states calculations, the trend in $\Delta G_{H_{ads}}$ when H binds to Mo atoms at the defect site is rationalised using the classic d-band model for adsorption on metals.[220] A strong linear relationship is observed between the position of the d-states in Mo and the $\Delta G_{H_{ads}}$ value. The slope of this relationship differs for armchair and zigzag nanotubes due to different coupling matrices in the Mo-H bond.

Overall, these findings suggest that MoS_2 nanotubes are highly relevant for hydrogen evolution applications, as this structural form serves to thermodynamically activate the MoS_2 basal plane. The HER activity may be readily modified by controlling the size distribution of the nanotubes. Additionally, the electronic explanations for the factors affecting H adsorption that are reported here can be used to assist in the rational improvement of current MoS_2 catalysts, or aid in the design of novel hydrogen evolution catalysts.

Chapter 6

Hydrogen evolution on transition metal nitrides

In this final results chapter we move slightly away from the prior focus on MoS_2, and begin to explore a related class of materials which also show promise as hydrogen evolution catalysts: transition metal nitrides (TMNs). After the in-depth studies on MoS_2 in Chapters 3 to 5, this shift in focus acknowledges the fact that there are a number of materials that could ultimately be used as Earth-abundant catalysts, and a green hydrogen economy may rely on the development of more than just one of these. Similar to MoS_2, TMNs are also binary materials, and the hydrogen evolution reaction (HER) activity of the flat extended surfaces is thought to be roughly equivalent to that of MoS_2.[60] Given the possibility for improved activity when moving from extended planes to nanostructured morphologies (seen for MoS_2 in Chapters 3 to 5), in this chapter we study the nanostructured forms of one particularly active TMN, tantalum nitride or Ta_xN_y. Specifically, we compare the activity of nanoparticulate Ta_xN_y structures to that of the extended surfaces, and gain a preliminary understanding of how hydrogen evolution catalysis may change at the nanoscale.

We begin by generating a series of Ta_xN_y nanoparticle geometries (also called clusters) using a machine-learning accelerated *ab initio* global optimisation code: "Global Optimization with First-Principles Energy Expression," or GOFEE.[254] Two different compositions

are considered: TaN and Ta_3N_5, at two different sizes: 16 and 24 atoms. We comment on the types of structures observed, and explore whether the *ab initio* global optimisation technique is suitable for application to these systems and size ranges. The reliability with which GOFEE is able to find consistent low energy clusters is also examined by repeat trials.

Following this, we perform a simple study of H adsorption to the various novel sites on each of the lowest energy Ta_xN_y clusters obtained. We also examine the (100) and (111) surfaces of TaN for comparison. This serves as a starting point to contrast trends in H adsorption between the clusters and the pristine surfaces, and also allows comparisons between different cluster compositions and sizes. A full exploration of hydrogen evolution activity at realistic H coverages is not performed, though this is a target for future work.

This work was performed in collaboration with the group of Professor Bjørk Hammer (Åarhus University, Denmark), who are the developers of the GOFEE code. Andreas Slavensky provided instruction on how to use GOFEE and technical support, but all calculations and data reported here are solely the work of the author of this thesis.

6.1 Introduction

Transition metal nitrides are a general class of compounds referring to any transition metal structure where nitrogen has been integrated into the interstitial sites between metals.[255] These compounds can take a number of common crystal structures depending on the choice of transition metal and synthetic conditions,[256] including face centred cubic (e.g. rock salt TiN),[257] hexagonal close packed (e.g. Wurtzite TaN),[258] or orthorhombic (e.g. Ta_3N_5).[259] TMNs can also form with different ratios of transition metal to nitrogen. For the bulk structures of early transition metals, 1:1 MN or 2:1 M_2N structures are often favoured, but the later transition metals can have more options,[260] such as the orthorhombic Ta_3N_5 mentioned earlier.[259]

Interestingly, many of the synthesised forms of TMN materials also have high activity towards hydrogen evolution[79,81,82,255] For instance, WN crystals have shown modest activity, with onset potentials towards the HER of -840 mV.[261] Extended 2-dimensional MoN

nanosheets are found to have very promising low onset potentials to hydrogen evolution (in the range of -100 to -200 mV at 10 mA cm^{-2} current densities),[262,263] which is attributed to their large surface area and the presence of defects.[263] Some investigations into Ta_3N_5 thin films have also been performed, and these are found to have onset potentials to the HER of around -540 mV.[259]

While the recent experimental literature has many examples of HER-active TMNs, considerably fewer theoretical works have looked into the activity of these materials. Critically, very little is understood about how this activity is affected by the morphology and active sites of the material. One recent study of the HER on the bulk structures of a series of mononitrides has been conducted.[60] The authors considered the (100) surfaces of the rock salt structures of ScN, TiN, YN, HfN, MoN and TaN, and calculated the free energies of H adsorption ($\Delta G_{H_{ads}}$) as well as the barriers to Volmer-Tafel combination. The authors identify TaN as having a promising H adsorption energy, close to 0 eV, as well as a low barrier to H_2 combination that could be competitive with Pt(111). YN and TiN are also identified as having particularly low H_2 combination barriers, yet the thermodynamic cost to adsorb H to these surfaces is high, suggesting the reaction would only occur at a high onset potential. Therefore, in this thesis we have specific interest in TaN, as both experimental[85] and computational[60] studies affirm its appreciable HER activity.[a]

While prior computational work has considered the extended surface of TaN,[60] these materials can also form nanoparticulate structures.[85] TaN nanoparticles have previously been synthesised with sizes ranging anywhere between 2 and 25 nm,[264] whereas Ta_3N_5 nanoparticles sized between 7 and 15 nm have been reported supported on mesoporous graphitic carbon nitride.[265] It is often the case that nanoparticulate structures expose active sites that offer improved catalytic activity (e.g. in the case of MoS_2 observed earlier in this thesis),[64,143] and some experimental reports indicate this is the case for Ta_3N_5 too, with the nanoparticle form offering 3-10 times greater photocatalytic HER

[a]Here, we would like to recognise the fact that Ta metal is not as cheap or Earth-abundant as would be desirable for a catalyst; though, it does offer a cost advantage over pure Pt. Therefore, the results generated here will aid in assessing whether the activity of TaN may be worth the use of Ta, and may also be generalised to cheaper TMNs in the future.

activity than the bulk (depending on the nanoparticle size).[265] Thus, in the present work we will specifically examine these nanoscale cluster structures, where no current computational studies on their HER activity have been reported. Past computational work on the bulk structures of TaN considered the mononitride with a 1:1 Ta:N ratio;[60] however, experimental work often reports materials with a 3:5 ratio of Ta:N when they are synthesised at the nanoscale.[78,85] Thus, in this work, both the TaN and Ta_3N_5 compositions are considered.

There exists a large hurdle to computationally studying the HER activity of TaN and Ta_3N_5 nanoparticles in that the structure of these nanoparticles in unknown. Indeed, this is a general problem for computationally modelling most nanoparticles, as they have complex potential energy surfaces (with $3N - 6$ degrees of freedom, N being the number of atoms in the cluster) that have many local minima.[266] Each local minimum represents a possible structure the particle could take. However, it is often assumed that the thermodynamically favoured structure with the lowest energy (referred to as the global minimum) will be representative of an experimental sample. At the very least, the global minimum structure provides a good starting point for examining the properties of a nanoparticle. Locating the global minimum, or even simply low energy clusters, requires significant computational time as the potential energy surface (PES) must be explored in detail.[267] A number of different types of algorithms exist to efficiently perform this search, including basin hopping algorithms,[268] which explore by moving between local minima on the PES, and evolutionary algorithms,[254,269,270] which search based on the mating and mutating of different nanoparticle structures. As a group, these algorithms are referred to as global optimisation algorithms.

In searching the PES, all global optimisation algorithms require a method with which to evaluate the energy of candidate structures. Over the course of a single run, a great number of these energy evaluations must be performed at many different points on the PES. Thus, it is common practice to use a cheap interatomic potential to describe the interactions between atoms.[270] However, because of its higher accuracy and greater generalisability, it would be desirable to use density functional theory (DFT) for energy

evaluations.[b] Naturally, this results in a high computational cost for each evaluation. As a result, DFT global optimisations are usually limited to nanoparticles smaller than around 10 atoms in size.[271–273] To obtain larger structures using a DFT-based global optimisation algorithm, its efficiency or speed must be somehow improved. Very recently Bisbo and Hammer have developed one such improved algorithm,[254] named "Global Optimisation with First-principles Energy Expression," or GOFEE for short. GOFEE is a type of evolutionary algorithm that uses Gaussian process regression machine learning to fit a surrogate PES to points sampled from the more accurate DFT-based PES. New candidate structures can be optimised and their energy evaluated using this machine-learned PES, greatly saving computational time.

Therefore, in this chapter we calculate the low energy structures of 16 and 24 atom TaN and Ta_3N_5 clusters using GOFEE.[254] The reliability with which GOFEE is able to locate certain minima is noted, and common structural features that arise in the clusters are interpreted. The H adsorption free energy is the studied on the lowest energy cluster at each size and composition. This allows us to ascertain how the HER activity may change on nanostructured Ta_xN_y materials relative to the bulk, and to compare behaviour between the features in different cluster structures.

6.2 Methodology

6.2.1 Obtaining low energy cluster structures

All cluster structures studied here are obtained using the GOFEE code, very recently developed by Bisbo and Hammer.[254] This method is specifically designed to accelerate searches for global minima in nanoparticle (or cluster) potential energy surfaces where DFT (or another higher level method) is the desired tool for calculating energies. A single GOFEE run can be summarised in the following seven steps, which are outlined individually below and presented diagrammaticality in Figure 6.1.

[b] Additionally, at the time of writing, there are no known interatomic potentials that can correctly capture the interactions for Ta_xN_y materials.

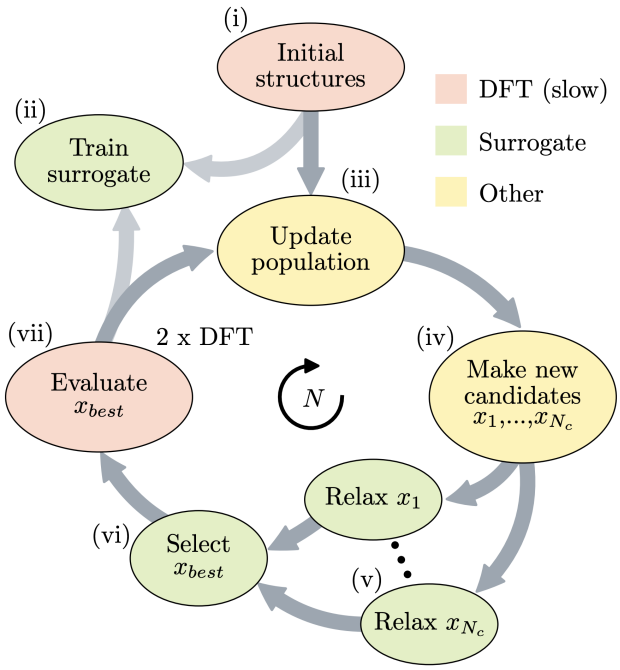

Figure 6.1: A flowchart showing the processes involved in a single GOFEE run. Steps (i) to (vii) are all discussed separately in the main text. The image is reproduced directly from Bisbo and Hammer.[254]

In step (i), an initial population of nanoparticle structures is generated by placing atoms randomly into a box of defined volume.[c] In this work, the volume of the box is based on the size of cluster studied. TaN or Ta_3N_5 clusters with 16 atoms were given a cubic box with a volume of 5.59^3 Å^3, 24 atom clusters had a cubic box of 6.4^3 Å^3 volume, and the tests performed on 32 atom clusters had a cubic box 7.1^3 Å^3 volume. The edge length of the boxes (l) was chosen based on the bulk equilibrium bond length of Ta-N ($r = 2.22$ Å)[60] using Equation 6.1, following past work in the field.[274]

$$l = r(N_a)^{\frac{1}{3}} \tag{6.1}$$

where N_a is the number of atoms in the cluster. For each atom added, it was ensured that they were not closer than 0.7 Å to any other atom, nor further apart than 1.4 Å from all other atoms. In this work, the size of the initial population was 10 clusters. The energy

[c]Note, to avoid potential confusion, this box does not refer to the unit cell of the simulation, but rather the volume in which atoms were placed when generating clusters.

of each of these clusters was evaluated directly with DFT (these calculation parameters are given in the following section).

In step (ii), a Gaussian process regression (GPR) model is trained from the energies and geometries of all structures that have been evaluated with DFT. The training constitutes combining Gaussian functions of the bond lengths and bond angles of a cluster (features together referred to as $\mathbf{x}$) to fit an expression for the energy (E) in the form of:

$$E(\mathbf{x}) = \mathbf{k}_*^T (K + \sigma_n^2 I)^{-1} (E - \mu(\mathbf{x})) + \mu(\mathbf{x}) \tag{6.2}$$

where K represents the features (i.e. bond lengths and bond angles) of the training structures, $\mathbf{k}_*$ is the covariance function, σ_n is a constant uncertainty factor of 5×10^{-2} eV, and $\mu(\mathbf{x})$ is the prior mean function. The uncertainty with which the GPR model predicts the energy of a new structure ($\sigma_{sur}(\mathbf{x}_*)$) can also be quantified directly as:

$$\sigma_{sur}(\mathbf{x}_*) = k(\mathbf{x}_*, \mathbf{x}_*) - \mathbf{k}_*^T (K + \sigma_n^2 I)^{-1} k_* \tag{6.3}$$

where $k(\mathbf{x}_*, \mathbf{x}_*)$ is the covariance function of the new structure, $\mathbf{x}_*$. This is an example of a reinforcement learning process, where the model can begin to perform fairly well even with little training data.[275]

In step (iii) the population of the evolutionary algorithm is updated. This is done by considering all structures that have currently been evaluated with DFT, taking just the clusters that are within 5 eV in energy of the current lowest-energy cluster,[d] and performing a principal components analysis on their structural feature space (i.e. bond lengths and angles). These structures are then clustered into N_{pop} groups in feature space using the k-means method.[276] Each of these groups should, in principle, represent distinct structural geometries. The single lowest energy structure from each group is added to the population. The population size, N_{pop}, can be set to any value, but here a size of five structures is used.

[d] This 5 eV limit is based on testing of the algorithm by Bisbo and Hammer.[254]

In step (iv), N_c new candidate structures are generated by performing perturbations on those already in the population. A key part of this step is exploring new areas of the PES, which is important for sampling a diverse enough selection for structures, and also for improving the training of the GPR model. Possible perturbations currently include a "rattle," where three of the atoms in a given structure are randomly moved by up to 3 Å, and a permutation, where the atomic coordinates of up to two different elements (i.e. Ta and N in this case) are directly swapped. Here, we generated $N_c = 10$ new candidate structures each generation, where each one had a 60% chance of being generated by a rattle, 20% chance of being generated by a permutation, and 20% chance of being generated by a completely random re-initialisation in the same manner as the starting population was generated.

The geometry of each of these N_c candidate structures is then relaxed in step (v) using the trained GPR model. Energy evaluations with this surrogate PES are very rapid (seconds, as opposed to minutes with DFT), and thus the full geometric relaxations come at a low computational cost.

In step (vi) the "best" candidate structure is selected, based on the value of a fitness function, $f(\mathbf{x})$. The fitness value is composed partly of an expression for the energy of the structure calculated using the trained GPR model, $E(\mathbf{x})$, and partly of an expression for the uncertainty with which the GPR model estimates this energy, $\sigma_{sur}(\mathbf{x}_*)$. A structure's fitness is therefore calculated as:

$$f(x) = -E(\mathbf{x}) + 2\sigma_{sur}(\mathbf{x}_*) \tag{6.4}$$

This means that structures with lower energy generally have higher fitness. But, critically, those structures which the GPR model has higher uncertainty around also have higher fitness. This latter point is important to for improving the training of the GPR model, as it can get information about regions of the PES it was previously uncertain about. The weighting factor of 2 on the uncertainty in Equation 6.4 was chosen after extensive testing by Bisbo and Hammer.[254]

Finally, in step (vii), the energy of the selected best candidate structure is evaluated with DFT. Two single-point energy calculations are performed: one on the fully relaxed structure from the GPR model, and one on the geometry from a step along the local optimisation path of this same high-fitness candidate. Performing both these calculations gives the GPR model more training information going into subsequent generations.

Together, steps (ii) to (vii) represent a generation of the global optimisation, and these repeat a fixed number of times (N in Figure 6.1). In all calculations reported here this number of generations was set to 1000.[e] In each new generation, additional structures that have had their energy evaluated with DFT are available from the past generations. Thus, when fitting the GPR model in step (ii), these additional training cases are always used, resulting in a progressive improvement to the accuracy of the surrogate PES.

6.2.2 Structural models and computational details

Two different stoichiometric ratios of Ta_xN_y are considered here: the mononitride TaN, and the more complex Ta_3N_5 composition. The former was chosen because a past computational study has indicated the bulk form of TaN is active for the HER,[60] and the latter is chosen because it is typically observed in experimental studies, especially those on nanoparticles.[85] Two key cluster sizes are selected for detailed study: 16 atoms and 24 atoms. These sizes are significantly smaller that the approximately 2 to 25 nm sized nanoparticles observed in experiments,[264,265] but they represent some of the larger sizes that are computationally possible to perform DFT-based global optimisations with.[277] The overall formulae of the nanoparticles studied in detail here are: Ta_8N_8, Ta_6N_{10}, $Ta_{12}N_{12}$, and Ta_9N_{15}. For each of these compositions, five separate GOFEE runs were performed in order to ascertain the reliability with which the algorithm was converging on the same lowest energy structures. The most stable structure from each run was locally optimised with DFT, performed externally from GOFEE in VASP. In the vast majority of cases, the energy changed by less than 0.1 eV during this optimisation and the structure

[e]Note that in order to be confident a global minimum has been located this number of generations would have to be set such that the entire PES was searched. Given this is impossible, one performs enough generations that low energy structures should be confidently located in a way that is still computationally feasible. The choice of 1000 generations will be discussed later, in light of the results reported here.

remained visually identical. This suggests the trained GPR model is accurately finding local minima on the target DFT potential energy surface.

A brief exploration of larger 32 atom clusters was also performed. While the cost in terms of electronic structure calculations naturally increased at these larger sizes, this alone was not expected to be prohibitive given that GOFEE is able to avoid many DFT energy evaluations by relying on its machine-learned PES. However, it was found here that the increased dimensionality of the PES for larger systems greatly increased the computational cost. Taking one example of $Ta_{16}N_{16}$, after 800 generations the 32 atom cluster was still producing highly unrealistic structures, and the energy profile of the lowest energy structure currently obtained was still decreasing considerably (Figure 6.2). This suggests that the global optimisation is still in the early phases of locating minima and accurately training the surrogate PES. As a result, many more generations would likely be required for these larger 32 atom clusters. Thus, we were unable to obtain structures for these clusters within the time-frame of the present work. However, extension to larger cluster sizes remains a goal for the future.

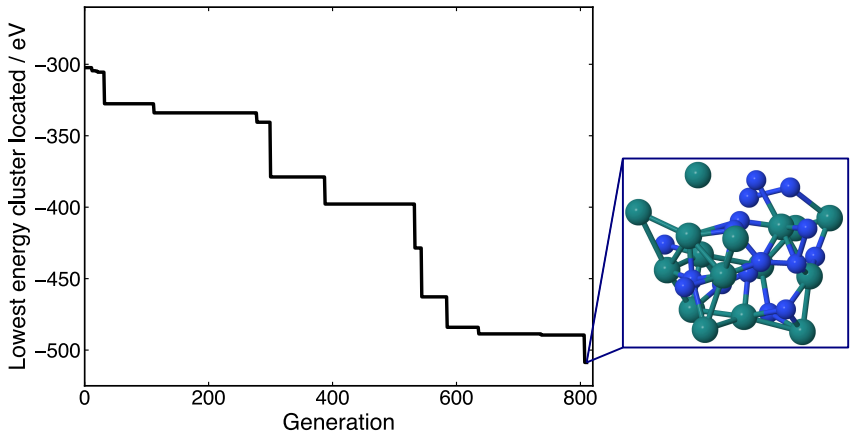

Figure 6.2: An energy profile showing the energy of the most favourable structure located across around 800 generations of a GOFEE run for $Ta_{16}N_{16}$. It can clearly be seen by the end of this run the energy is still regularly falling, and the structure produced looks disordered with an isolated Ta atom. Key: Ta – green, N – blue.

DFT relaxations were also performed on the (100) and (111) surfaces of the mononitride, TaN, in order to provide a comparison point for cluster structures and H adsorption

energies. A 2×2 surface unit cell of a five-layer slab was used to represent each surface. The bottom two layers of the slab were constrained to mimic the bulk material. The lattice constant was set to 4.44 Å, matching that found previously by Abghoui *et al.*[60] Top-down views of the two surface models (along the z-direction) are shown in Figure 6.3.

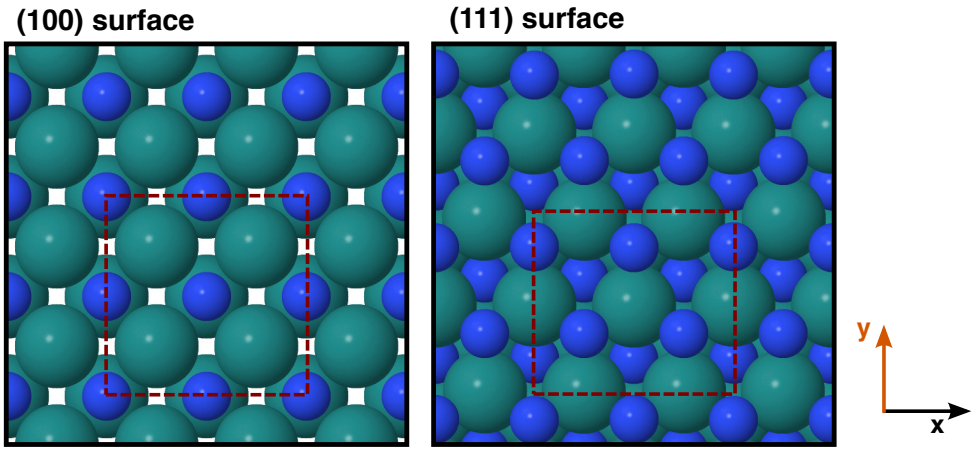

Figure 6.3: Top views of the (100) and (111) surfaces of TaN with the simulated unit cell marked by a red dashed line.

All DFT energy evaluations were performed using the methodology outlined at the end of Chapter 2. However, instead of the BEEF-vdW functional applied to MoS_2 systems, a Perdew-Burke-Ernzerhof (PBE) exchange-correlation functional[278] was used here. There is less need to account for long-range van der Waals forces that were important to the MoS_2/support structures in previous chapters, thus a non-vdW functional is suitable. A gamma k-point sampling scheme was used for cluster structures, which are non-periodic in all dimensions. The unit cell was large enough to allow at least 15 Å between periodic repeats in all directions. For the (100) and (111) surface models, a 8×8×1 Monkhorst-pack scheme was employed, and there was a vacuum spacing of approximately 15 Å between periodic repeats in the z-direction. The electronic and free adsorption energies of H were calculated as described in Chapter 2, Section 2.5.1. Cluster binding energies, E_b, which represent the stability of a composition at a specific size, were calculated as:

$$E_B = E_{\text{cluster}} - [n(E_{\text{Ta}_{\text{bulk}}}) + m(E_{\frac{1}{2}\text{N}_2})] \tag{6.5}$$

where E_{cluster} is the electronic energy of the cluster structure, $E_{\text{Ta}_{\text{bulk}}}$ is the energy of a single Ta atom in the body-centred cubic bulk, and $E_{\frac{1}{2}\text{N}_2}$ is the half the energy of N_2 in vacuum. Here, n and m stand for the number of Ta and N atoms in a cluster, respectively.

6.3 Results and discussion

In the following sections the structures of the low energy Ta_xN_y clusters (also referred to as nanoparticles) that were identified using GOFEE at each of the sizes and compositions studied are discussed separately. Attention is directed specifically towards common motifs, comparison to the bulk TaN structure, and comparison to other small binary metal/non-metal clusters. We also consider the reliability of GOFEE for obtaining these cluster structures. The results are discussed in order of composition, dealing first with both sizes for the TaN clusters, and then for the Ta_3N_5 clusters.

6.3.1 Structures of low energy TaN nanoparticles

Ta_8N_8

The lowest energy structures from each of the five GOFEE runs performed on the Ta_8N_8 nanoparticles were locally optimised with DFT and are presented in Figure 6.4. Due to the difficulty of visualising these small 3D structures, three different viewing angles on each structure are presented. Alternative space-filling models are also given in Appendix D.1.[f] It is clear that, while the same low energy structure is found in runs 2 and 3, GOFEE is not consistently converging to the same minimum each time it is run. Given that evolutionary algorithms (and indeed, all global optimisation techniques) cannot sample the whole PES, it is inherently stochastic as to whether they locate the true global minimum in a given run, or simply a local minimum elsewhere on the PES.[266] As a result, when analysing the success of a global optimisation algorithm, one often performs many trials (e.g. numbering in the hundreds of attempts).[254,269] Hundreds of trials are naturally not possible when

[f] The reader may find that the space-filling models are more suitable for viewing certain features of the clusters discussed here. The specific places where a space-filling model may be clearer are noted in the text.

applying a DFT-based algorithm such as GOFEE, and therefore the structures generated here should be treated as reasonable guesses for those that could stably exist.

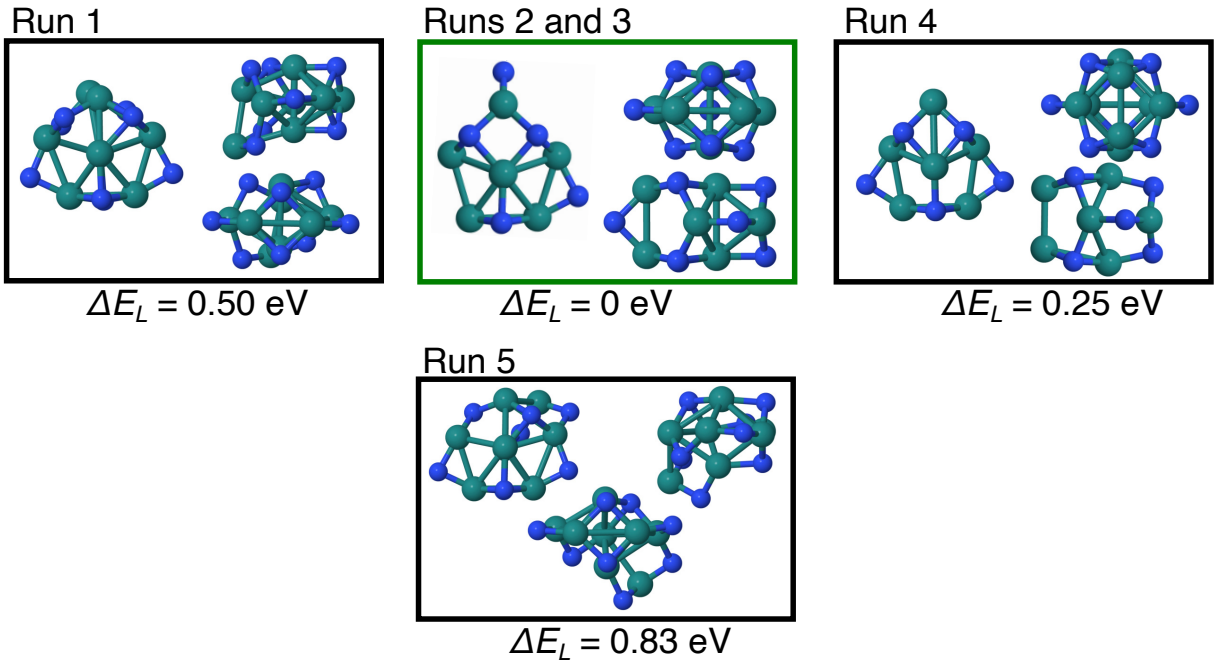

Figure 6.4: The lowest energy structures of Ta_8N_8 obtained from five separate GOFEE global optimisations. These structures have all been locally optimised using DFT. The green box indicates the lowest energy structure identified, and the energies of all clusters are given relative to this structure. Key: Ta – green, N – blue.

One common element between each of the structures produced is the existence of a pentagonal arrangement of Ta atoms, which is best viewed looking at the top-down view of each cluster (the left most image in each box in Figure 6.4). This arrangement is also always accompanied by two additional Ta atoms, located in the centre of the pentagon with one above and one below the plane. This seven-atom arrangement resembles the core of a decahedral cluster, a structure which is common in metallic nanoparticles.[279] Because GOFEE routinely finds this high symmetry arrangement, this suggests it is a particularly low energy motif, that could be commonly observed in experiment. However, in Ta_8N_8 there are eight Ta atoms, leaving one additional Ta that is surplus to the seven-atom decahedral motif. For some of the structures found by GOFEE, we observe this final Ta atom situates itself in an auxiliary position around the decahedral core. For instance, in the structures from runs 1 and 5, this extra Ta appears to be bonded to one of the points

of the decahedron without changing its structure.[g] In contrast, in runs 2, 3 and 4, the additional Ta appears to slightly perturb the decahedron, integrating directly under one of the other Ta atoms on the points of the pentagonal arrangement, and slightly altering its symmetry. In all cases, this double-Ta arrangement is best viewed in the bottom right image in each box in Figure 6.4 (left hand side of the cluster).

Another structural feature observed in the low energy clusters across all GOFEE runs is the existence of "capping" N atoms around the decahedral Ta core. These N atoms tend to be bonded to either two or three Ta atoms, and never form N-N bonds. This pattern somewhat resembles N adsorption to pure transition metal surfaces (best observed in the space-filling models in Appendix D.1), where it is found that N tends to adsorb at a threefold or bridged site.[280] We will return to this point in the following section when discussing $Ta_{12}N_{12}$ structures.

Considering the overall framework of a Ta atom core with adsorbed N, this is somewhat similar to what is observed in similarly sized molybdenum carbide clusters,[277] where an Mo-Mo bond framework is also always maintained, though its structure varies with cluster size. Furthermore, in work on small molybdenum sulfide clusters,[h] Gemming *et al.*[281] observe a repeatedly occurring triangular structure of Mo atoms capped by S, that is maintained when modifying composition and size.

The lowest energy cluster found here for Ta_8N_8 is the repeat structure from runs 2 and 3. It is identified as having C_s symmetry, and has a binding energy relative to bulk Ta and gaseous N_2 of $E_b = 3.50$ eV (see Equation 6.5 in the methodology of this chapter). Interestingly, for runs 2 and 3, this C_s structure was stably located fairly early in the GOFEE run – at the 285^{th} and 404^{th} generation, respectively. For the remaining generations in the 1000 performed, no lower energy structure was located. Similar to the cluster generated by run 4, this lowest energy structure has the 8^{th} Ta atom directly integrated into the decahedron core, forming the double-Ta point mentioned above. However, the most clear distinguishing feature about this particular cluster, which

[g] Indeed, in both cases the Ta appears to be "hanging" off the decahedron in a somewhat disordered and asymmetrical fashion.

[h] Note that these are not the same ordered nanomaterials that were the focus of prior chapters, but instead very small clusters with variable Mo:S ratios.

could possibly explain its stability, is that this double-Ta point is capped by N. This exact pattern does not occur in any other structure.

$Ta_{12}N_{12}$

Figure 6.5 shows the low energy structures of $Ta_{12}N_{12}$ obtained from five different GOFEE runs. Here, there is a great deal of similarity observed across the clusters. The same structure is found in runs 1 and 3, and a separate structure is found in both runs 4 and 5. These two structures are very similar to each other, both having a regular Ta atom core, which is a 13-atom icosahedron with a single vertex atom missing. Indeed, it is very hard to distinguish the two different structures when looking from two of the three views in Figure 6.5. Only when looking at the top-left view does it become apparent that they differ by the position of N atoms around this Ta core. A marked contrast is seen in the structure produced by run 2, which appears disordered, and is around 1 eV higher in energy. However, this structure could be described as being part of the way towards assembling the central Ta core (best seen from the top right view in Figure 6.5). It is possible that GOFEE has simply not yet sampled the lower energy (more regular) arrangements.

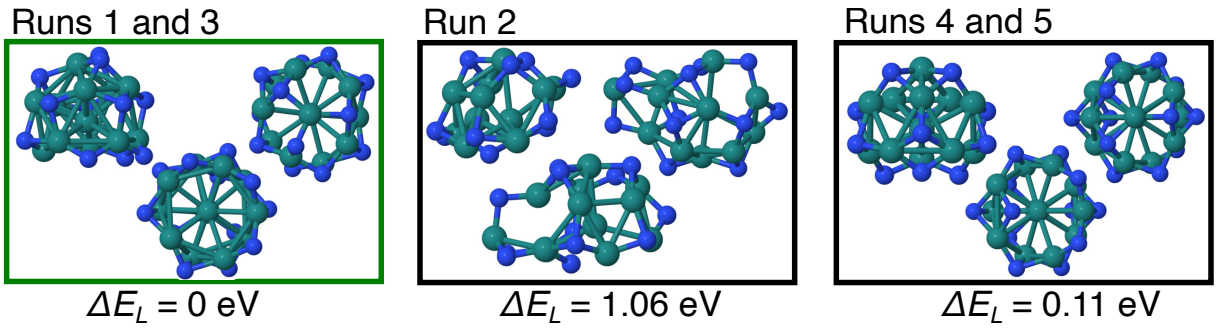

Figure 6.5: The lowest energy structures of $Ta_{12}N_{12}$ obtained from five separate GOFEE global optimisations. These structures have all been locally optimised using DFT. The green box indicates the lowest energy structure identified, and the energies of all clusters are given relative to this structure.

Returning to the common near-icosahedral motif of Ta in the favourable structures from runs 1, 3, 4, and 5, this represents a central Ta atom bonded to 11 other Ta atoms in a shell around it. If the last corner of the icosahedron were filled with one additional Ta

atom, this would yield the perfect icosahedron with 12 bonds to the central Ta – matching the coordination number of Ta in the body-centred cubic bulk. Around the outside of the cluster's Ta core, the N atoms again appear to take capping positions, similar to what was observed for the smaller Ta_8N_8 cluster. In this case, each N atom is bound in a threefold or a bridged site between Ta (see Appendix D.1 for the space-filling models). The threefold sites closely match what is observed for N atoms in the (111) surface of bulk TaN (observed in Figure 6.3). This overall pattern of an icosahedral Ta core and adsorbed N is nearly identical to that previously modelled for similarly sized $Mo_{13}N_{14}$ clusters,[282] with the extra metal atom here simply completing the icosahedron. The N atoms in the $Mo_{13}N_{14}$ cluster are also situated around the outside of the metal core in threefold sites. We suggest that the bonding preferences of the non-metal species in these 1:1 (or close to 1:1) binary clusters closely matches the favourable adsorption geometries on a pure metal surface.[280]

For $Ta_{12}N_{12}$, the near-icosahedral structure found in runs 1 and 3 was the lowest energy cluster located across all GOFEE runs. This structure was stable relative to its constituent atoms, with a binding energy of -0.20 eV. The other near-icosahedral structure from runs 4 and 5 with a slightly different arrangement of N atoms was competitive, being only 0.11 eV higher in energy. We suggest this energy difference could be attributed to N slightly favouring the first set of adsorption geometries around the Ta core. These different arrangements could easily both occur due to the statistical nature of the global optimisation, and both could be present in an experimental sample given the small energy difference between them.

Comparing the structures found for $Ta_{12}N_{12}$ to those from the smaller Ta_8N_8, it is clear that there are some general similarities. For clarity, a single view of the lowest energy structures at both sizes are presented as space-filling models in Figure 6.6. The five-fold arrangement of Ta atoms, which formed a decahedron in the Ta_8N_8 structure, can again be seen here for $Ta_{12}N_{12}$, this time as a 2-dimensional structure making up the faces of the icosahedral Ta core. This further affirms the idea that it is the favourable packing of Ta that determines the overall structure at this 1:1 composition. Indeed, in force-field molecular dynamics simulations of rapid cooling of pure Ta systems, Wu *et al.*[283]

observed both the decahedral arrangement of Ta and the full icosahedron of Ta as the most common local arrangements in their large 10,000 Ta simulation cell. This suggests these two structures of Ta are particularly favourable, and it is likely the preference for forming specifically these arrangements that is determining the types of TaN clusters we observe here.

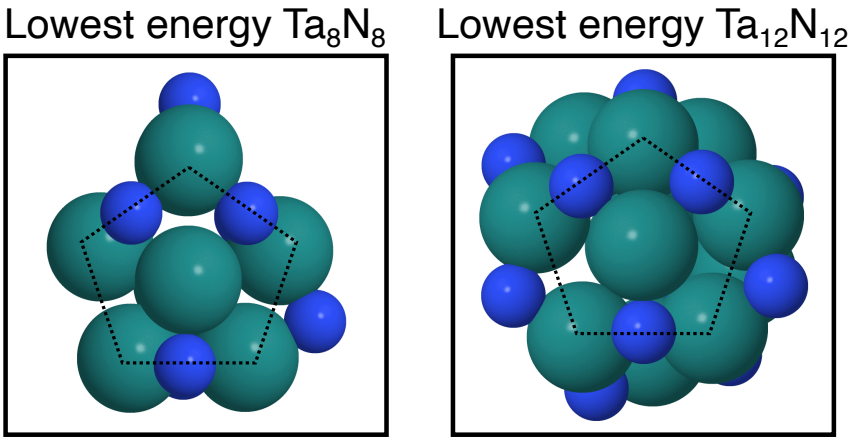

Figure 6.6: Space-filling models of the lowest energy structures of Ta_8N_8 and $Ta_{12}N_{12}$ side-by-side. The two structures are viewed from the angle where the five-fold motif of Ta atoms is visible in both, which is indicated by the dashed pentagon.

6.3.2 Structures of low energy Ta_3N_5 nanoparticles

Ta_6N_{10}

The low energy structures obtained for Ta_6N_{10} nanoparticles are presented in Figure 6.7, again across five different GOFEE runs. Here, both runs 1 and 5, as well as runs 3 and 4, converge to the same geometries. The structure found in runs 3 and 4 has the lowest energy, and has C_s symmetry with a single mirror plane.

Possibly the most striking general feature at this composition (3:5 ratio of Ta:N), is that two of the GOFEE runs converged to structures where N_2 had fully separated from the rest of the nanoparticle structure to exist as a free molecule (runs 1 and 5). While constraints are placed on the new structures generated by GOFEE, such that each atom has to be no more than 1.4 Å from all other atoms, this does not rule out the case of *two* atoms concordantly separating from the main structure. Furthermore, during the local

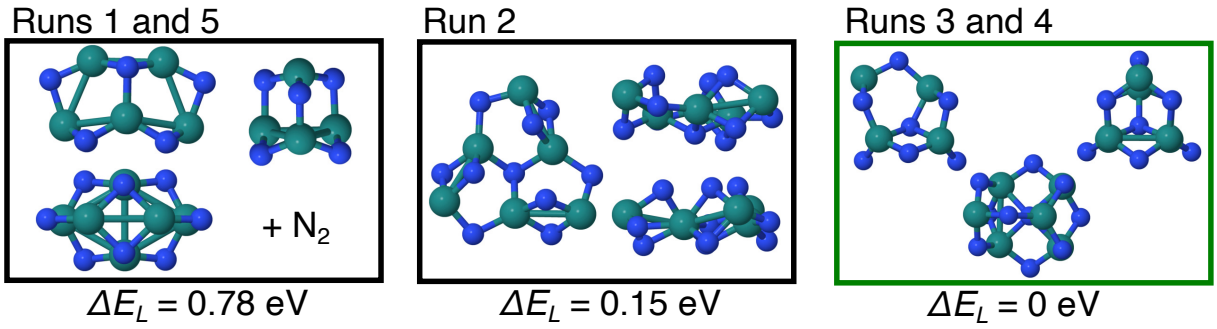

Figure 6.7: The lowest energy structures of Ta_6N_{10} obtained from five separate GOFEE global optimisations. These structures have all been locally optimised using DFT. The green box indicates the lowest energy structure identified, and the energies of all clusters are given relative to this structure.

optimisation steps in the algorithm, all atoms are free to move which could have resulted in the separation of N_2 as observed. Because N_2 has a strong triple bond,[144] it follows that there may be a thermodynamic preference towards forming this molecule. However, encountering this phenomenon in two out of the five GOFEE runs is surprising, especially considering the Ta_3N_5 ratio tends to arise more commonly in experimental studies.[85]

The binding energy of the lowest energy Ta_6N_{10} cluster (from runs 3 and 4) was calculated at 0.20 eV relative to its constituent atoms. This was significantly more stable than that for the equivalent Ta_8N_8 structure, at 3.50 eV, which suggests the 3:5 Ta:N ratio is indeed more stable. These binding energies are also consistent with predictions of bulk Ta_3N_5 having a more favourable heat of formation than bulk TaN.[284] Thus, the formation of N_2 in the GOFEE runs at this composition could perhaps reflect that the minima of Ta_6N_{10} are simply more statistically difficult structures to locate. This may be caused by the existence of a stable and symmetric Ta_6N_8 cluster (i.e. two N atoms short of the starting point) that we observe left behind after N_2 has separated.

Methods do exist for removing structures from an evolutionary algorithm population where one or more atoms have separated off the main body.[285] These methods are important in the global optimisation of larger metallic nanoparticles, which may separate into two or more smaller structures. The present findings suggest implementing one of these methods into GOFEE could be a priority.

Looking at the general types of structures observed across all the GOFEE runs, a great deal of diversity is seen. The almost-planar structure observed from run 2 is rather unique, and bears close resemblance to triangular global minimum that is found for Au_6 clusters.[286] For this run 2 structure, the planar triangle of metal atoms has N integrated around it, yet it retains the same general pattern. Additionally, if two extra N atoms were added in selected positions to the structure from run 2 (one above the central N and one on the edge), it would also closely resemble a particularly small version of the triangular 2D MoS_2 nanoparticles that were the focus of prior chapters in this thesis.[64,251]

Interestingly the ordered close-packed arrangements of Ta atoms that were observed for most of the structures at the 1:1 composition (e.g. decahedral arrangements or icosahedra) do not appear to be present in any of the structures found here for Ta_6N_{10}. Instead, the N atoms appear to be integrated directly into most of the structures observed. This is more akin to the interstitial integration of N that is the structure of bulk TMNs. Although most N atoms across the structures observed here retain a preference for being coordinated to two or three metal atoms, in runs 3 and 4 a structure with a higher coordinate N in the core is observed. Here, the N has bonds to four Ta atoms – a pattern which was never observed at the 1:1 composition. This highly coordinated N is the most notably distinct structural feature of the C_s cluster from runs 3 and 4, and perhaps contributes to it being the lowest energy structure found.

Ta_9N_{15}

Finally, the low energy structures of Ta_9N_{15} are displayed in Figure 6.8. Here, a number of energetically competitive structures are observed, with runs 1, 3, 4 and 5 all producing structures that are within 0.07 eV in energy. While this energy difference is comfortably within the range of error one may expect from DFT methods, all of these structures are still visibly unique. This suggests there could be a number of distinct motifs available at this size and composition that are all close in energy (i.e. a multi-funnelled PES), which contrasts the reliable preference for specific ordered Ta structures observed at the 1:1 composition.

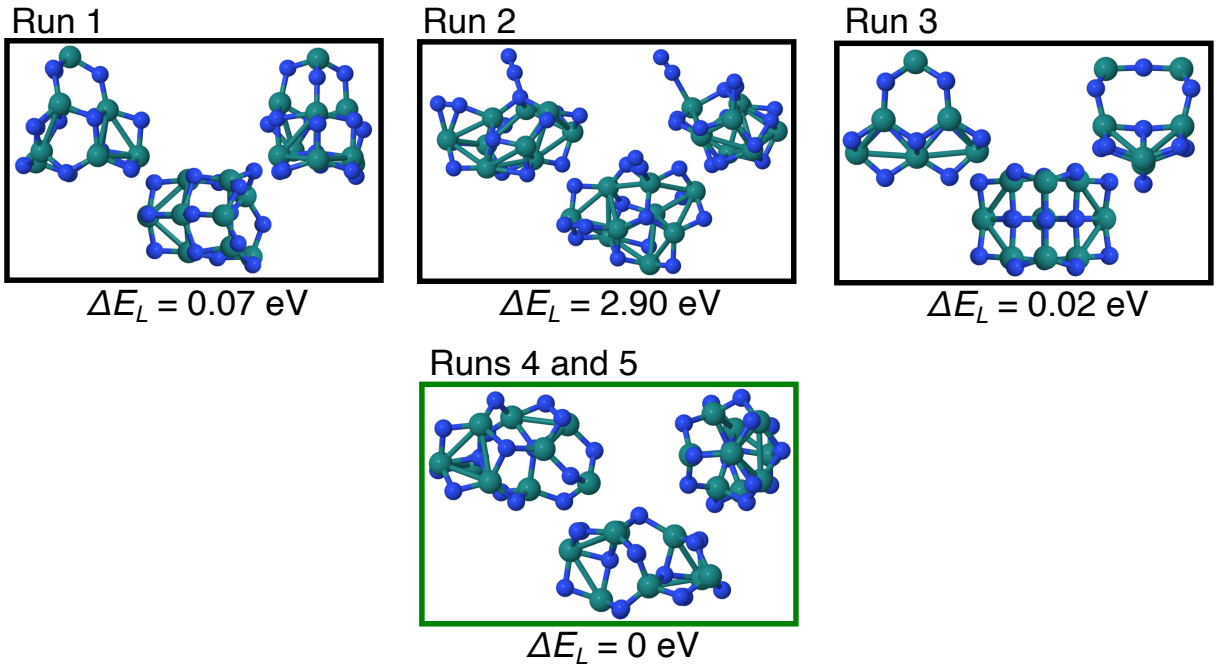

Figure 6.8: The lowest energy structures of Ta_9N_{15} obtained from five separate GOFEE global optimisations. These structures have all been locally optimised using DFT. The green box indicates the lowest energy structure identified, and the energies of all clusters are given relative to this structure.

In terms of the general structural trends for Ta_9N_{15}, we again observe N atoms being integrated between Ta in an interstitial fashion, as was the case for the smaller Ta_6N_{10} clusters (but was not seen for the 1:1 composition). This feature is most clear in the structure from run 3 where there exist two highly coordinated N atoms in the centre of the structure bonded to four Ta. Additionally, in one portion of the cluster, N forms a direct bridge between two Ta atoms. Both features are best observed in the top-right view in Figure 6.8.

The structure from run 2 is of particular note, as it was significantly less stable than those generated by the other runs (around 2.90 eV higher in energy). Recall that the smaller Ta_6N_{10} nanoparticles discussed in the previous section also had a tendency to lose N_2 as a separate and isolated molecule during a GOFEE run. The structure from run 2 here also shows hints of this behaviour, with N_2 loosely associated with a Ta atom (see the top right view of run 2 in Figure 6.8). Indeed, this pattern looks geometrically as

though N_2 is adsorbed on the Ta, rather than these two N atoms being a direct structural component of the cluster.

The lowest energy structure obtained here was that from runs 4 and 5, with a binding energy of $E_b = -3.89$ eV. This is substantially lower than the E_b of 0.20 eV for the $Ta_{12}N_{12}$ cluster of the same size, once again indicating the increased stability of the 3:5 composition. The lowest energy structure appears somewhat disordered and lacks symmetry. The specific feature(s) that distinguish it from the other GOFEE runs are not abundantly clear. However, given the very narrow range in energies (0.07 eV) between the structures from runs 1, 3, 4 and 5, it is perhaps unsurprising that they would share some similar features. For instance, akin to the structure from run 3 discussed above, in the lowest energy structure from runs 4 and 5 there are also two highly coordinated N atoms with four bonds in the core.

In Figure 6.9, space-filling models for the lowest energy structures for Ta_6N_{10} and Ta_9N_{15} are presented side-by-side, clearly depicting the locations of the highly-coordinated N atoms (red arrows) that appear to be common at this 3:5 composition. This demonstrates that, at the 3:5 composition, N is not merely capping or adsorbing onto a structured Ta core, but is directly integrated into the structure.

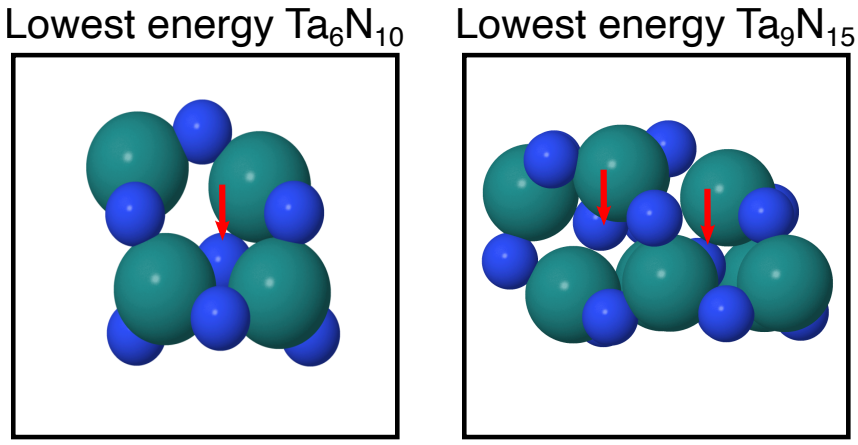

Figure 6.9: Space-filling models of the lowest energy structures of Ta_6N_{10} and Ta_9N_{15} side-by-side. Red arrows point to the location of the centrally-integrated, four-coordinate, N atoms that are a common feature in both clusters.

6.3.3 H adsorption studies

The lowest energy cluster at each size and composition, determined in Sections 6.3.1 (Ta_8N_8 and $Ta_{12}N_{12}$) and 6.3.2 (Ta_6N_{10} and Ta_9N_{15}), was carried through to H adsorption free energy ($\Delta G_{H_{ads}}$) studies. Here, we looked at only the first H adsorption energy to each cluster, considering adsorption to N atoms, Ta atoms, and the sites in-between them. Due to the number of inequivalent adsorption sites on all the cluster structures, an in-depth search for the most favourable H adsorption site had to first be conducted. This constituted trialling at least 40 different sites on each cluster, including on-top, bridged, and threefold sites, where the H adsorbed geometry was optimised and the energy obtained in each case. The most favourable adsorption geometries for H associated with either an N or a Ta atom are presented for each cluster in Figure 6.10. The respective $\Delta G_{H_{ads}}$ values are given in Table 6.1. Additionally, $\Delta G_{H_{ads}}$ was also calculated on N and Ta atoms for the pristine (100) and (111) TaN surfaces to provide a comparison point.

Table 6.1: The first H adsorption free energies ($\Delta G_{H_{ads}}$) on N and Ta atoms for Ta_xN_y clusters of different sizes and compositions. The adsorption energy at the favoured site is shown in bold. The values on for the (100) and (111) surfaces of bulk TaN are also presented. *Indicates that H was adsorbed bridged between two Ta atoms, rather than a single atom.

Structure	$\Delta G_{H_{ads}}$ N / eV	$\Delta G_{H_{ads}}$ Ta / eV
(100) surface	0.65	**-0.10**
(111) surface	0.02	**-0.18**
Ta_8N_8	-0.08	**-0.84***
$Ta_{12}N_{12}$	**-0.65**	-0.33
Ta_6N_{10}	**-0.21**	0.10
Ta_9N_{15}	**-0.33**	0.27

As was first described in Chapter 3, under electrochemical conditions H will continue to adsorb to a material until $\Delta G_{H_{ads}}$ is positive, representing the point where the Volmer reaction becomes non-spontaneous. Therefore, to provide a true estimate of HER activity, $\Delta G_{H_{ads}}$ should be taken from a surface with an H coverage that is representative of what would be spontaneously covered around electrochemically relevant potentials (close to 0 V). Many of the first H adsorption energies reported here on the TaN clusters are

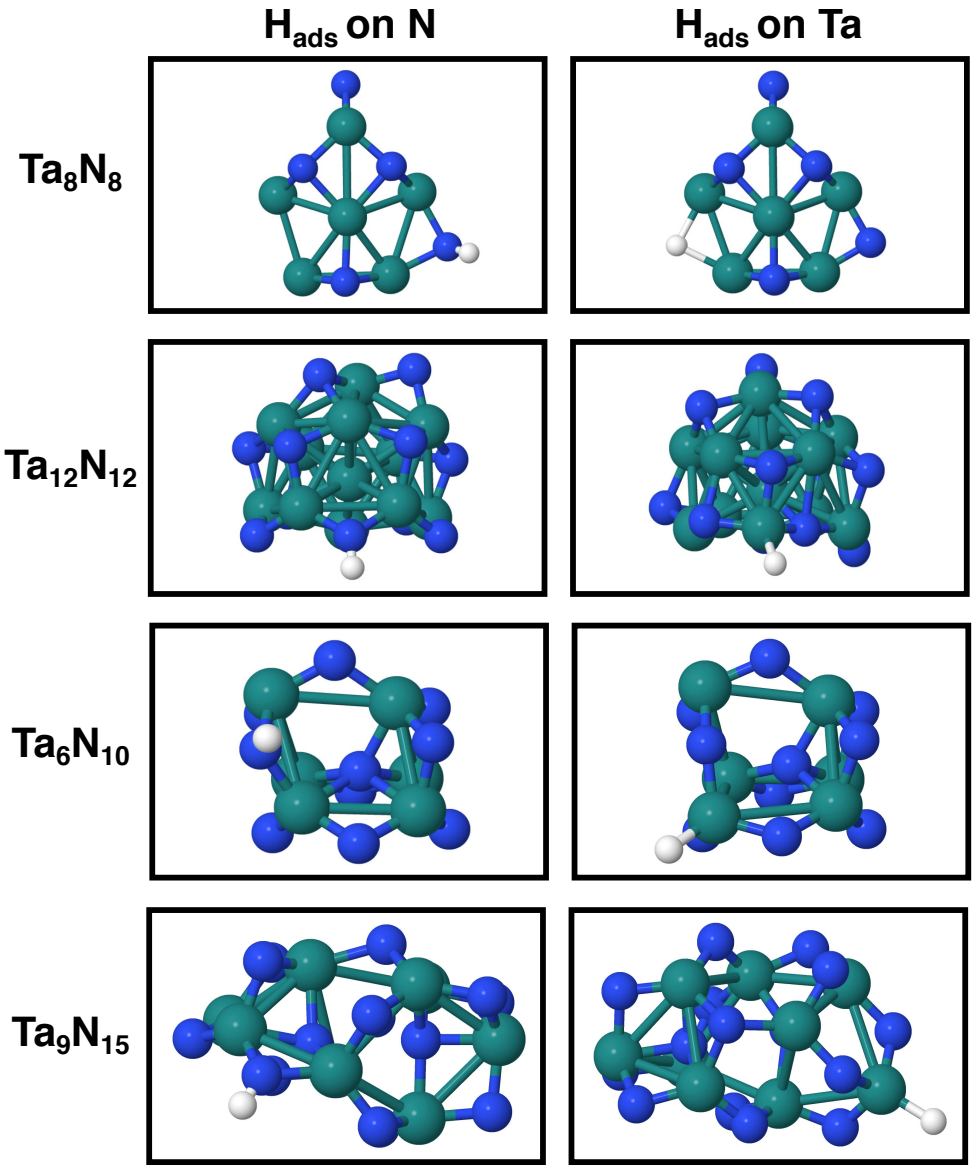

Figure 6.10: The most favourable adsorption geometries of H on clusters of TaN and Ta_3N_5 at different sizes and compositions. In each case, the cluster structure is the lowest energy one obtained from global optimisation, as outlined in the previous section. Adsorption to an N atom, a Ta atom, on bridged sites, and threefold sites were all considered. The most favourable geometry where H being associated with either Ta or N are both presented.

very negative (see Table 6.1). Therefore, they cannot be used as a direct proxy to HER activity, as more H would spontaneously cover the cluster in reality. This was not an issue for Chapters 4 and 5, which looked at H adsorption to various sites on MoS_2, because the $\Delta G_{H_{ads}}$ values were all either positive, or close to 0 eV indicating they were around the spontaneous/non-spontaneous cut-off. Returning to the Ta_xN_y structures at hand, exploring higher H coverages was unfortunately outside the time-frame of the present work. However, the first H adsorption energies can still be compared between clusters and to the bulk TaN structure in order to understand how sensitive H adsorption may be to different features.

On the (100) surface of TaN, Abghoui *et al.*[60] have previously calculated a first H adsorption free energy of -0.10 eV on the Ta atom. This site is reported to be more favourable than the N atom site (though no $\Delta G_{H_{ads}}$ value for the latter is given). Here, we find the exact same $\Delta G_{H_{ads}}$ value for the Ta site, and report that this is 0.75 eV more favourable than the neighbouring N. We also calculate $\Delta G_{H_{ads}}$ on the (111) surface, and find that the Ta site is favoured with an H adsorption energy of -0.18 eV. This is 0.20 eV lower than that for the N site. Together, these two surfaces indicate a moderate-to-strong preference for H adsorption at Ta, and both surfaces yield $\Delta G_{H_{ads}}$ values that are similar to other binary Earth-abundant catalysts (e.g. the Mo-edge of MoS_2 has a $\Delta G_{H_{ads}}$ of -0.30 eV for the first H, as found in Chapter 4).[143]

Considering H adsorption on the cluster structures, for Ta_8N_8 a strong preference for binding at Ta is also observed ($\Delta G_{H_{ads}} = -0.84$ eV, about 0.76 eV lower in energy than adsorption on the most favourable N site). The H adsorption geometry on the cluster is not directly on-top of a Ta atom, but rather bridged between two of the exposed Ta atoms on the side of the cluster. These two Ta are under-coordinated and likely high in energy given that there exist a set of analogous Ta on the opposite side of the cluster that accommodate an N atom between them. Thus, it makes sense that adsorbing H at the bridge between these two unsaturated Ta atoms would be favourable. The magnitude of $\Delta G_{H_{ads}}$ on the Ta_8N_8 cluster is notably more negative than for the (100) and (111) surfaces, by around 0.70 eV. However, an analogous bridged H adsorption site between under-coordinated Ta atoms does not exist on either pristine surface.

The preference for adsorption at Ta site did not extend to the larger $Ta_{12}N_{12}$ cluster of the same composition, where it was more favourable for H to adsorb at an N atom (0.32 eV lower in energy than at a Ta). In this larger 24 atom cluster, there were no sites that looked quite analogous to the favourable under-coordinated bridged Ta site in Ta_8N_8. However, even when H was placed at a series of different bridged Ta sites, the adsorption energy remained much higher than on the N site (by at least 0.63 eV). Interestingly, bridged Ta sites in general were even less favourable than having H directly on-top of one of the Ta atoms in $Ta_{12}N_{12}$, seen in Figure 6.10. This H on-top geometry yielded the strongest $\Delta G_{H_{ads}}$ value at a Ta, and is presented in Table 6.1.

In terms of N atom adsorption sites, the most favourable on $Ta_{12}N_{12}$ was at an N atom with only two bonds to Ta. This N was situated towards the "bottom" of the cluster where the corner of the icosahedron was missing (see Figure 6.10), such that there were fewer neighbouring atoms. H adsorption to this under-coordinated N was very favourable with a $\Delta G_{H_{ads}}$ of -0.65 eV. Indeed, adsorption to under-coordinated atoms (both Ta and N) with as few neighbours as possible appears to be a common theme in the favourable sites throughout all the clusters studied here.

Moving to the 3:5 Ta:N composition, it is seen that the N atom adsorption sites are always favourable over the Ta sites (by 0.31 eV for Ta_6N_{10}, and 0.60 eV for Ta_9N_{15}). This is in stark contrast to the (100) and (111) surfaces, where the Ta sites were always favoured by similar magnitudes. Furthermore, in the Ta_3N_5 clusters, the most favourable $\Delta G_{H_{ads}}$ values are consistently less negative than the 1:1 Ta:N clusters, indicating that H does not adsorb quite so strongly. This may be a feature of the higher stability of the 3:5 composition clusters, as evidenced by their lower binding energies at both sizes tested here. The atoms in a more stable cluster would receive less of an energetic benefit for adsorbing H, thus resulting in weaker adsorption.

For the favourable N adsorption sites in both Ta_6N_{10} and Ta_9N_{15}, we once again observe a preference for H to adsorb at an under-coordinated N atom situated on the edge of the cluster and bound to only two other species. Recall that this composition yielded structures where N was often integrated into the centre of the cluster, surrounded by Ta. Here, we find that no stable adsorption geometries for H could be located on these

interstitial N sites, and the adsorbate would always optimise towards atoms on the surface of the cluster.

The preference for H adsorption at an N atom, which is observed across several of the clusters reported here, is particularly noteworthy. This is because there exists an electrochemical reaction that can compete with hydrogen evolution on certain transition metal nitride surfaces: ammonia formation from the stepwise addition of H to an N atom followed by release as NH_3.[287,288] In the past, the (100) facets of VN, CrN, NbN and ZrN have all shown activity towards ammonia formation, where a key intermediate to this process has H adsorbed to a surface N.[288] In contrast, (100) TaN is believed to be active for the HER without competing ammonia formation. This is a result of H adsorbing to metal atoms at modest electrochemical potentials, and therefore avoiding the adsorbed NH, NH_2, and NH_3 intermediates towards ammonia.[60] For the cluster structures studied here, we cannot rule out the possibility that these intermediates would be accessible, especially considering the strong preference for H adsorption at an N atom in several cases. Thus, in the future, we wish to explore the possibility that these nanostructures may make more suitable catalysts towards ammonia synthesis than for the HER. Of course, N_2 reduction towards ammonia is still a critical reaction in the production of nitrogenous fertilizers,[144] so this could still prove a fruitful avenue for study.

In summary, the H adsorption results for the Ta_xN_y materials reported here indicate large differences in $\Delta G_{H_{ads}}$ depending on the specific cluster structure. There are also notable changes in $\Delta G_{H_{ads}}$ with the size of the cluster, even when keeping the composition the same. H adsorption appears to favour either a under-coordinated bridged Ta site if it is available, or otherwise on-top of an N atom in the cluster (which is more common). The significant differences in $\Delta G_{H_{ads}}$ across the small sample of structures reported here indicates nanostructuring of these Ta_xN_y materials is a rich area for the optimisation of catalysis.

6.4 Future work

The clear next steps for studying hydrogen evolution on these TaN and Ta_3N_5 clusters is to extend the H adsorption analysis to higher coverages. Ideally, H could continue to be added to each model until $\Delta G_{H_{ads}}$ was no longer negative, indicating all spontaneous adsorptions had occurred. Following this, Tafel combination barriers could be calculated and compared to those calculated by Abgoui *et al.*[60] for the (100) surface. This would also allow us to test whether the NH_x intermediates towards ammonia formation would dominate on these clusters.

Reaching higher H coverages would likely prove to be both computationally expensive and time consuming, given the number of possible inequivalent adsorption sites on each cluster that must be manually tested. One possible way to mitigate this cost could be to explore using global optimisation techniques through GOFEE to identify the lowest energy H adsorption sites. Indeed, some preliminary testing down this line has already been performed. GOFEE is given an input of the already optimised cluster structure and uses this as a "seed" on which to place H in different positions, following rules similar to how the software generates new cluster structures. A machine-learned PES could then be trained to direct H towards the low energy sites.

Currently, it is unknown whether this approach will be able to locate reasonable H adsorption sites. To the best of our knowledge, this is not an established type of procedure in the literature. One problem that may arise is a lack of ability to generate reasonable adsorption geometry guesses when using semi-random placement methods. Additionally, it is unclear whether the process would result in saved computational time, as GOFEE may have to sample a number of unrealistic adsorption sites which could be rapidly discounted with human oversight. Therefore, this approach to determine adsorption geometries and energies would first have to be extensively tested before being applied to reach higher H coverages.

It is also our intent to extend this study to larger Ta_xN_y clusters, and perhaps to introduce support materials beneath the clusters in order to more realistically capture experimental environments. It is known that the structure of synthesized clusters can

be strongly influenced by the material that they are supported on.[289,290] In experimental works on catalysis, synthesized catalysts are often placed on electrode materials such as graphite,[85] which could be a starting point for our investigations.

Lastly, we intend to continue collaborating with the group of Professor Bjørk Hammer at Aarhus University in Denmark, in order to test the capabilities and robustness of GOFEE. Hammer's group are currently implementing a "mating" scheme into the evolutionary algorithm, which would generate new clusters *via* the combination of two pre-existing structures in the population. Mating schemes are already implemented in many modern genetic algorithms,[270,291] and are important for introducing and maintaining diversity in the population. Once implemented, we wish to test this mating scheme version of GOFEE on the current TaN clusters to see if it can improve the consistency with which GOFEE finds specific minima.

6.5 Conclusions

In this exploratory work on TaN and Ta_3N_5 clusters at two different sizes (16 and 24 atoms) we sampled a range of low energy structures using an evolutionary global optimisation algorithm (GOFEE). For the TaN composition, a consistent pattern of a Ta core with N adsorbed on the surface was observed. The Ta core tended to arrange in similar ways to pure Ta structures, favouring motifs that were as close as possible to either decahedral or icosahedral arrangements with the number of Ta atoms provided. The Ta_3N_5 composition behaved very differently, favouring more open structures with N integrated into the core. Multiple structures with a highly coordinated N atom bonded to four Ta were observed.

To explore hydrogen evolution activity, the first H adsorption energy was calculated for the most stable structure found at each composition and size. The wide array of inequivalent adsorption sites around each cluster were all explored, and the most favourable Ta and N atom adsorption sites were reported. It was found that all clusters adsorbed H much stronger than the (100) and (111) surfaces of TaN. For the 1:1 Ta:N composition, the 16 atom cluster adsorbed H at a bridged site between Ta, whereas the

24 atom cluster adsorbed H to N. At the 3:5 composition, N was always the favourable adsorption site. Overall, the H adsorption energy was strongly dependent on what specific local sites existed in a cluster, suggesting the hydrogen evolution activity may be very size and composition dependent. These findings highlight the high degree of tunability possible with nanoscale materials, and their great potential for optimisation of catalysis. This project is ongoing, and there are many facets we wish to continue to explore, including additional cluster sizes, compositions, and higher hydrogen coverages.

Chapter 7

Conclusions

The efficient and sustainable production of molecular H_2 for use as an energy transport mechanism is one key step towards a carbon-zero energy economy in the future. However, Earth-abundant and economically viable hydrogen evolution catalysts are critical to this goal. In this thesis, we have used density functional theory calculations to explore the optimisation of one such Earth-abundant catalyst – nanostructured MoS_2 – in great depth. We have been able to recommend specific modifications to MoS_2 that yield significantly improved hydrogen evolution activity on both the edges and the basal plane of the catalyst. In addition we have also conducted a preliminary study of hydrogen evolution on a related binary material – TaN – that has presently received little attention from a computational perspective, despite its experimental promise.

This work began by exploring the possible mechanisms for the hydrogen evolution reaction on the most active portion of flat MoS_2 nanostructures (the Mo-edge site). Knowledge of these reaction mechanisms is critical to understanding what features of a catalyst are important in driving a reaction, and the calculation of kinetic barriers is required to determine quantitative reaction rates. Here, we studied MoS_2 supported by two materials commonly used in experiment: Au(111) and graphene. It was found that the Volmer-Heyrovský mechanism was dominant on both supported catalysts, with a similar barrier of about 1.3 eV at 0 V (*versus* the standard hydrogen electrode). Despite the similar overall barriers, it was found that the choice of catalyst support had a large

influence on the thermodynamics of hydrogen adsorption. There was a large energy cost to adsorb H to MoS_2/Au(111), and for MoS_2/graphene there was a similar energy cost for H to migrate from the favourable adsorption site to the preferred reaction site for Heyrovský combination. Thus, our mechanistic calculations suggested the effect of a support under MoS_2 on the rate of hydrogen evolution at 0 V is primarily controlled through altering the H adsorption free energy ($\Delta G_{H_{ads}}$). However, these data also suggested that different steps were limiting the hydrogen evolution rate in each supported system. This results in different catalytic behaviour with changes to the applied potential. Specifically, the reaction rate on MoS_2/Au(111) increased more rapidly when moving to more negative potentials, which is qualitatively in-line with experimental findings. However, neither Au(111) nor graphene supports were found to enhance the hydrogen evolution activity of MoS_2 relative to the unsupported catalyst.

Given that Au(111) and graphene supports were primarily seen to induce changes in $\Delta G_{H_{ads}}$ on MoS_2, and this related closely to the reaction rate at 0 V, in Chapter 4 we went on to screen across a large array of support materials to see if one that had a more beneficial effect on the catalyst could be located. Here, supports that were doped graphene derivatives were the sole focus, as these materials are synthetically accessible and have multiple dopant coverages that could offer fine tuning of $\Delta G_{H_{ads}}$. We also expanded our study to encompass not just the Mo-edge of MoS_2 but also the basal plane, as this surface makes up a large area of the catalyst. In this search we looked for materials that could induce a $\Delta G_{H_{ads}}$ value close to 0 eV on MoS_2, representing no thermodynamic cost to adsorb or desorb H. It was found that the graphene-derivative supports were able to induce fairly large changes in $\Delta G_{H_{ads}}$ on the MoS_2 basal plane (ranging between 1.4 and 2.2 eV), but no support produced a $\Delta G_{H_{ads}}$ value close to 0 eV. In contrast, less variation in $\Delta G_{H_{ads}}$ was observed for the edge of MoS_2 (ranging between -0.30 and 0.10 eV), but an N-doped graphene support produced an ideal thermoneutral $\Delta G_{H_{ads}}$ value of 0 eV. The variability in $\Delta G_{H_{ads}}$ produced by different supports was rationalised using electronic structure arguments. For the basal plane we found that the energy of the S p-states relative to the Fermi level directly related to $\Delta G_{H_{ads}}$, whereas for the Mo-edge, we observed that $\Delta G_{H_{ads}}$ linearly related to the amount of excess negative charge a support

displaces into MoS_2 when they adhere together. Knowledge of these trends is invaluable for understanding the factors which govern hydrogen evolution thermodynamics. These findings may also apply more broadly than just to supported MoS_2, such as to other two-component catalysts with similar electronic structures (e.g. WS_2 or $MoSe_2$).[72]

Because no carbon-based supports were found to bring the $\Delta G_{H_{ads}}$ value on the MoS_2 basal plane close to the thermodynamically ideal (0 eV) value, in Chapter 5 we went on to look at an interesting structural analogue of the flat surface – a nanotube structure – which could perhaps activate the basal plane by inducing strain. This work represents the first computational study conducted towards hydrogen evolution on MoS_2 nanotube materials. $\Delta G_{H_{ads}}$ was calculated for nanotubes ranging from 12 to 22 Å in diameter considering both a pristine surface and S-vacancy defect site. We observed a strong dependency of $\Delta G_{H_{ads}}$ on the nanotube diameter, with smaller nanotubes adsorbing H more strongly. This relationship was mediated by the strain energy of the nanotube. At the S-vacancy site specifically, we found that armchair nanotubes of diameters between 17 and 22 Å adsorbed H with an ideal thermoneutral $\Delta G_{H_{ads}}$ value. The trends in $\Delta G_{H_{ads}}$ with nanotube size were rationalised using the electronic structure arguments, with specific attention to the states involved in adsorbing H. For the pristine MoS_2 nanotubes, the energy gap between the filled S p-states (which lose electron density on H adsorption) and the unfilled Mo d-states (which accept electron density on H adsorption) was related linearly to $\Delta G_{H_{ads}}$. For the S-vacancy site, where H adsorbs at an Mo atom, a classic d-band model explained the trends, with lower values for $\Delta G_{H_{ads}}$ as the Mo d-states approached the Fermi level.

Taken together, Chapters 3, 4 and 5 represent a detailed exploration of hydrogen evolution on MoS_2 where multiple routes to improve the activity of this promising catalyst were found. Thus, in Chapter 6, we shifted focus slightly to a related binary class of materials – the transition metal nitrides. Here, we were specifically interested in TaN, the bulk form of which has recently shown hydrogen evolution activity both experimentally and in a single computational study. In this chapter we explored nanoparticulate forms of TaN and Ta_3N_5, which have not been computationally studied before. A density functional theory based global optimisation of the nanoparticle structures of Ta_8N_8, Ta_6N_{10}, $Ta_{12}N_{12}$ and Ta_9N_{15} was conducted, and several common motifs between the different sizes and

compositions were identified. The TaN clusters favoured a Ta core with regular decahedral or icosahedral arrangements. N atoms took up capping positions around this Ta core. In contrast, Ta_3N_5 clusters favoured interstitial integration of N into the core. $\Delta G_{H_{ads}}$ was calculated on the lowest energy cluster at each size and composition, demonstrating that they adsorb H more strongly than the (100) and (111) surfaces of TaN. This work suggested the cluster structures of Ta_xN_y likely have very different hydrogen evolution activity to the bulk, and this activity would be dependent on the specific sites available in each cluster. Further examination of H adsorption and hydrogen evolution activity is ongoing, with the aim of predicting whether these nanomaterials would be suitable hydrogen evolution electrocatalysts.

Overall, the work in this thesis represents a concrete step towards the design of cheap and effective hydrogen evolution catalysts. It is not simply the promising materials that we report here that are pertinent, but also the trends in activity that are observed. In particular, being able to rationalise changes in the H adsorption energy using precise electronic structure arguments has wider relevance than just for hydrogen evolution. These principles may be applied across the wider field of heterogeneous catalysis, and similar methodology could be used to understand the factors governing key adsorption steps in other critical reactions in sustainability, such as CO_2 reduction[292] or oxygen evolution.[293]

Furthermore, in this work we have gained insights into potentially generalisable behaviours of 2-dimensional materials, such as alterations to the density of states and charge density with the addition of support materials. This could have relevance to other catalyst/support systems, such as metal/graphene catalysts,[294] where tuning properties using support materials is a recent and rapidly evolving field.[204] Additionally, the effects of curvature-strain and the induction of defects on MoS_2 nanotubes raise promising directions towards improving the properties of other 2-dimensional materials which may also be able to assemble similar types of structures. Lastly, we suggest these 2-dimensional and nanostructured materials provide a rich ground for the optimisation of catalysis. Specifically, the methodology of screening for catalytic activity then performing detailed electronic structure analyses to explain the trends could be readily applied to improve other 2-dimensional materials and understand their novel properties.

Bibliography

[1] Arrhenius, S. *Phil. Mag. S.* **1896**, *41*, 273–276.

[2] Meinshausen, M.; Meinshausen, N.; Hare, W.; Raper, S. C.; Frieler, K.; Knutti, R.; Frame, D. J.; Allen, M. R. *Nature* **2009**, *458*, 1158–1162.

[3] Allen, M. R.; Frame, D. J.; Huntingford, C.; Jones, C. D.; Lowe, J. A.; Meinshausen, M.; Meinshausen, N. *Nature* **2009**, *458*, 1163–1166.

[4] Bockris, J. O.; Potter, E. C. *J. Electrochem. Soc.* **1952**, *99*, 169–186.

[5] Hinnemann, B.; Moses, P. G.; Bonde, J.; Jørgensen, K. P.; Nielsen, J. H.; Horch, S.; Chorkendorff, I.; Nørskov, J. K. *J. Am. Chem. Soc.* **2005**, *127*, 5308–5309.

[6] Glenk, G.; Reichelstein, S. *Nat. Energy* **2019**, *4*, 216–222.

[7] Veziro, T. N.; Barbir, F. *Int. J. Hydrog. Energy* **1992**, *17*, 391–404.

[8] Züttel, A.; Borgschulte, A.; Schlapbach, L. *Hydrogen as a Future Energy Carrier*; Wiley: Weinheim, 2008.

[9] Züttel, A.; Remhof, A.; Borgschulte, A.; Friedrichs, O. *Philos. Trans. R. Soc. A* **2010**, *368*, 3329–3342.

[10] Abdalla, A. M.; Hossain, S.; Nisfindy, O. B.; Azad, A. T.; Dawood, M.; Azad, A. K. *Energy Convers. Manag.* **2018**, *165*, 602–627.

[11] Park, J. H.; Ahn, J. W.; Kim, K. H.; Son, Y. S. *Chem. Eng. J.* **2019**, *355*, 351–366.

[12] White, C. M.; Steeper, R. R.; Lutz, A. E. *Int. J. Hydrog. Energy* **2006**, *31*, 1292–1305.

[13] Koroneos, C.; Dompros, A.; Roumbas, G.; Moussiopoulos, N. *Resour. Conserv. Recy.* **2005**, *44*, 99–113.

[14] Steven K. Ritter, *Chem. Eng. News* **2008**, *86*.

[15] Brightling, J. *Johnson Matthey Technol. Rev.* **2018**, *62*, 32–47.

[16] Ramachandran, R.; Menon, R. K. *Int. J. Hydrogen Energy* **1998**, *23*, 593–598.

[17] Le Duigou, A.; Quéméré, M. M.; Marion, P.; Menanteau, P.; Decarre, S.; Sinegre, L.; Nadau, L.; Rastetter, A.; Cuni, A.; Mulard, P.; Antoine, L.; Alleau, T. *Energy Policy* **2013**, *62*, 1562–1569.

[18] Schlapbach, L.; Züttel, A. *Nature* **2001**, *414*, 353–358.

[19] Wang, Z.; Wang, Y.; Afshan, S.; Hjalmarsson, J. *Int. J. Hydrogen Energy* **2021**, *46*, 6151–6179.

[20] Zhou, L. *Renew. Sustain. Energy Rev.* **2005**, *9*, 395–408.

[21] Sakintuna, B.; Lamari-Darkrim, F.; Hirscher, M. *Int. J. Hydrog. Energy* **2007**, *32*, 1121–1140.

[22] Wang, H.; Lin, H. J.; Cai, W. T.; Ouyang, L. Z.; Zhu, M. *J. Alloy. Compd.* **2016**, *658*, 280–300.

[23] Murray, L. J.; Dincă, M.; Long, J. R. *Chem. Soc. Rev.* **2009**, *38*, 1294–1314.

[24] Dillon, A.; Jones, K. M.; Bekkedahl, T. A.; Kiang, C. H.; Bethune, D. S.; Heben, M. J. *Nature* **1997**, *386*, 377–379.

[25] Prinzhofer, A.; Tahara Cissé, C. S.; Diallo, A. B. *Int. J. Hydrogen Energy* **2018**, *43*, 19315–19326.

[26] Turner, J. A. *Science* **2004**, *305*, 972–974.

[27] Dincer, I.; Acar, C. *Int. J. Hydrogen Energy* **2014**, *40*, 11094–11111.

[28] Muradov, N. Z.; Veziroğlu, T. N. *Int. J. Hydrogen Energy* **2005**, *30*, 225–237.

[29] Zanfir, M.; Gavriilidis, A. *Chem. Eng. Sci.* **2003**, *58*, 3947–3960.

[30] Crabtree, G. W.; Dresselhaus, M. S.; Buchanan, M. V. *Phys. Today* **2004**, *57*, 39–44.

[31] Dresselhaus, M. S.; Thomas, I. L. *Nature* **2001**, *414*, 332–337.

[32] Lasia, A. Hydrogen evolution reaction. In *Handbook of Fuel Cells - Fundamentals, Technology and Applications*; Vielstich, W., Lamm, A., Gasteiger, H. A., Eds.; Wiley: West Sussex, 2010; pp 416–440.

[33] Zou, X.; Zhang, Y. *Chem. Soc. Rev.* **2015**, *44*, 5148–5180.

[34] Mahmood, N.; Yao, Y.; Zhang, J. W.; Pan, L.; Zhang, X.; Zou, J. J. *Adv. Sci.* **2018**, *5*, 1700464.

[35] McCrory, C. C. L.; Jung, S.; Ferrer, I. M.; Chatman, S. M.; Peters, J. C.; Jaramillo, T. F. *J. Am. Chem. Soc.* **2015**, *137*, 4347–4357.

[36] Greeley, J.; Jaramillo, T.; Bonde, J.; Chorkendorff, I.; Nørskov, J. K. *Nat. Mater.* **2006**, *5*, 909–913.

[37] Chen, S.; Takata, T.; Domen, K. *Nat. Rev. Mater.* **2017**, *2*, 1–17.

[38] Fang, S.; Hu, Y. H. *Int. J. Energy Res.* **2019**, *43*, 1082–1098.

[39] Jamesh, M. I.; Kuang, Y.; Sun, X. *ChemCatChem* **2019**, *11*, 1550–1575.

[40] Yan, Y.; Xia, B. Y.; Zhao, B.; Wang, X. *J. Mater. Chem. A* **2016**, *4*, 17587–17603.

[41] Jiang, N.; You, B.; Sheng, M.; Sun, Y. *Angew. Chem. Int. Ed.* **2015**, *127*, 6349–6352.

[42] Walter, M. G.; Warren, E. L.; McKone, J. R.; Boettcher, S. W.; Mi, Q.; Santori, E. A.; Lewis, N. S. *Chem. Rev.* **2010**, *110*, 6446–6473.

[43] Wang, H.; Lee, H. W.; Deng, Y.; Lu, Z.; Hsu, P. C.; Liu, Y.; Lin, D.; Cui, Y. *Nat. Commun.* **2015**, *6*, 1–8.

[44] Yu, F.; Zhou, H.; Huang, Y.; Sun, J.; Qin, F.; Bao, J.; Goddard, W. A.; Chen, S.; Ren, Z. *Nat. Commun.* **2018**, *9*, 1–9.

[45] Skúlason, E.; Karlberg, G. S.; Rossmeisl, J.; Bligaard, T.; Greeley, J.; Jónsson, H.; Nørskov, J. K. *Phys. Chem. Chem. Phys.* **2007**, *9*, 3241–3250.

[46] Skúlason, E.; Tripkovic, V.; Bjorketun, M. E.; Gudmundsdottir, S.; Karlberg, G.; Rossmeisl, J.; Bligaard, T.; Jónsson, H.; Nørskov, J. K. *J. Phys. Chem. C* **2010**, *114*, 18182–18197.

[47] Safizadeh, F.; Ghali, E.; Houlachi, G. *Int. J. Hydrog. Energy* **2015**, *40*, 256–274.

[48] Gómez, R.; Orts, J. M.; Álvarez-Ruiz, B.; Feliu, J. M. *J. Phys. Chem. B* **2004**, *108*, 228–238.

[49] Ogasawara, H.; Ito, M. *Chem. Phys. Lett.* **1994**, *221*, 213–218.

[50] Marković, N. M.; Grgur, B. N.; Ross, P. N. *J. Phys. Chem. B* **1997**, *101*, 5405–5413.

[51] Christmann, K.; Ertl, G.; Pignet, T. *Surf. Sci.* **1976**, *54*, 365–392.

[52] Skúlason, E.; Faraj, A. A.; Kristinsdóttir, L.; Hussain, J.; Garden, A. L.; Jónsson, H. *Top. Catal.* **2014**, *57*, 273–281.

[53] Bao, D. *Resour. Policy* **2020**, *68*, 101772.

[54] Grzeszczuk, M.; Poks, P. *Electrochim. Acta* **2000**, *45*, 4171–4177.

[55] Nørskov, J. K.; Bligaard, T.; Rossmeisl, J.; Christensen, C. H. *Nat. Chem.* **2009**, *1*, 37–46.

[56] Lewis, N. S.; Nocera, D. G. *Proc. Natl. Acad. Sci. U. S. A.* **2006**, *103*, 15729–15735.

[57] McKone, J. R.; Marinescu, S. C.; Brunschwig, B. S.; Winkler, J. R.; Gray, H. B. *Chem. Sci.* **2014**, *5*, 865–878.

[58] Raj, I. A.; Vasu, K. I. *J. Appl. Electrochem.* **1992**, *22*, 471–477.

[59] Ito, Y.; Cong, W.; Fujita, T.; Tang, Z.; Chen, M. *Angew. Chem. Int. Ed.* **2015**, *54*, 2131–2136.

[60] Abghoui, Y.; Skúlason, E. *J. Phys. Chem. C* **2017**, *121*, 24036–24045.

[61] Li, Y.; Wang, H.; Xie, L.; Liang, Y.; Hong, G.; Dai, H. *J. Am. Chem. Soc.* **2011**, *133*, 7296–7299.

[62] Voiry, D.; Salehi, M.; Silva, R.; Fujita, T.; Chen, M.; Asefa, T.; Shenoy, V. B.; Eda, G.; Chhowalla, M. *Nano Lett.* **2013**, *13*, 6222–6227.

[63] Fujita, T.; Ito, Y.; Tan, Y.; Yamaguchi, H.; Hojo, D.; Hirata, A.; Voiry, D.; Chhowalla, M.; Chen, M. *Nanoscale* **2014**, *6*, 12458–12462.

[64] Jaramillo, T. F.; Jørgensen, K. P.; Bonde, J.; Nielsen, J. H.; Horch, S.; Chorkendorff, I. *Science* **2007**, *317*, 100–102.

[65] Evans, D. J.; Pickett, C. J. *Chem. Soc. Rev.* **2003**, *32*, 268–275.

[66] Jaegermann, W.; Tributsch, H. *Prog. Surf. Sci.* **1988**, *29*, 161–167.

[67] Margulis, L.; Salitra, G.; Tenne, R.; Talianker, M. *Nature* **1993**, *365*, 113–114.

[68] Feldman, Y.; Wasserman, E.; Srolovitz, D. J.; Tenne, R. *Science* **1995**, *267*, 222–228.

[69] Helveg, S.; Lauritsen, J. V.; Lægsgaard, E.; Stensgaard, I.; Nørskov, J. K.; Clausen, B. S.; Topsøe, H.; Besenbacher, F. *Phys. Rev. Lett.* **2000**, *84*, 951–955.

[70] Lauritsen, J. V.; Kibsgaard, J.; Helveg, S.; Topsøe, H.; Clausen, B. S.; Lægsgaard, E.; Besenbacher, F. *Nat. Nanotechnol.* **2007**, *2*, 53–58.

[71] Li, T.; Galli, G. *J. Phys. Chem. C* **2007**, *111*, 16192–16196.

[72] Bonde, J.; Moses, P. G.; Jaramillo, T. F.; Nørskov, J. K.; Chorkendorff, I. *Farad. Discuss.* **2009**, *140*, 219–231.

[73] Benck, J. D.; Hellstern, T. R.; Kibsgaard, J.; Chakthranont, P.; Jaramillo, T. F. *ACS Catal.* **2014**, *4*, 3957–3971.

[74] Nørskov, J. K.; Bligaard, T.; Logadottir, A.; Kitchin, J. R.; Chen, J. G.; Pandelov, S.; Stimming, U. *J. Electrochem. Soc.* **2005**, *152*, 23–26.

[75] Kibsgaard, J.; Jaramillo, T. F.; Besenbacher, F. *Nat. Chem.* **2014**, *6*, 248–253.

[76] Tsai, C.; Chan, K.; Nørskov, J. K.; Abild-Pedersen, F. *Surf. Sci.* **2015**, *640*, 133–140.

[77] Tsai, C.; Abild-Pedersen, F.; Nørskov, J. K. *Nano Lett.* **2014**, *14*, 1381–1387.

[78] Theerthagiri, J.; Lee, S. J.; Murthy, A. P.; Madhavan, J.; Choi, M. Y. *Curr. Opin. Solid State Mater. Sci.* **2020**, *24*, 100805.

[79] Chen, W. F.; Muckerman, J. T.; Fujita, E. *Chem. Commun.* **2013**, *49*, 8896–8909.

[80] Xie, J.; Xie, Y. *Chem. Eur. J.* **2016**, *22*, 3588–3598.

[81] Zheng, P.; Zhao, J.; Zheng, J.; Ma, G.; Zhu, Z. *J. Mater. Chem.* **2012**, *22*, 12116–12120.

[82] Han, Y.; Yue, X.; Jin, Y.; Huang, X.; Shen, P. K. *J. Mater. Chem. A* **2016**, *4*, 3673–3677.

[83] Chen, W. F.; Sasaki, K.; Ma, C.; Frenkel, A. I.; Marinkovic, N.; Muckerman, J. T.; Zhu, Y.; Adzic, R. R. *Angew. Chem. Int. Ed.* **2012**, *51*, 6131–6135.

[84] Cao, B.; Veith, G. M.; Neuefeind, J. C.; Adzic, R. R.; Khalifah, P. G. *J. Am. Chem. Soc.* **2013**, *135*, 19186–19192.

[85] Wirth, S.; Harnisch, F.; Weinmann, M.; Schröder, U. *Appl. Catal. B Environ.* **2012**, *126*, 225–230.

[86] Peng, X.; Pi, C.; Zhang, X.; Li, S.; Huo, K.; Chu, P. K. *Sustain. Energy Fuels* **2019**, *3*, 366–381.

[87] Karaballi, R. A.; Monfared, Y. E.; Dasog, M. *Chem. Eur. J.* **2020**, *26*, 8499–8505.

[88] Reinholdt, A.; Pecenka, R.; Pinchuk, A.; Runte, S.; Stepanov, A. L.; Weirich, T. E.; Kreibig, U. *Eur. Phys. J. D* **2004**, *31*, 69–76.

[89] Dreizler, R. M.; Engel, E. *Density Functional Theory: An Advanced Course*; Springer: London, 2011.

[90] Cramer, C. J. *Essentials of Computational Chemistry: Theories and Models*; Wiley: Chichester, 2013.

[91] Born, M.; Oppenheimer, R. *Ann. Phys.* **1927**, *389*, 457–484.

[92] Hartree, D. R.; Hartree, W. *Proc. R. Soc. A* **1935**, *150*, 9–33.

[93] Helgaker, T.; Jørgensen, P.; Olsen, J. *Molecular Electronic-structure Theory*; Wiley: Chichester, 2014.

[94] Levine, I. N. *Quantum Chemistry*, 5th ed.; Prentice Hall: New York, 1999.

[95] Jensen, F. *Introduction to Computational Chemistry*, 2nd ed.; Wiley: Chichester, 2008.

[96] Rossi, E.; Bendazzoli, G. L.; Evangelisti, S.; Maynau, D. *Chem. Phys. Lett.* **1999**, *310*, 530–536.

[97] Mach, P.; Hubač, I.; Mavridis, A. *Chem. Phys. Lett.* **1994**, *226*, 469–474.

[98] Møller, C.; Plesset, M. S. *Phys. Rev.* **1934**, *46*, 618–622.

[99] Kohn, W. *Rev. Mod. Phys.* **1999**, *71*, 1253–1259.

[100] Levy, M.; Perdew, J. P. The Constrained Search Formulation of Density Functional Theory. In *Density Functional Methods In Physics*; Dreizler, R. M., Providência, J., Eds.; Springer: Boston, 1985; pp 11–30.

[101] Young, D. Density Functional Theory. In *Computational Chemistry: A Practical Guide for Applying Techniques to Real-World Problems.*; Wiley: New York, 2020; pp 42–48.

[102] Hohenberg, P.; Kohn, W. *Phys. Rev.* **1964**, *136*, B864.

[103] Parr, R. Density Functional Theory of Atoms and Molecules. In *Horizons of Quantum Chemistry*; Fukui, K., Pullman, A., Eds.; D. Reidel: London, 2012; Vol. 3; pp 5–15.

[104] Kohn, W.; Sham, L. J. *Phys. Rev.* **1965**, *140*, A1133.

[105] Goerigk, L.; Hansen, A.; Bauer, C.; Ehrlich, S.; Najibi, A.; Grimme, S. *Phys. Chem. Chem. Phys.* **2017**, *19*, 32184–32215.

[106] Perdew, J. P.; McMullen, E. R.; Zunger, A. *Phys. Rev. A* **1981**, *23*, 2785–2789.

[107] Johnson, B. G.; Gill, P. M. W.; Pople, J. A. *J. Chem. Phys.* **1993**, *98*, 5612–5626.

[108] Pederson, M. R.; Jackson, K. A.; Pickett, W. E. *Phys. Rev. B* **1991**, *44*, 3891–3893.

[109] Haas, P.; Tran, F.; Blaha, P. *Phys. Rev. B* **2009**, *79*, 85104.

[110] Stampfl, C.; Mannstadt, W.; Asahi, R.; Freeman, A. J. *Phys. Rev. B* **2001**, *63*, 155106.

[111] Mardirossian, N.; Head-Gordon, M. *Mol. Phys.* **2017**, *115*, 2315–2372.

[112] Rappoport, D.; Crawford, N. R. M.; Furche, F.; Burke, K. Approximate Density Functionals: Which Should I Choose? In *Encyclopedia of Inorganic Chemistry*; King, B. R., Ed.; Wiley: New York, 2009; pp 5191–5203.

[113] Perdew, J. P.; Chevary, J. A.; Vosko, S. H.; Jackson, K. A.; Pederson, M. R.; Singh, D. J.; Fiolhais, C. *Phys. Rev. B* **1992**, *46*, 6671–6674.

[114] Jones, R. O.; Gunnarsson, O. *Rev. Mod. Phys.* **1989**, *61*, 689–691.

[115] Tuma, C.; Boese, A. D.; Handy, N. C. *Phys. Chem. Chem. Phys.* **1999**, *1*, 3939–3947.

[116] Wellendorff, J.; Lundgaard, K. T.; Møgelhøj, A.; Petzold, V.; Landis, D. D.; Nørskov, J. K.; Bligaard, T.; Jacobsen, K. W. *Phys. Rev. B* **2012**, *85*, 235149.

[117] Santra, G.; Martin, J. M. *J. Chem. Theory Comput.* **2021**, *17*, 1368–1379.

[118] Becke, A. D. *Phys. Rev.* **1988**, *38*, 3098–3101.

[119] Heyd, J.; Scuseria, G. E.; Ernzerhof, M. *J. Chem. Phys.* **2003**, *118*, 8207–8215.

[120] Grimme, S. *J. Comput. Chem.* **2004**, *25*, 1463–1473.

[121] Allen, M. J.; Tozer, D. J. *J. Chem. Phys.* **2002**, *117*, 11113–11120.

[122] Sherrill, C. D. *J. Chem. Phys.* **2010**, *132*, 18–301.

[123] Grimme, S.; Antony, J.; Ehrlich, S.; Krieg, H. *J. Chem. Phys.* **2010**, *132*, 241733.

[124] Dion, M.; Rydberg, H.; Schröder, E.; Langreth, D. C.; Lundqvist, B. I. *Phys. Rev. Lett.* **2004**, *92*, 246401.

[125] Yuan, D.; Liao, H.; Hu, W. *Phys. Chem. Chem. Phys.* **2019**, *21*, 21049–21056.

[126] Gautier, S.; Steinmann, S. N.; Michel, C.; Fleurat-Lessard, P.; Sautet, P. *Phys. Chem. Chem. Phys.* **2015**, *17*, 28921–28930.

[127] Hofmann, P. *Solid State Physics: An Introduction*, 8th ed.; Wiley: New York, 2015.

[128] Bloch, F. *Z. Phys.* **1929**, *52*, 555–600.

[129] Kittel, C. In *Introduction to Solid State Physics*; Johnson, S., Ed.; Wiley: Hoboken, 2005.

[130] Blöchl, P. E. *Phys. Rev. B* **1994**, *50*, 17953–17979.

[131] Mortensen, J. J.; Hansen, L. B.; Jacobsen, K. W. *Phys. Rev. B* **2005**, *71*, 035109.

[132] Chase, M. W. *J. Phys. Chem. Ref. Data.* **1996**, *25*, 551–603.

[133] Irikura, K. K. *J. Phys. Chem. Ref. Data.* **2007**, *36*, 389–397.

[134] Jónsson, H.; Mills, G.; Jacobsen, K. W. Nudged elastic band method for finding minimum energy paths of transitions. In *Classical and Quantum Dynamics in Condensed Phase Simulations*; Berne, B., Ciccotti, G., Coker, D., Eds.; World Scientific: Singapore, 1998; pp 385–404.

[135] Henkelman, G.; Uberuaga, B. P.; Jónsson, H. *J. Chem. Phys.* **2000**, *113*, 9901–9904.

[136] Lopez-Acevedo, O.; Akola, J.; Whetten, R. L.; Grönbeck, H.; Häkkinen, H. *J. Phys. Chem. C* **2009**, *113*, 5035–5038.

[137] Schebarchov, D.; Gaston, N. *Phys. Chem. Chem. Phys.* **2011**, *13*, 21109–21115.

[138] Bader, R. F. *Chem. Rev.* **1991**, *91*, 893–928.

[139] Henkelman, G.; Arnaldsson, A.; Jónsson, H. *Comput. Mater. Sci.* **2006**, *36*, 354–360.

[140] Tang, W.; Sanville, E.; Henkelman, G. *J. Phys. Condens. Matter* **2009**, *21*, 084204.

[141] Kresse, G.; Furthmüller, J. *Comput. Mater. Sci.* **1996**, *6*, 15–50.

[142] Kresse, G.; Joubert, D. *Phys. Rev. B* **1999**, *59*, 1758.

[143] Ruffman, C.; Gordon, C. K.; Skúlason, E.; Garden, A. L. *J. Phys. Chem. C* **2020**, *124*, 17015–17026.

[144] Casey-Stevens, C. A.; Lambie, S. G.; Ruffman, C.; Skúlason, E.; Garden, A. L. *J. Phys. Chem. C* **2019**, *123*, 30458–30466.

[145] Dahl, S.; Logadottir, A.; Egeberg, R. C.; Larsen, J. H.; Chorkendorff, I.; Törnqvist, E.; Nørskov, J. K. *Phys. Rev. Lett.* **1999**, *83*, 1814–1817.

[146] Urabe, K.; Aika, K. I.; Ozaki, A. *J. Catal.* **1974**, *32*, 108–113.

[147] Schöneich, C. *Biochim. Biophys. Acta* **2005**, *1703*, 111–119.

[148] Kunimatsu, K.; Senzaki, T.; Tsushima, M.; Osawa, M. *Chem. Phys. Lett.* **2005**, *401*, 451–454.

[149] Tavares, M. C.; Machado, S. A. S.; Mazo, L. H. *Electrochim. Acta* **2001**, *46*, 4359–4369.

[150] Cheng, X.; Li, Y.; Zheng, L.; Yan, Y.; Zhang, Y.; Chen, G.; Sun, S.; Zhang, J. *Energy Environ. Sci.* **2017**, *10*, 2450–2458.

[151] Li, Y.; Chen, S.; Long, R.; Ju, H.; Wang, Z.; Yu, X.; Gao, F.; Cai, Z.; Wang, C.; *et al.*, *Nano Energy* **2017**, *34*, 306–312.

[152] Wang, G.; Liu, J.; Sui, Y.; Wang, M.; Qiao, L.; Du, F.; Zou, B. *J. Mater. Chem. A* **2019**, *7*, 14876–14881.

[153] Rendón-Calle, A.; Builes, S.; Calle-Vallejo, F. *Curr. Opin. Electrochem.* **2018**, *9*, 158–165.

[154] O'Mullane, A. P. *Nanoscale* **2014**, *6*, 4012–4026.

[155] Holewinski, A.; Linic, S. *J. Electrochem. Soc.* **2012**, *159*, H864–H870.

[156] Anantharaj, S.; Noda, S.; Driess, M.; Menezes, P. W. *ACS Energy Lett.* **2021**, *6*, 1607–1611.

[157] Tafel, J. *Z. Phys. Chem.* **1905**, *50*, 641–712.

[158] Heyrovsky, J. *Rec. Travaux Chim. Pays-Bas* **1927**, *46*, 582–585.

[159] Trasatti, S. *J. Electroanal. Chem.* **1972**, *39*, 163–184.

[160] Tang, S.; Wu, W.; Zhang, S.; Ye, D.; Zhong, P.; Li, X.; Liu, L.; Li, Y. F. *Phys. Chem. Chem. Phys.* **2018**, *20*, 1861–1871.

[161] Markovića, N. M.; Sarraf, S. T.; Gasteiger, H. A.; Ross, P. N. *J. Chem. Soc., Faraday Trans.* **1996**, *92*, 3719–3725.

[162] Marković, N. M.; Ross, P. N. *Surf. Sci. Rep.* **2002**, *45*, 117–229.

[163] Vitos, L.; Ruban, A. V.; Skriver, H. L.; Kollár, J. *Surf. Sci.* **1998**, *411*, 186–202.

[164] McCrum, I. T.; Hickner, M. A.; Janik, M. J. *Langmuir* **2017**, *33*, 7043–7052.

[165] Santana, J. A.; Mateo, J. J.; Ishikawa, Y. *J. Phys. Chem. C* **2010**, *114*, 4995–5002.

[166] Huang, Y.; Nielsen, R. J.; Goddard III, W. A.; Soriaga, M. P. *J. Am. Chem. Soc.* **2015**, *137*, 6692–6698.

[167] Hansen, L. P.; Ramasse, Q. M.; Kisielowski, C.; Brorson, M.; Johnson, E.; Topsøe, H.; Helveg, S. *Angew. Chem. Int. Ed.* **2011**, *50*, 10153–10156.

[168] Bruix, A.; Lauritsen, J. V.; Hammer, B. *Faraday Discuss.* **2016**, *188*, 323–343.

[169] Bollinger, M. V.; Lauritsen, J. V.; Jacobsen, K. W.; Nørskov, J. K.; Helveg, S.; Besenbacher, F. *Phys. Rev. Lett.* **2001**, *87*, 196803.

[170] Raybaud, P.; Hafner, J.; Kresse, G.; Kasztelan, S.; Toulhoat, H. *J. Catal.* **2000**, *190*, 128–143.

[171] Li, H.; Tsai, C.; Koh, A. L.; Cai, L.; Contryman, A. W.; Fragapane, A. H.; Zhao, J.; Han, H. S.; Manoharan, H. C.; Abild-Pedersen, F.; Nørskov, J. K.; Zheng, X. *Nat. Mater.* **2016**, *15*, 48–53.

[172] Nørskov, J. K.; Rossmeisl, J.; Logadottir, A.; Lindqvist, L.; Kitchin, J. R.; Bligaard, T.; Jonsson, H. *J. Phys. Chem. B* **2004**, *108*, 17886–17892.

[173] Peterson, A. A.; Abild-Pedersen, F.; Studt, F.; Rossmeisl, J.; Nørskov, J. K. *Energy Environ. Sci.* **2010**, *3*, 1311–1315.

[174] Wu, Z.-Y. et al. *Nat. Commun.* **2021**, *12*, 1–10.

[175] Tang, Q.; Jiang, D. E. *ACS Catal.* **2016**, *6*, 4953–4961.

[176] Rostamikia, G.; Mendoza, A. J.; Hickner, M. A.; Janik, M. J. *J. Power Sources* **2011**, *196*, 9228–9237.

[177] Nie, X.; Esopi, M. R.; Janik, M. J.; Asthagiri, A. *Angew. Chem. Int. Ed.* **2013**, *52*, 2459–2462.

[178] Nie, X.; Luo, W.; Janik, M. J.; Asthagiri, A. *J. Catal.* **2014**, *312*, 108–122.

[179] Akhade, S. A.; Bernstein, N. J.; Esopi, M. R.; Regula, M. J.; Janik, M. J. *Catal. Today* **2017**, *288*, 63–73.

[180] Chan, K.; Nørskov, J. K. *J. Phys. Chem. Lett.* **2015**, *6*, 2663–2668.

[181] Chan, K.; Nørskov, J. K. *J. Phys. Chem. Lett.* **2016**, *7*, 1686–1690.

[182] Guidelli, R.; Schmickler, W. *Electrochim. Acta* **2000**, *45*, 2317–2338.

[183] Gross, A.; Gossenberger, F.; Lin, X.; Naderian, M.; Sakong, S.; Roman, T. *J. Electrochem. Soc.* **2014**, *161*, E3015–E3020.

[184] Holmberg, N.; Laasonen, K. *J. Phys. Chem. C* **2015**, *119*, 16166–16178.

[185] Nosé, S. *J. Chem. Phys.* **1984**, *81*, 511–519.

[186] Schnur, S.; Groß, A. *New J. Phys.* **2009**, *11*, 125003.

[187] Marenich, A. V.; Ho, J.; Coote, M. L.; Cramer, C. J.; Truhlar, D. G. *Phys. Chem. Chem. Phys.* **2014**, *16*, 15068–15106.

[188] Kötz, E. R.; Neff, H.; Müller, K. *J. Electroanal. Chem.* **1986**, *215*, 331–344.

[189] Fawcett, W. R. *Langmuir* **2008**, *24*, 9868–9875.

[190] Tayyebi, E.; Hussain, J.; Abghoui, Y.; Skúlason, E. *J. Phys. Chem. C* **2018**, *122*, 10078–10087.

[191] Fearon, J.; Watson, G. W. *J. Mater. Chem.* **2006**, *16*, 1989–1996.

[192] Kristinsdóttir, L.; Skúlason, E. *Surf. Sci.* **2012**, *606*, 1400–1404.

[193] Rossmeisl, J.; Chan, K.; Skúlason, E.; Björketun, M. E.; Tripkovic, V. *Catal. Today* **2016**, *262*, 36–40.

[194] Hakala, M.; Kronberg, R.; Laasonen, K. *Sci. Rep.* **2017**, *7*, 15243.

[195] Ouyang, Y.; Ling, C.; Chen, Q.; Wang, Z.; Shi, L.; Wang, J. *Chem. Mater.* **2016**, *28*, 4390–4396.

[196] Mathew, K.; Sundararaman, R.; Letchworth-Weaver, K.; Arias, T. A.; Hennig, R. G. *J. Chem. Phys.* **2014**, *140*, 84106.

[197] Mathew, K.; Kolluru, V. S.; Mula, S.; Steinmann, S. N.; Hennig, R. G. *J. Chem. Phys.* **2019**, *151*, 234101.

[198] Van Den Bossche, M.; Skúlason, E.; Rose-Petruck, C.; Jónsson, H. *J. Phys. Chem. C* **2019**, *123*, 4116–4124.

[199] Ruffman, C.; Gordon, C. K.; Gilmour, J. T.; Mackenzie, F. D.; Garden, A. L. *Nanoscale* **2021**, *13*, 3106–3118.

[200] Zhang, X.; Zhou, F.; Zhang, S.; Liang, Y.; Wang, R. *Adv. Sci.* **2019**, *6*, 1900090.

[201] Voiry, D. et al. *Nat. Mater.* **2016**, *15*, 1003–1009.

[202] Chen, W.; Santos, E. J.; Zhu, W.; Kaxiras, E.; Zhang, Z. *Nano Lett.* **2013**, *13*, 509–514.

[203] Duan, J.; Chen, S.; Jaroniec, M.; Qiao, S. Z. *ACS Catal.* **2015**, *5*, 5207–5234.

[204] Kumar, A.; Xu, Q. *ChemNanoMat* **2018**, *4*, 28–40.

[205] Deng, J.; Li, H.; Wang, S.; Ding, D.; Chen, M.; Liu, C.; Tian, Z.; Novoselov, K. S.; Ma, C.; Deng, D.; Bao, X. *Nat. Commun.* **2017**, *8*, 1–8.

[206] Liu, M.; Hybertsen, M. S.; Wu, Q. *Angew. Chem. Int. Ed.* **2020**, *59*, 14835–14841.

[207] Bollinger, M. V.; Jacobsen, K. W.; Nørskov, J. K. *Phys. Rev. B* **2003**, *67*, 085410.

[208] Li, X.; Guo, S.; Li, W.; Ren, X.; Su, J.; Song, Q.; Sobrido, A. J.; Wei, B. *Nano Energy* **2019**, *57*, 388–397.

[209] Stankovich, S.; Dikin, D. A.; Dommett, G. H.; Kohlhaas, K. M.; Zimney, E. J.; Stach, E. A.; Piner, R. D.; Nguyen, S. B. T.; Ruoff, R. S. *Nature* **2006**, *442*, 282–286.

[210] Saxena, S.; Tyson, T. A.; Negusse, E. *J. Phys. Chem. Lett.* **2010**, *1*, 3433–3437.

[211] Ma, C.; Shao, X.; Cao, D. *J. Mater. Chem.* **2012**, *22*, 8911–8915.

[212] Jing, Y.; Zhou, Z. *ACS Catal.* **2015**, *5*, 4309–4317.

[213] Woldetinsay, M.; Refera, T.; Olu, F.; Maiyalagan, T. *Mater. Chem. Phys.* **2020**, *251*, 123106.

[214] Shahzad, F.; Kumar, P.; Yu, S.; Lee, S.; Kim, Y. H.; Hong, S. M.; Koo, C. M. *J. Mater. Chem. C* **2015**, *3*, 9802–9810.

[215] Melissen, S.; Le Bahers, T.; Steinmann, S. N.; Sautet, P. *J. Phys. Chem. C* **2015**, *119*, 25188–25196.

[216] Agnoli, S.; Favaro, M. *J. Mater. Chem. A* **2016**, *4*, 5002–5025.

[217] Tang, Y. B.; Yin, L. C.; Yang, Y.; Bo, X. H.; Cao, Y. L.; Wang, H. E.; Zhang, W. J.; Bello, I.; Lee, S. T.; Cheng, H. M.; Lee, C. S. *ACS Nano* **2012**, *6*, 1970–1978.

[218] Li, X. F.; Lian, K. Y.; Liu, L.; Wu, Y.; Qiu, Q.; Jiang, J.; Deng, M.; Luo, Y. *Sci. Rep.* **2016**, *6*, 23495.

[219] Lu, X.; Wang, D.; Ge, L.; Xiao, L.; Zhang, H.; Liu, L.; Zhang, J.; An, M.; Yang, P. *New J. Chem.* **2018**, *42*, 19665–19670.

[220] Hammer, B.; Nørskov, J. K. *Surf. Sci.* **1995**, *343*, 211–220.

[221] Shi, Y.; Zhou, Y.; Yang, D. R.; Xu, W. X.; Wang, C.; Wang, F. B.; Xu, J. J.; Xia, X. H.; Chen, H. Y. *J. Am. Chem. Soc.* **2017**, *139*, 15479–15485.

[222] Park, S.; Park, J.; Abroshan, H.; Zhang, L.; Kim, J. K.; Zhang, J.; Guo, J.; Siahrostami, S.; Zheng, X. *ACS Energy Lett.* **2018**, *3*, 2685–2693.

[223] Tsai, C.; Li, H.; Park, S.; Park, J.; Han, H. S.; Nørskov, J. K.; Zheng, X.; Abild-Pedersen, F. *Nat. Commun.* **2017**, *8*, 15113.

[224] Xie, J.; Zhang, H.; Li, S.; Wang, R.; Sun, X.; Zhou, M.; Zhou, J.; Lou, X. W.; Xie, Y. *Adv. Mater.* **2013**, *25*, 5807–5813.

[225] Wang, Z.; Chen, Q.; Wang, J. *J. Phys. Chem. C* **2015**, *119*, 4752–4758.

[226] Gao, G.; Sun, Q.; Du, A. *J. Phys. Chem. C* **2016**, *120*, 16761–16766.

[227] Lukowski, M. A.; Daniel, A. S.; Meng, F.; Forticaux, A.; Li, L.; Jin, S. *J. Am. Chem. Soc.* **2013**, *135*, 10274–10277.

[228] Song, L.; Zhao, M.; Li, X.; Zhang, Z.; Qu, L. *RSC Adv.* **2016**, *6*, 70740–70746.

[229] Zhou, X.; Prikryl, J.; Krbal, M.; Macak, J. M.; Schmuki, P. *Electrochem. Commun.* **2017**, *82*, 112–116.

[230] Jian, W.; Cheng, X.; Huang, Y.; You, Y.; Zhou, R.; Sun, T.; Xu, J. *Chem. Eng. J.* **2017**, *328*, 474–483.

[231] Remskar, M.; Mrzel, A.; Skraba, Z.; Jesih, A.; Ceh, M.; Demšar, J.; Stadelmann, P.; Lévy, F.; Mihailovic, D. *Science* **2001**, *292*, 479–481.

[232] Deepak, F. L.; Jose-Yacaman, M. *Isr. J. Chem.* **2010**, *50*, 426–438.

[233] Shi, W.; Wang, Z.; Fu, Y. Q. *J. Nanoparticle Res.* **2017**, *19*, 1–7.

[234] de Alencar Rocha, R.; da Cunha, W. F.; Ribeiro, L. A. *J. Mol. Model.* **2019**, *25*, 290.

[235] Li, W.; Zhang, G.; Guo, M.; Zhang, Y.-W. W. *Nano Res.* **2014**, *7*, 518–527.

[236] Xiao, J.; Long, M.; Li, X.; Xu, H.; Huang, H.; Gao, Y. *Sci. Rep.* **2014**, *4*, 4327.

[237] Cardoso, G. L.; Piquini, P. C.; Ahuja, R. *Energy Fuels* **2021**, *35*, 6282–6288.

[238] Seifert, G.; Terrones, H.; Terrones, M.; Jungnickel, G.; Frauenheim, T. *Phys. Rev. Lett.* **2000**, *85*, 146–149.

[239] Ansari, R.; Malakpour, S.; Faghihnasiri, M.; Sahmani, S. *Superlattices Microstruct.* **2015**, *82*, 188–200.

[240] Zhou, W.; Zou, X.; Najmaei, S.; Liu, Z.; Shi, Y.; Kong, J.; Lou, J.; Ajayan, P. M.; Yakobson, B. I.; Idrobo, J. C. *Nano Lett.* **2013**, *13*, 2615–2622.

[241] Qiu, H.; Xu, T.; Wang, Z.; Ren, W.; Nan, H.; Ni, Z.; Chen, Q.; Yuan, S.; Miao, F.; Song, F.; Long, G.; Shi, Y.; Sun, L.; Wang, J.; Wang, X. *Nat. Commun.* **2013**, *4*, 2642.

[242] Yang, Y.; Liu, Y.; Man, B.; Zhao, M.; Li, W. *RSC Adv.* **2019**, *9*, 17203–17210.

[243] Xiong, Q. L.; Zhang, J.; Xiao, C.; Li, Z. H. *Phys. Chem. Chem. Phys.* **2017**, *19*, 19948–19958.

[244] Xiong, S.; Cao, G. *Nanotechnology* **2016**, *27*, 105701.

[245] Li, W.; Liu, G.; Li, J.; Wang, Y.; Ricardez-Sandoval, L.; Zhang, Y.; Zhang, Z. *Appl. Surf. Sci.* **2019**, 143869.

[246] Niyitanga, T.; Evans, P. E.; Ekanayake, T.; Dowben, P. A.; Jeong, H. K. *J. Electroanal. Chem.* **2019**, *845*, 39–47.

[247] Wang, J.; Liu, J.; Yang, H.; Chen, Z.; Lin, J.; Shen, Z. X. *J. Mater. Chem. A* **2016**, *4*, 7565–7572.

[248] Honkala, K.; Hellman, A.; Remediakis, I. N.; Logadottir, A.; Carlsson, A.; Dahl, S.; Christensen, C. H.; Nørskov, J. K. *Science* **2005**, *307*, 555–558.

[249] Légaré, P. *Surf. Sci.* **2004**, *559*, 169–178.

[250] Zhang, M.; Weng, M.; Tamura, T.; Goto, M.; Yamane, I.; Yanase, T.; Nagahama, T.; Shimada, T. *Phys. E Low-Dimensional Syst. Nanostructures* **2021**, *130*, 114693.

[251] Enyashin, A.; Gemming, S.; Seifert, G. *Eur. Phys. J. Spec. Top.* **2007**, *149*, 103–125.

[252] Jin, B.; Zhou, X.; Huang, L.; Licklederer, M.; Yang, M.; Schmuki, P. *Angew. Chem. Int. Ed* **2016**, *128*, 12440–12444.

[253] Wang, Y.; Ma, Z.; Chen, Y.; Zou, M.; Yousaf, M.; Yang, Y.; Yang, L.; Cao, A.; Han, R. P. *Adv. Mater.* **2016**, *28*, 10175–10181.

[254] Bisbo, M. K.; Hammer, B. *Preprint*, **2020**.

[255] Wang, H.; Li, J.; Li, K.; Lin, Y.; Chen, J.; Gao, L.; Nicolosi, V.; Xiao, X.; Lee, J. M. *Chem. Soc. Rev.* **2021**, *50*, 1354–1390.

[256] Zhong, Y.; Xia, X.; Shi, F.; Zhan, J.; Tu, J.; Fan, H. J. *Adv. Sci.* **2016**, *3*, 1500286.

[257] Lengauer, W. *Surf. Interface Anal.* **1990**, *15*, 377–382.

[258] Shin, C. S.; Gall, D.; Kim, Y. W.; Hellgren, N.; Petrov, I.; Greene, J. E. *J. Appl. Phys.* **2002**, *92*, 5084–5093.

[259] Ishikawa, A.; Takata, T.; Kondo, J. N.; Hara, M.; Domen, K. *J. Phys. Chem. B* **2004**, *108*, 11049–11053.

[260] Oyama, S. T. Introduction to the Chemistry of Transition Metal Carbides and Nitrides. In *The Chemistry of Transition Metal Carbides and Nitrides*; Chapman & Hall: Glasgow, 1996; pp 1–27.

[261] Choi, D.; Kumta, P. N. *J. Am. Ceram. Soc.* **2007**, *90*, 3113–3120.

[262] Xie, J.; Li, S.; Zhang, X.; Zhang, J.; Wang, R.; Zhang, H.; Pan, B.; Xie, Y. *Chem. Sci.* **2014**, *5*, 4615–4620.

[263] Xiong, J.; Cai, W.; Shi, W.; Zhang, X.; Li, J.; Yang, Z.; Feng, L.; Cheng, H. *J. Mater. Chem. A* **2017**, *5*, 24193–24198.

[264] Ho, C. T.; Low, K. B.; Klie, R. F.; Maeda, K.; Domen, K.; Meyer, R. J.; Snee, P. T. *J. Phys. Chem. C* **2011**, *115*, 647–652.

[265] Yuliati, L.; Yang, J. H.; Wang, X.; Maeda, K.; Takata, T.; Antonietti, M.; Domen, K. *J. Mater. Chem.* **2010**, *20*, 4295–4298.

[266] Doye, J. P.; Wales, D. J. *J. Chem. Phys.* **1996**, *105*, 8428–8445.

[267] Leary, R. H. *J. Glob. Optim.* **2000**, *18*, 367–383.

[268] Wales, D. J.; Doye, J. P. *J. Phys. Chem. A* **1997**, *101*, 5111–5116.

[269] Kolsbjerg, E. L.; Peterson, A. A.; Hammer, B. *Phys. Rev. B* **2018**, *97*, 195424.

[270] Weal, G. R.; McIntyre, S. M.; Garden, A. L. *J. Chem. Inf. Model.* **2021**, *61*, 1732–1744.

[271] Demiroglu, I.; Yao, K.; Hussein, H. A.; Johnston, R. L. *J. Phys. Chem. C* **2017**, *121*, 10773–10780.

[272] Aslan, M.; Davis, J. B.; Johnston, R. L. *Phys. Chem. Chem. Phys.* **2016**, *18*, 6676–6682.

[273] Davis, J. B.; Horswell, S. L.; Johnston, R. L. *J. Phys. Chem. A* **2014**, *118*, 208–214.

[274] Johnston, R. L. *Dalt. Trans.* **2003**, *3*, 4193–4207.

[275] Mortensen, H. L.; Meldgaard, S. A.; Bisbo, M. K.; Christiansen, M. P. V.; Hammer, B. *Phys. Rev. B* **2020**, *102*, 075427.

[276] Lloyd, S. *IEEE Trans. Inf. Theory* **1982**, *28*, 129–137.

[277] Gao, J.; Zheng, Y.; Fitzgerald, G. B.; De Joannis, J.; Tang, Y.; Wachs, I. E.; Podkolzin, S. G. *J. Phys. Chem. C* **2014**, *118*, 4670–4679.

[278] Perdew, J.; Burke, K.; Ernzerhof, M. *Phys. Rev. Lett.* **1996**, *77*, 3865–3868.

[279] Rossi, G.; Rapallo, A.; Mottet, C.; Fortunelli, A.; Baletto, F.; Ferrando, R. *Phys. Rev. Lett.* **2004**, *93*, 105503.

[280] Munter, T. R.; Bligaard, T.; Christensen, C. H.; Nørskov, J. K. *Phys. Chem. Chem. Phys.* **2008**, *10*, 5202–5206.

[281] Gemming, S.; Seifert, G.; Götz, M.; Fischer, T.; Ganteför, G. *Phys. Status Solidi B* **2010**, *247*, 1069–1076.

[282] Howalt, J. G.; Vegge, T. *Phys. Chem. Chem. Phys.* **2013**, *15*, 20957–20965.

[283] Wu, Z.; Mo, Y.; Lang, L.; Yu, A.; Xie, Q.; Liu, R.; Tian, Z. *Phys. Chem. Chem. Phys.* **2018**, *20*, 28088–28104.

[284] Stampfl, C.; Freeman, A. J. *Phys. Rev. B* **2005**, *71*, 024111.

[285] Davis, J. B.; Shayeghi, A.; Horswell, S. L.; Johnston, R. L. *Nanoscale* **2015**, *7*, 14032–14038.

[286] Assadollahzadeh, B.; Schwerdtfeger, P. *J. Chem. Phys.* **2009**, *131*, 114309.

[287] Abghoui, Y.; Skúlasson, E. *Procedia Comput. Sci.* **2015**, *51*, 1897–1906.

[288] Abghoui, Y.; Skúlason, E. *Catal. Today* **2017**, *286*, 69–77.

[289] Engel, J.; Francis, S.; Roldan, A. *Phys. Chem. Chem. Phys.* **2019**, *21*, 19011–19025.

[290] Van Den Berg, R.; Prieto, G.; Korpershoek, G.; Van Der Wal, L. I.; Van Bunningen, A. J.; Lægsgaard-Jørgensen, S.; De Jongh, P. E.; De Jong, K. P. *Nat. Commun.* **2016**, *7*, 13057–13057.

[291] Darby, S.; Mortimer-Jones, T. V.; Johnston, R. L.; Roberts, C. *J. Chem. Phys.* **2002**, *116*, 1536–1550.

[292] Hussain, J.; Jónsson, H.; Skúlason, E. *ACS Catal.* **2018**, *8*, 5240–5249.

[293] Mohanty, B.; Ghorbani-Asl, M.; Kretschmer, S.; Ghosh, A.; Guha, P.; Panda, S. K.; Jena, B.; Krasheninnikov, A. V.; Jena, B. K. *ACS Catal.* **2018**, *8*, 1683–1689.

[294] Julkapli, N. M.; Bagheri, S. *Int. J. Hydrogen Energy* **2015**, *40*, 948–979.

Appendix A

Additional data for Chapter 3

A.1 *Ab initio* molecular dynamics snapshots of water above MoS_2

Several snapshots of the water structure above MoS_2 at 298 K were isolated and are presented in Figure A.1 (graphene-supported MoS_2) and Figure A.2 (Au-supported MoS_2). From these snapshots it is clear that, while some hexagonal ordering may be transiently present, there is no persistent ordering in the water structure. The structures of water generated here serve well enough to allow charge separation to be induced through the addition of an additional H to the water layer. However, additional investigation may be performed to determine if there is any ordering that can be observed above MoS_2 over longer duration of molecular dynamics simulations.

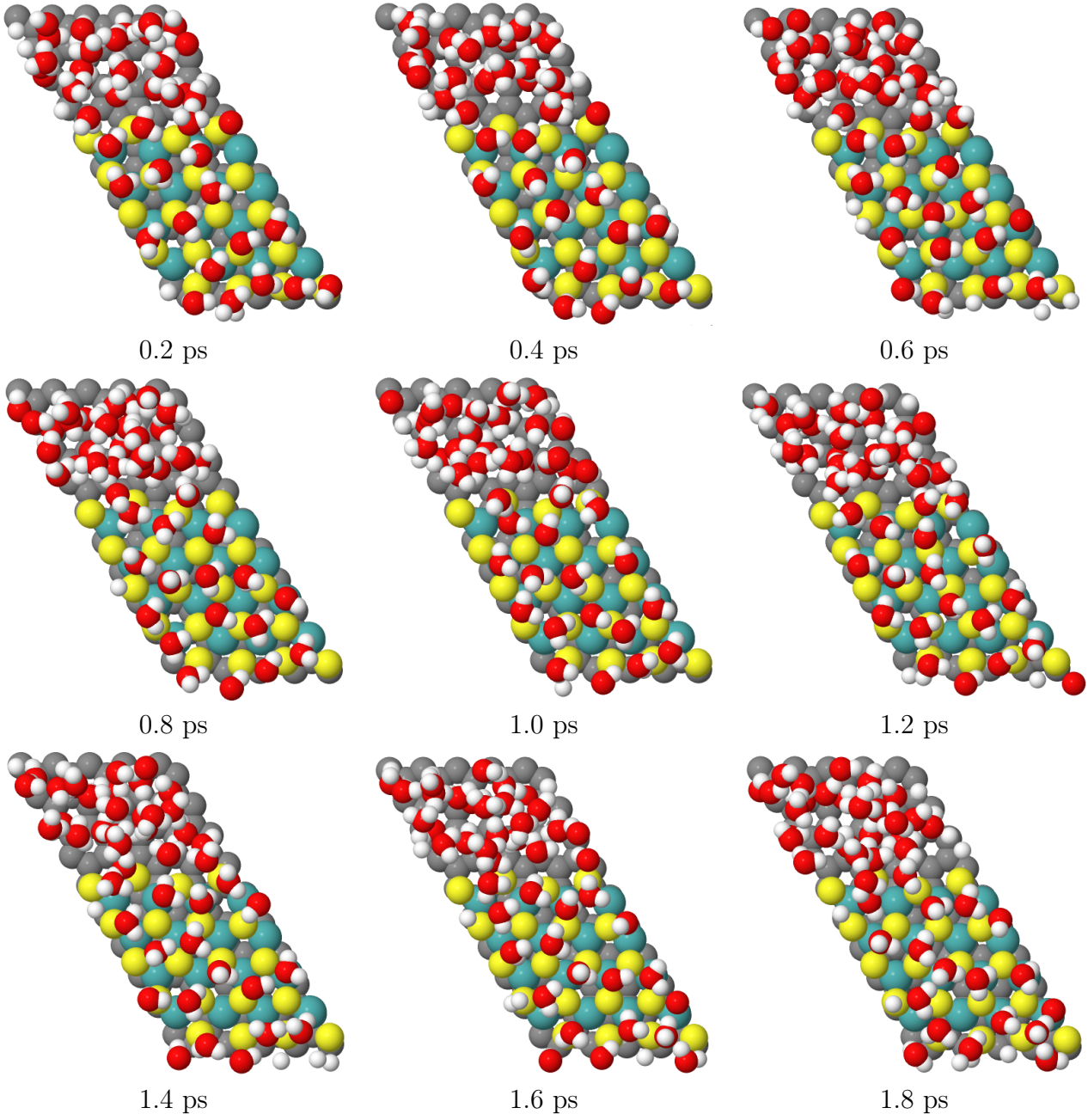

Figure A.1: Water structures above graphene-supported MoS_2 from *ab-initio* molecular dynamics. Snapshots are shown every 0.2 ps through a 2 ps equilibration phase at 298 K.

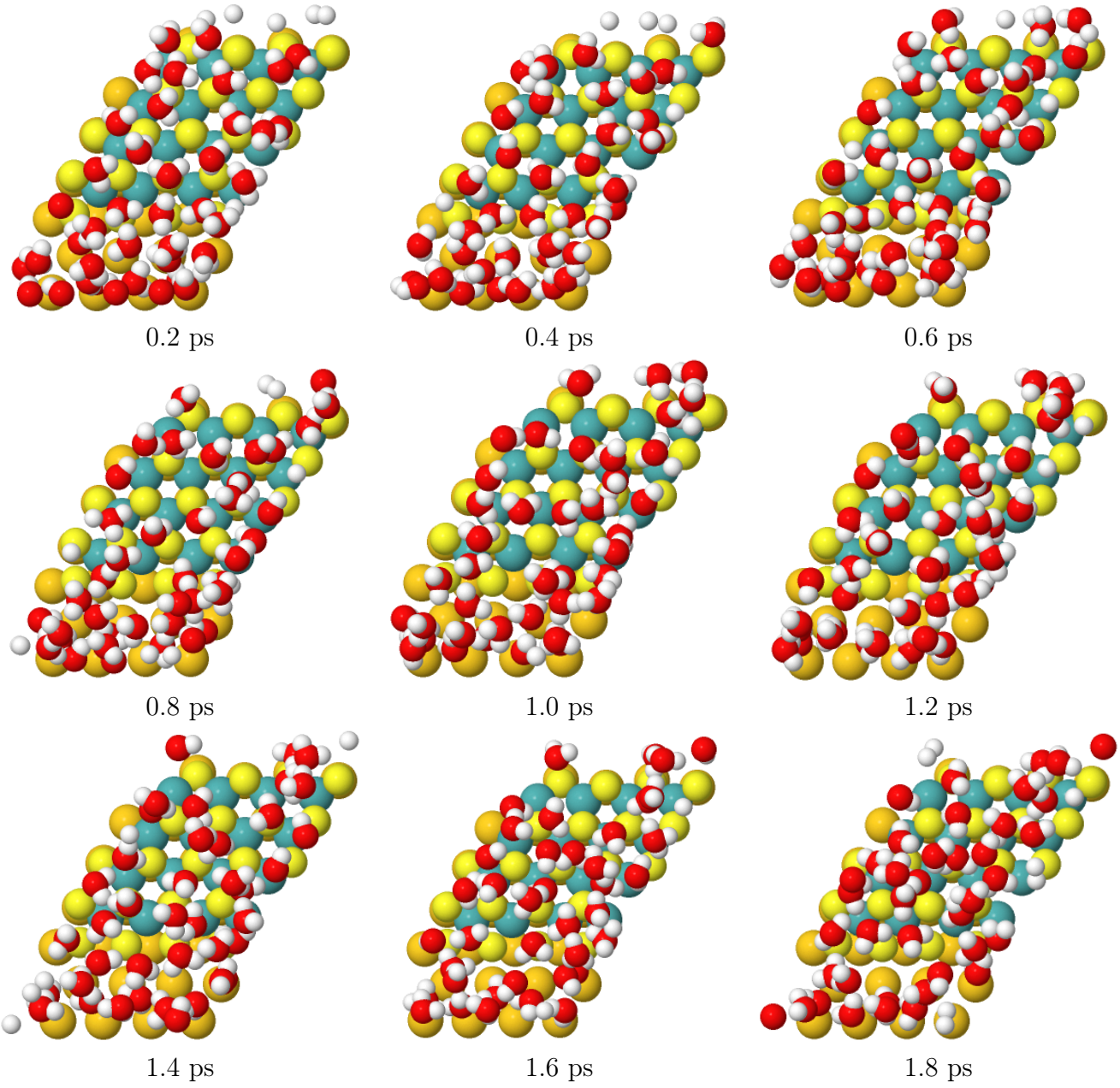

Figure A.2: Water structures above Au-supported MoS_2 from *ab-initio* molecular dynamics. Snapshots are shown every 0.2 ps through a 2 ps equilibration phase at 298 K.

A.2 Structure of the Mo-edge of MoS_2

Based on past theoretical works,[71,166] the under-coordinated Mo atoms on the 50% sulfided Mo edge are believed to cluster into groups in order to satisfy electronic requirements. By testing various model sizes, we find here that the length of unit cell in the periodic direction determines what groupings of Mo arise. If the unit cell is a multiple of two Mo atoms long then pairs (or dyads) form, whereas if it is a multiple of three triads form instead. If the unit cell is neither a multiple of two or three, then a combination of pairs and triads can form. The structures of these pairs and triads are pictured in Figure A.3.

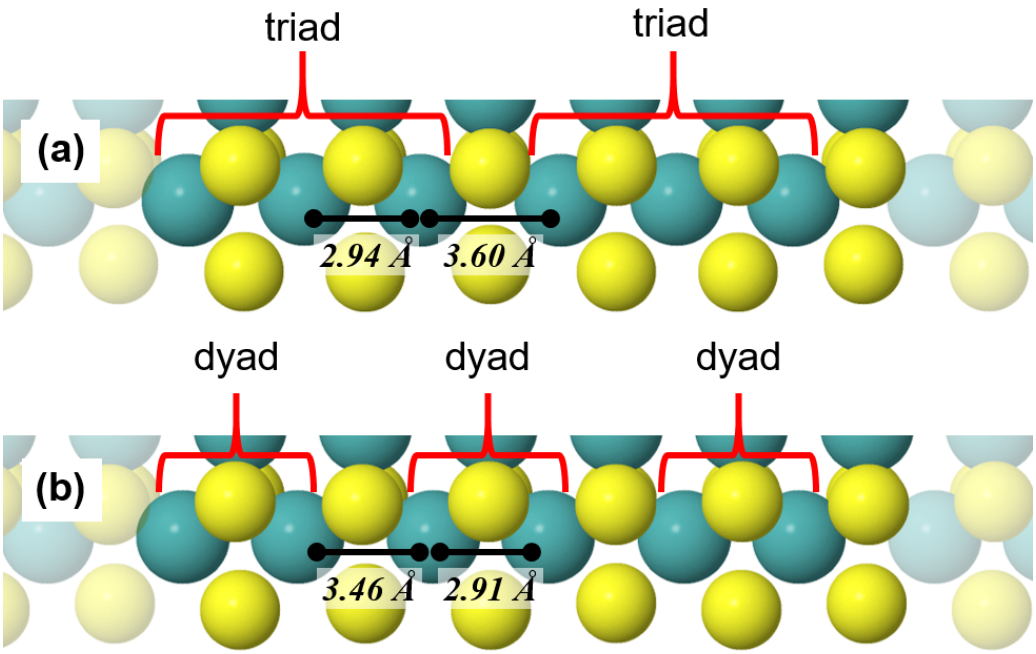

Figure A.3: Structural models showing the Mo-edge of MoS_2 reconstructing into (A) Mo triads and (B) pairs of Mo atoms. The spacing between non-equivalent Mo atoms is shown also. S atoms which sit between two Mo that are close together are termed "close S" and those that sit between separated Mo are termed "spaced S".

A 6-Mo wide model can be optimised with an initial guess such that it optimises to a structure where the Mo are in pairs instead of triads, yet the energy of this model is approximately 0.1 eV higher per edge Mo atom. While this would suggest a triadic model would be favoured under experimental conditions, any effects are likely highly size

dependent as MoS_2 nanoparticles that have edge lengths which are not a multiple of three must have at least some edge which is not constructed as triads.

We have attempted to quantify some of the energetic differences in having the Mo-edge in a triadic construction compared to one with the Mo atoms as paired by testing the H adsorption energy various sites on 4-Mo (forms pairs) and 6-Mo (forms triads) wide models of unsupported, graphene-supported and Au(111)-supported MoS_2 (Table A.1). Looking first at unsupported MoS_2, it can be seen that ΔG_{Hads} on the 6-Mo wide model is up to 0.60 eV higher than than on the 4-Mo model. When H is adsorbed to the edge, we consistently observe the triadic structure breaking into pairs of Mo. We believe this explains the H adsorption energy difference, as there will be an energy cost associated with breaking the triadic structure on the Mo-edge. A similar difference between the 4- and 6-Mo wide models is observed for graphene-supported MoS_2, yet the magnitude of potential difference is smaller at approximately up to 0.50 eV. In contrast, no difference between model sizes is observed for Au(111)-supported MoS_2. This is because the Au-supported MoS_2 naturally reconstructs into pairs of Mo, and is never observed to form triads without fixing certain atomic centres. We observe an energy difference of less than 0.01 eV per Mo between having Mo pairs and triads for Au-supported MoS_2.

Overall, it can be concluded that the graphene-supported MoS_2 model may be prone to differences in H adsorption energy based on the reconstruction present on the Mo-edge and therefore its model size. The magnitude of these differences should not exceed 0.50 eV. These model size effects should not be present on Au-supported MoS_2.

Table A.1: First H adsorption free energies (ΔG_{Hads}, eV) at different sites for 4-Mo wide and 6-Mo wide model sizes.

	Site	Unsupported	Graphene	Au(111)
4-Mo	Spaced S	-0.30	-0.23	0.29
	Close S	0.15	0.19	0.67
	Mo	0.88	0.97	1.08
6-Mo	Spaced S	0.28	0.26	0.29
	Close S	-0.15	-0.03	0.67
	Centre Mo	1.13	1.04	1.04
	Peripheral Mo	1.17	1.01	–

A.3 Additional Data for Volmer-Tafel barriers

The Volmer-Tafel barriers are presented at different H coverages in Figure A.4. To construct a plot of the Volmer-Tafel barriers against potential, the potential required to reach each of the displayed H coverages is considered based on the H adsorption free energy.

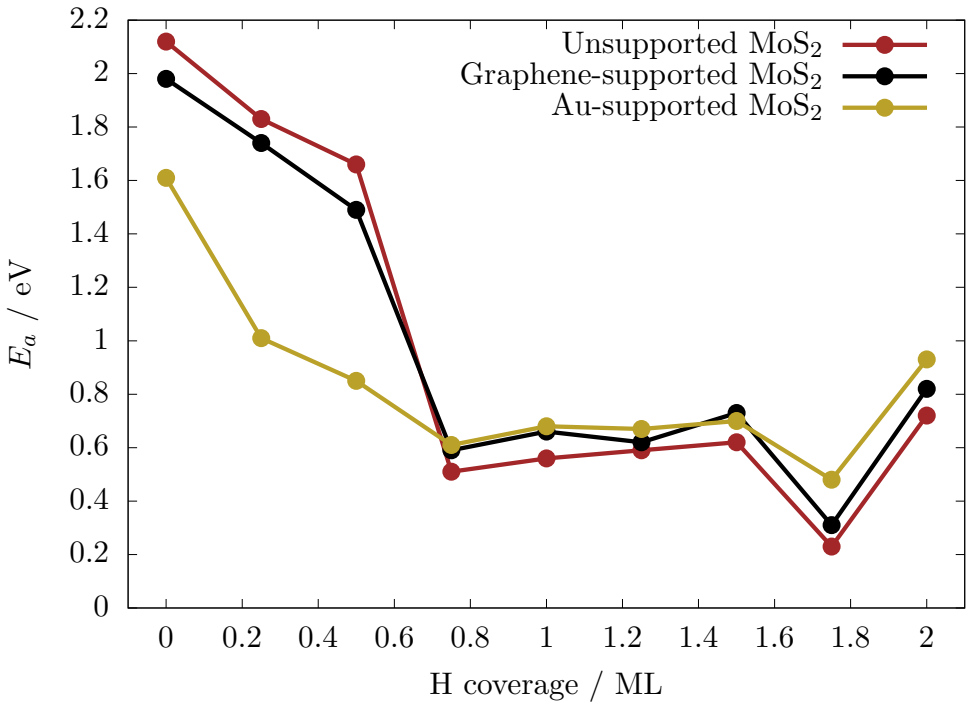

Figure A.4: Volmer-Tafel activation barriers and different H coverages on the Mo-edge of unsupported and supported MoS_2.

The Volmer-Tafel barrier on unsupported MoS_2 are compared to those with a graphene or Au support in Figure A.5. The difference between unsupported and graphene-supported MoS_2 is approximately 0.1 eV at 0 V potential, and all potentials more negative then this barriers differ by less than 0.05 eV. This demonstrates the graphene support is having a minimal effect on the catalytic behaviour of MoS_2, which could be attributed to the fact that MoS_2 does not adhere strongly to graphene with an adhesion energy of only -0.15 eV per Mo atom.

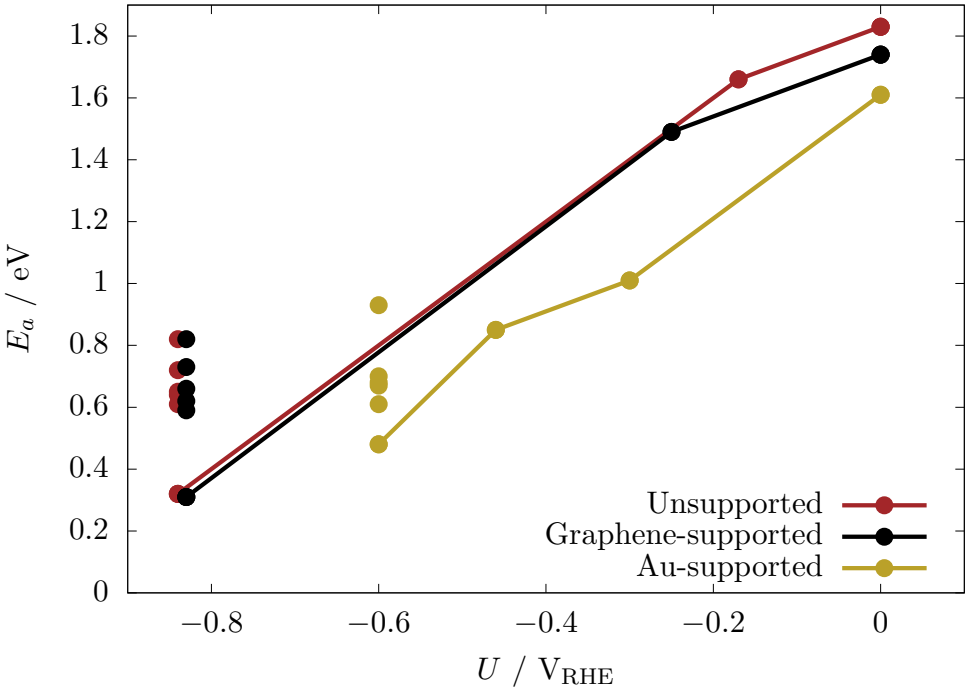

Figure A.5: Volmer-Tafel barriers as a function of applied potential on unsupported and supported MoS_2.

A.4 Tested Tafel combination paths

In order to determine the favourable reaction geometry and site for Tafel combination several different pathways were tested (Table A.2). The only pathways which barriers could be found for were Mo-S combination, and S-S combination. The remainder of the pathways either converged to Mo-S combination, or could not find a reasonable reaction path.

Table A.2: Tested Tafel desorption paths with two H on the surface.

Path		Barrier
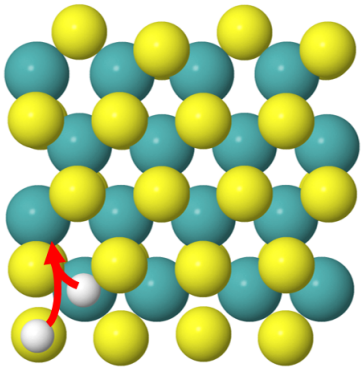	Mo-S combination	0.76 eV
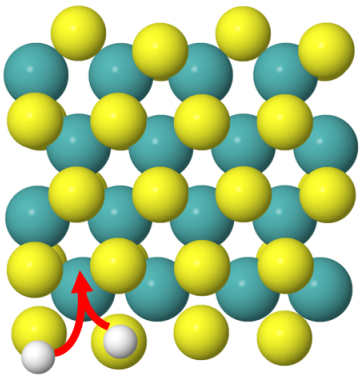	S-S combination	1.56 eV (*Difficult to converge*)

Table A.2: *continued.*

Path		Barrier
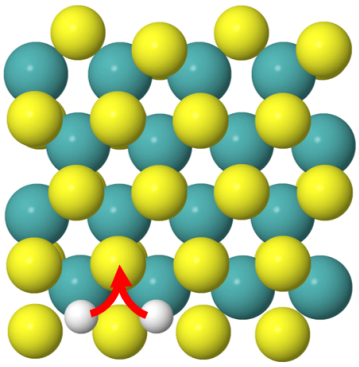	Mo-Mo combination	*Converged to Mo-S desorption*
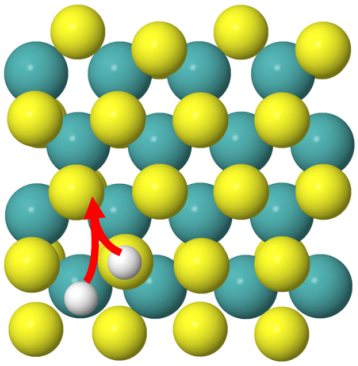	Mo-S_{top} combination	*Could not be converged*
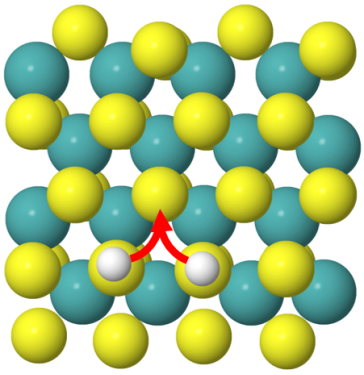	S_{top}-S_{top} combination	*Could not be converged*

A.5 Tafel barriers

The tested Tafel barriers for each type of MoS_2 combination across H coverages ranging from 0.5 to 2 ML are presented in Table A.3. As discussed in the main text, a particularly low barrier was found at 1.75 ML coverage. At 1.75 ML the atomic centre of the S with the reacting H_{ads} on it is 0.11 Å higher than the adjacent Mo, whereas at all other coverages this S atom ranges between 0.25 and 0.58 Å below the adjacent Mo. We postulate that this key S atom being raised up above the Mo causes the reacting H to adsorb in an on-top geometry, and lowers the energy of the path to this H moving to and reacting at the the bridge between Mo and S. It should be noted that this initial state geometry with the H on centrally on-top of S is unique, and is not seen at other coverages.

Table A.3: The structures of some of the Tafel reaction paths tested on unsupported MoS_2 viewed from the z and y directions. The minimum energy pathways (MEPs) for Tafel combination are also shown.

Coverage / ML	z-view	y-view	MEP
0.50	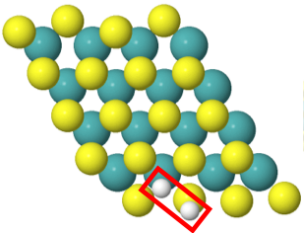	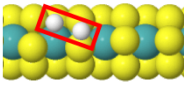	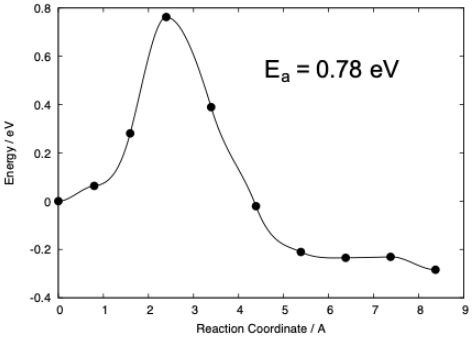
0.75	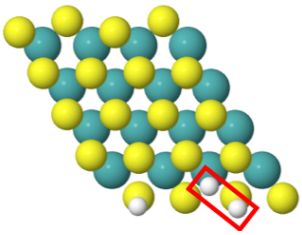	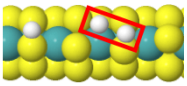	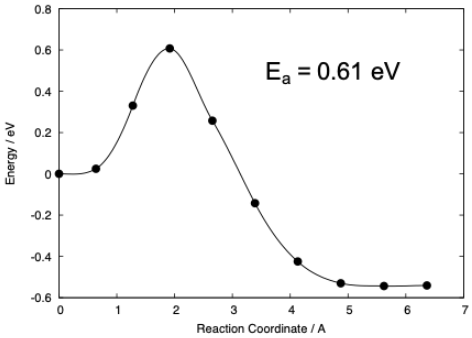
1.00 ($Mo+S_{spaced}$)	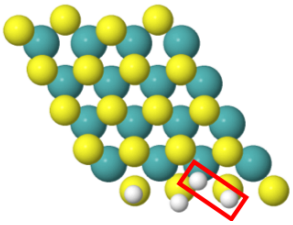	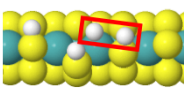	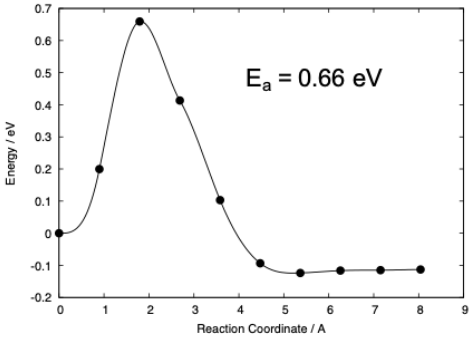
1.00 ($Mo+S_{close}$)	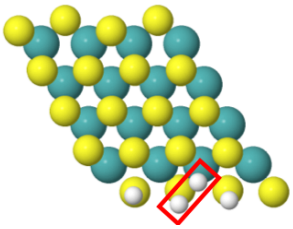	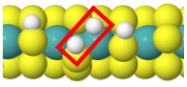	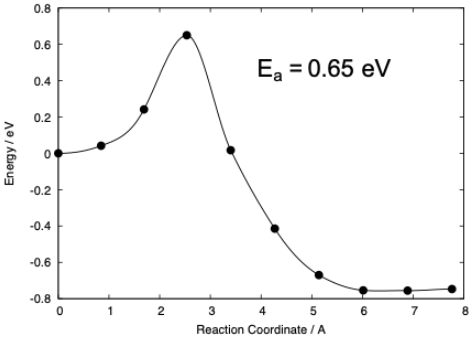

Table A.3: *continued.*

Coverage / ML	*z*-view	*y*-view	MEP
1.25 ($Mo+S_{spaced}$)	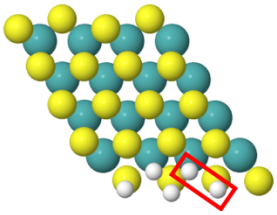	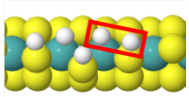	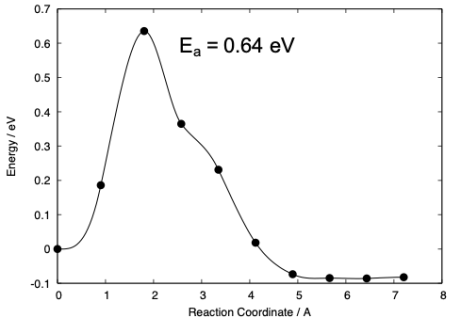
1.25 ($Mo+S_{close}$)	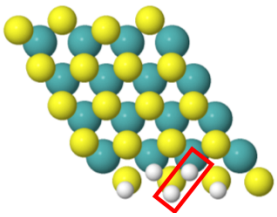	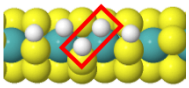	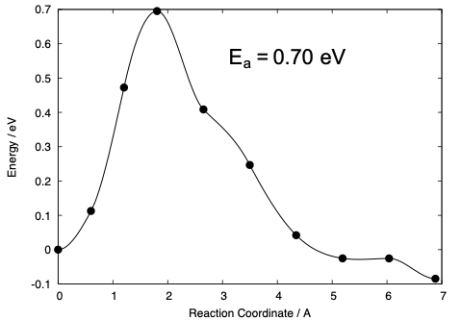
1.50 ($Mo+S_{spaced}$)	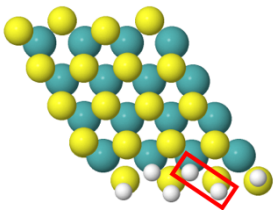	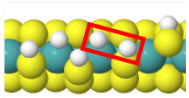	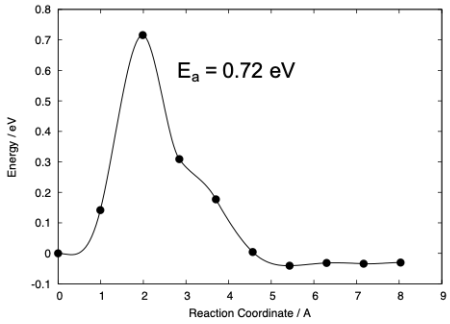
1.50 ($Mo+S_{close}$)	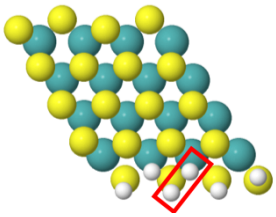	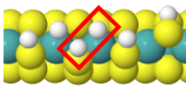	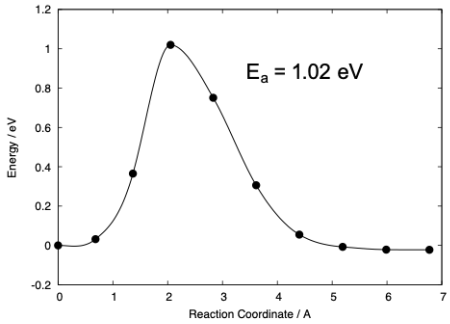
1.75 ($Mo+S_{spaced}$)	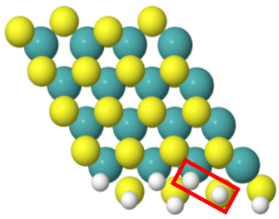	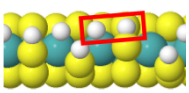	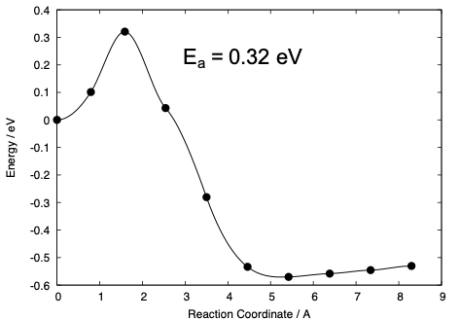

Table A.3: *continued.*

Coverage / ML	*z*-view	*y*-view	MEP
1.75 (Mo+S_{close})	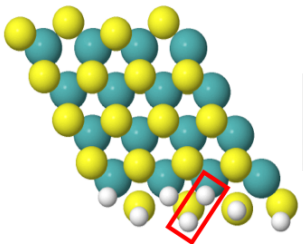		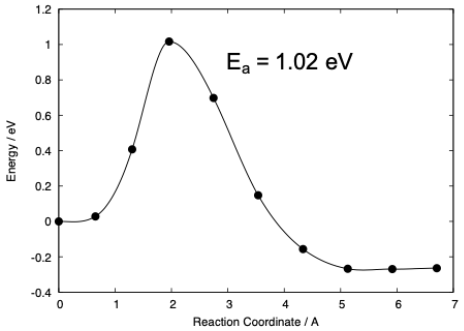
1.75 (Mo+S_{close})	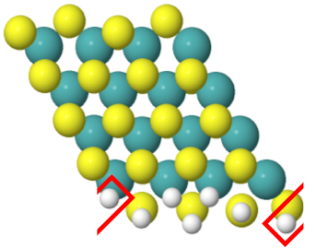		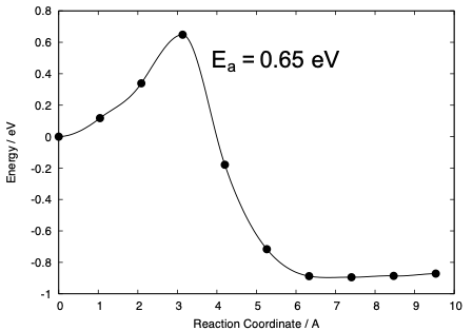
2.00 (Mo+S_{spaced})	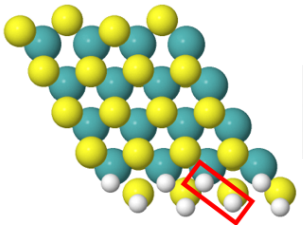		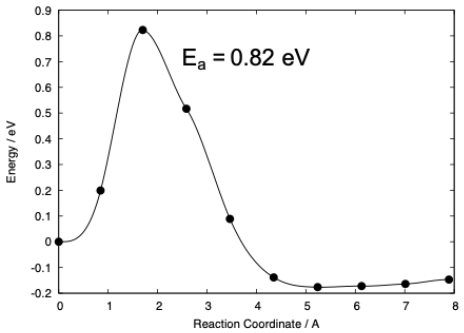
2.00 (Mo+S_{close})	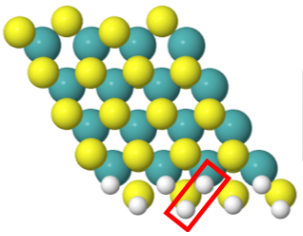		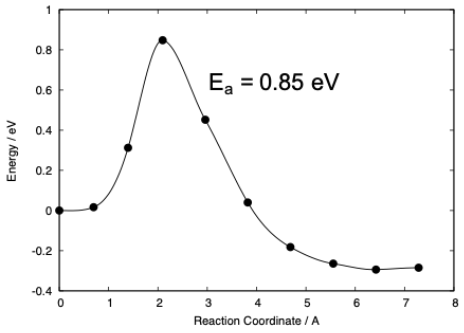

A.6 Free energy diagrams for the Volmer-Tafel reaction

The free energy diagrams for the overall Volmer-Tafel process are presented for graphene-supported MoS_2 in Figures A.6 and A.7, and for Au-supported in Figures A.8 to A.10. For both catalysts, the diagrams are presented at 0 V_{RHE} and at the potential required to reach H coverages that have up to two H on the surface (0.5 ML). In all cases, the Volmer-Tafel barrier was taken relative to the lowest energy preceding state.

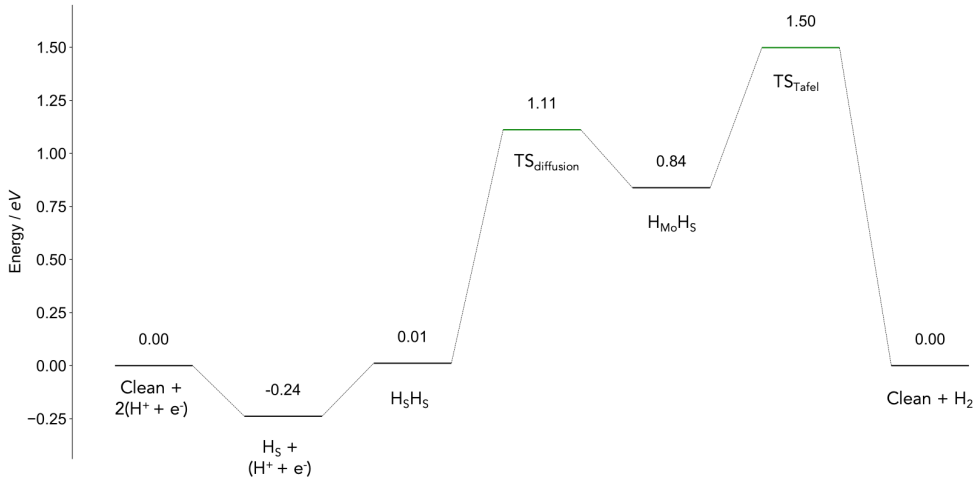

Figure A.6: Graphene-supported MoS_2 Volmer-Tafel free energy diagram at 0 V.

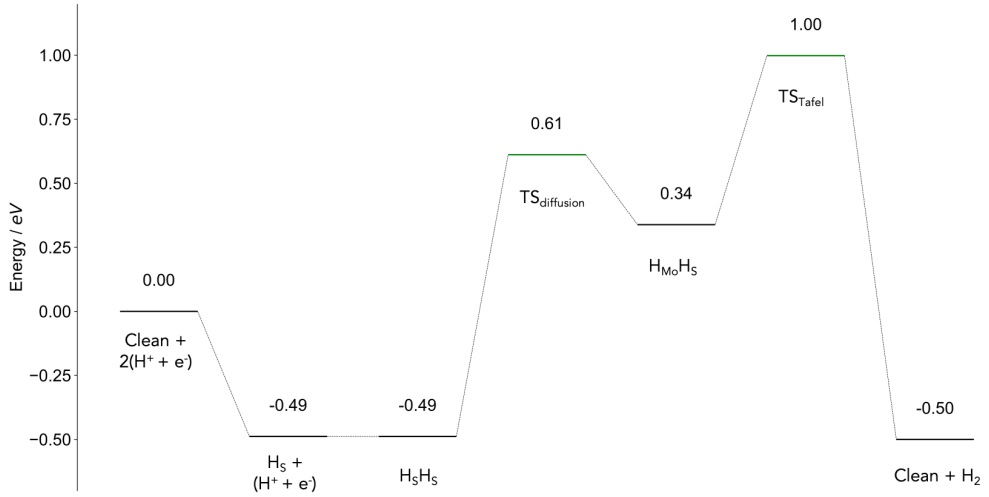

Figure A.7: Graphene-supported MoS_2 Volmer-Tafel free energy diagram at -0.25 V.

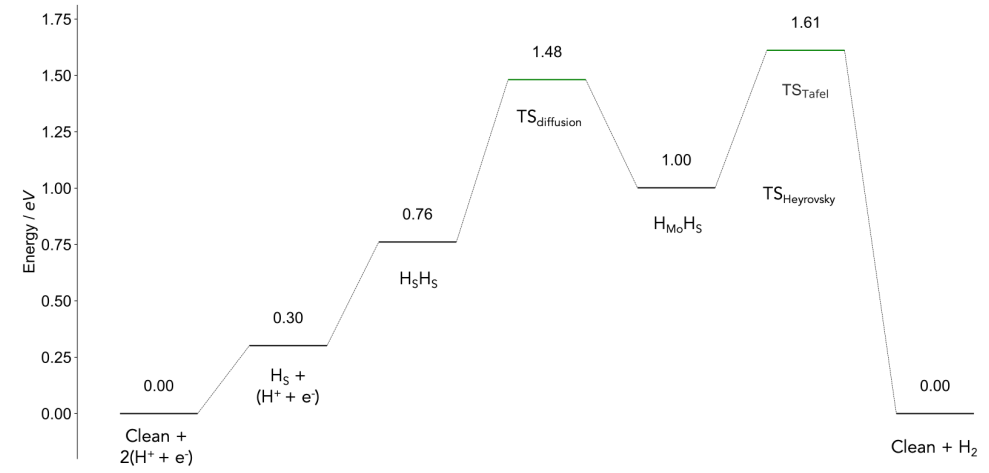

Figure A.8: Au-supported MoS_2 Volmer-Tafel free energy diagram at 0 V.

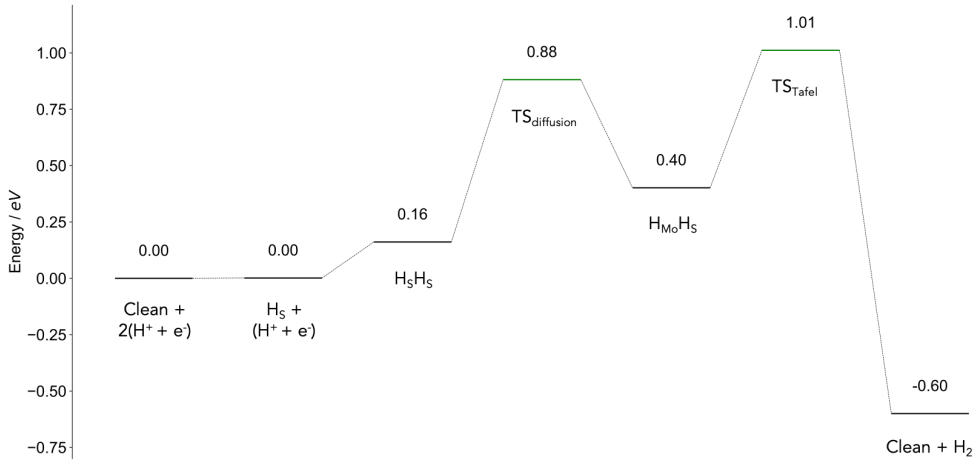

Figure A.9: Au-supported MoS_2 Volmer-Tafel free energy diagram at -0.30 V.

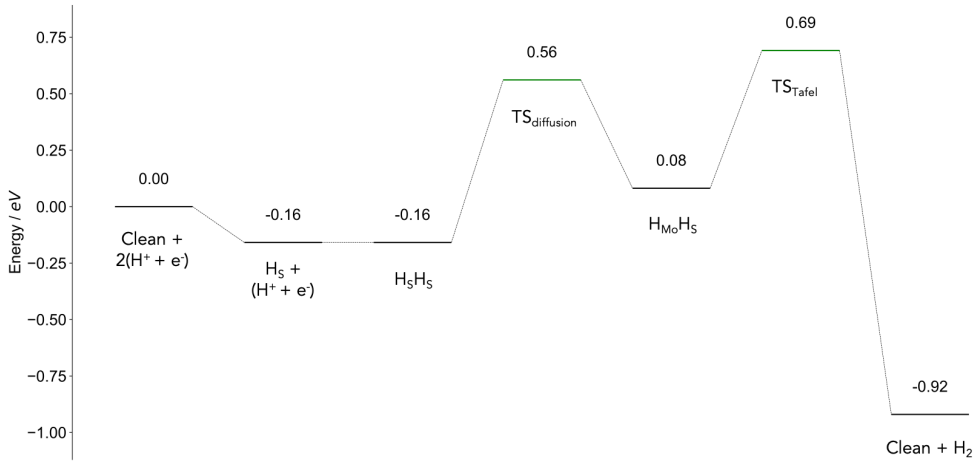

Figure A.10: Au-supported MoS_2 Volmer-Tafel free energy diagram at -0.46 V.

A.7 Free energy diagrams for the Volmer-Heyrovský reaction

The free energy diagrams for the Volmer-Heyrovský reaction on graphene (Figures A.11 to A.13) and Au-supported MoS_2 (Figures A.14 to A.17) are presented here at different potentials.

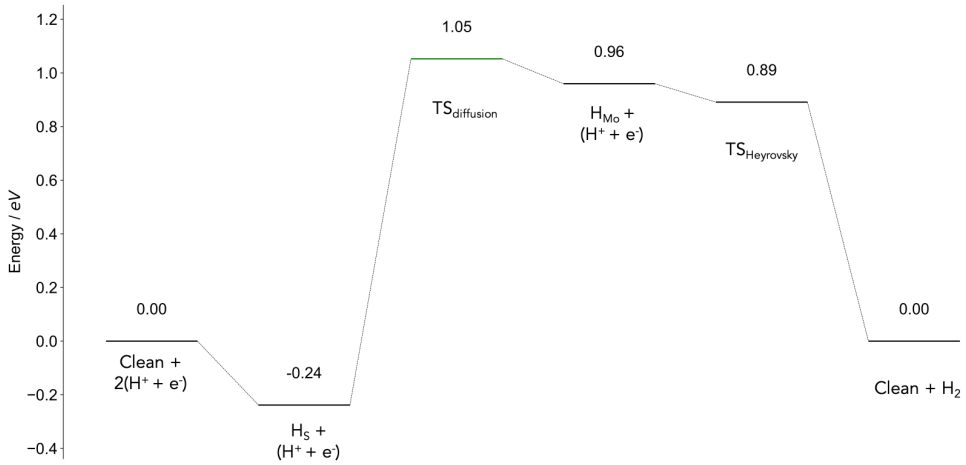

Figure A.11: Graphene-supported MoS_2 Volmer-Heyrovský free energy diagram at 0 V.

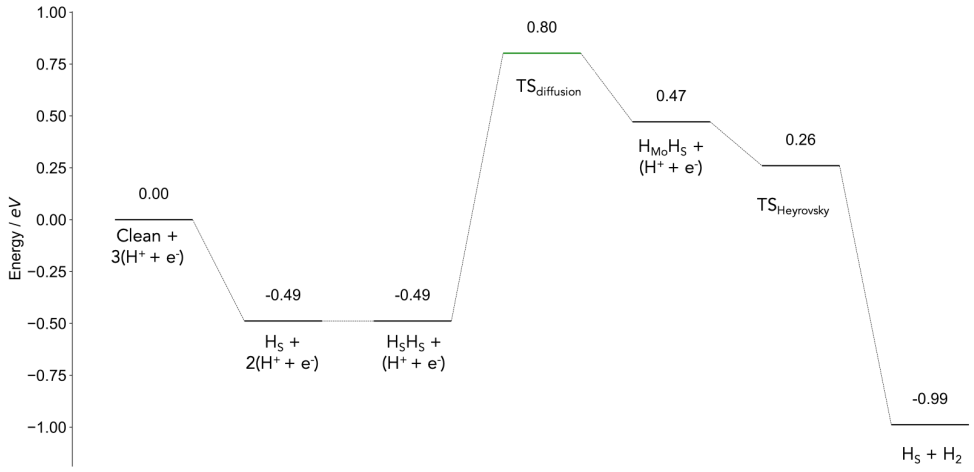

Figure A.12: Graphene-supported MoS_2 Volmer-Heyrovský free energy diagram at -0.25 V. Note that all reaction barriers are calculated with a single H on the surface for computational tractability.

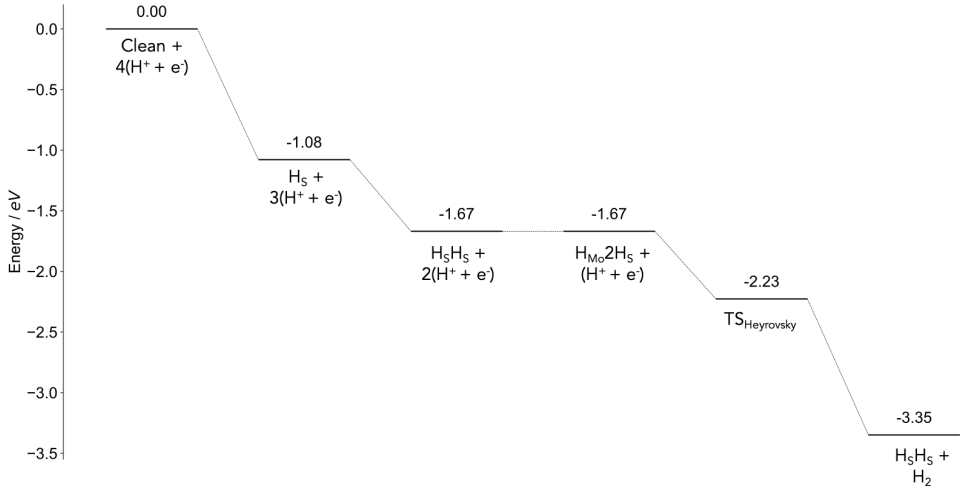

Figure A.13: Graphene-supported MoS_2 Volmer-Heyrovský free energy diagram at -0.84 V. Note that the pathway is different in this case compared to the above, as the Mo site can be spontaneously populated with H (i.e. no uphill steps) at a 3H coverage on the surface. Therefore H diffusion does not need to take place. Note that all reaction barriers are calculated with a single H on the surface for computational tractability.

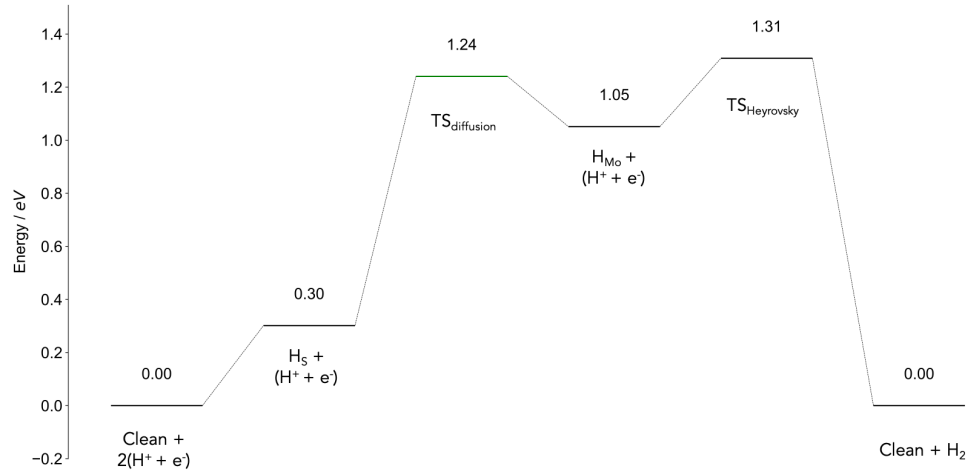

Figure A.14: Au-supported MoS_2 Volmer-Heyrovský free energy diagram at 0 V.

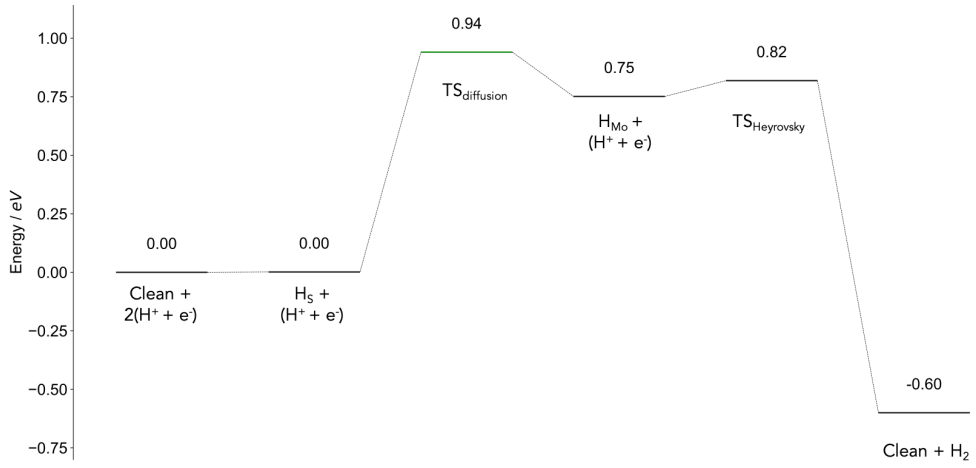

Figure A.15: Au-supported MoS_2 Volmer-Heyrovský free energy diagram at -0.30 V.

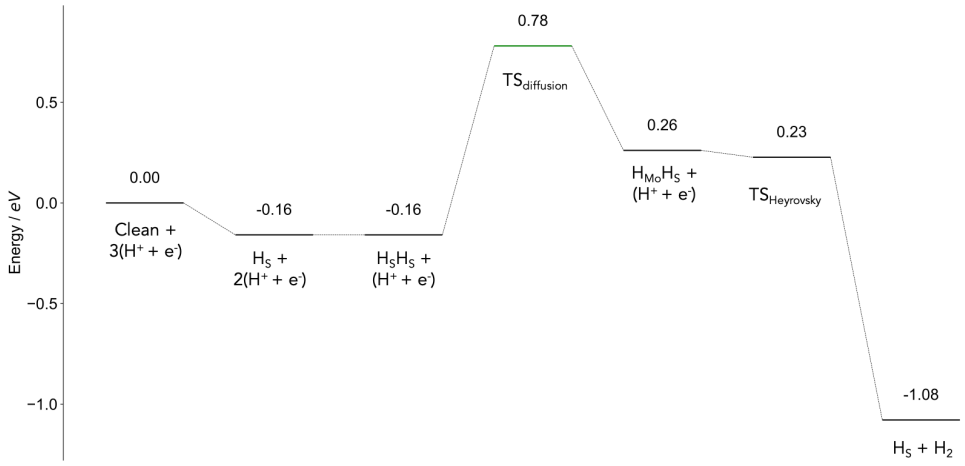

Figure A.16: Au-supported MoS_2 Volmer-Heyrovský free energy diagram at -0.46 V. Note that all reaction barriers are calculated with a single H on the surface for computational tractability.

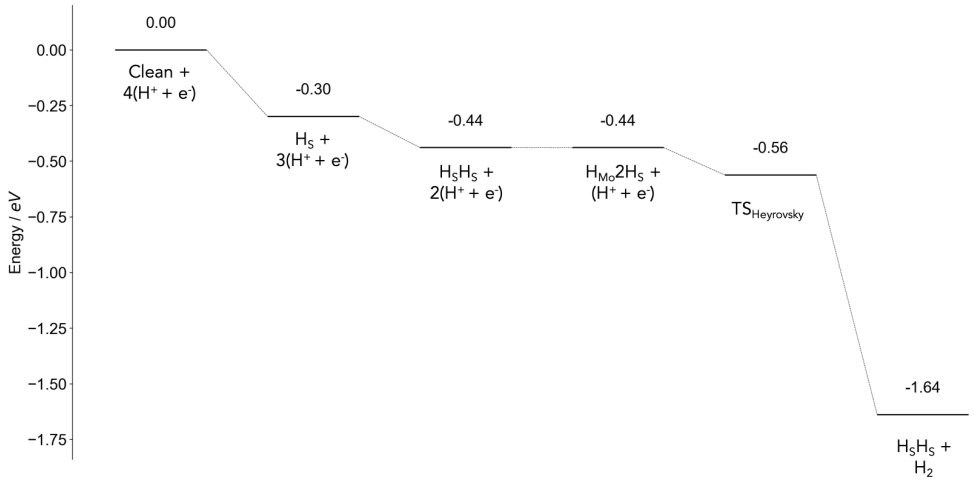

Figure A.17: Au-supported MoS_2 Volmer-Heyrovský free energy diagram at -0.60 V. The pathway is different in this case compared to the above, as the Mo site can be spontaneously populated with H (i.e. no uphill steps) at a 3H coverage on the surface. Therefore H diffusion does not need to take place. Note that all reaction barriers are calculated with a single H on the surface for computational tractability.

Appendix B

Additional data for Chapter 4

B.1 Ball and stick models of MoS_2 and supports

To provide an alternate view of the models examined in Chapter 4, ball and stick models are provided here for MoS_2/graphene (Figure B.1) and for the carbon supports of interest (Figure B.2). These models show the connectivity between atoms, and can be helpful for visualisation.

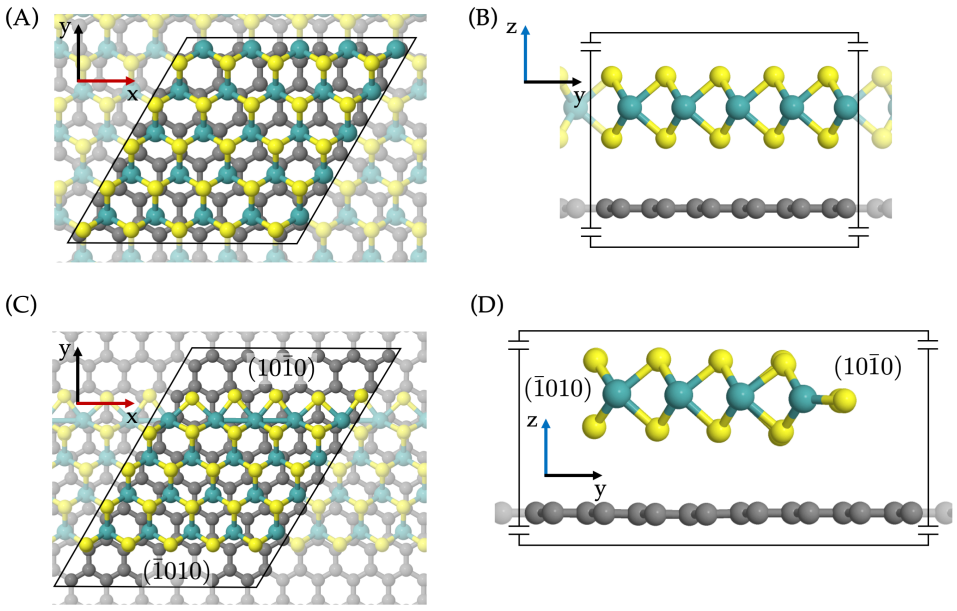

Figure B.1: The MoS_2 basal plane model shown with a pristine graphene support from the (A) top and (B) side view. (C) Top and (D) side views of a supported MoS_2 stripe model that exposes the Mo-edge (10$\bar{1}$0) and the S-edge ($\bar{1}$010).

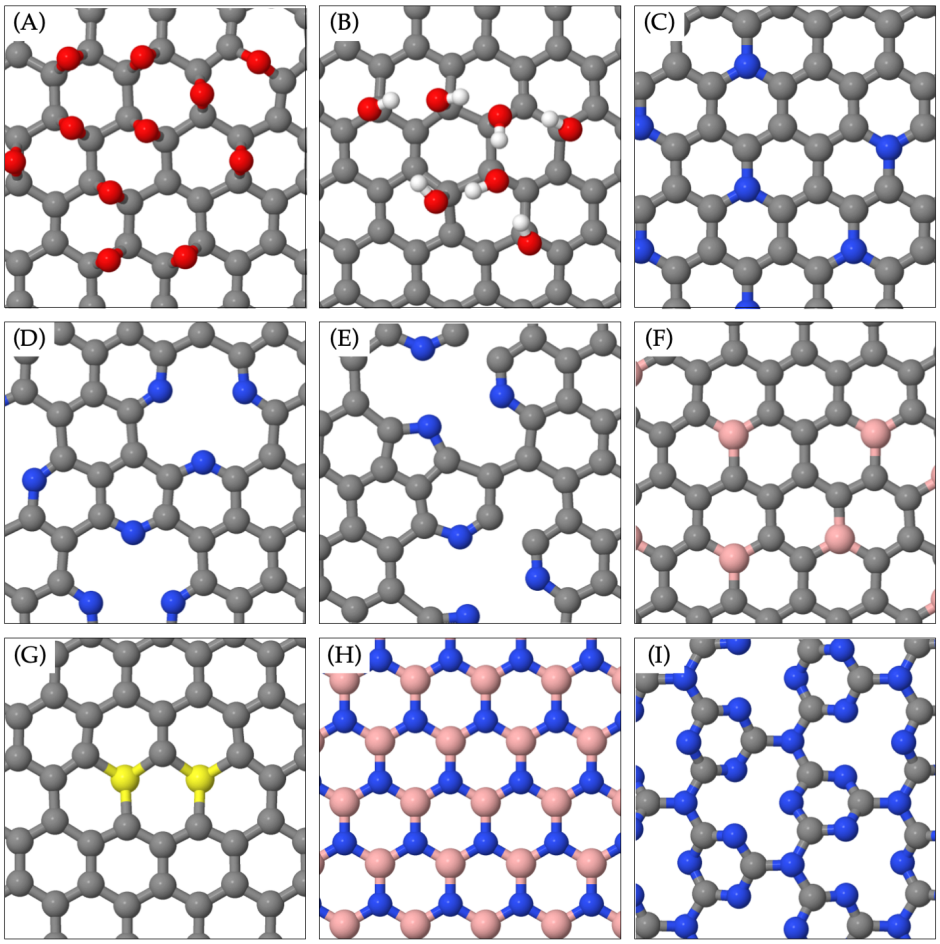

Figure B.2: Structures of the carbon-based support materials studied in the present work (in addition to pristine graphene, which is not shown). Most supports are graphene derivatives with different functional groups. (A) GO-epoxide, (B) GO-hydroxide, (C) NDG-graphitic, (D) NDG-pyridinic, (E) NDG-pyrrolic, (F) BDG, (G) SDG, (H) h-BN, (I) *gt*-C_3N_4.

B.2 Lattice constants and strains of support materials

In Table B.1 the optimised cell lengths for the support models are presented, and the percent strain required to match the length of a 5×5 MoS_2 surface is also given. It can be seen that most strains are around 7-8%, and none exceed 9%. Furthermore, because the vast majority of reported strains are in the same direction and of similar magnitude,

it is suggested that any effect this straining may have should be similar for all support materials. Thus, any trends observed should not be influenced by the strain. It is in principle possible to use a large enough model that there would be no lattice mismatch between MoS_2 and support, but this would require models many times the size used here, which was not overly feasible.

Table B.1: The lattice constants of the different support materials studied in the main text, and the percentage strain required for them to match with 5×5 MoS_2 models (cell length: 15.91 Å). For most support materials the closest match was obtained with 6×6 unit cells of the support, the exception being *gt*-C_3N_4, where only two unit cells were required.

Support material	Cell length Å	Percent strain to match MoS_2
Graphene	14.82	7.3
GO-epoxide 5	14.80	7.5
GO-epoxide 10	14.77	7.7
GO-epoxide 15	14.81	7.4
GO-epoxide 25	15.01	6.0
GO-hydroxide 5	14.75	7.8
GO-hydroxide 10	14.74	7.9
NDG-graphitic 4 %	14.76	7.8
NDG-graphitic 8 %	14.73	8.0
NDG-graphitic 12 %	14.69	8.3
NDG-graphitic 16 %	14.64	8.6
NDG-pyridinic 4 %	14.79	7.5
NDG-pyridinic 8 %	14.79	7.5
NDG-pyridinic 12 %	14.79	7.5
NDG-pyridinic 16 %	14.75	7.8
NDG-pyrrolic 4 %	14.79	7.5
NDG-pyrrolic 8 %	14.72	8.1
BDG 1.4 %	14.82	7.3
BDG 4 %	14.92	6.6
BDG 8 %	15.01	6.0
BDG 12 %	15.13	5.1
SDG 1.4 %	14.82	7.3
SDG 2.8 %	14.85	7.1
h-BN	15.06	5.6
gt-C_3N_4	15.94	-0.2

B.3 Images of support materials at different dopant coverages

In Table B.2, the structure of all different coverages for the supports examined in this work are shown. In each case the 6×6 model is shown, which was used to support the MoS_2 basal plane. However, the edge supports are simply generated by repeating the model once in the y-direction.

Table B.2: Structures of the support materials studied in the present work at the different dopant coverages of interest. The supports for the MoS_2 basal plane are shown here, and the supports for the edge models are created by doubling their length in the vertical direction.

Graphene 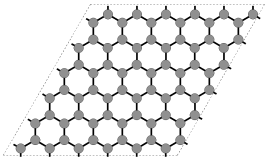			
GO-epoxide 5 % 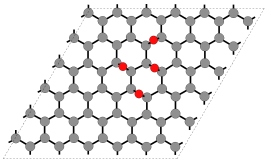	GO-epoxide 10 % 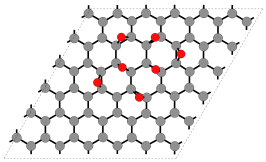	GO-epoxide 15 % 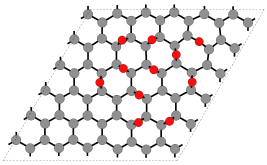	GO-epoxide 25 % 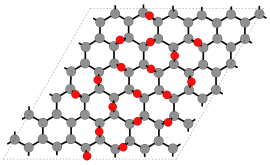
GO-hydroxide 5 % 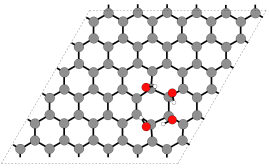	GO-hydroxide 10 % 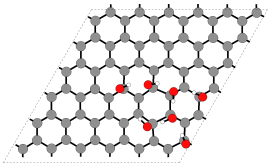		
NDG-graphitic 4 % 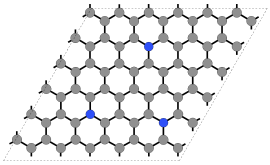	NDG-graphitic 8 % 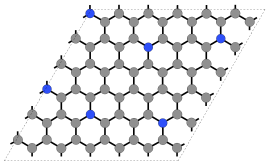	NDG-graphitic 12 % 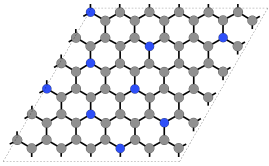	NDG-graphitic 16 % 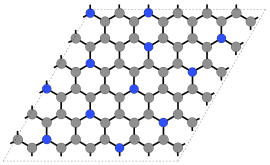
NDG-pyrdinic 4 % 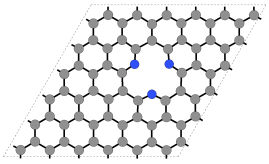	NDG-pyridinic 8 % 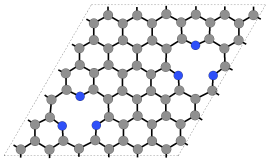	NDG-pyridinic 12 % 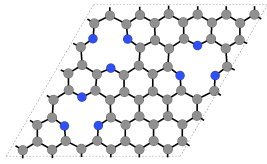	NDG-pyridinic 16 % 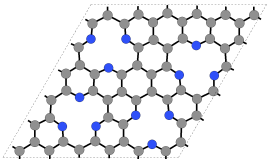
NDG-pyrrolic4 % 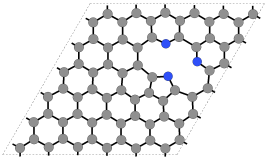	NDG-pyrrolic 8 % 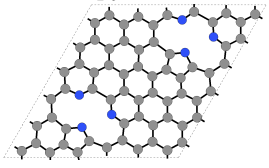		

Table B.2: *Cont.*

BDG 1.4 % 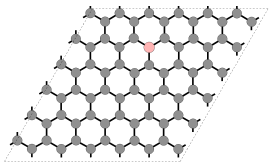	BDG 4 % 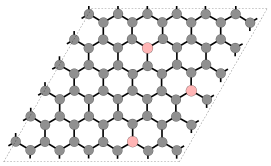	BDG 8 % 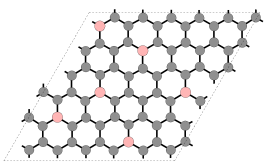	BDG 12 % 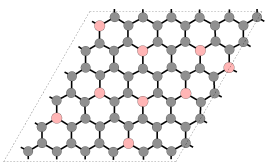
SDG 1.4% 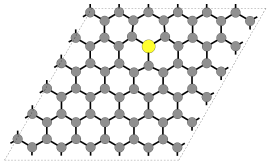	SDG 2.8 % 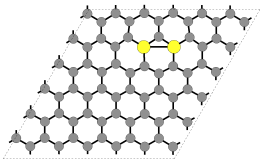		
h-BN 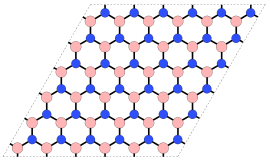			
gt-C_3N_4 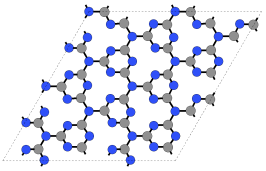			

B.4 Data showing the effect of a two-sided GO support

In Table B.3 the data from several high-coverage test cases from the graphene oxides are presented. These cases explore the possibility of two-sided GO materials having a different effect on H adsorption than one-sided materials, where the oxide or hydroxide functional groups are facing the MoS_2. We find here that the addition of the same coverage of oxide or hydroxide groups on the side of the support that faces away from MoS_2 typically has very little effect on the H adsorption energy. Therefore, in the main text of this chapter, we examine only one-sided GO materials.

Table B.3: Electronic H adsorption energies ($\Delta E_{\mathrm{H_{ads}}}$) for a series of one- and two-sided graphene oxide (GO) supports for MoS_2. These data show that the addition of GO groups on the side of the support facing away from MoS_2 usually has very little effect on the adsorption energy of H when there are already groups on the MoS_2 side.

System	$\Delta E_{\mathrm{H_{ads}}}$/ eV
GO-epoxide	
25% MoS_2 side	1.48
25% on both sides	1.56
50% MoS_2 side	2.00
50% on both sides	1.99
GO-hydroxide	
25% MoS_2 side	1.73
25% on both sides	1.96
50% MoS_2 side	2.00
50% on both sides	1.97

B.5 Density of states plots for MoS_2 with and without H adsorbed

In Table B.4 the density of states plots are presented for all MoS_2 systems tested here with and without H adsorbed. These data listings are provided for reference, and to corroborate the overall trends reported in the main body of the thesis.

Table B.4: Density of states plots for the clean MoS_2/support structures (top), with H adsorbed in a tilted configuration (middle), and with H adsorbed on-top (bottom). For structures where only on-top H adsorption could be located only two plots are presented: clean MoS_2/support structures (top), and with H adsorbed on-top (bottom).

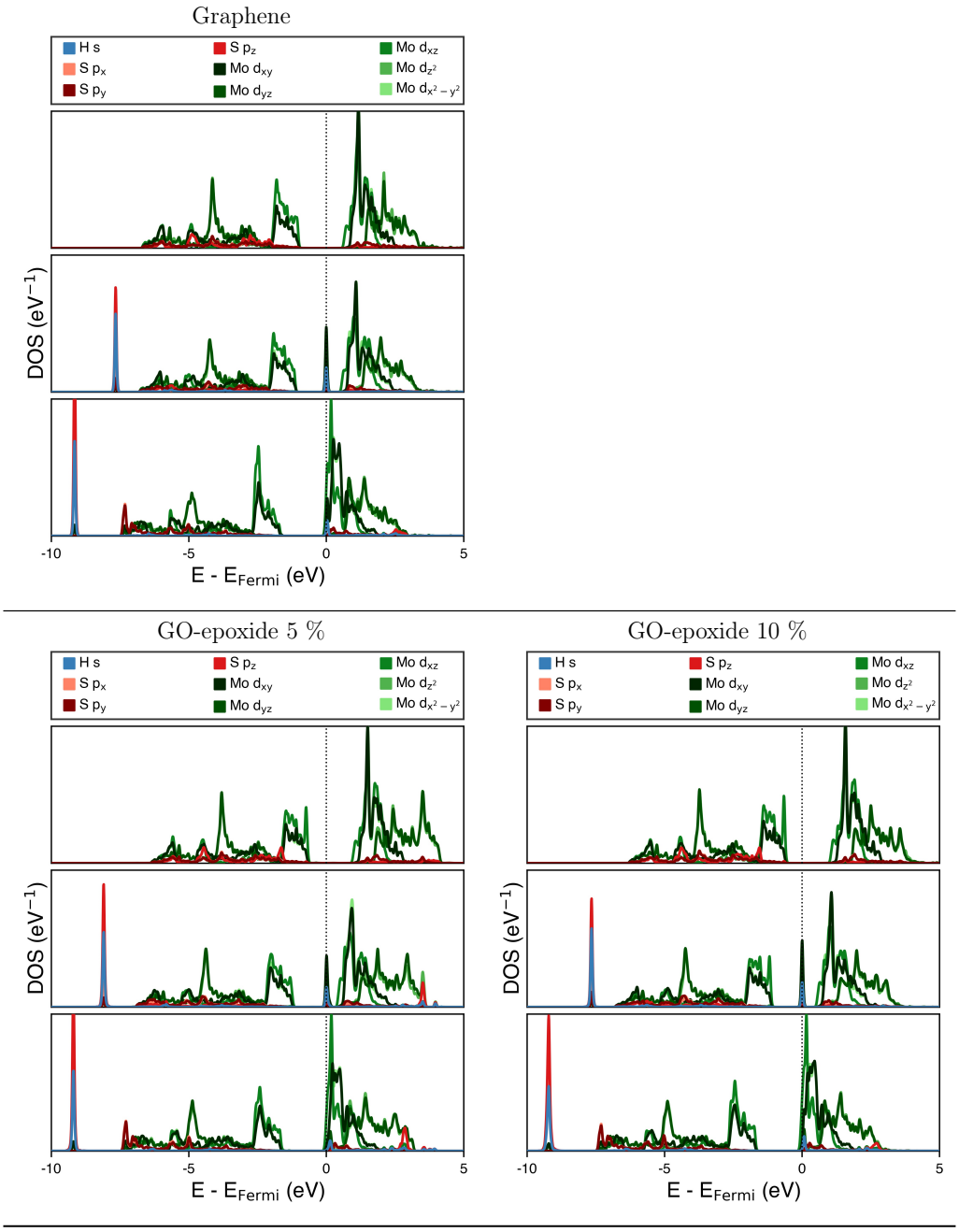

Table B.3: *Cont.*

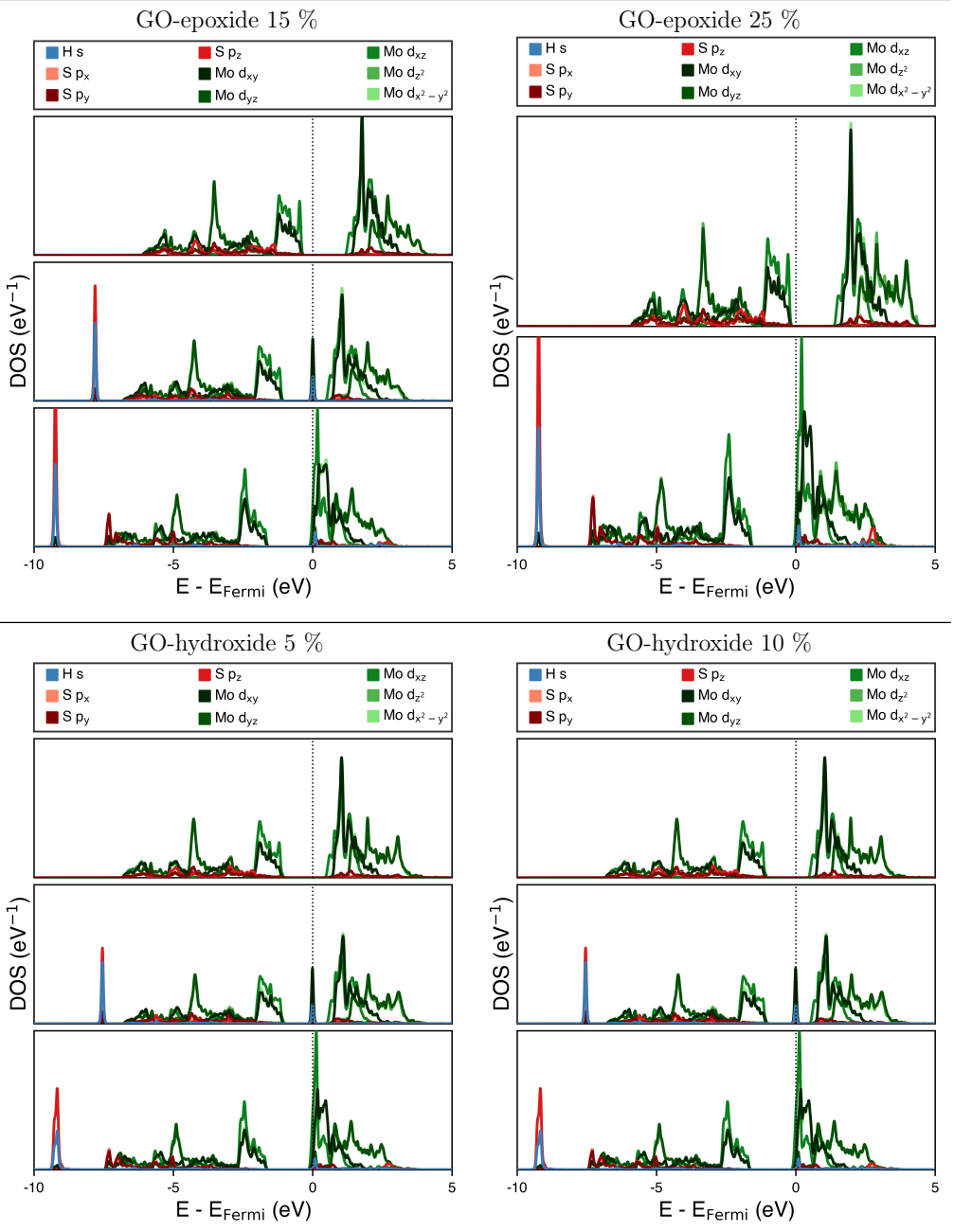

Table B.3: *Cont.*

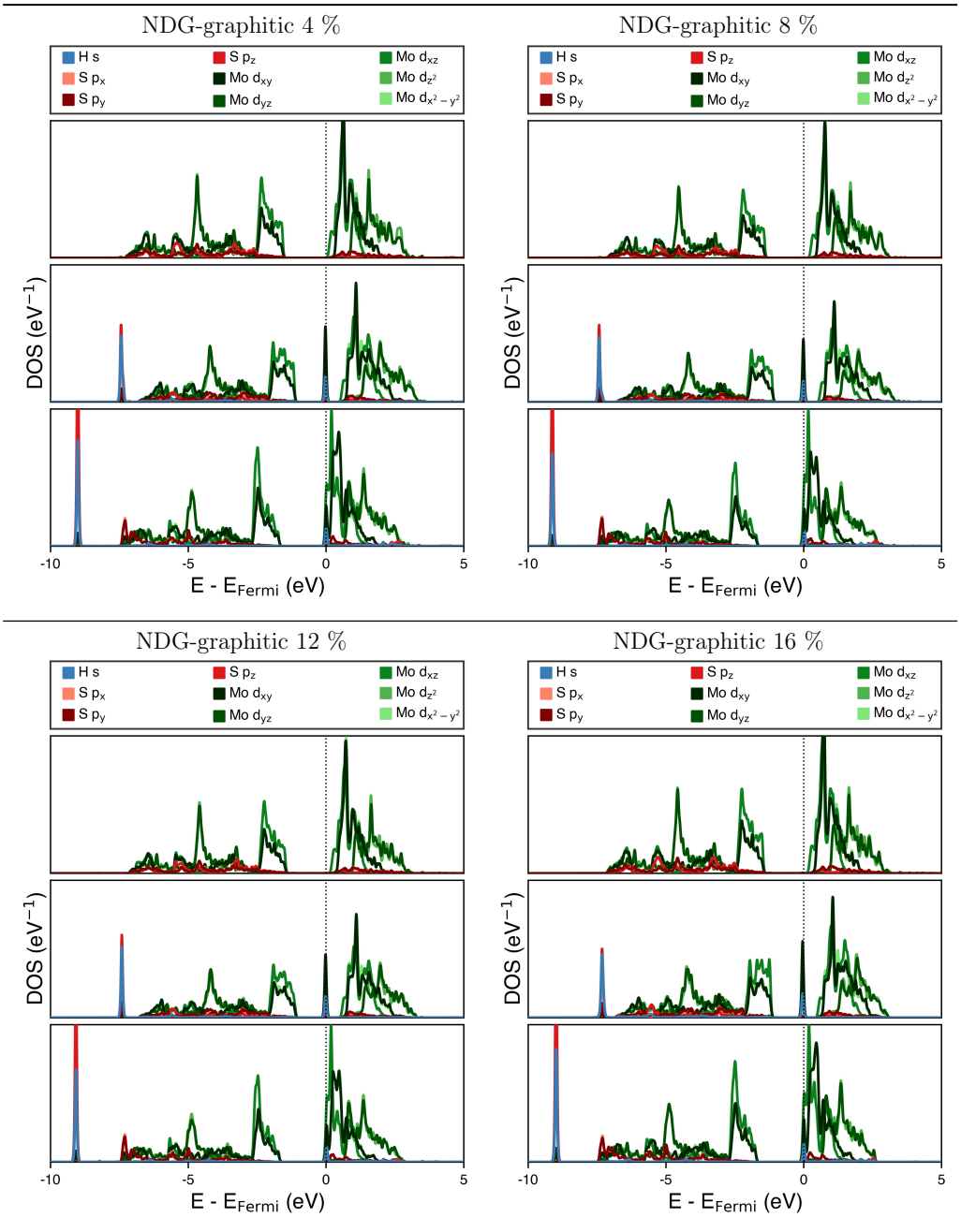

Table B.3: *Cont.*

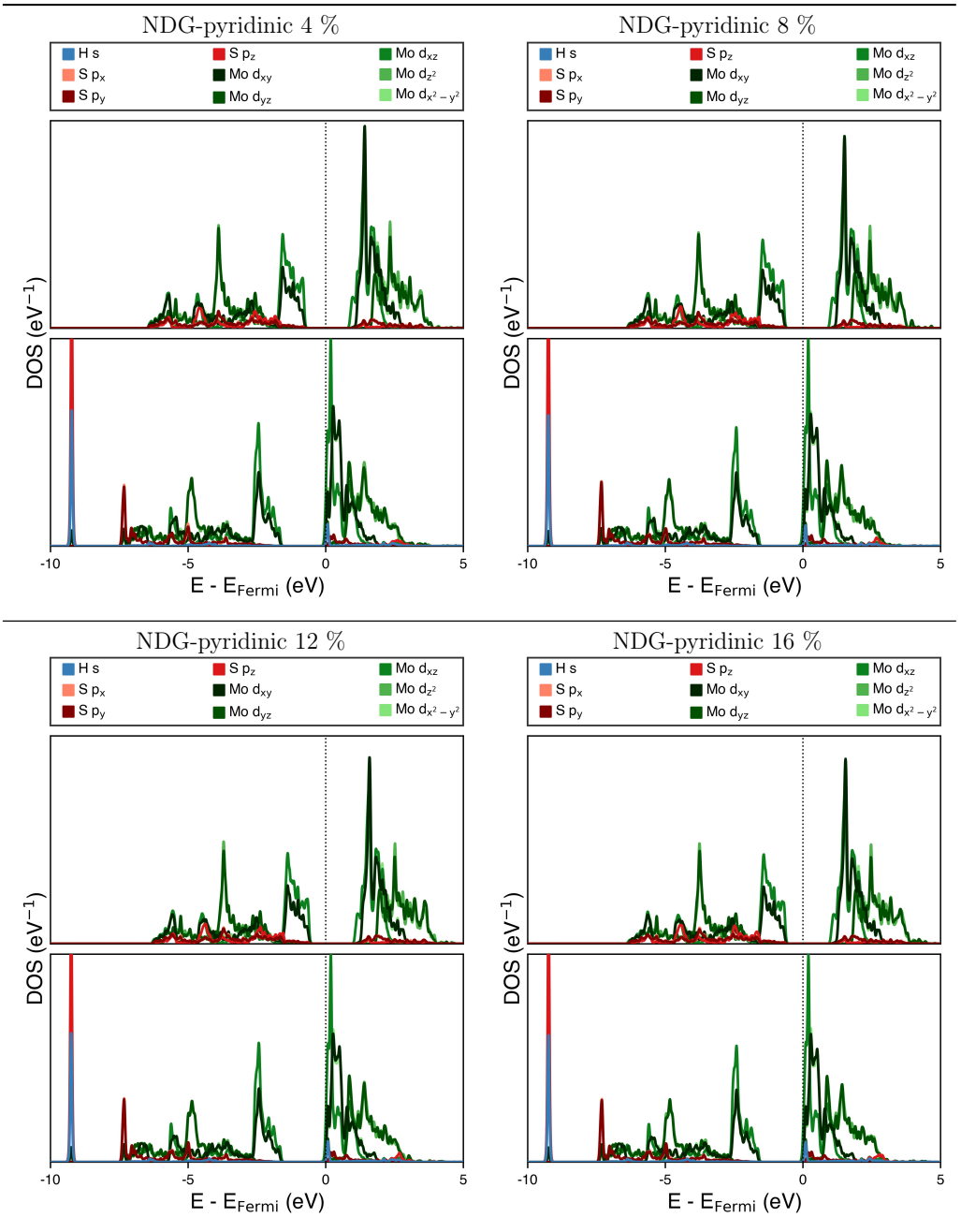

Table B.3: *Cont.*

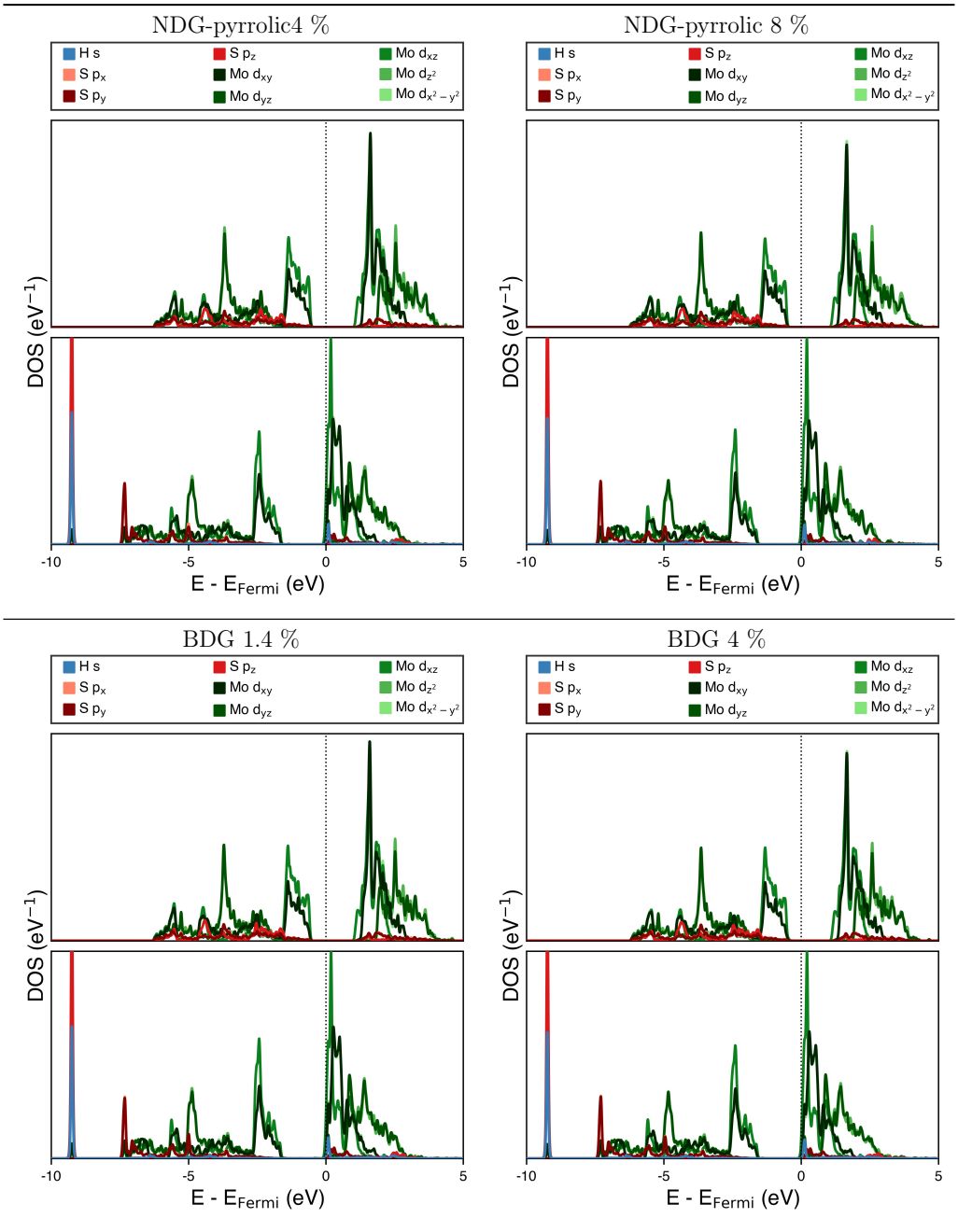

Table B.3: *Cont.*

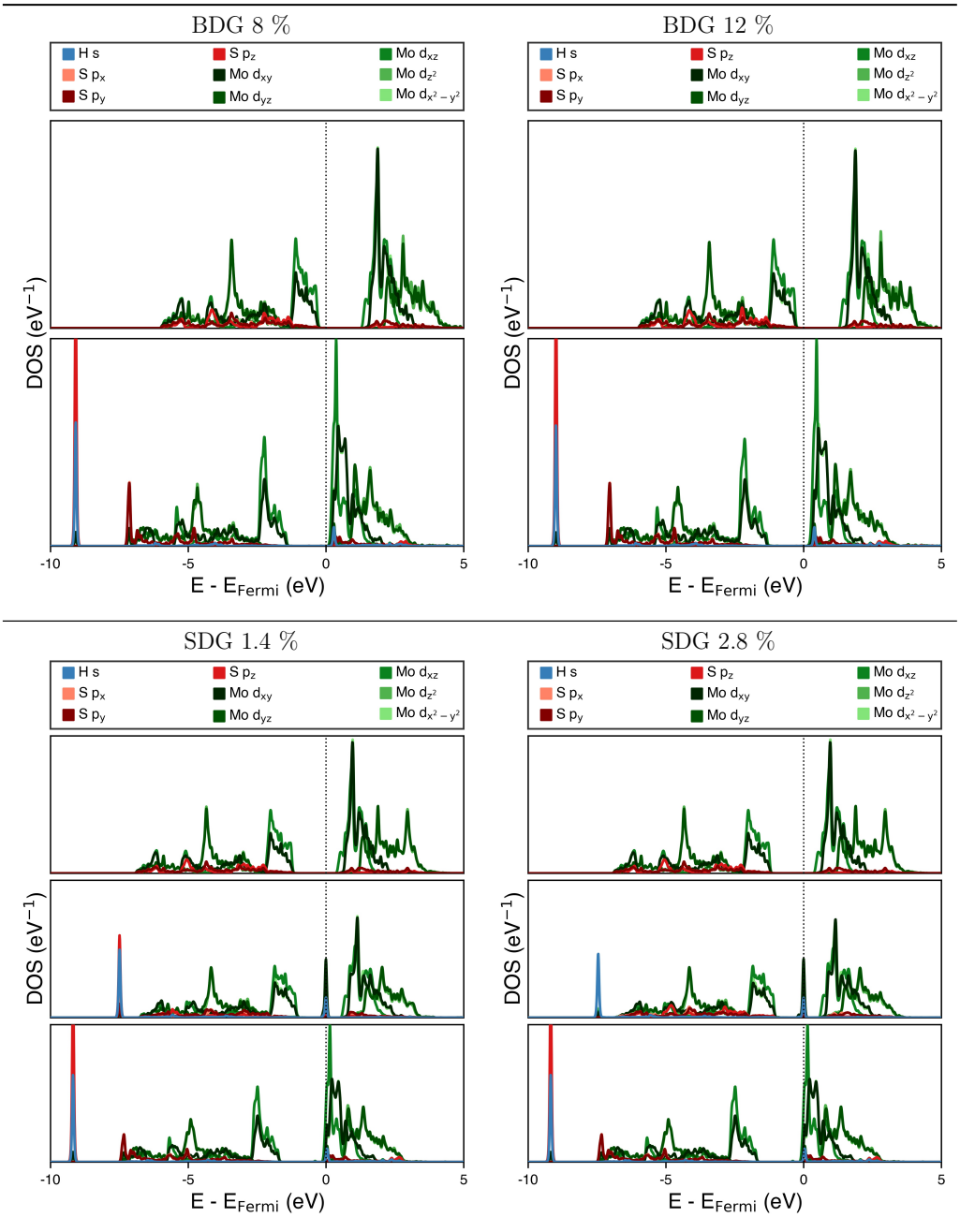

Table B.3: *Cont.*

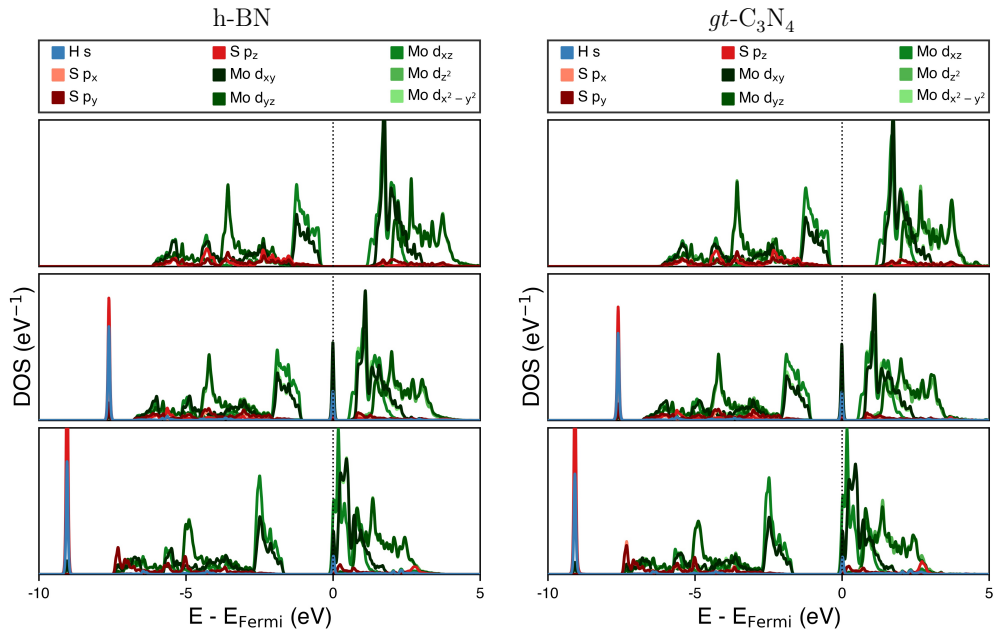

B.6 Density of states plots for MoS_2 supports

In this section the density of states plots for all the support systems are provided for reference, and to corroborate the examples selected for the main body of the thesis. In the main text, we noted that the states in the support are most perturbed when H adsorbs to MoS_2 in the on-top geometry. This observed across supports here, as the position of the peaks shifts most relative to the clean support in the H on-top case.

There is once case where an unusual Δ plot is observed for both the on-top and tilted geometries: the NDG-graphitic 16% support. This is because it was difficult to align the maximum peaks in order to perform the subtraction in this case. Thus, this Δ plot should not be relied on closely.

Table B.4: Density of states (DOS) plots for all the support materials tested here where both the on-top and tilted configurations of H binding could be located on MoS_2.

Graphene

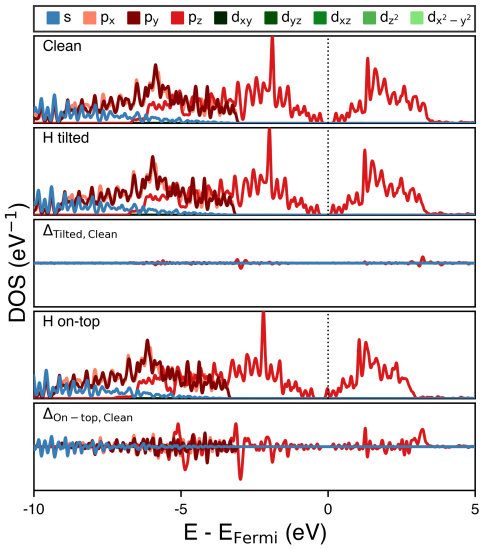

GO-epoxide 5 %

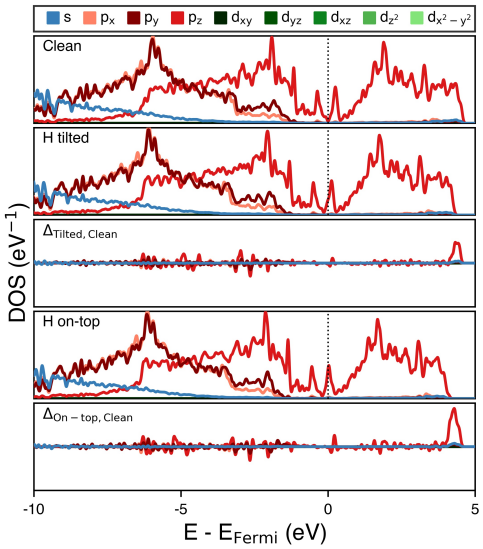

GO-epoxide 10 %

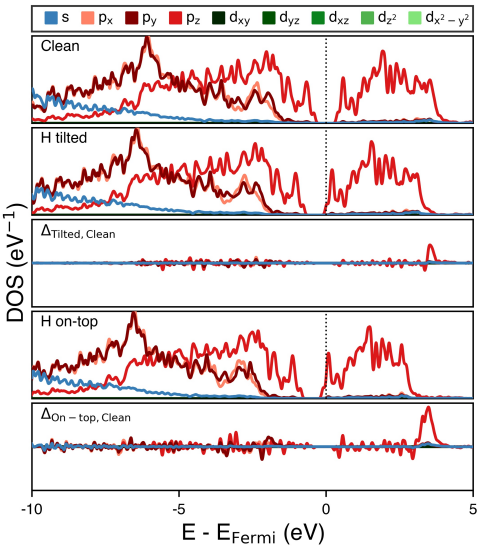

Table B.5: *Cont.*

GO-Epoxide 5 %

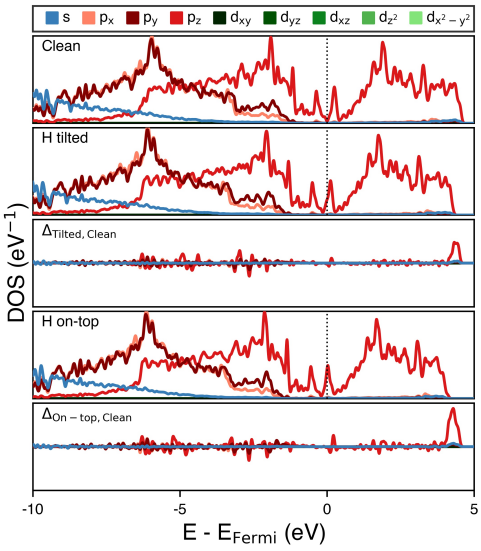

GO-Epoxide 10 %

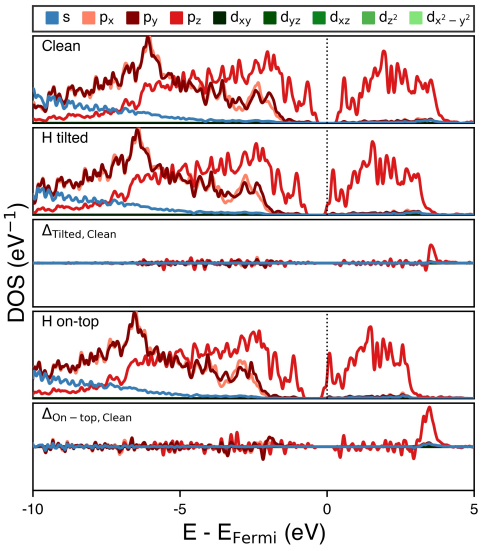

GO-Epoxide 15 %

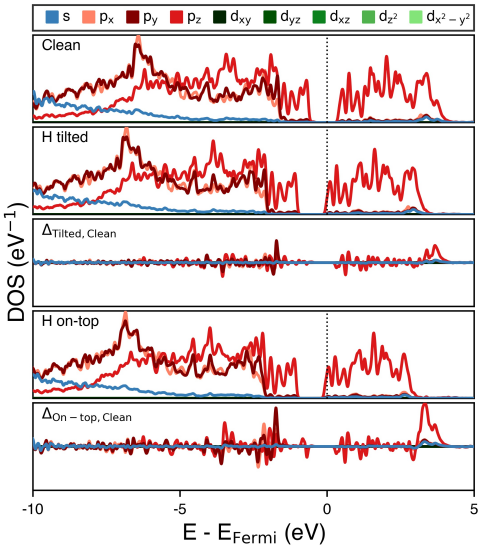

Table B.6: *Cont.*

NDG-graphitic 4 %

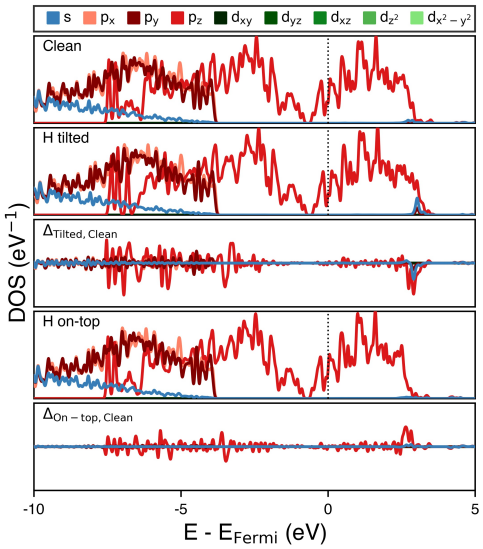

NDG-graphitic 8 %

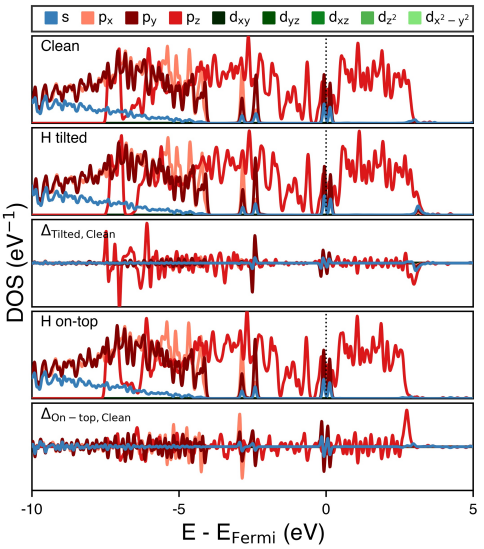

NDG-graphitic 12 %

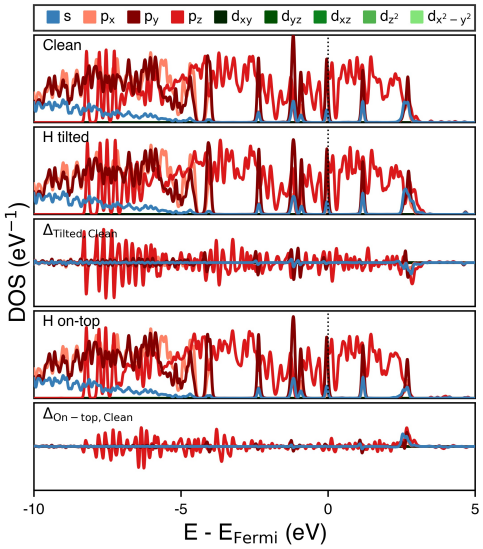

NDG-graphitic 16 %

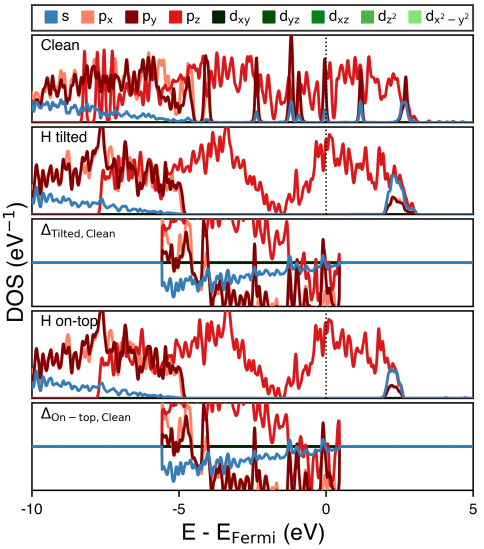

Table B.7: *Cont.*

SDG 1.4 %	SDG 2.8 %
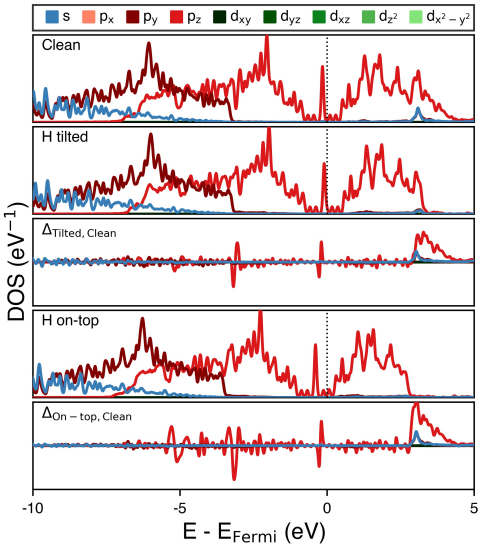	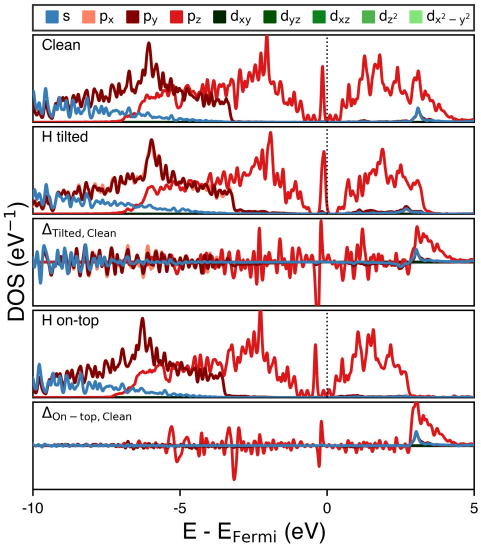

B.7 Charge density difference for tilted H binding

Figure B.3 shows a plot indicating that tilted H adsorption produces a very similar charge density difference plot to on-top H adsorption on the MoS_2 basal plane.

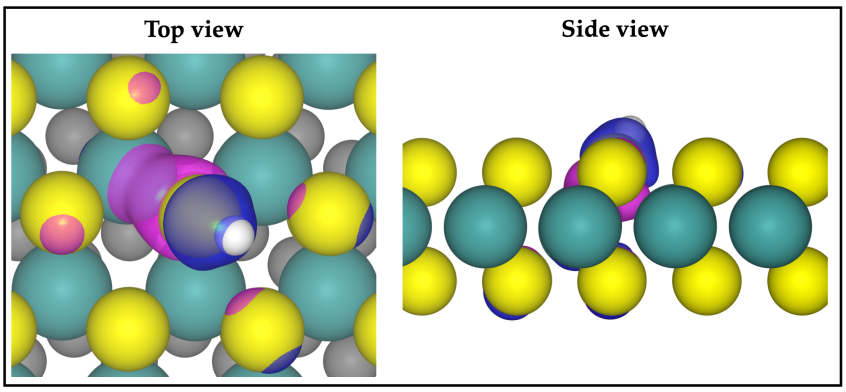

Figure B.3: Charge density difference plot showing the movement of charge in a graphene supported MoS_2 after H is adsorbed ($\rho_{MoS_2/graphene+H} - (\rho_{MoS_2/graphene} + \rho_H)$) to an S on the basal plane in the tilted configuration. Blue indicates negative charge accumulation and pink indicates negative charge depletion. Isosurface level = 0.006 e^-/A^3.

Appendix C

Additional data for Chapter 5

C.1 Plots showing the Bader charge on S atoms in MoS_2 nanotubes

In Figures C.1 to C.6, the net Bader charge on all S atoms in three test sizes for armchair and zigzag MoS_2 nanotubes are shown. The S atoms are coloured according to whether they are on the inside or the outside of the nanotube. A clear preference for electrons to accumulate slightly more on the outside S atoms is observed, and this becomes slightly more pronounced at the smaller nanotube sizes. The difference in charge is fairly small in most cases, around one tenth of an electron per S atom. But, given the consistency of this trend, it represents a reliable preference for electrons to be present on the outside of the nanotube. This is a possible reason for the difference in H adsorption energy observed on the inside *versus* outside of the tube.

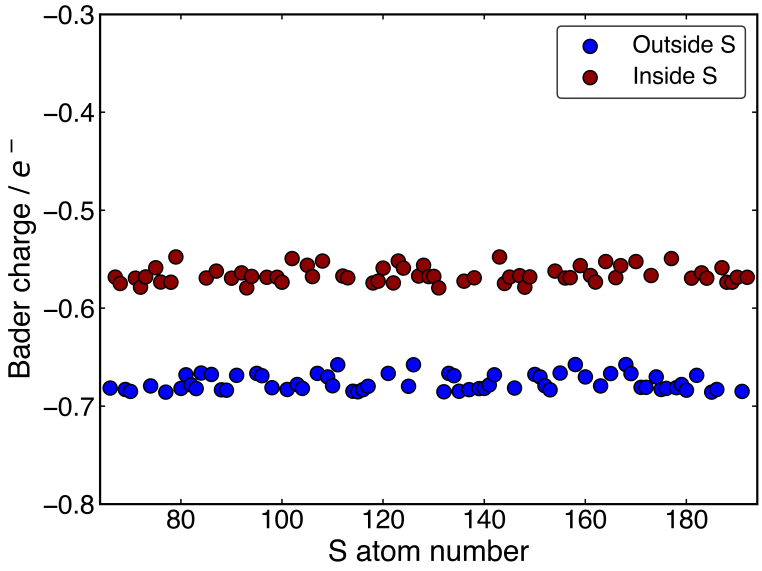

Figure C.1: Bader charge on the inside and outside S atoms in an armchair (8, 8) nanotube. The average charge gap between inside and outside is 0.11 e^-.

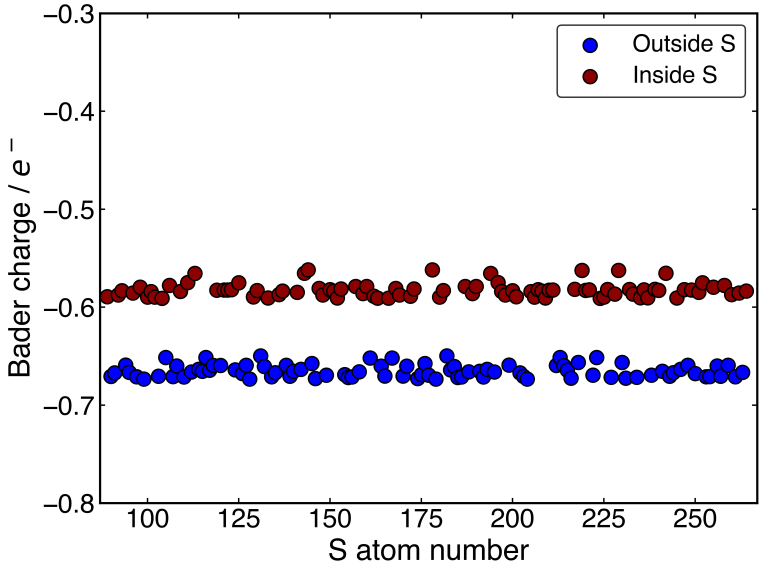

Figure C.2: Bader charge on the inside and outside S atoms in an armchair (11, 11) nanotube. The average charge gap between inside and outside is 0.10 e^-.

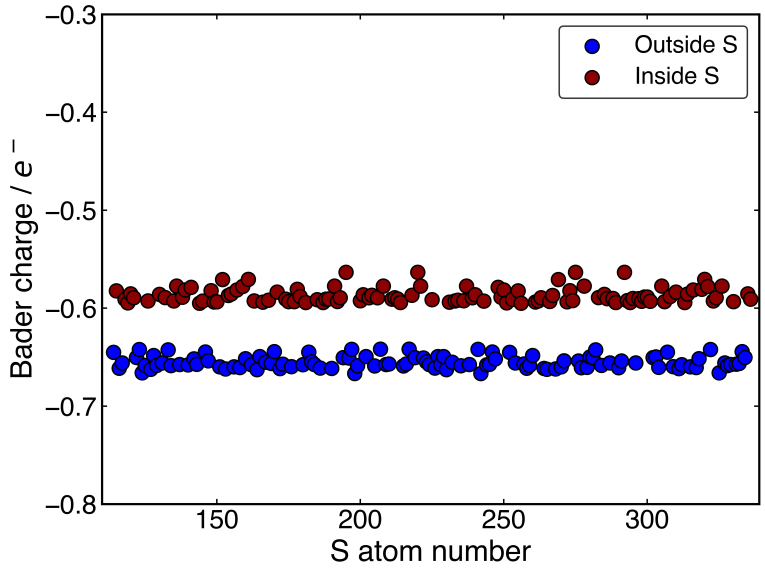

Figure C.3: Bader charge on the inside and outside S atoms in an armchair (14, 14) nanotube. The average charge gap between inside and outside is 0.07 e^-.

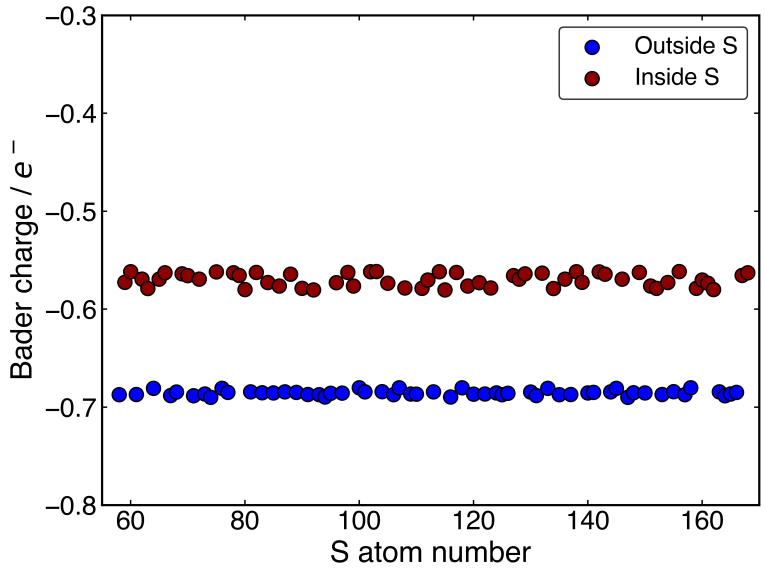

Figure C.4: Bader charge on the inside and outside S atoms in a zigzag (14, 0) nanotube. The average charge gap between inside and outside is 0.12 e^-.

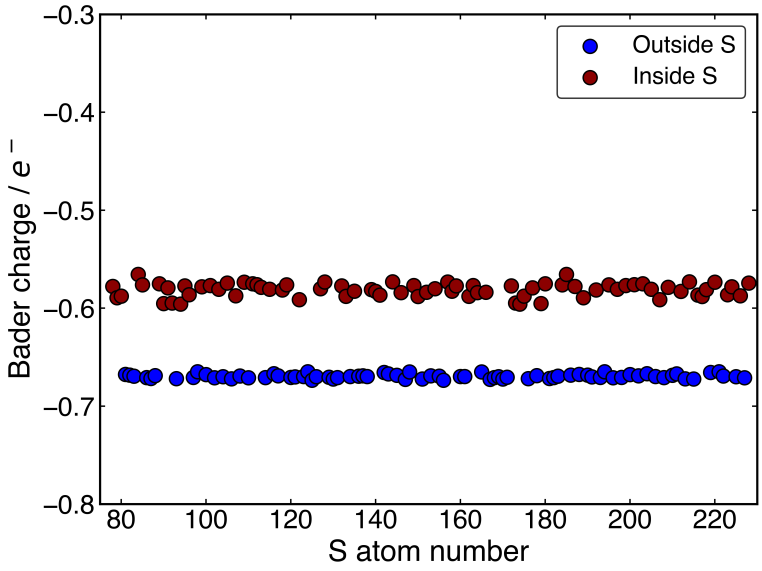

Figure C.5: Bader charge on the inside and outside S atoms in a zigzag (19, 0) nanotube. The average charge gap between inside and outside is 0.09 e^-.

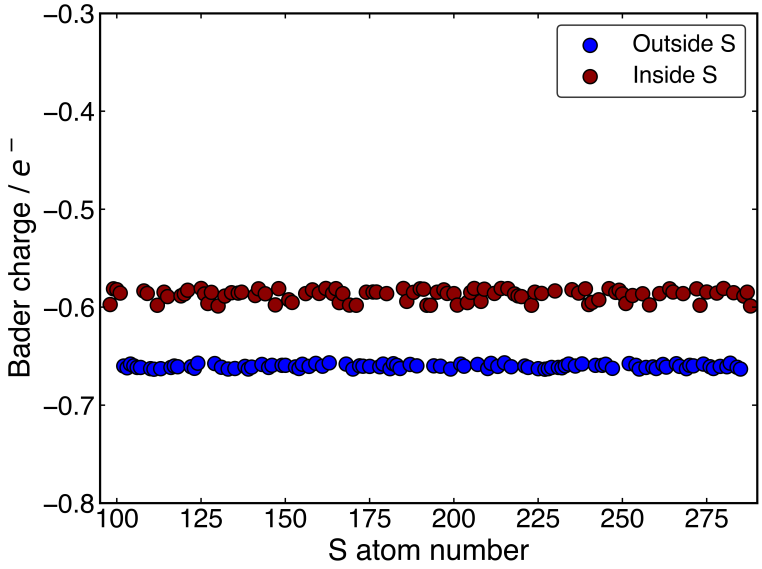

Figure C.6: Bader charge on the inside and outside S atoms in a zigzag (24, 0) nanotube. The average charge gap between inside and outside is 0.07 e^-.

C.2 Relationships involving the d-band centre

Figure C.7 demonstrates the lack of linear relationship between the Mo d-state centre and $\Delta G_{\mathrm{H_{ads}}}$. This highlights the importance of considering only the higher energy Mo d-states which are involved in bonding H, rather than all the d-states. The former quantity is captured by the upper edge of the filled d-states, which is discussed in the main body of the thesis.

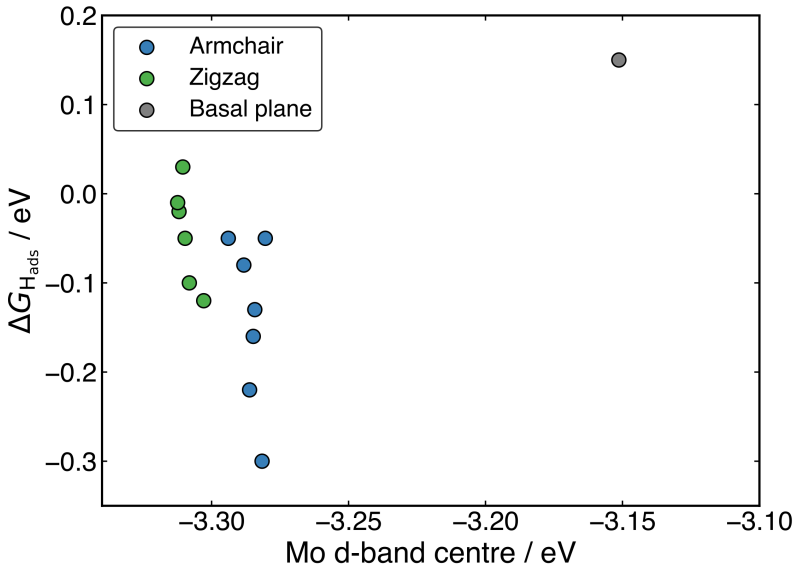

Figure C.7: A plot demonstrating the lack of relation between the Mo d-band centre and $\Delta G_{\mathrm{H_{ads}}}$ at the S-vacancy defect site. This demonstrates it is only the energy of the Mo d-states directly involved in bonding, captured by the energy of the d-state edge, which determines $\Delta G_{\mathrm{H_{ads}}}$ at this site.

C.3 Density of states plots for pristine materials studied

The following section contains the collection of density of states plots for each of pristine the materials studied in the main text. They are all organised to show the clean surface and the surface with H adsorbed at the relevant site. In each case, the specific system is noted in the Figure caption.

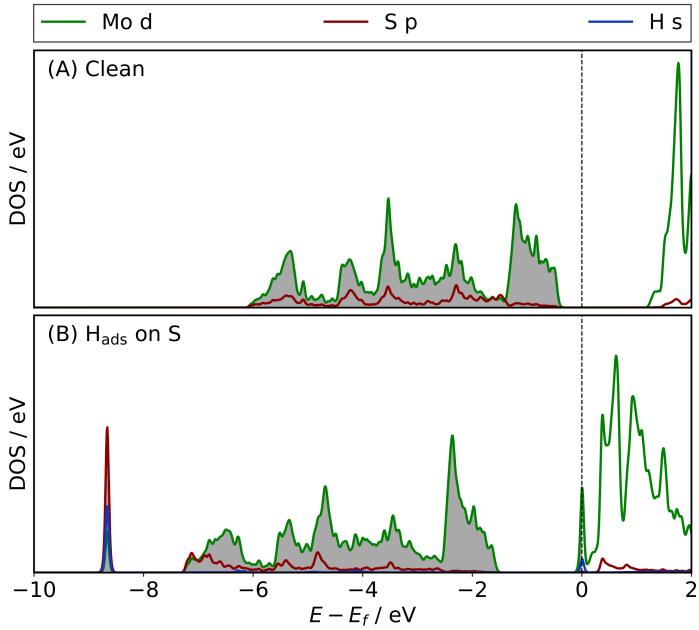

Figure C.8: Density of states plots for the flat basal plane as (A) a clean surface, and (B) with H adsorbed to S.

C.3.1 Armchair nanotubes

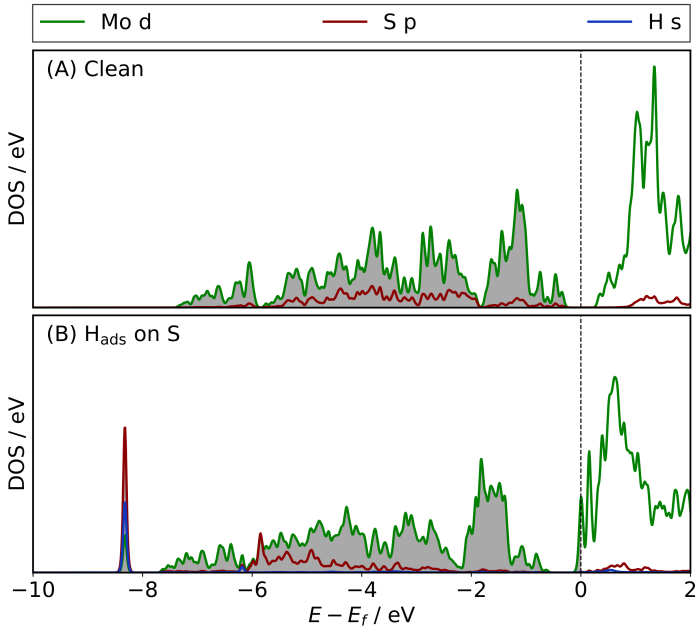

Figure C.9: Density of states plots for the (8, 8) armchair nanotube as (A) a clean surface, and (B) with H adsorbed to S.

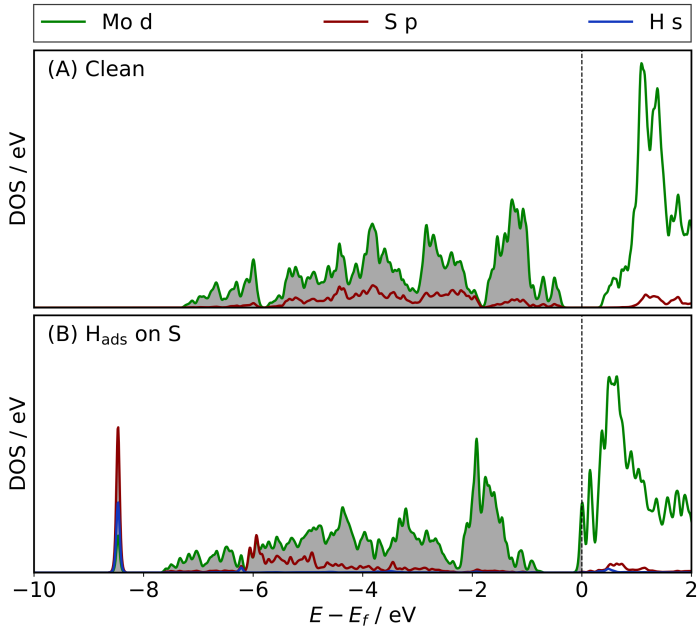

Figure C.10: Density of states plots for the (9, 9) armchair nanotube as (A) a clean surface, and (B) with H adsorbed to S.

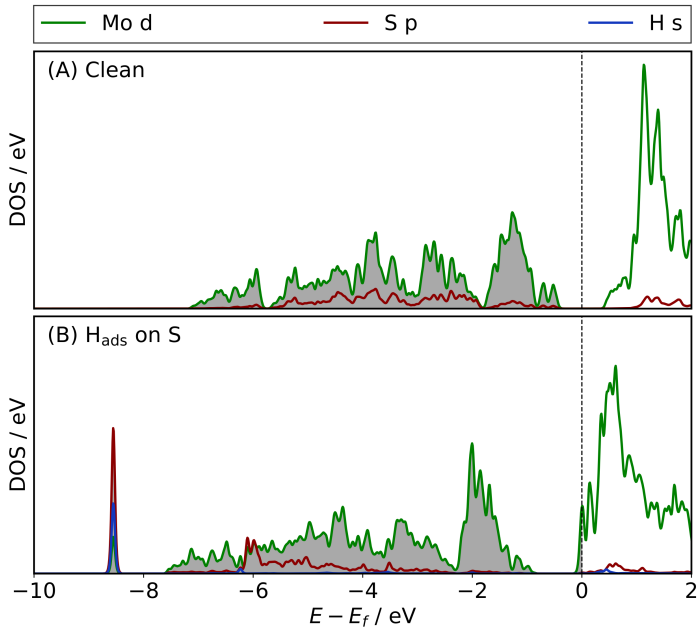

Figure C.11: Density of states plots for the (10, 10) armchair nanotube as (A) a clean surface, and (B) with H adsorbed to S.

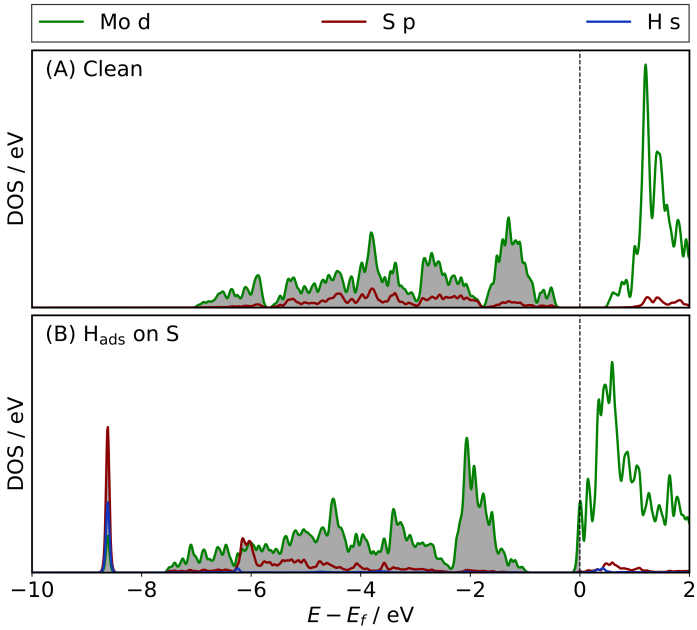

Figure C.12: Density of states plots for the (11, 11) armchair nanotube as (A) a clean surface, and (B) with H adsorbed to S.

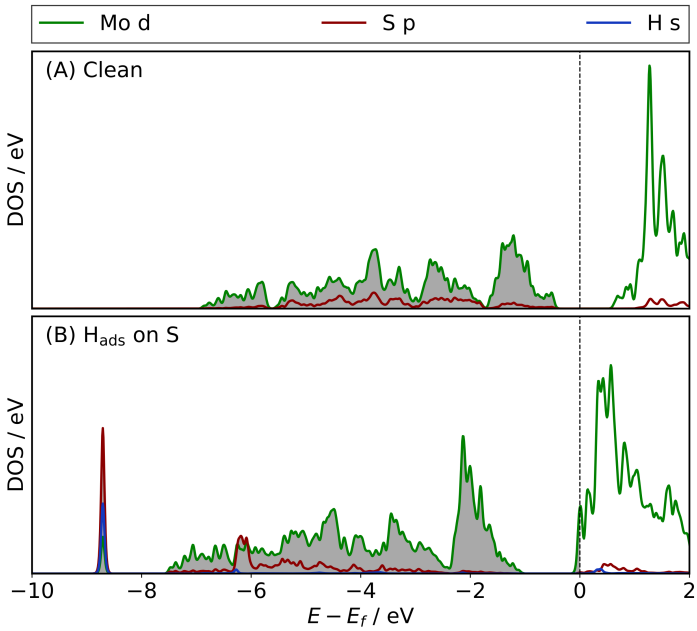

Figure C.13: Density of states plots for the (12, 12) armchair nanotube as (A) a clean surface, and (B) with H adsorbed to S.

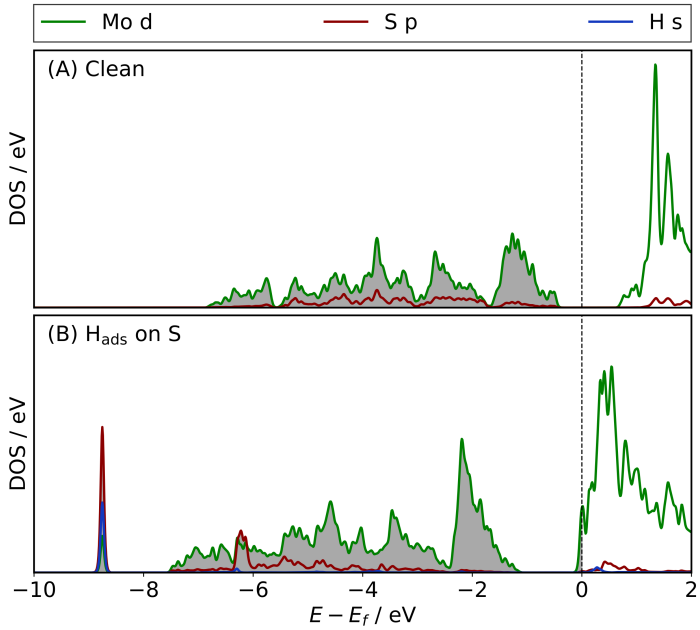

Figure C.14: Density of states plots for the (13, 13) armchair nanotube as (A) a clean surface, and (B) with H adsorbed to S.

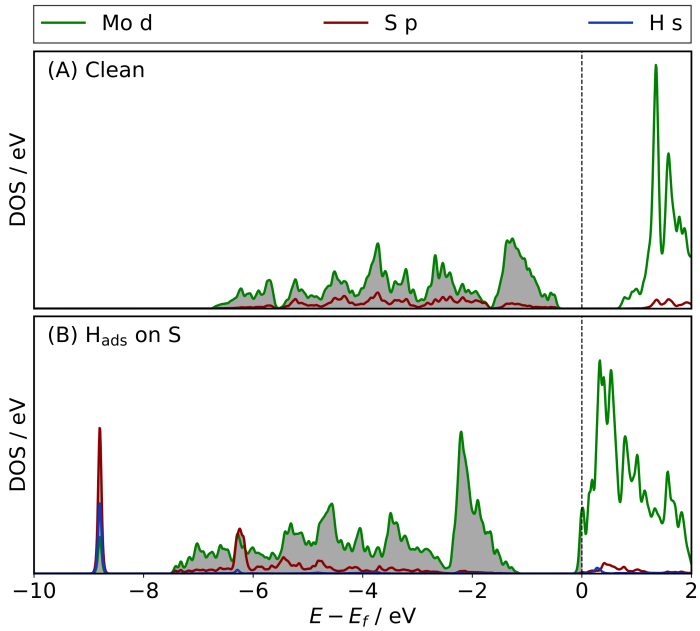

Figure C.15: Density of states plots for the (14, 14) armchair nanotube as (A) a clean surface, and (B) with H adsorbed to S.

C.3.2 Zigzag nanotubes

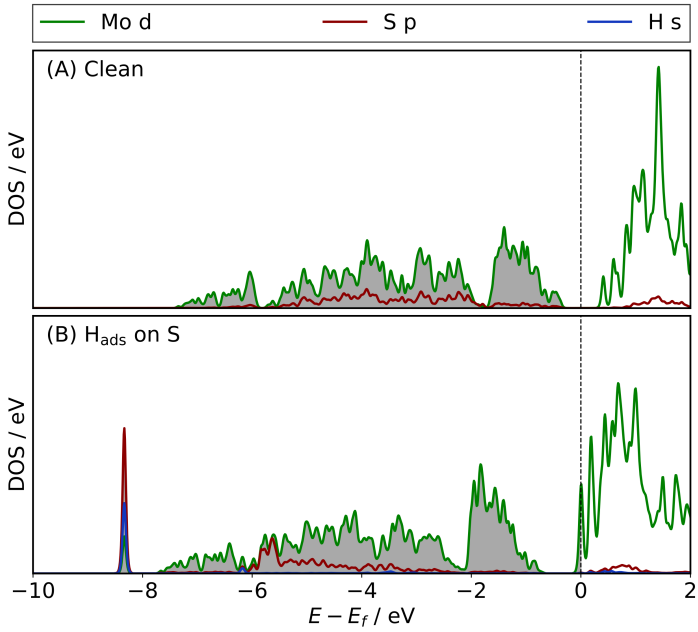

Figure C.16: Density of states plots for the (14, 0) zigzag nanotube as (A) a clean surface, and (B) with H adsorbed to S.

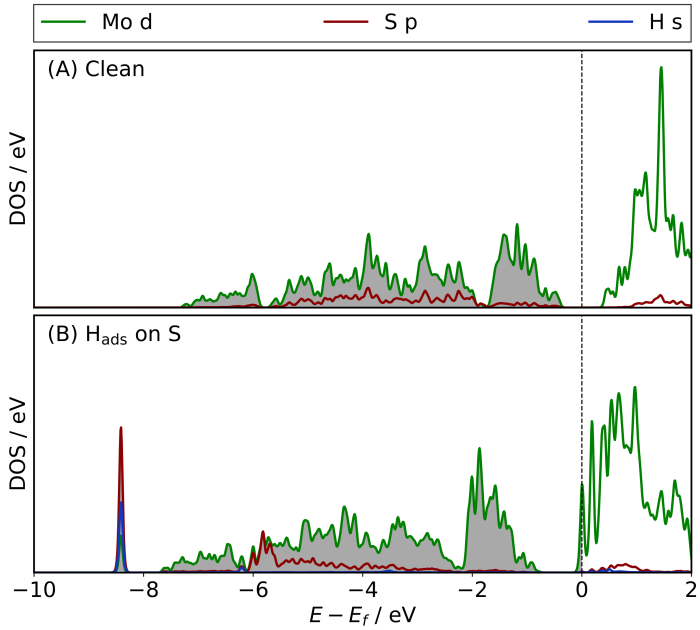

Figure C.17: Density of states plots for the (15, 0) zigzag nanotube as (A) a clean surface, and (B) with H adsorbed to S.

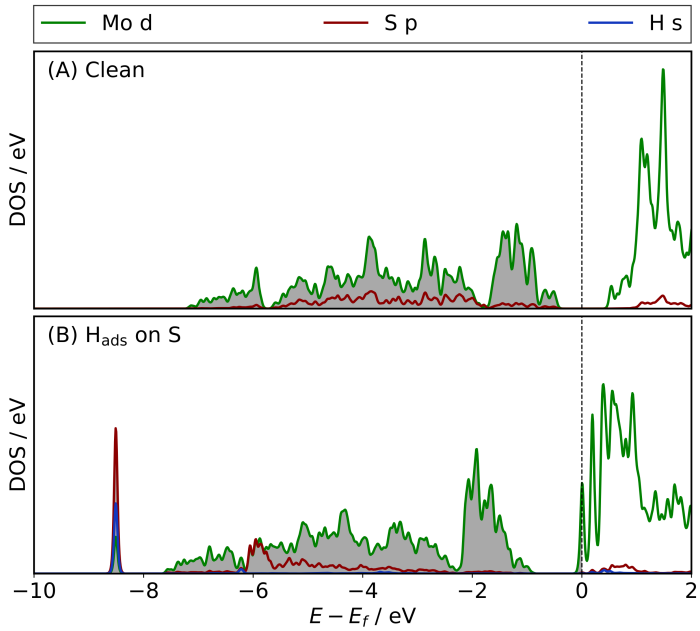

Figure C.18: Density of states plots for the (17, 0) zigzag nanotube as (A) a clean surface, and (B) with H adsorbed to S.

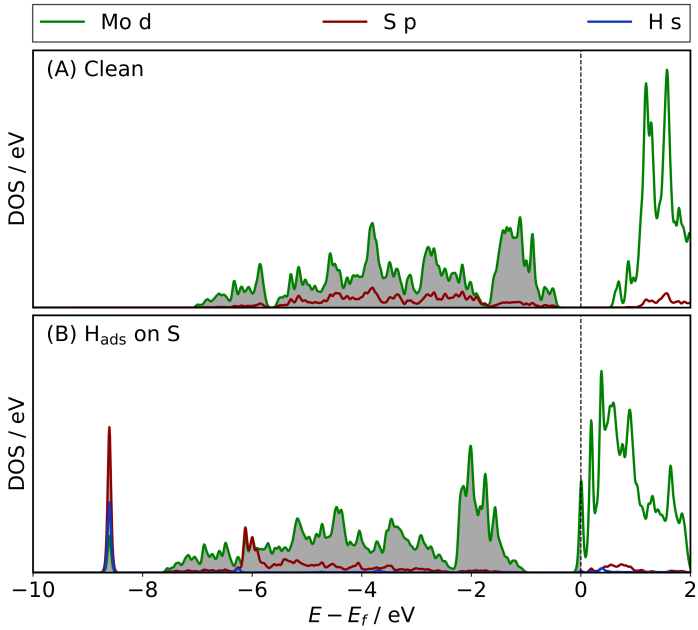

Figure C.19: Density of states plots for the (19, 0) zigzag nanotube as (A) a clean surface, and (B) with H adsorbed to S.

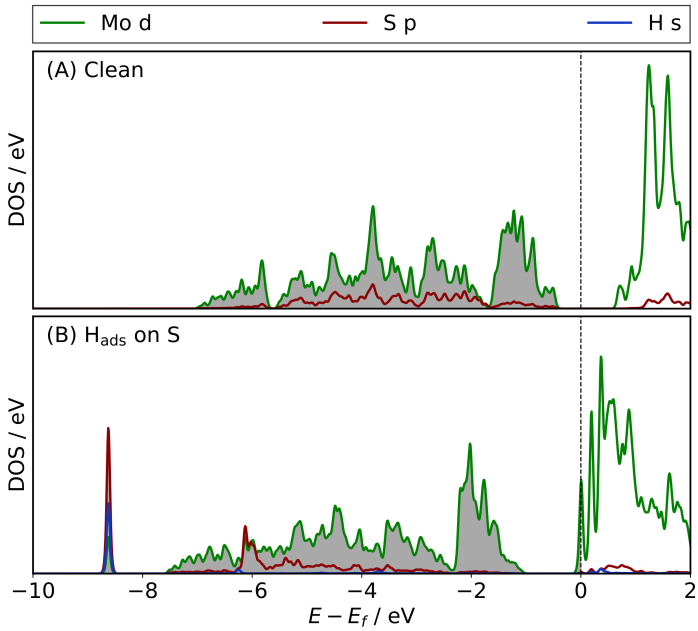

Figure C.20: Density of states plots for the (20, 0) zigzag nanotube as (A) a clean surface, and (B) with H adsorbed to S.

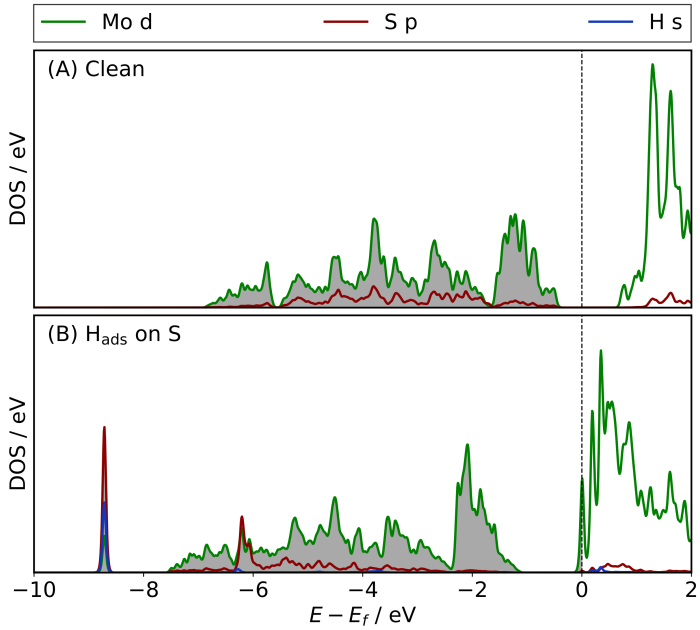

Figure C.21: Density of states plots for the (22, 0) zigzag nanotube as (A) a clean surface, and (B) with H adsorbed to S.

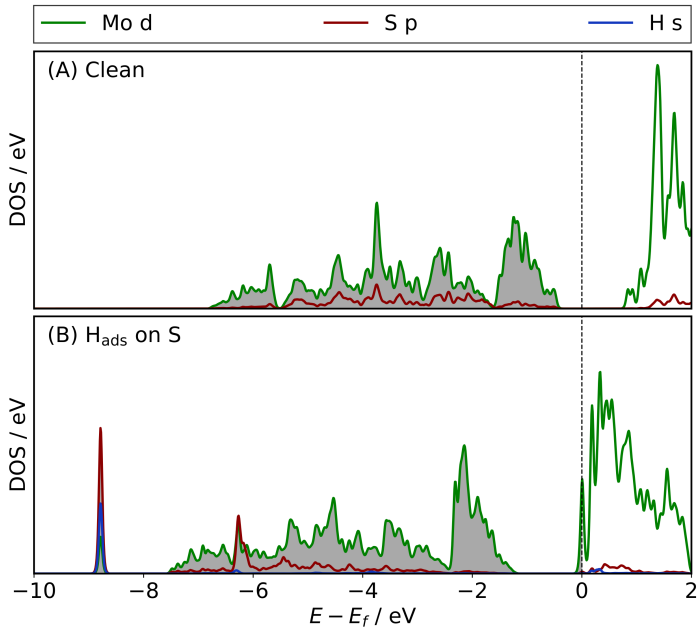

Figure C.22: Density of states plots for the (24, 0) zigzag nanotube as (A) a clean surface, and (B) with H adsorbed to S.

C.4 Density of states plots for S-vacancy defect materials studied

The following section contains the collection of density of states plots for all the S-vacancy defect sites in the materials studied in the main text. They are all organised to show the clean surface and the surface with H adsorbed at the relevant site. In each case, the specific system is noted in the Figure caption.

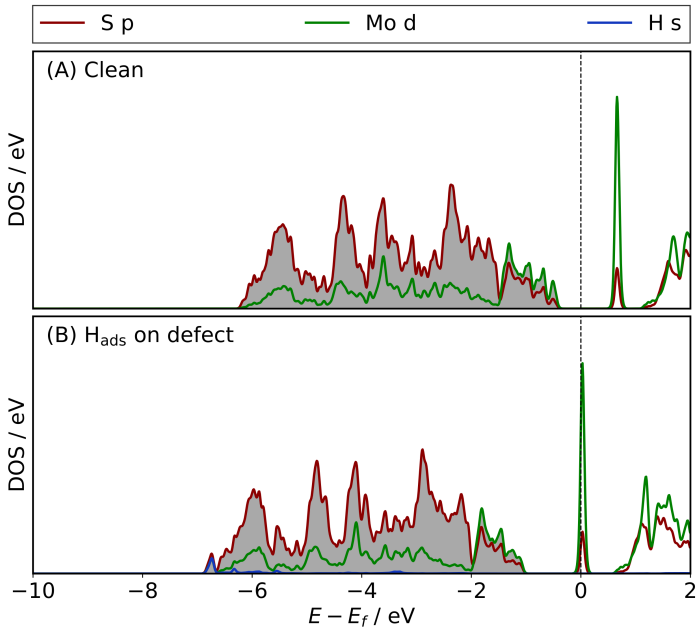

Figure C.23: Density of states plots for the S-vacancy site on the flat basal plane as (A) a clean surface, and (B) with H adsorbed to S.

C.4.1 S-vacancy armchair nanotubes

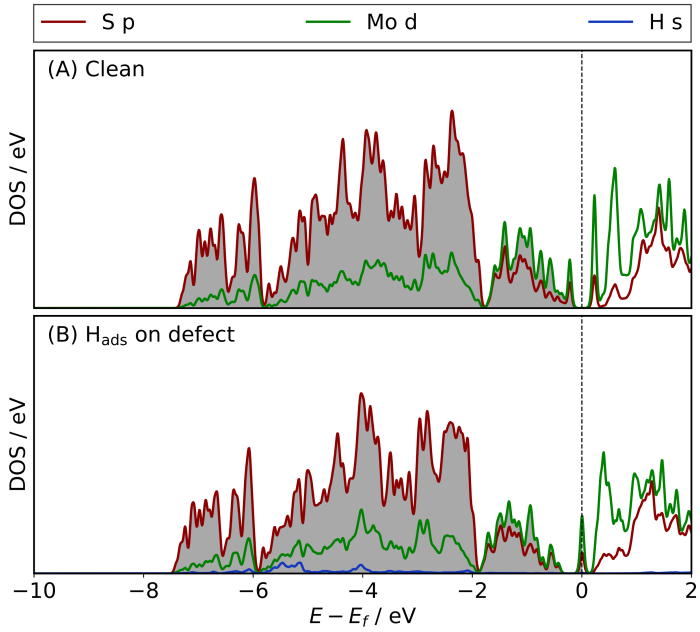

Figure C.24: Density of states plots for the S-vacancy defect on the (8, 8) armchair nanotube as (A) a clean surface, and (B) with H adsorbed at the S-vacancy-.

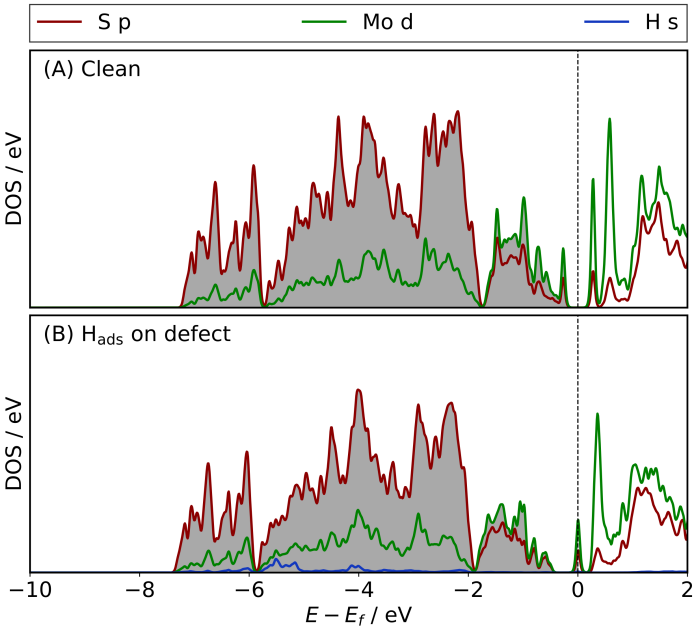

Figure C.25: Density of states plots for the S-vacancy defect on the (9, 9) armchair nanotube as (A) a clean surface, and (B) with H adsorbed at the S-vacancy.

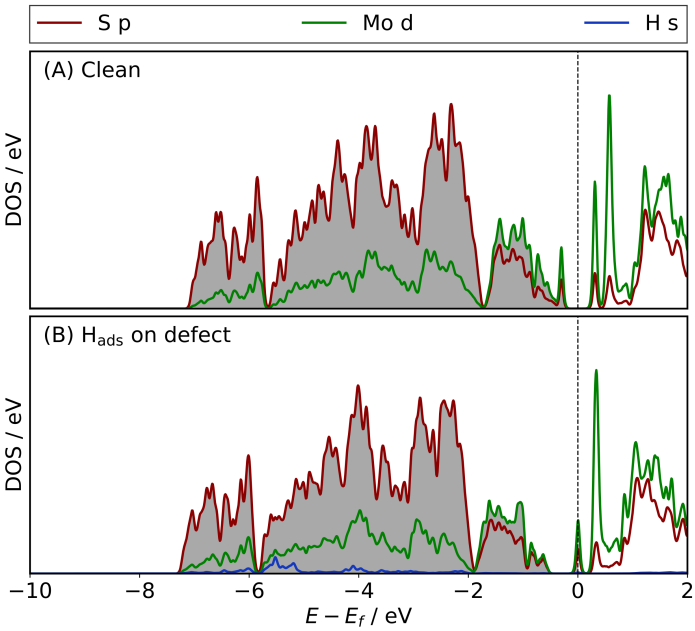

Figure C.26: Density of states plots for the S-vacancy defect on the (10, 10) armchair nanotube as (A) a clean surface, and (B) with H adsorbed at the S-vacancy.

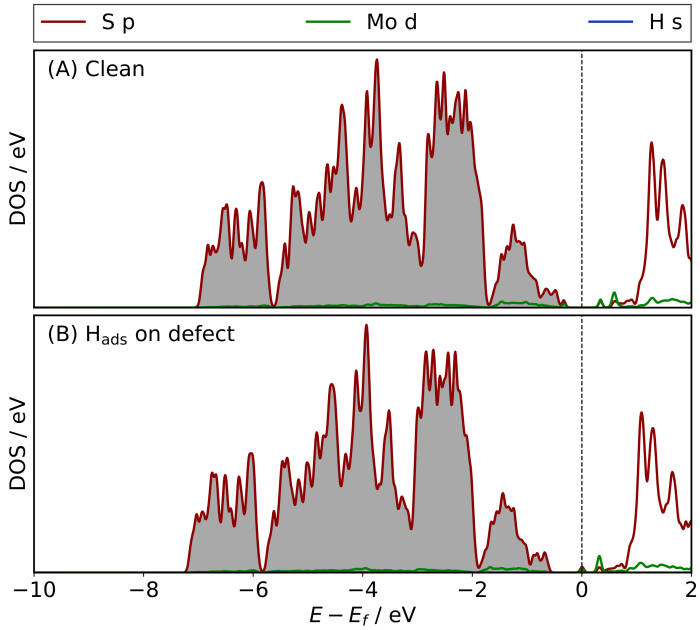

Figure C.27: Density of states plots for the S-vacancy defect on the (11, 11) armchair nanotube as (A) a clean surface, and (B) with H adsorbed at the S-vacancy.

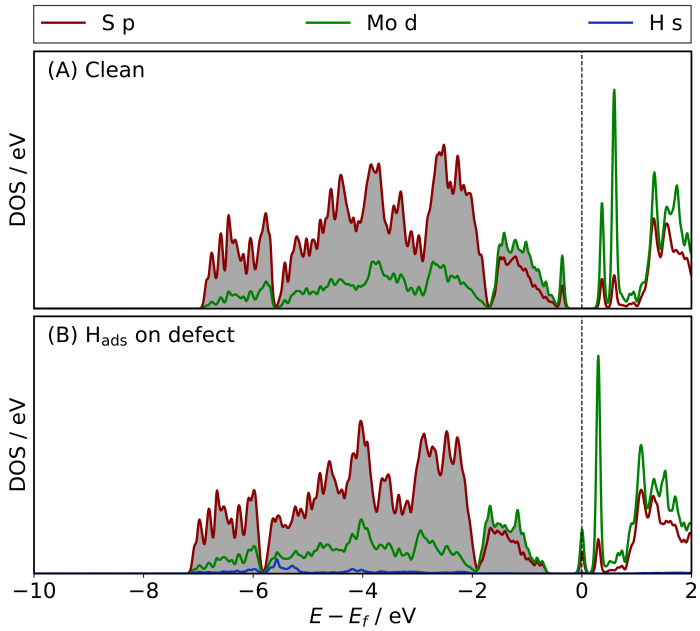

Figure C.28: Density of states plots for the S-vacancy defect on the (12, 12) armchair nanotube as (A) a clean surface, and (B) with H adsorbed at the S-vacancy.

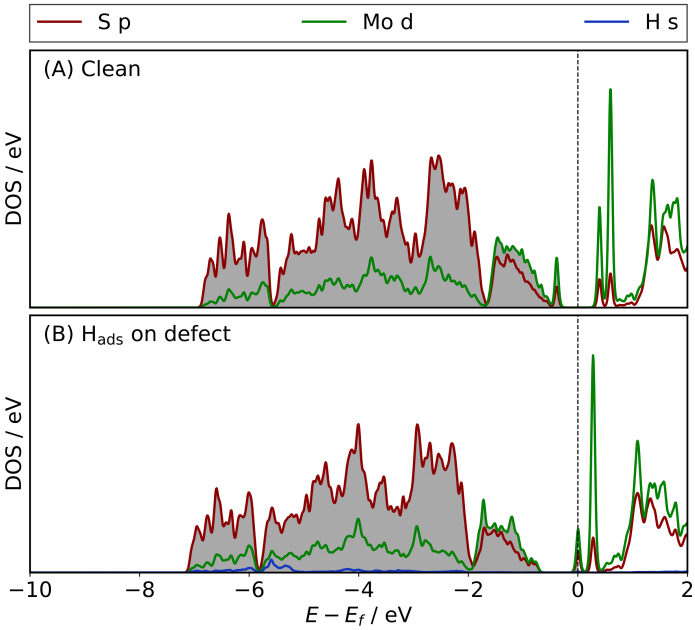

Figure C.29: Density of states plots for the S-vacancy defect on the (13, 13) armchair nanotube as (A) a clean surface, and (B) with H adsorbed at the S-vacancy.

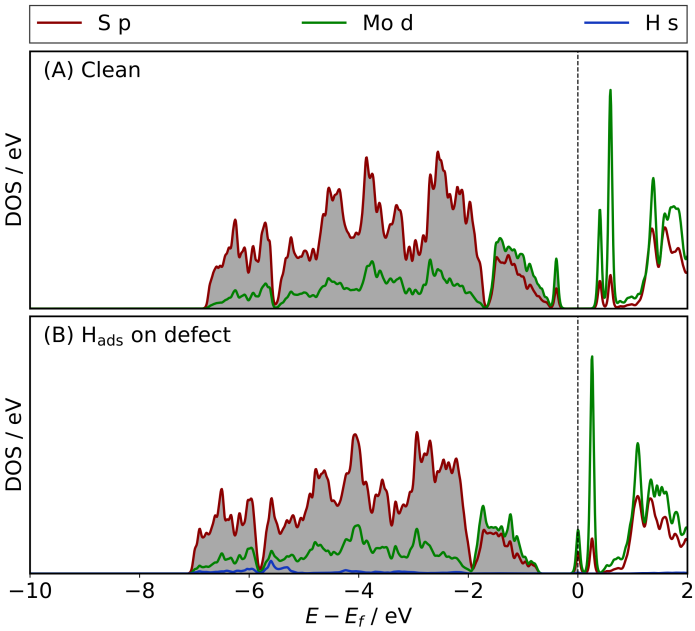

Figure C.30: Density of states plots for the S-vacancy defect on the (14, 14) armchair nanotube as (A) a clean surface, and (B) with H adsorbed at the S-vacancy.

C.4.2 S-vacancy zigzag nanotubes

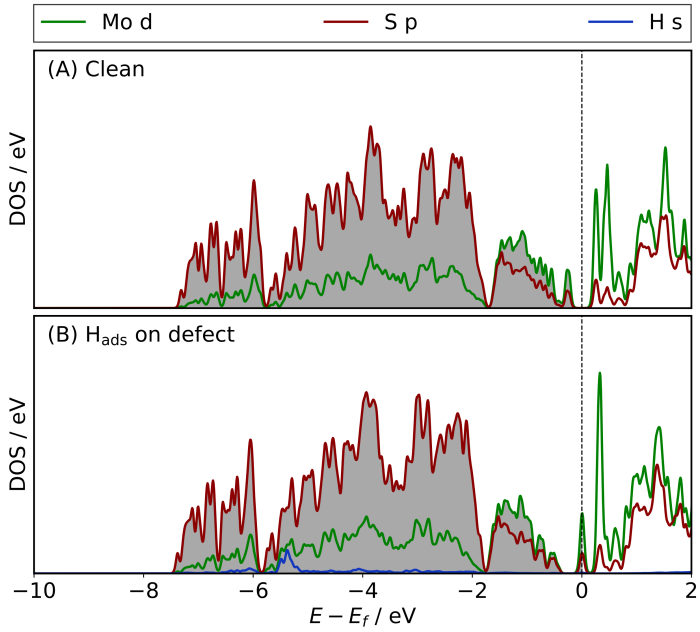

Figure C.31: Density of states plots for the S-vacancy defect on the (14, 0) zigzag nanotube as (A) a clean surface, and (B) with H adsorbed at the S-vacancy.

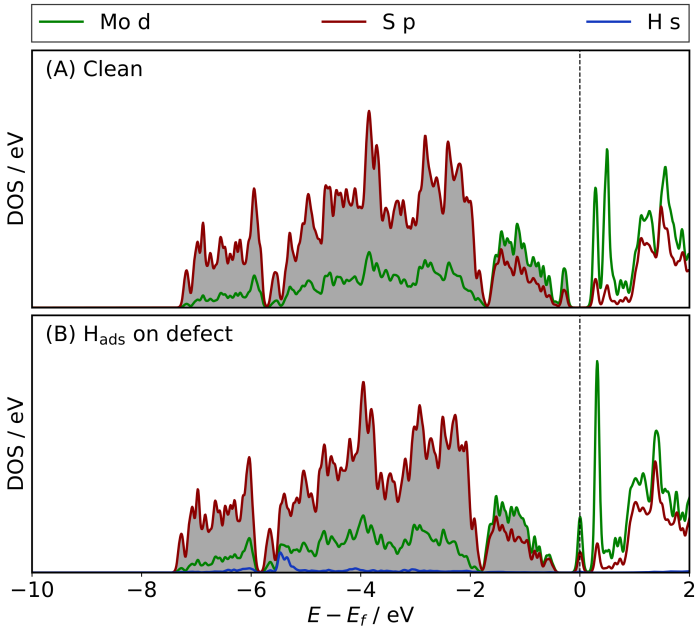

Figure C.32: Density of states plots for the S-vacancy defect on the (15, 0) zigzag nanotube as (A) a clean surface, and (B) with H adsorbed at the S-vacancy.

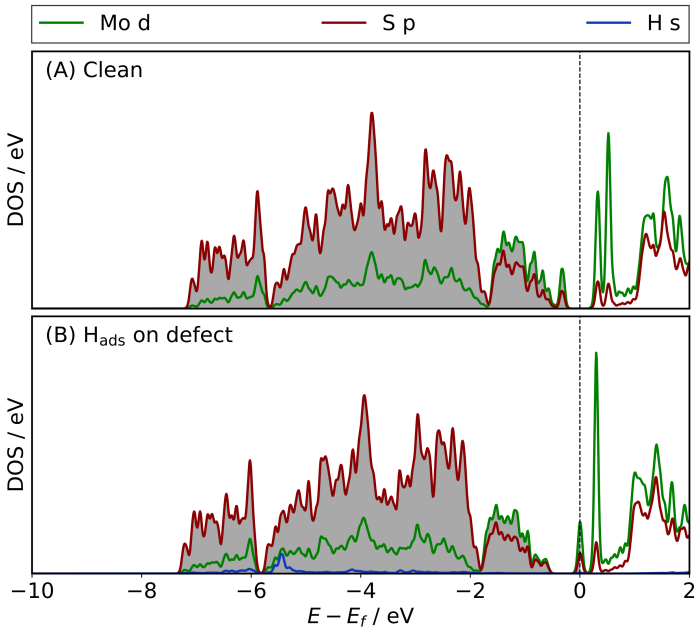

Figure C.33: Density of states plots for the S-vacancy defect on the (17, 0) zigzag nanotube as (A) a clean surface, and (B) with H adsorbed at the S-vacancy.

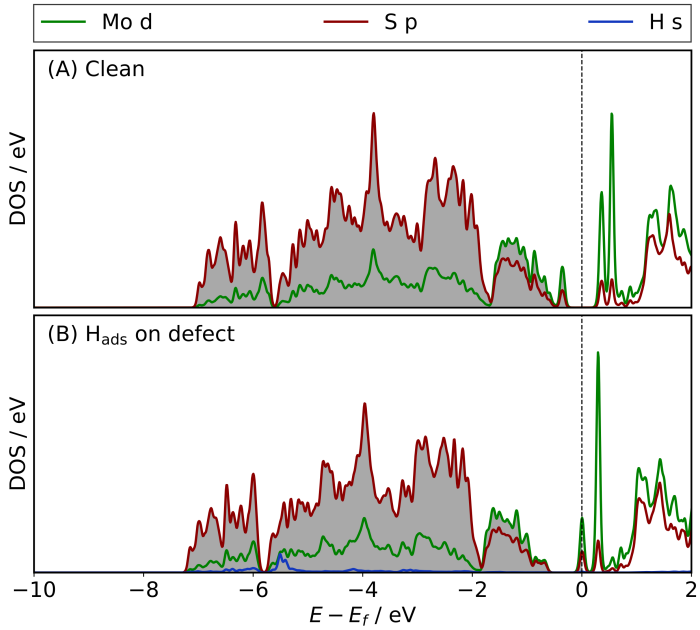

Figure C.34: Density of states plots for the S-vacancy defect on the (19, 0) zigzag nanotube as (A) a clean surface, and (B) with H adsorbed at the S-vacancy.

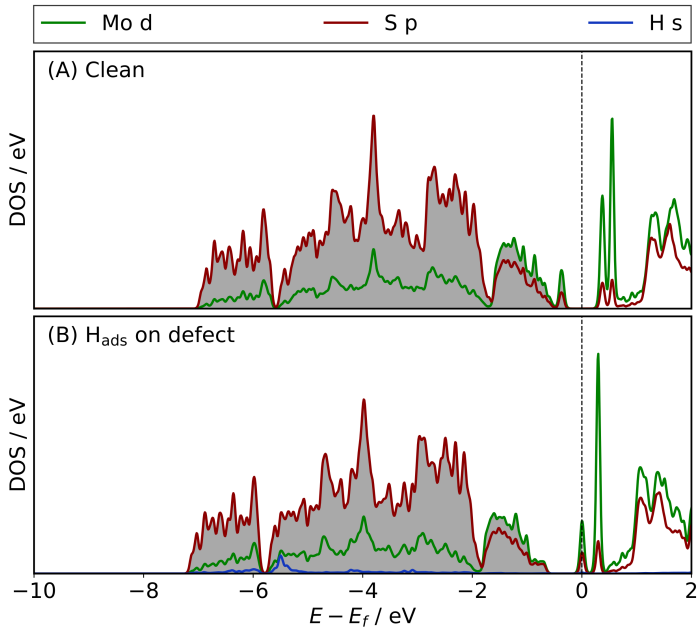

Figure C.35: Density of states plots for the S-vacancy defect on the (20, 0) zigzag nanotube as (A) a clean surface, and (B) with H adsorbed at the S-vacancy.

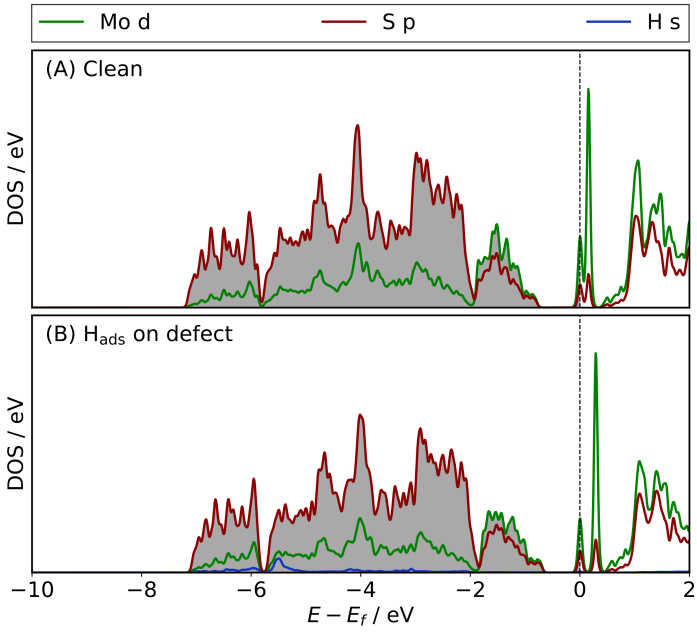

Figure C.36: Density of states plots for the S-vacancy defect on the (22, 0) zigzag nanotube as (A) a clean surface, and (B) with H adsorbed at the S-vacancy.

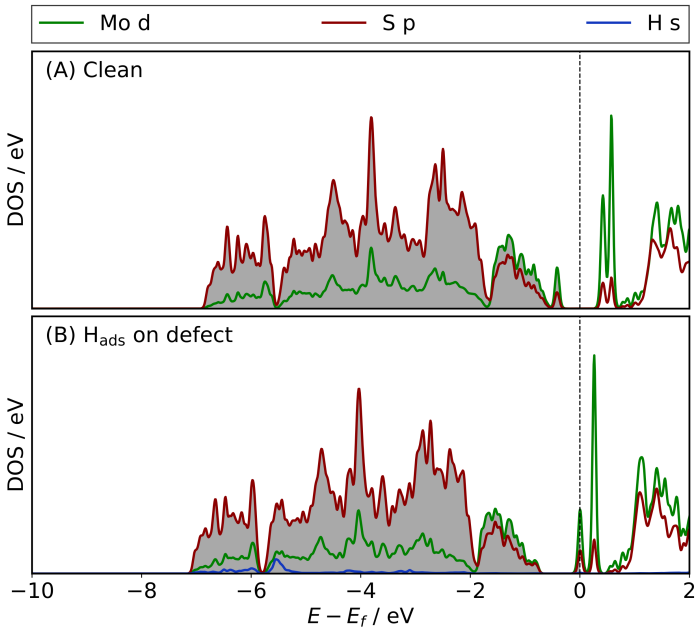

Figure C.37: Density of states plots for the S-vacancy defect on the (24, 0) zigzag nanotube as (A) a clean surface, and (B) with H adsorbed at the S-vacancy.

Appendix D

Additional data for Chapter 6

D.1 Space-filling models for TaN and Ta_3N_5 clusters

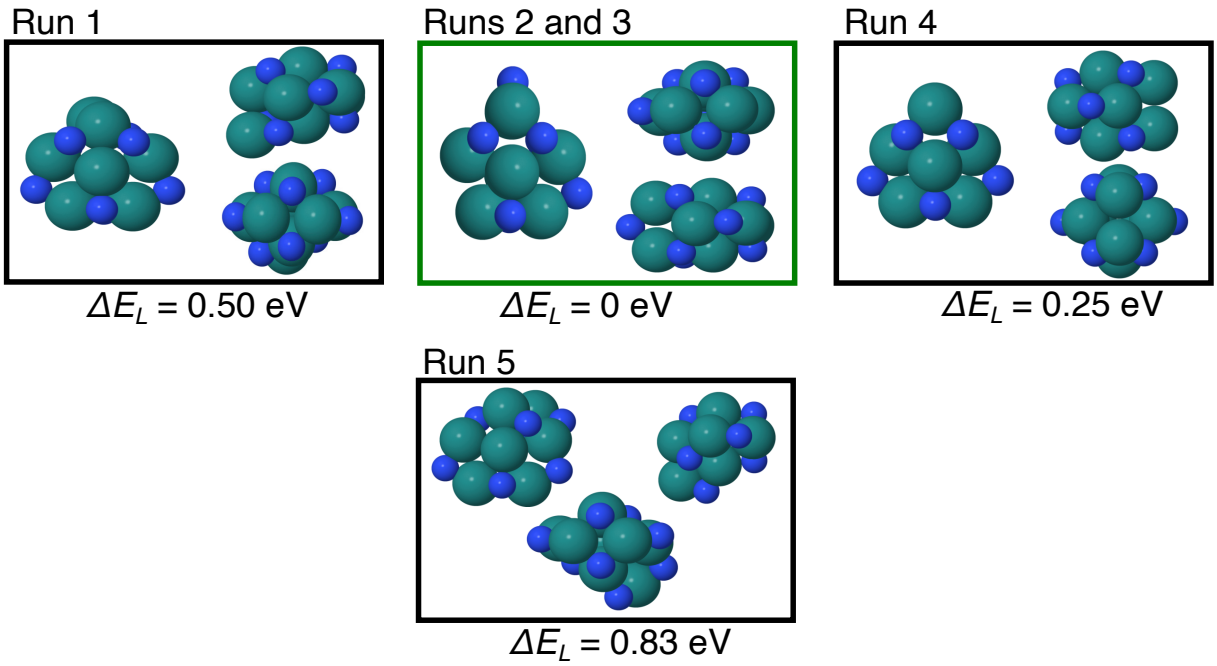

Figure D.1: The lowest energy structures of Ta_8N_8 obtained from five separate GOFEE global optimisations presented as space-filling models. These structures have all been locally optimised using DFT. A green box indicates the lowest energy structure identified, and the energies of all clusters are given relative to this structure. Key: Ta – green, N – blue.

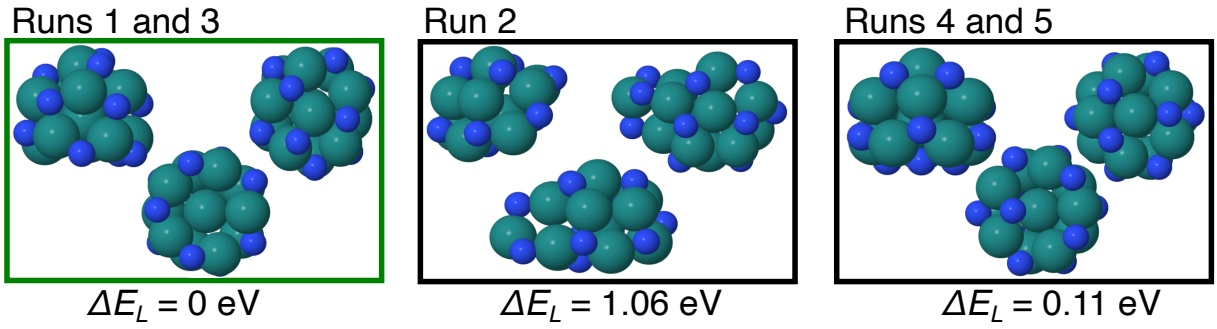

Figure D.2: The lowest energy structures of $Ta_{12}N_{12}$ obtained from five separate GOFEE global optimisations presented as space-filling models. These structures have all been locally optimised using DFT. A green box indicates the lowest energy structure identified, and the energies of all clusters are given relative to this structure. Key: Ta – green, N – blue.

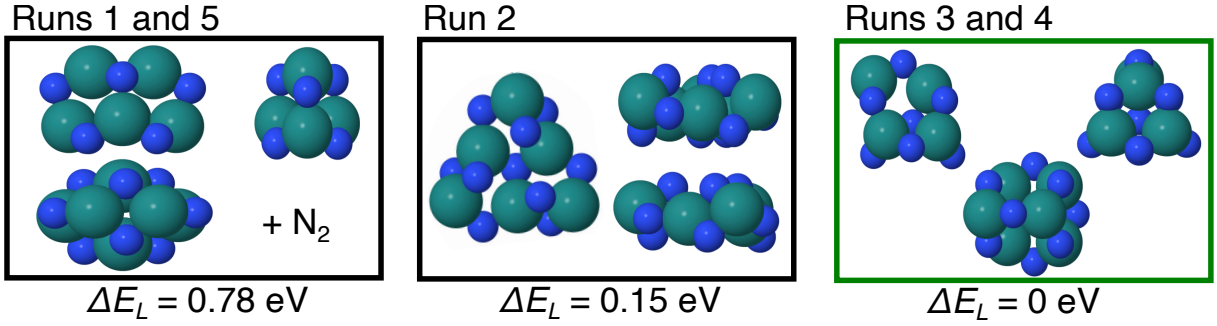

Figure D.3: The lowest energy structures of Ta_6N_{10} obtained from five separate GOFEE global optimisations presented as space-filling models. These structures have all been locally optimised using DFT. A green box indicates the lowest energy structure identified, and the energies of all clusters are given relative to this structure. Key: Ta – green, N – blue.

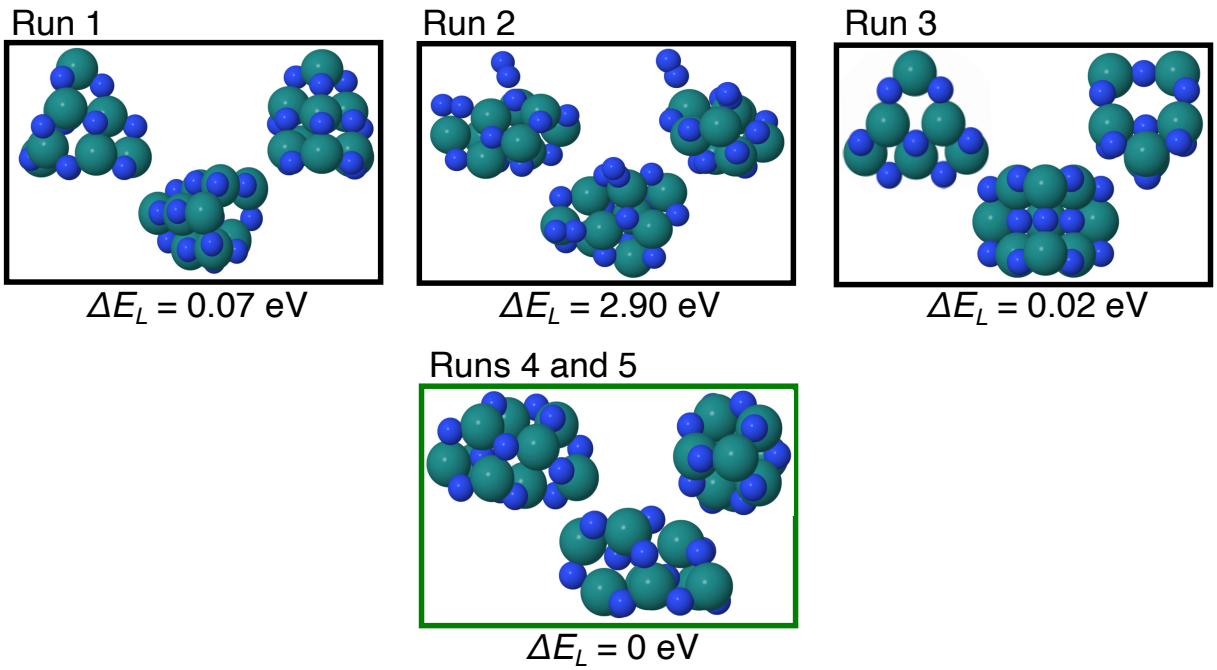

Figure D.4: The lowest energy structures of Ta_9N_{15} obtained from five separate GOFEE global optimisations presented as space-filling models. These structures have all been locally optimised using DFT. A green box indicates the lowest energy structure identified, and the energies of all clusters are given relative to this structure. Key: Ta – green, N – blue.